

CMUG Phase 2 Deliverable

Reference: D3.1: Quality Assessment Report
Due date: June 2017
Submission date: 21 December 2017
Version: 4



Climate Modelling User Group

Phase 2 Deliverable 3.1 Quality Assessment Report

Version 4

Centres providing input: Met Office, MPI-M, ECMWF, MétéoFrance, SMHI, DLR, IPSL, BSC, VUB, ULB

Version nr.	Date	Status
3.0a	19 May 2017	First Draft
3.0b	8 June 2017	Contributions from all partners
3.0c	18 August 2017	First submission to ESA
4.0	20 December 2017	Updated Section 3.1 with OC_CCI v2 results from Met Office Updated Section 3.11 with CCI Land Cover and CCI Glaciers results from SMHI Updated section 3.14 with CCI Ice Sheets results from ULB



Max-Planck-Institut
für Meteorologie



Institut
Pierre
Simon
Laplace



CMUG Phase 2 Deliverable

Reference: D3.1: Quality Assessment Report
Due date: June 2017
Submission date: 21 December 2017
Version: 4



CMUG Phase 2 Deliverable 3.1

Quality Assessment Report

1.	Purpose and scope of this report	3
2.	CMUG methodology and approach for assessing quality in CCI products.....	3
3	Summary of CMUG Assessment of Quality by WP	6
3.1	<i>Assessment of Marine ECVs in FOAM Ocean Model [WP 3.1].....</i>	<i>6</i>
3.2	<i>Integrated assessment of Marine ECVs in the ORA system [WP O3.1].....</i>	<i>20</i>
3.3	<i>Assimilation of several L2 ozone products in the ERA system [WP 3.2].....</i>	<i>32</i>
3.4	<i>Integrated assessment of the CCI Aerosols, GHG, and Ozone datasets [WP3.3].....</i>	<i>34</i>
3.5	<i>Integrated assessment of CCI terrestrial ECVs impact in the MPI-ESM [WP3.4]</i>	<i>52</i>
3.6	<i>Cross assessment of clouds, water vapour, aerosols, ozone, GHG, SST, radiation and soil moisture impact on global climate variability and trends [WP_O3.4].....</i>	<i>57</i>
3.7	<i>Coupled climate model assessment [WP3.5].....</i>	<i>72</i>
3.8	<i>Improved process understanding from Arctic and Antarctic cross ECV assessment [WP3.6].....</i>	<i>89</i>
3.9	<i>Cross-Assessment of Aerosols, Cloud and Radiation CCI ECVs [WP3.7].....</i>	<i>98</i>
3.10	<i>Cross assessments of clouds, water vapour, radiation, soil moisture for regional climate models [WP3.8].....</i>	<i>100</i>
3.11	<i>Cross assessments of ESA CCI glacier, land cover and sea level data for hydrological modelling of the Arctic Ocean drainage basin [WP3.9].....</i>	<i>108</i>
3.12	<i>Cross-assessment of CCI-ECVs over the Mediterranean domain [WP3.10]</i>	<i>124</i>
3.13	<i>Assessment of sea ice concentration observational uncertainty from a data assimilation point of view [WPO3.11].....</i>	<i>133</i>
3.14	<i>Assessment of Antarctic ice sheet ECVs for modelling [WP3.12].....</i>	<i>147</i>
3.15	<i>Assessment of Greenland ice sheet ECVs for modelling [WP3.13].....</i>	<i>155</i>
4.	References.....	162
	Appendix 1: Status of WP research reported on in this deliverable	174

CMUG Phase 2 Deliverable

Reference: D3.1: Quality Assessment Report
Due date: June 2017
Submission date: 21 December 2017
Version: 4



1. Purpose and scope of this report

This document is a continuation from the 2016 version 2 which reported on CMUG CCI evaluations during Year 2 of Phase 2. Its purpose is to assess the quality of the latest (final or near final depending on availability) versions of CCI products and update feedback to ESA and the CCI teams. This assessment is being conducted by the climate modelling and reanalysis centres in the CMUG consortium using CCI Phase 2 data and includes a wide range of data and model interactions (assimilation, boundary conditions, optimisation, reanalysis, sensitivity studies etc.). This second phase of evaluation continues to examine the following top level questions:

- Are the CCI data products of ‘climate quality’ i.e. is their quality adequate for use in climate modelling, reanalysis and for wider research applications?
- Are the error characteristics provided by CCI products adequate?
- Do the products meet the Global Climate Observing System (GCOS) quality requirements for satellite for Essential Climate Variables (ECV)?
- Is the quality of the products sufficient for climate service applications?

2. CMUG methodology and approach for assessing quality in CCI products

This report describes the results in the last year of CMUG Phase 2 from CMUG Task 3 “Assessing consistency and quality of CCI products”. The work is spread across fifteen Work Packages¹ (WP) listed in Table 1, which includes the CCI product being assessed, the CMUG model being used to make the assessment, and the type of climate modeling experiment.

The CMUG results presented here provide information on the accuracy, consistency and usefulness of the latest CCI data sets. The analysis assesses the suitability of the CCI datasets for coupled climate model and reanalysis applications and evaluates the impact of the data products on model based studies, including quantification of the uncertainties associated with both the models and the observations (see Table 1). This information is aimed at the CCI teams producing the data but is also of use to other modelling centres which will use CCI data in the future.

The modeling experiments are described in the following sections of this report, and cover the following topics: assimilation of CCI data into climate models; cross assessments of CCI data (those which have physical links/interactions); applications for reanalysis; integrated assessment of CCI data in climate models; boundary condition forcing experiments; regional

¹ Three new WPs have been included in the CMUG work plan since version 1 of this report in June 2015.

CMUG Phase 2 Deliverable

Reference: D3.1: Quality Assessment Report
Due date: June 2017
Submission date: 21 December 2017
Version: 4



modeling; earth system process studies. The CMUG work reported here was conducted with the CCI data available at the time, which in most cases were from the final Phase 2 Climate Record Data Packages produced by the CCI projects. Where the results are not yet available, the section is marked “To be completed”. A planned update of this report in the Autumn of 2017 will include assessments missing from this version.

Appendix 1 summarises the status of the research results for each of the WPs contributing to this report.

CMUG Phase 2 Deliverable

Reference: D3.1: Quality Assessment Report

Due date: June 2017

Submission date: 21 December 2017

Version: 4



		CCI products													
		SST	SSH	Sea ice	OC	Cloud	Ozone	Aerosol	GHG	LC	SM	Fire	Ice sheets	Glacier	
CMUG Task 3: Assessing consistency and quality of CCI products															
WP	CMUG Model	Ocean				Atmosphere				Land				Experiment Type	
3.1	FOAM	X	X	X	X										Assimilation
O3.1	NEMOVAR, ORA	X	X	X	X										Assimilation and Detection
3.2	ERA-Clim						X								Assimilation
3.3	MACC-II						X	X	X						Assimilation
3.4	JSBACH, TM3								X	X	X				Assimilation
O3.4	EC-Earth/CMIP5	X				X	X	X	X	X					Assessment, evaluation
3.5	LMDz, ORCHIDEE								X	X	X	X			Boundary Condition
3.6	MPI-OM, MPI-ESM	X		X	X	X									Assimilation (Polar Regions)
3.7	EMAC-MADE					X		X							Comparison
3.8	RCA HARMONIE	X				X					X				Comparison/Eval (CORDEX Africa)
3.9	Arctic HYPE		X							X				X	Assessment
3.10	CNRM-RCM	X	X			X		X			X				Comparison (Med CORDEX)
O3.11	EC-Earth3	X	X	X	X										Cross-assessment
3.12	BISICLES / FETISH	X											X		Assessment, evaluation
3.13	GISM-VUB												X		Assessment, evaluation
3.14	EC-Earth/CMIP5	X		X		X									Benchmarking, process study

Table 1: Summary of the CMUG Work Packages, CMUG models, CCI products, and CMUG experiments for assessing quality of the CCI products, as given in this report. Includes the three new WPs added during the last two years of the programme.



3 Summary of CMUG Assessment of Quality by WP

3.1 Assessment of Marine ECVs in FOAM Ocean Model [WP 3.1]

Aim

The aim of this research is to make an integrated assessment of marine ECVs to assess their consistency within a global and shelf seas regional data assimilation environment, and to provide an assessment of the uncertainty. It will address the following scientific questions:

- Are the individual marine CCI CDRs good enough for assimilation purposes?
- What are the changes made to the analyses by assimilating the CCI data?
- Are the uncertainties provided useful to assign observation errors to the measurements?
- Are the four marine ECVs mutually consistent from an ocean assimilation point of view?

Key Outcomes of CMUG Research

- OC-CCI V1 products are of at least equal quality to predecessor products, with some improvements due to increased spatial coverage and stability.
- Improvements are seen from OC-CCI V1 to V2 to V3.
- Assimilating OC-CCI data improves surface and sub-surface model chlorophyll, with some evidence of improvement in nutrients and carbon variables.
- OC-CCI uncertainty estimates are beneficial for data assimilation.
- Spatial and temporal features in the four marine ECVs appear consistent, with this consistency also evident in resulting reanalyses.
- Information gained by assimilating CCI products can be beneficial for model and assimilation development.
- Reanalyses assimilating CCI products produce realistic variability in response to climatic events, allowing their use as a tool for climate studies.

Summary of Results

Initial work focused on assessment of the ocean colour CCI (OC-CCI) data for assimilation purposes. This has now been extended to an integrated assessment of all four marine ECVs. The pieces of work are summarised in turn below.

i) Comparison of OC-CCI V1 and GlobColour

At the end of Phase 1, a global ocean reanalysis was produced by assimilating OC-CCI V1 chlorophyll products into the FOAM-HadOCC coupled physical-biogeochemical ocean model (Storkey et al., 2010; Palmer and Totterdell, 2001; Hemmings et al., 2008; Ford et al., 2012), covering the period from September 1997 to July 2012. For comparison, a reanalysis was also

CMUG Phase 2 Deliverable

Reference: D3.1: Quality Assessment Report
Due date: June 2017
Submission date: 21 December 2017
Version: 4



produced assimilating the predecessor GlobColour products, as well as a control run with no data assimilation. A thorough assessment of the results has been performed during Phase 2, and a paper on the work has been accepted for publication in the forthcoming CCI special issue of Remote Sensing of Environment (Ford and Barciela, 2017).

The OC-CCI V1 products were found to be of sufficient quality for data assimilation purposes, and of at least equal quality to the GlobColour products (more detail on the comparison with GlobColour is included in the “Quality relevant outcomes” sub-section below). Assimilating OC-CCI chlorophyll data improved the model’s representation of sea surface chlorophyll compared with both satellite data sets, and also a range of independent *in situ* observations. An example of this is shown in Figure 1, which plots a time series of sea surface chlorophyll from all three model runs at the Hawaii Ocean Time Series (HOT) site in the North Pacific, along with *in situ* observations. The assimilation results in a much better match for both the magnitude and seasonality of the observations. It is also able to produce a reanalysis which is stable with time whilst displaying inter-annual variability.

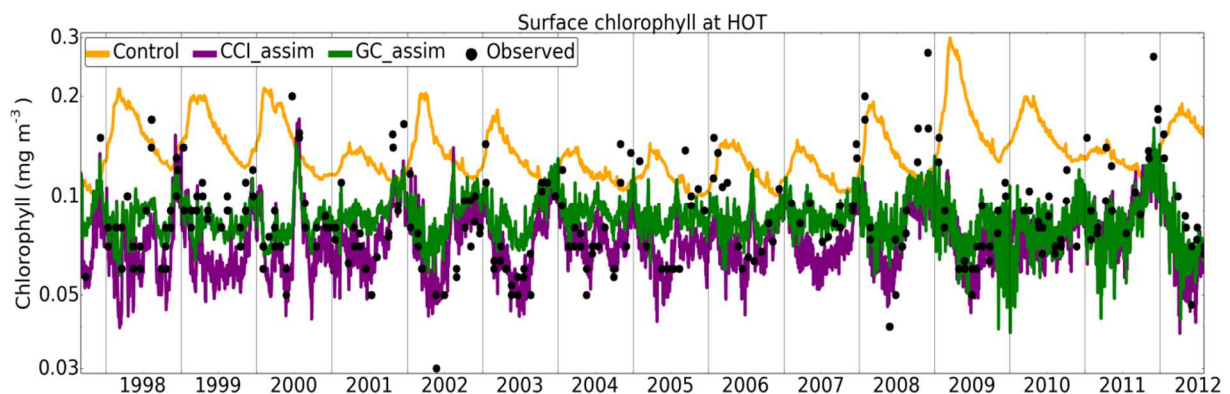


Figure 1: Time series of modelled and observed chlorophyll concentration in the surface 10 m at the HOT site. Observations have been obtained from <http://hahana.soest.hawaii.edu/hot>.

The largest impact of the assimilation was on sea surface chlorophyll, but an improved representation of chlorophyll was also found throughout the water column, including an improved representation of deep chlorophyll maxima, which are an important contribution to global primary production and not directly observed by ocean colour sensors. Corresponding changes were found in phytoplankton and zooplankton biomass, although limited observational data are available for validation. Changes to nutrient concentrations were small, with some evidence of improvement compared with *in situ* observations. This is an important result, as some studies have found a degradation of nutrients due to chlorophyll assimilation.

Validation has also focused on the impact of the assimilation on the model carbon cycle, as this is of particular relevance for climate studies. Validation has been performed against surface

CMUG Phase 2 Deliverable

Reference: D3.1: Quality Assessment Report

Due date: June 2017

Submission date: 21 December 2017

Version: 4



fugacity of carbon dioxide ($f\text{CO}_2$) observations from the SOCAT V2 database (Bakker et al., 2014). Overall, the effect of the chlorophyll assimilation was small compared with the magnitude of model biases. In part, this is because there are large physical controls on the carbon cycle. The impact on these of additionally assimilating physical ECVs is being addressed as part of the integrated marine ECV assessment detailed below. In regions of strong biological activity, the chlorophyll assimilation was found to have a beneficial impact on air-sea CO_2 fluxes, an example of which is shown in Figure 2. In some areas, the assimilation was found to improve representation of the biological component of the carbon cycle, but overall degrade $f\text{CO}_2$ compared with observations due to compensating errors in the physical component of the carbon cycle. This provides important information on model biases which can be fed back into model development activities. Again, the impact in these cases of combined assimilation of all marine ECVs is being assessed as part of the integrated marine ECV assessment detailed below.

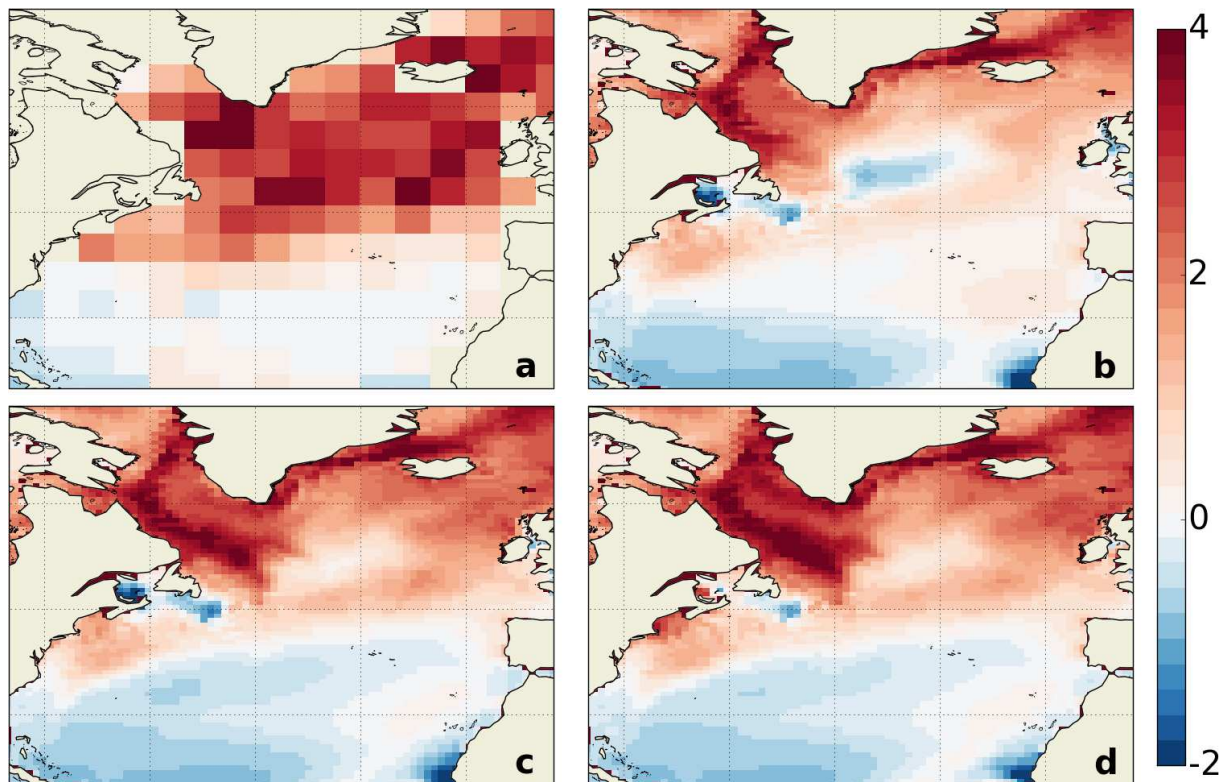


Figure 2: June mean air-sea CO_2 flux ($\text{mol C m}^{-2} \text{ yr}^{-1}$) in the North Atlantic from a) climatology of Takahashi et al. (2009), b) FOAM-HadOCC control, c) reanalysis assimilating GlobColour data, d) reanalysis assimilating OC-CCI data. Positive values represent a flux into the ocean. The reduction in spurious outgassing in the centre of the domain in c) and d) compared with b) is due to the assimilation reducing the chlorophyll bias in this area. An alternative version of this figure, not including OC-CCI data but mentioning the CCI project, has been published in Gehlen et al. (2015).

CMUG Phase 2 Deliverable

Reference: D3.1: Quality Assessment Report
Due date: June 2017
Submission date: 21 December 2017
Version: 4



ii) Comparison of OC-CCI V1, V2 and V3, and use for CMEMS

Technical issues with the OC-CCI V1 products were reported on during Phase 1. OC-CCI V2 products were released in April 2015, and CMUG have tested these in comparison with V1. The Product User Guide was expanded on and improved, particularly regarding use of the uncertainty estimates, which is highly beneficial for users. The V2 products were not quite “plug-and-play” with the V1 products, since the variable names for the chlorophyll uncertainty have been changed in the NetCDF files. Whilst consistency between releases is generally preferred, in this case the change of variable name makes the contents of the variable clearer, so is a reasonable change to have made. Minor metadata errors which had been identified in the V1 products were corrected, and no new errors identified. Short like-for-like assimilation runs were performed with FOAM-HadOCC using the V1 and V2 products, with similar results obtained, but small regional differences, indicating the V2 products to be of at least equal scientific quality to the V1 products, as well as of improved technical quality.

OC-CCI V3 products were then released in August 2016, and updated in May 2017. The V3 products were “plug-and-play” with the V2 products, allowing the new products to be used with no system changes, which is extremely important from a user perspective. A major scientific development for V3 was to introduce a blend of chlorophyll algorithms based on water type, increasing the applicability of the products to Case 2 (largely coastal) waters. This has allowed the assimilation of V3 OC-CCI products in a reanalysis of the North-West European Shelf Seas which is currently being produced for release through the Copernicus Marine Environment Monitoring Service (CMEMS). The assimilation of these products has been found to improve the consistency of model chlorophyll values with independent *in situ* observations, both on and off the continental shelf. In particular, the timing of the spring bloom is much improved by the assimilation. In sediment-dominated coastal waters, the OC-CCI products can still over-estimate chlorophyll compared with *in situ* observations, suggesting further research is still required to improve the accuracy of these global products in complex regional seas. However, in these regions the uncertainty estimates provided with the OC-CCI products appear to accurately reflect these differences. Whilst insufficient *in situ* observations exist to perform a detailed study, this suggests that the uncertainty estimates are of good quality and confidence can be had in their use. The assimilation methodology has therefore been developed to make direct use of these uncertainty estimates, which resulted in a further improved match of model chlorophyll values with independent *in situ* observations.

iii) Integrated assessment of marine ECVs

The assessment of OC-CCI V1 products has been extended to an integrated assessment of the four marine ECVs, ocean colour (OC), sea surface temperature (SST), sea level anomaly (SLA), and sea ice concentration (SIC). The model and assimilation framework is still FOAM-HadOCC, but upgraded to use the GO5 configuration of the NEMO ocean model (Megann et al., 2014) and the 3D-Var implementation of the NEMOVAR data assimilation scheme (Waters

CMUG Phase 2 Deliverable

Reference: D3.1: Quality Assessment Report
Due date: June 2017
Submission date: 21 December 2017
Version: 4



et al., 2015). Surface forcing comes from ERA-Interim (Dee et al., 2011). Some runs have included the assimilation of *in situ* temperature and salinity (T&S) profiles from the EN4 database (Good et al., 2013), in order to assess the complementarity of *in situ* and remote sensing observations. An overview of results is given here; more detailed assessment will be presented in a publication currently being prepared for submission to a peer-reviewed journal.

The CCI products used are the latest that were publicly released at the time this work was started: V2 OC, V1.1 SST, V1.1 SLA, and OSI SAF sea ice. The use of OSI SAF rather than CCI sea ice was on the advice of the sea ice CCI team (who also produce OSI SAF), who could not recommend use of their CCI products if wishing to perform a consistent assessment through the year 2002, as required for this work. In order to provide an assessment of the final Phase 2 CCI products for each ECV, including sea ice, an additional run has been performed using the latest products (V3.1 OC, V1.1 SST, V2.0 SLA, V2.0 SIC), documented at the end of this section.

Following processing of the observations and associated inputs (e.g. mean dynamic topography for SLA), two sets of model runs have been performed with FOAM-HadOCC, summarised in Table 2. Long 1° resolution runs covering the overlapping period of the data sets (1998-2010) have been used to assess the consistency of inter-annual variability and the response to climate drivers such as the El Niño Southern Oscillation (ENSO). Higher resolution 0.25° resolution runs covering the final three years of this period (2008-2010) have been used to assess the consistency of spatial features. In each case, there is a non-assimilative control run, runs assimilating each ECV individually, a run assimilating the ECVs in combination, and runs using other selected combinations of products. The impact on non-observed variables of climatic importance, such as air-sea CO₂ fluxes, has also been assessed.

Run	OC	SST	SLA	SIC	T&S
Free					
OC	X				
SST		X			
SLA			X		
SIC				X	
OC+SST+SIC	X	X	X		
OC+SST+SIC+SLA	X	X	X	X	
OC+SST+SIC+SLA+T&S	X	X	X	X	X
SST+T&S		X			X
SLA+T&S			X		X

Table 2. Model runs performed, with X marking the assimilation of a particular variable. Each run has been performed at both 1/4° from 2008-2010 and 1° from 1998-2010.

CMUG Phase 2 Deliverable

Reference: D3.1: Quality Assessment Report
Due date: June 2017
Submission date: 21 December 2017
Version: 4



When assessing the consistency of observation products by performing data assimilation experiments, it is important to distinguish between what the results are saying about the observations, and what the results are saying about the model and assimilation system. In the latter case this is still vital information for climate modellers, as it means the use of the observation products allows the partitioning of errors, which can inform the future development of reanalysis systems. For instance, it would intuitively be expected that if the satellite ECV products are consistent, then the assimilation of one variable would improve the simulation of another. This has been investigated in these runs, and found to not necessarily be the case, but further assessment has demonstrated that this is highlighting issues with the assimilation scheme, rather than inconsistencies in the CCI products. For instance, when assimilating SST and SLA in combination, the mean assimilation increments for each field are larger than when assimilating the variables individually, indicating that the assimilation has to overcome larger biases despite the extra information. This has helped highlight an issue with the way in which the assimilation scheme propagates information from the surface ocean throughout the water column, and so is not a reflection of the consistency of the input observations. Similarly, the assimilation of physical data, in particular SLA and T&S, has been found to degrade the simulation of biogeochemical variables, due to an unsolved problem within the scientific community that physical data assimilation can cause spurious vertical mixing (see e.g. Raghukumar et al., 2015, While et al., 2010), bringing excessive nutrients and carbon to the surface and fuelling production. However, for the simulation of chlorophyll, the assimilation of OC-CCI products has been found to effectively mitigate this.

Despite the issues with the assimilation that use of the CCI products has highlighted, the experiments are still able to provide valuable information about the consistency of the CCI data sets. An example is shown in Figure 3, which shows the spatial gradients of different variables in the Gulf Stream region of the North Atlantic, for an example month (June 2009). For SST, SLA, and $\log_{10}(\text{chlorophyll})$, the satellite observations over the month have been binned into $1/4^\circ$ boxes, and the spatial gradients calculated and plotted (Figure 3a-c). The $1/4^\circ$ model runs have been sub-sampled at the observation locations and times, and binned and processed in exactly the same manner. The resulting gradients are plotted for the free run (Figure 3d-f) and the OC+SST+SIC+SLA assimilation run (Figure 3g-i). In the SST observations the gradients seen mark the northern extent of the Gulf Stream, whilst in the SLA observations the gradients show eddy activity within the Gulf Stream. The edges of these gradients match neatly, demonstrating the position of the Gulf Stream to be consistent in the SST and SLA CCI products. A less clear relationship is expected with $\log_{10}(\text{chlorophyll})$, due to the complexity of the underlying dynamics, but given the SST and SLA gradients, and expected nutrient gradients, the OC products appear consistent with the SST and SLA products. In the model free run the SST gradients are well represented, but there is insufficient variability in the SLA and $\log_{10}(\text{chlorophyll})$ fields, as would be expected from an eddy-permitting rather than eddy-resolving resolution model. When the ECVs are assimilated in combination, the representation of gradients in all fields is greatly improved compared with the observations. Crucially, the



consistency of spatial gradients in the different fields is maintained, with assimilation of CCI products giving a consistent reanalysis product. Similar conclusions are reached when an assessment of frontal positions is performed in the North Atlantic (not shown). For instance, assimilating only SST gives a better match of the positions of $\log_{10}(\text{chlorophyll})$ fronts with a run assimilating OC data than the free run does. This suggests a consistency of information about spatial ocean dynamics in the OC and SST CCI data, which is being successfully transferred to model reanalysis fields.

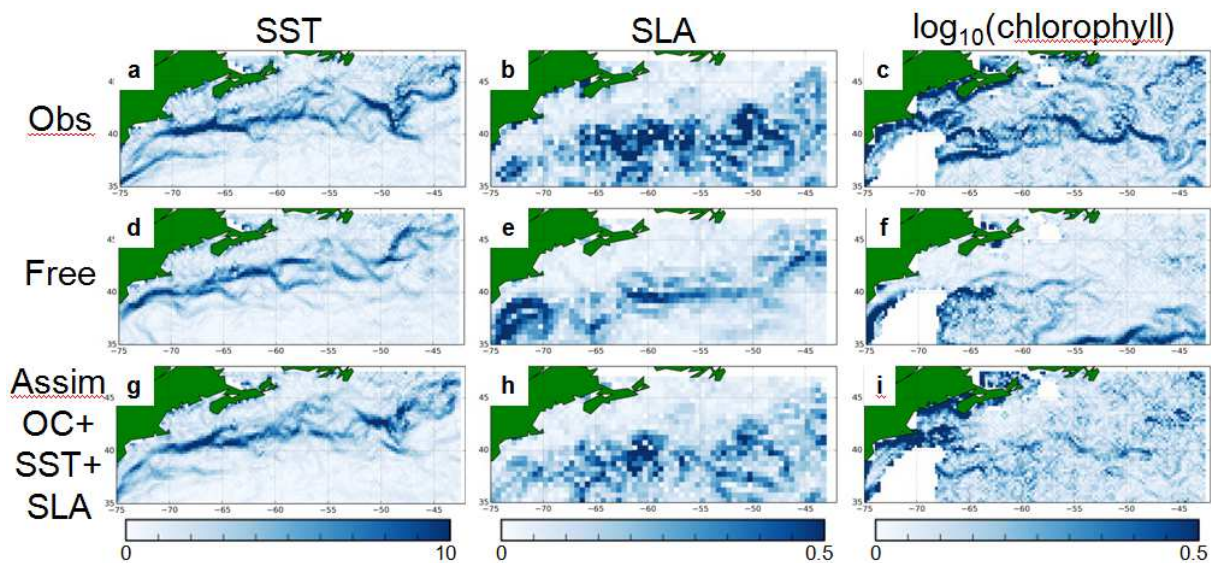


Figure 3. Spatial gradients of SST, SLA and $\log_{10}(\text{chlorophyll})$ in the Gulf Stream region of the North Atlantic, for June 2009, from a-c) CCI data, d-f) $1/4^\circ$ free run, and g-i) $1/4^\circ$ run assimilating ECVs.

Another important area in which to assess the consistency of the CCI products is around the edge of the sea ice extent. There is an obvious relationship between SST and the presence of sea ice, and there can often also be observed intense biological activity around the sea ice edge, due to changes in stratification and light limitation. For an example day (01 June 2009), Figure 4 shows the chlorophyll concentration in the Arctic Ocean, overlaid by the sea ice extent as defined by the 15% ice concentration contour, from CCI products and three of the $1/4^\circ$ model runs. In the observations plot (Figure 4a), the chlorophyll concentration plotted is from the OC-CCI 5-day composite containing 01 June 2009, in order to reduce gaps due to cloud cover, and the ice extent comes from the L4 OSTIA reanalysis product produced by SST-CCI, incorporating CCI SST and OSI SAF SIC data. The edge of the OC coverage and the edge of the ice extent generally match well, suggesting consistency of ice extent in both products. Where there are OC observations within the 15% ice contour, such as in the Greenland Sea, ice concentrations in these regions are still well below 100%, so OC data would be expected, especially in a 5-day composite. A chlorophyll bloom is observed in the Barents Sea, near the sea ice edge. The model free run captures this bloom (Figure 4b), but it is too large and extends too far into the Norwegian Sea. The representation of it is much improved when OC-CCI data



is assimilated (Figure 4c), but uncorrected errors in the sea ice extent prohibit the capturing of the details around the ice edge. When SIC data is additionally assimilated (Figure 4d), the ice extent is better represented, allowing the details of the chlorophyll bloom to be better captured. This further demonstrates consistency between the ECVs, and that for the best reanalysis results they should be assimilated in conjunction with each other. Assimilating the ECVs together also gives more variability in modeled chlorophyll concentrations under sea ice. Lack of observations prohibits the validation of these results, but recent studies (Horvat et al., 2017) suggest such blooms are to be expected.

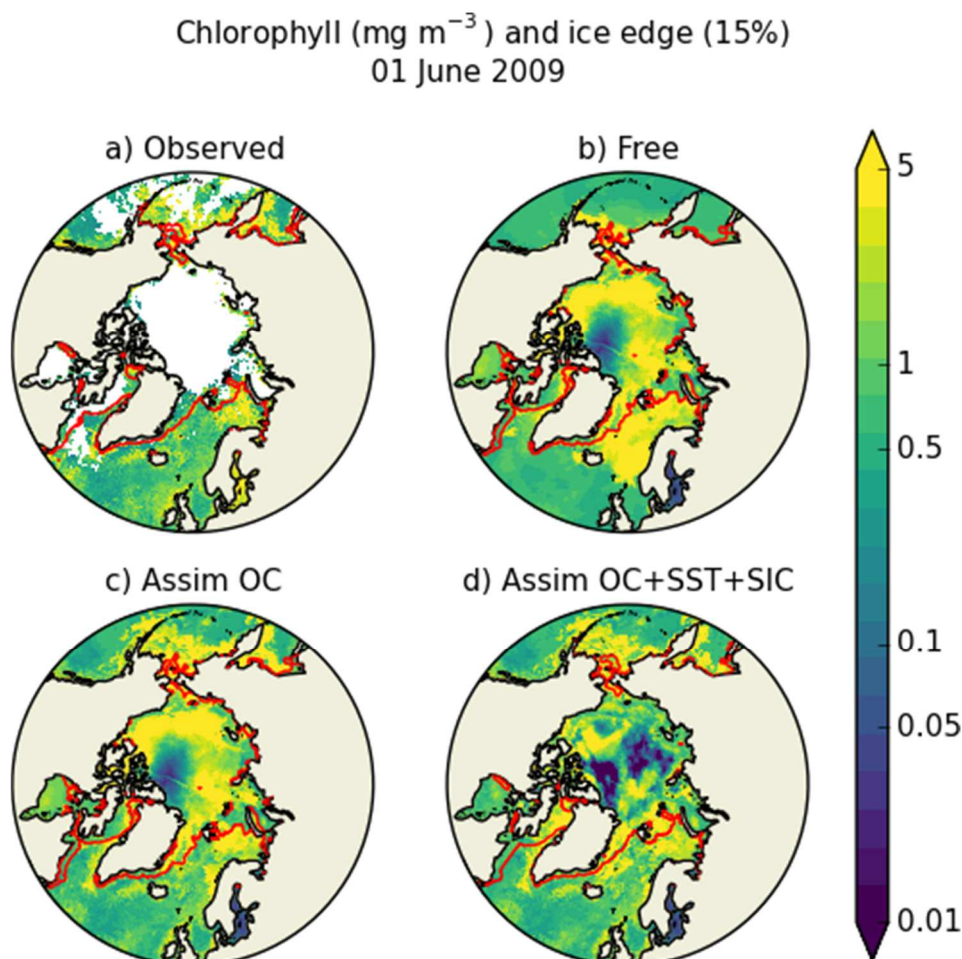


Figure 4. Chlorophyll concentration on 01 June 2009 from a) OC-CCI data and b-d) three $1/4^\circ$ model runs. Overlaid in red is the sea ice extent as defined by the 15% concentration contour from a) SST-CCI L4 OSTIA reanalysis and b-d) the corresponding model fields.

An important feature for climate studies is the Atlantic Meridional Overturning Circulation (AMOC), and recent studies have begun to assess the representation of AMOC variability in assimilative reanalyses (Jackson et al., 2016). Figure 5 shows a Hovmöller plot of the AMOC at 26°N from 2008-2010, from independent *in situ* observations at the RAPID array (http://www.rsmas.miami.edu/users/mocha/mocha_results.htm), and different $1/4^\circ$ model runs.

CMUG Phase 2 Deliverable

Reference: D3.1: Quality Assessment Report

Due date: June 2017

Submission date: 21 December 2017

Version: 4



A clear feature in the observations is a large slowdown in the AMOC around January 2010, which has been linked with extreme weather events in the Northern Hemisphere (Bryden et al., 2014). CMUG work has also demonstrated an impact on the variability of the carbon cycle (Ford and Barciela, 2017), benefitting from the assimilation of OC-CCI data. This event is well-captured by the free-running model, suggesting the variability to be largely atmospherically-driven, supporting the conclusions of Roberts et al. (2013). However, as with most forced ocean models, the magnitude of the AMOC is consistently too weak. When CCI ECV products are assimilated (SST+SIC+SLA; OC assimilation has no impact on the physical circulation in these runs), the magnitude of the AMOC is duly strengthened, but there is a negative impact on the sub-surface variability. When *in situ* T&S data (not including the RAPID data) are assimilated in addition to the satellite products, this gives the best representation of the AMOC of all the model runs. This demonstrates that whilst satellite ECVs have an important role to play, *in situ* observations are also required in order to accurately capture the ocean circulation and sub-surface variability.

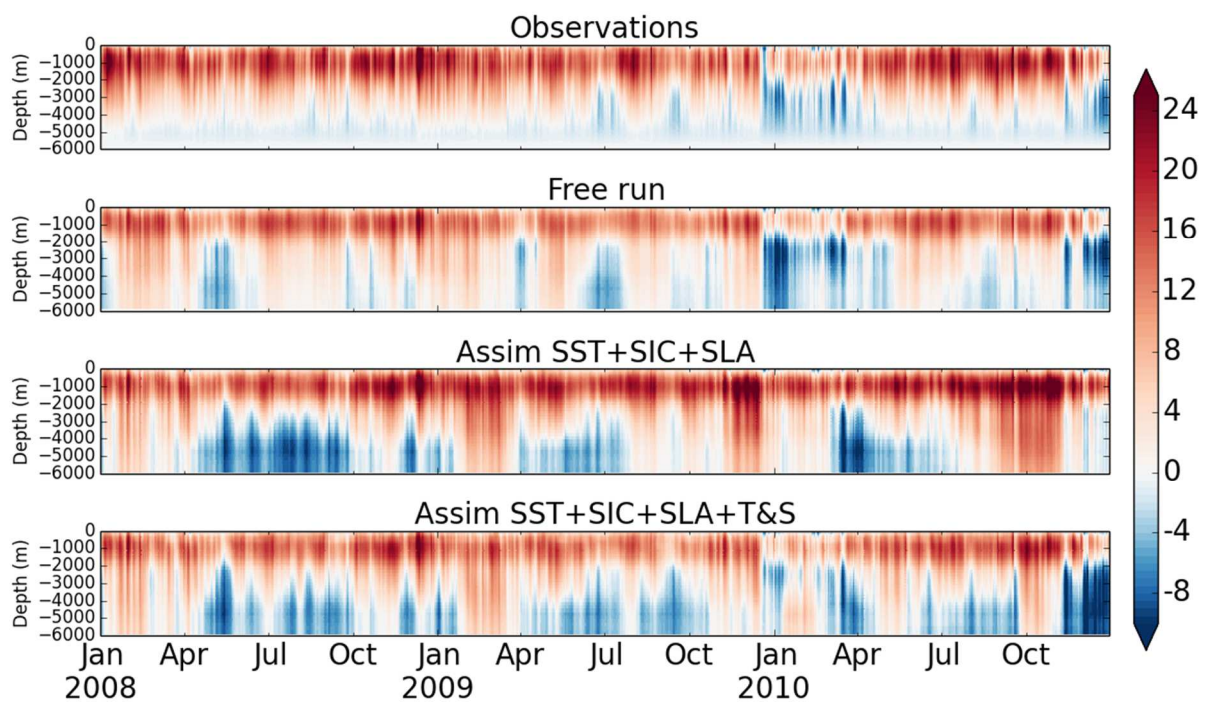


Figure 5. Hovmöller plot of the AMOC at 26°N from RAPID observations and three 1/4° model runs.

As stated above, in order to assess the final Phase 2 products for each ECV (apart from SST, whose Phase 2 release is not expected until March 2018), an additional run has been performed using V3.1 OC, V1.1 SST, V2.0 SLA, and V2.0 SIC. This repeats the 1/4° OC+SST+SLA+SIC assimilation run for the year 2008. For SIC a choice of 25 km or 50 km resolution is available, and the higher resolution product has been used.

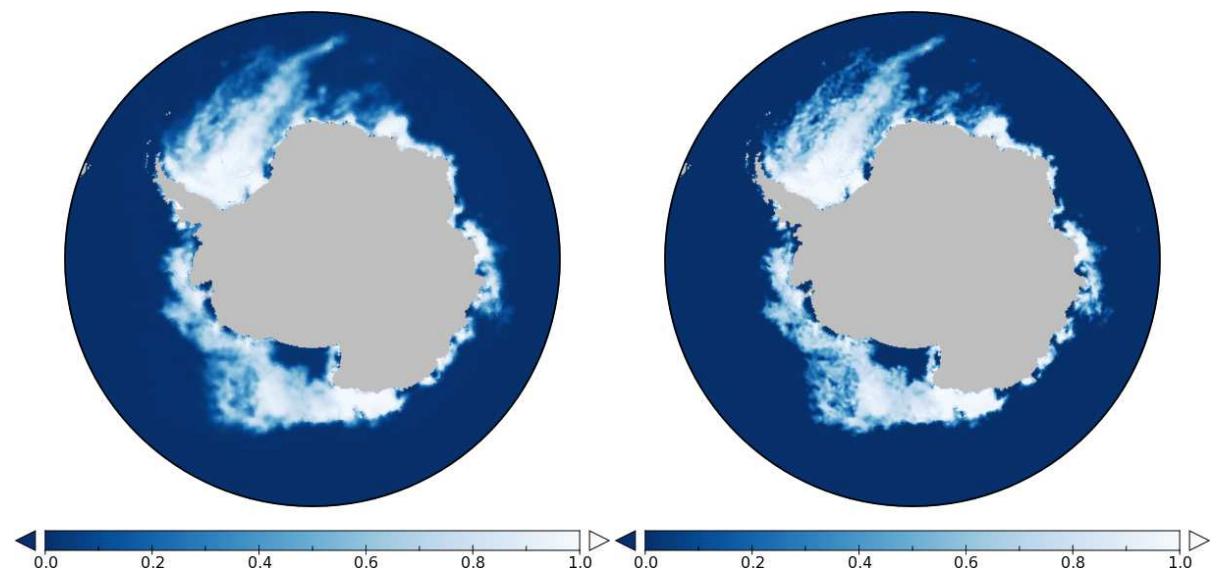


Figure 6. Model Antarctic sea ice concentration for 31st December 2008, assimilating OC+SST+SLA+SIC. Left: using OSI SAF SIC, right: using CCI V2.0 SIC.

In terms of model SIC, the spatial patterns of ice concentration are very similar whether OSI SAF or CCI V2.0 products are used, but as shown in Figure 6, the higher resolution V2.0 observation product allows the model to capture finer details in the structure of the sea ice. In turn, this should allow more detailed study of biogeochemical and other processes around the ice edge.

The conclusion from the previous runs was that the different ECVs appear to be consistent, and this is maintained with the updated product versions. As an example, Figure 7 shows spatial gradients of observation and model fields for December 2008 in the South Atlantic sector of the Southern Ocean, calculated in the same way as for Figure 3. There are no major differences between the two sets of observations, although the V3.1 OC data extends further south, better matching the sea ice concentration and the SST and SLA coverage. In the Agulhas region in particular the SST and $\log_{10}(\text{chlorophyll})$ gradients match up very clearly, demonstrating consistency in placement of the detailed current features in this area. These are in turn consistent with the eddies seen in the SLA products. Both sets of products improve the spatial features of all model fields compared with the free run, and the consistency between the ECV products is maintained in the resulting reanalyses.

CMUG Phase 2 Deliverable

Reference: D3.1: Quality Assessment Report
Due date: June 2017
Submission date: 21 December 2017
Version: 4

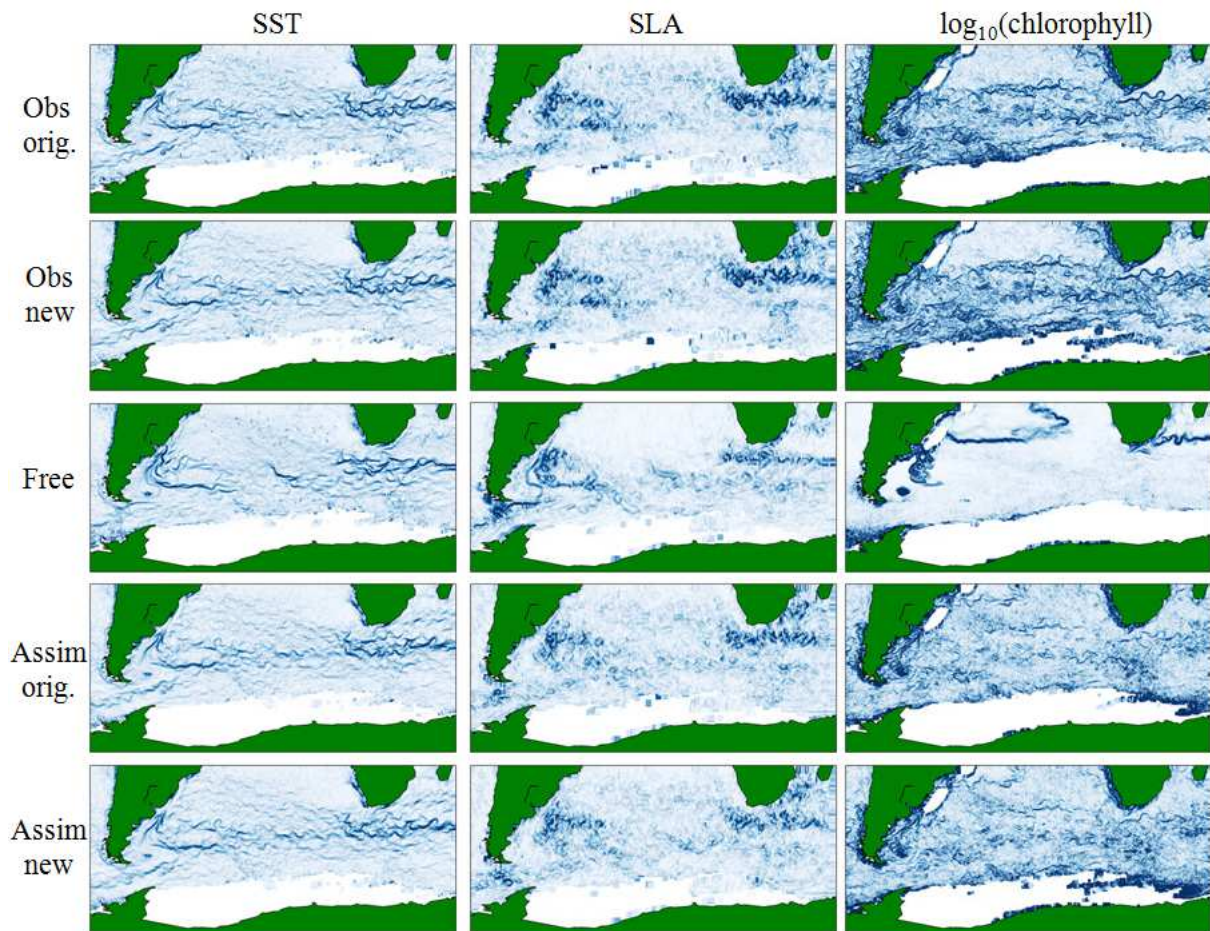


Figure 7. Spatial gradients of SST (column 1), SLA (column 2) and $\log_{10}(\text{chlorophyll})$ (column 3) in the South Atlantic sector of the Southern Ocean including the Agulhas region, for December 2008. Row 1: Original CCI data used (V1.1 SST, V1.1 SLA, V2.0 OC); row 2: new CCI data used (V1.1 SST, V2.0 SLA, V3.1 OC); row 3: $1/4^\circ$ model run with no assimilation; row 4: $1/4^\circ$ model run assimilating original data; row 5: $1/4^\circ$ model run assimilating new data.

Similar experiments to those detailed here have also been performed at ECMWF as part of WP O3.1, results from which are presented in Section 3.2 of this report. In particular, both centres have assimilated the marine ECVs combined with *in situ* T&S profiles into a 1° model covering 1998-2007. In each case the base model and assimilation code was NEMO v3.4 and NEMOVAR v3.0. However, despite these similarities, the way in which the assimilation is applied for each variable differs in many key aspects (Waters et al., 2015; Zuo et al., 2015). This gives an opportunity to compare the interaction between the CCI products and the assimilation methodology.

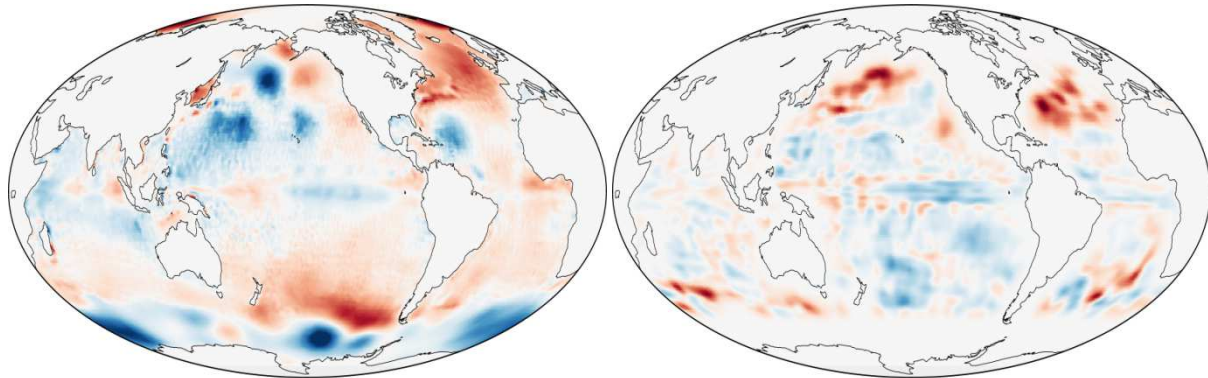


Figure 8. Mean SLA assimilation increments for 1998-2007 from 1° SST+SLA+SIC+T&S assimilation runs. Left: WP 3.1; right: WP O3.1.

Figure 8 shows the mean assimilation increments made to the model SSH fields over the period 1998-2007 in the 1° SST+SLA+SIC+T&S runs from a) WP 3.1 and b) WP O3.1. Broadly similar patterns are seen in a number of regions in each case, in particular the Tropical Pacific and North Atlantic, suggesting that the products are being similarly exploited to address common model biases. The differences in smaller-scale details in these regions will be largely due to technical differences between the two assimilation schemes, such as choice of error covariances and correlation length scales. The increments are more distinct in other areas, such as the South Pacific, reflecting model and assimilation sensitivity, and a latitudinal cutoff in the SLA assimilation in WP O3.1. Such comparisons are valuable for learning about the assimilation methodologies, and can form the basis of ongoing collaboration to improve the assimilation schemes and the use of CCI products in model reanalyses.

Quality relevant outcomes

A comparison between the OC-CCI V1 and GlobColour observation products has been performed to assess their stability and spatial coverage, building on that reported on at the end of Phase 1. GlobColour has greater spatial coverage prior to 2002, as it uses an older NASA SeaWiFS processing which discards fewer data points. Between 2002 and 2012, OC-CCI has greater coverage as more use is made of MERIS data. This is of particular benefit to the assimilation in certain regions, such as the Mauritanian upwelling region and the Arabian Sea during the Asian monsoon period, which were poorly covered by GlobColour. There is a lack of *in situ* observations with which to validate the results in these areas, but the model fields when assimilating OC-CCI data are in line with qualitative expectations. Furthermore, carbon cycle variables are improved in these regions when assimilating OC-CCI data, as a result of the improved coverage. The global mean and spatial standard deviation of the OC-CCI chlorophyll products are also more stable with time than for GlobColour. A reduction in variability is noted when MERIS is introduced in 2002, which could be due to differences in the properties of the sensors, or could simply be an artifact of the sudden increase in the number of data points. Such features are less clear in the reanalysis fields, as to some extent the model acts to smooth these

CMUG Phase 2 Deliverable

Reference: D3.1: Quality Assessment Report
Due date: June 2017
Submission date: 21 December 2017
Version: 4



out. Overall, very similar results are obtained whether OC-CCI or GlobColour products are assimilated, but where differences are found, there is evidence that results are improved due to the increased spatial coverage and improved stability of the OC-CCI data. Coverage is further improved in the V2 and V3 products, which is of further benefit. The uncertainty estimates provided with OC-CCI products have been found to accurately reflect differences compared with independent *in situ* data, and are being successfully used in the assimilation for a reanalysis of the North-West European Shelf Seas being produced for CMEMS. Use of these uncertainties in the assimilation leads to improved model results compared with the *in situ* observations. The uncertainties are also used in the quality control step for global assimilation studies. The only issue found was that not every observation has a corresponding uncertainty, as reported during Phase 1, leading to these observations being automatically rejected. This is a known issue which the OC-CCI team is aware of.

Along with the OC-CCI data, the SST-CCI and SL-CCI data were able to be processed and assimilated with no more than the expected effort required for the assimilation of a new data type. On the whole the assimilation was successful with no special tuning required (e.g. of error covariances), although there was an issue on 18 November 2000 with a few extreme SLA values associated with the Geosat Follow-On mission causing the model to crash. It is unclear whether or not these values are realistic, but for assimilation stability the assimilation of SLA needed to be turned off for this single day. This has been reported to the SL-CCI, who advised a threshold to apply for this mission for assimilation purposes.

As explained above, OSI SAF sea ice products have been used rather than CCI products. When CMUG researchers initially attempted to contact the sea ice CCI team about using their products, no helpdesk email address was apparent on their website (unlike for other ECVs), only an email address for the science lead. CMUG's email to this address went unanswered. A contact in the SST-CCI was able to put CMUG in contact with a member of the sea ice CCI team who could answer the queries, but this is not the most efficient route for a user to get support. It is also a concern that the CCI V1 product is not deemed consistent before and after 2002, and the V2 product only begins in 2002, meaning that an alternative product must be recommended for assimilation into long-term reanalyses, an important application of CDRs. Whilst scientific reasons have been given for the decision, it is likely to limit user uptake. Furthermore, whilst not tested in these experiments, the decision to not filter spurious noise in the V1 products would be expected to cause issues for the assimilation, as reported in WP O3.1 below. This appears not to be an issue for the V2 products.

All the assessment performed by CMUG so far, summarised above, concludes that the four marine ECVs are consistent in terms of their spatial features and temporal variability. When the ECVs are assimilated into the model the features and consistency are maintained, which is a highly positive result, meaning the use of the CCI products in combination can be recommended. There is an outstanding issue that the assimilation of one ECV does not necessarily improve the simulation of another, but this has been traced to issues with the model

CMUG Phase 2 Deliverable

Reference: D3.1: Quality Assessment Report

Due date: June 2017

Submission date: 21 December 2017

Version: 4



and assimilation scheme, rather than the CCI observations. In fact, their use is able to help highlight such issues, which is invaluable for future reanalysis development.

CMUG Phase 2 Deliverable

Reference: D3.1: Quality Assessment Report
Due date: June 2017
Submission date: 21 December 2017
Version: 4



3.2 *Integrated assessment of Marine ECVs in the ORA system* [WP O3.1]

Introduction

The aim of this WP is to perform an integrated assessment of CCI SST, SSH and SIC via assimilation using the ECMWF Ocean ReAnalysis (ORA) System. The focus is on multivariate detection of climate variability and change patterns in the set of CCI ECV in comparison with independent observational products.

The baseline ocean assimilation system ORAS5 used for this WP is closely related to the ORAP5 system described in Zuo et al. (2015) and Tietsche et al. (2015). It uses the ORCA1 global configuration of NEMO 3.4 forced by ERA-Interim (bulk formulas). Subsurface observations from EN4, SLA from Aviso V5, and SIC from OSI-SAF are assimilated using a 3DVar-FGAT algorithm with a 10 day assimilation window. SST is restored to observations from HadISST2 with a restoring strength of $200 \text{ Wm}^{-2}\text{K}^{-1}$.

Initial offline-inspection of the data has shown that the major climate modes of variability and change are very similar to pre-existing ECV data sets, as are the cross-variable statistics. However, for data assimilation, small differences in one variable can be amplified, or interact with how other variables are simulated. Therefore, we focus our discussion on the results of a series of assimilation experiments. In these assimilation experiments (see Table 3), observational products in the baseline assimilation system are exchanged one by one with their CCI equivalent, with an additional experiment which uses all marine CCI-ECV considered here together.

The following CCI data products were used:

- Sea surface temperature: level 4 data, analysed daily mean at 20cm depth on 1/20 degree regular grid, version 1.1, available 1992—2010
- Sea surface height: level 2 data (along-track anomalies referenced to DTU10 mean sea surface), and level 4 data to calculate global mean sea level for freshwater budget corrections, available 1993—2012
- Sea ice concentration: level 4 SSM/I data, analysed daily means on EASE2 hemispheric grids with 25km resolution, available 1992—2008

CMUG Phase 2 Deliverable

Reference: D3.1: Quality Assessment Report
Due date: June 2017
Submission date: 21 December 2017
Version: 4



Experiment	SST	SIC	SLA	Start	End
ORA REF	HadISST2	OSI-SAF	Aviso	1975	2014
ORA CCI-SST	CCI v1.1	OSI-SAF	Aviso	1992	2010
ORA CCI-SIC	HadISST2	CCI SSMI v1.1	Aviso	1992	2008
ORA CCI-SLA	HadISST2	OSI-SAF	CCI v1.1	1993	2013
ORA CCI-ALL	CCI v1.1	CCI SSMI v1.1	CCI v1.1	1993	2008

Table 3: Overview of assimilation runs

Ingesting ESA-CCI SST in the ORA system

This discusses results from the assimilation experiment ORA CCI-SST that ingested SST from CCI v1.1 instead of HadISST2. As shown in Figure 6, the variability and trend of global CCI SST agrees well with the non-ECV data set HadISST2. However, CCI SST are warmer by a constant amount of 0.05K. Global SST in the two assimilation experiments ORA REF and ORA CCI-SST reproduce trend and variability of the two observational products very well, each being close to the observational product which was ingested into the system. The fact that the ORA CCI-SST experiment simulates SST which are often halfway between HadISST2 and CCI-SST suggests that subsurface ocean observations and/or atmospheric forcing in the ORA system favour SST that are cooler than CCI-SST, but warmer than HadISST2.

To understand better the potential causes for differences between CCI-SST and HadISST2, maps of regional biases and trends are needed. As shown in Figure 7 (left), there are systematic regional modulations to the global-mean warm offset. Averaged over the whole data set 1992-2010, the tropical oceans tend to be 0.1 to 0.3 K warmer in CCI-SST than in HadISST2. However, CCI-SST are more than 0.2 K cooler in the North Pacific, and more than 0.5 K cooler in the Sea of Okhotsk. These regions are among the most cloudy in the world (Warren et al. 2015), which is challenging for satellite-only SST products. The North Atlantic exhibits a complex pattern of cold and warm differences, which might be partially related to boundary currents and the presence of sea ice.

From Figure 7 it can be seen that the assimilation systems tends to dampen the differences between the two data sets: in ORA CCI-SST, the tropical oceans SST is slightly cooler than in CCI-SST, and slightly warmer than it in the North Pacific. Disagreements in the upwelling regions of the west coast of South America and Africa are apparent, which might be partly due to well-known model biases in these regions.

CMUG Phase 2 Deliverable

Reference: D3.1: Quality Assessment Report

Due date: June 2017

Submission date: 21 December 2017

Version: 4

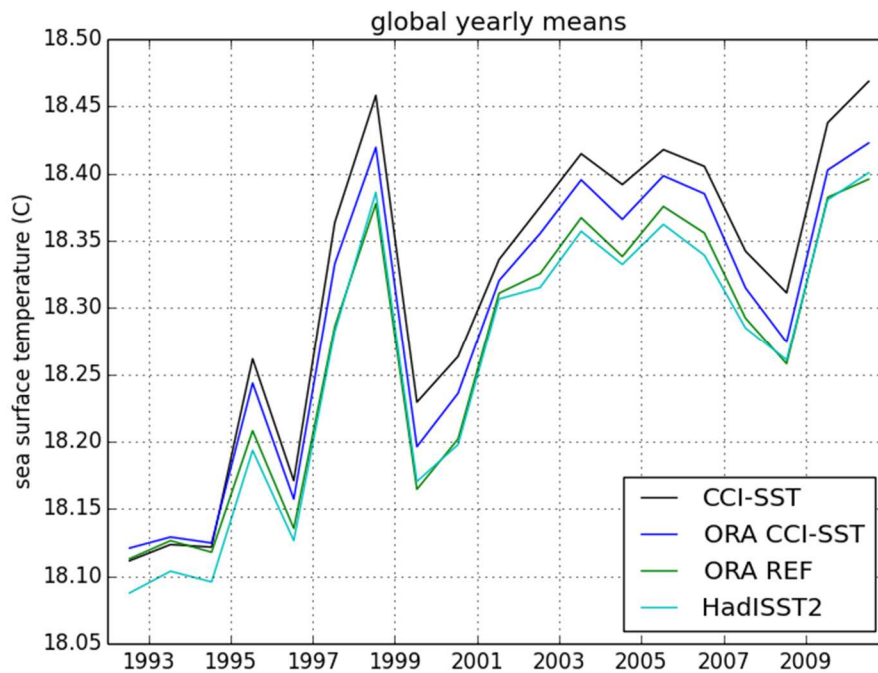


Figure 6: Global-mean SST in the observational data sets HadISST2 and CCI-SST, and the assimilation experiments ORA REF and ORA CCI-SST over 1992–2010.

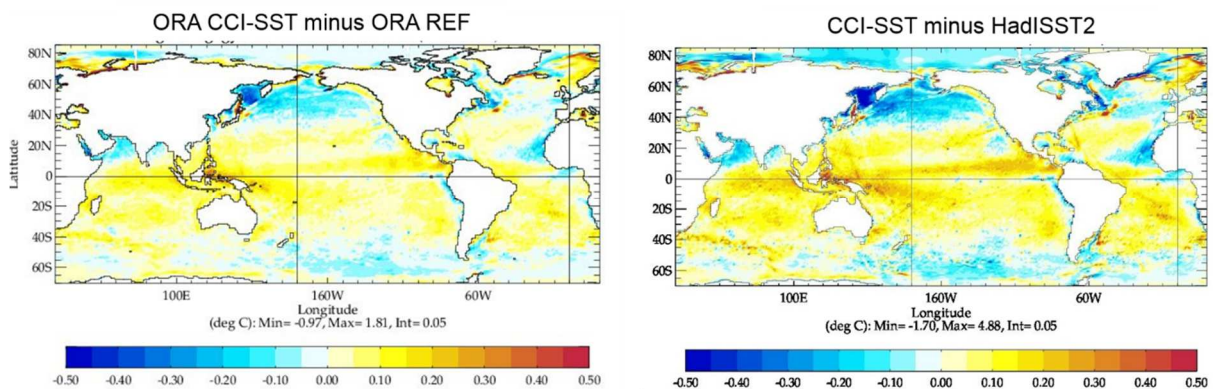


Figure 7: SST difference averaged over 1992-2010 between (left) ORA CCI-SST and ORA REF, (right) CCI-SST and HadISST2.

SST trends over the period 1992-2010 are not uniform, but depend on the ocean basin. While the Indian Ocean warmed at a rate of 0.1 to 0.5 K per decade, the Pacific exhibited a PDO-like pattern of warming SST in the west Pacific and cooling SST in the east Pacific, with a superimposed warming (Figure 8 left). The Atlantic warmed throughout, with a marked amplification at mid- and high northern latitudes, where warming in excess of 1 K per decade occurred. Differences in trends between observational data sets are not small (Figure 8 middle).

CMUG Phase 2 Deliverable

Reference: D3.1: Quality Assessment Report
Due date: June 2017
Submission date: 21 December 2017
Version: 4



Over the western boundary currents, the warming in CCI-SST was up to 0.5 K per decade less than in HadISST2, whereas other regions like the Sea of Okhotsk and the Labrador Sea show up to 0.3 K per decade more warming in CCI-SST than in HadISST. The impact of in-situ observations is also clearly visible in the trend difference: it takes the form of linear features corresponding to busy shipping routes. In the ORA assimilation experiments, the trend differences in the observational data sets are reproduced (Figure 8 right). The patterns of the trend differences are very similar, but the amplitude is generally damped, similar to what was found when discussing differences in the mean state.

Despite the differences discussed above, monthly-mean anomalies of SST are well correlated both between the two data sets, and between the model simulation and the data sets (Figure 9). Correlations between ORA CCI-SST and CCI-SST are generally 0.95 or higher, except in the presence of mesoscale eddies in the Southern Ocean and the western boundary currents, where correlations are degraded to values of 0.5 to 0.7. It is worth noting that the SST correlation is stronger between ORA CCI-SST and CCI-SST than it is between ORA-REF and HadISST2. This suggests that CCI-SST is better suited for ingestion into the ORA system than HadISST2.

The stated uncertainties of the CCI-SST analysis are consistent with uncertainty estimates from other sources. As Figure 10 (left) shows, the CCI-SST analysis uncertainty of daily fields time-averaged over 1992-2010 is mostly below 0.3 K in the interior of the ocean basins. Higher uncertainty exists in eddy-rich regions in the Gulf Stream and Kuroshio Current, and in the Southern Ocean. There, uncertainties exceed 1K in large areas. Regions characterized by upwelling off the tropical west coasts of South America and Africa also have elevated uncertainty levels of 0.5 to 1K. In the Arctic Ocean, CCI-SST uncertainty is high, and looks like a heavily interpolated field. Given that sea surface temperatures should on average deviate only very little from the freezing point of sea water, and given that remote sensing of SST in the presence of sea ice is difficult or even impossible, we suggest that neither the absolute values nor the uncertainty estimate of CCI-SST in the Arctic Ocean should be used.

It is instructive to compare the CCI-SST analysis uncertainty (Figure 10 left) with the RMS difference between CCI-SST and HadISST2 (Figure 10 middle) and the ORAS5 ocean analysis ensemble spread (Figure 10 right). The same spatial patterns of different uncertainty levels are present in both. Compared to the CCI-SST analysis uncertainty, the overall magnitude of the RMS difference between CCI-SST and HadISST2 is larger, whereas the magnitude of the ORAS5 ensemble spread is smaller. Overall, based on this comparison with other estimates of uncertainty, the CCI-SST uncertainty estimates seem plausible and should be very useful for data assimilation and model validation applications.

CMUG Phase 2 Deliverable

Reference: D3.1: Quality Assessment Report
 Due date: June 2017
 Submission date: 21 December 2017
 Version: 4

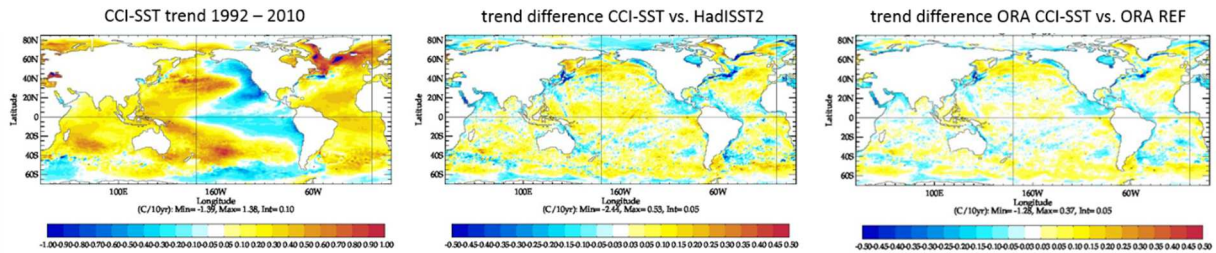


Figure 8: SST trend 1992-2010 in CCI-SST (left), and trend difference between (middle) CCI-SST and HadISST2, and (right) ORA CCI-SST and ORA REF.

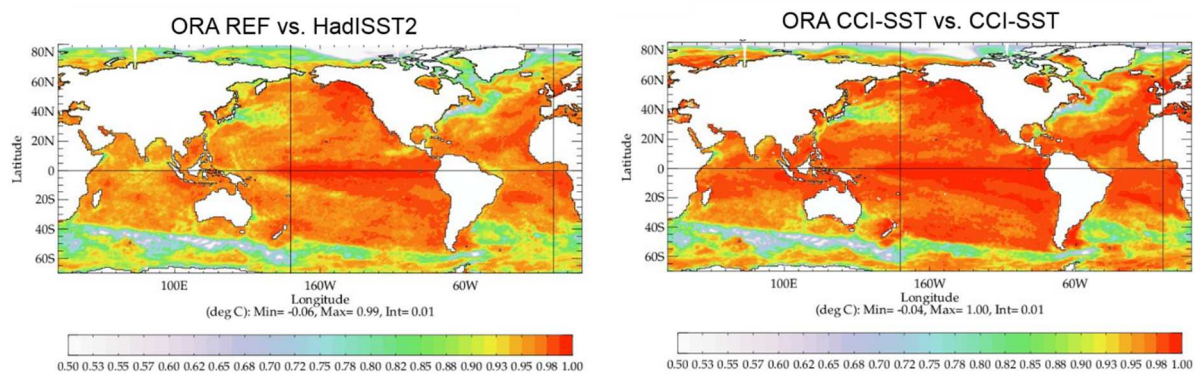


Figure 9: Correlation of monthly-mean SST anomalies from 1992–2010 between (left) ORA-REF and HadISST2, and (right) ORA CCI-SST and CCI-SST.

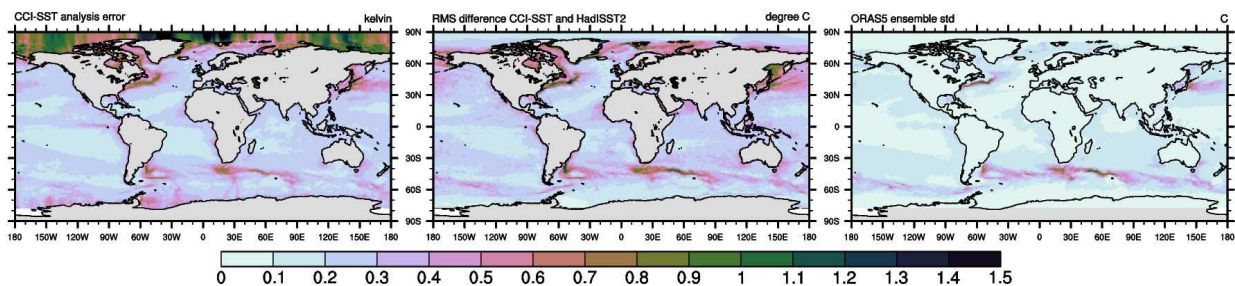


Figure 10: Comparison of SST uncertainties, averaged over all months 1992-2010. (Left) CCI-SST analysis uncertainty, (middle) RMS difference between CCI-SST and HadISST2, and (right) ORAS5 ensemble spread.

Assimilating ESA-CCI sea-level anomalies in the ORA system

We now briefly discuss the assimilation experiment ORA CCI-SLA, where CCI v1.1 sea level anomalies were assimilated in the ORA system instead of the Aviso sea level anomalies in the reference experiment ORA REF. We encountered two technical issues with the data, and we propose to address these in future data versions to increase suitability for modelling applications:



1. Due to the details of the analysis method, the MSLA gridded data contains spurious data over land points, but does not provide a land-sea mask. This is a well-known problem, but since it is not documented in the data themselves, it is easy to obtain wrong results when performing area averages. We suggest to either provide a land-sea mask in the files, or to remove the spurious data in future versions. To our knowledge, the problem has already been addressed for version 1.2 of the ESA-CCI SLA data.
2. The gridded MSLA data are only available as monthly means. While this is sufficient for most applications, it poses a problem when the global mean sea level is needed on a daily basis to constrain the daily fresh-water balance. Therefore, for data assimilation purposes, it would be very helpful to have the gridded MSLA data as daily means.

After addressing these issues, assimilation of CCI-SLA runs smoothly and gives global results that are very similar to what is obtained by assimilating AVISO data. Figure 11 shows global mean sea-level anomaly in the data products and in the assimilation experiments. The seasonal cycle, the year-to-year anomalies, and the overall trend match very well in the two data sets, with the exception of the late period from around 2011 on, when CCI-SLA shows a smaller trend than Aviso. This can be attributed to the fact that data from the CryoSat2 satellite is included in the Aviso product, but not in the CCI-SLA product. Assimilation of the products gives a difference in the model state that is proportional to the difference in the product, as shown in Figure 11 (right).

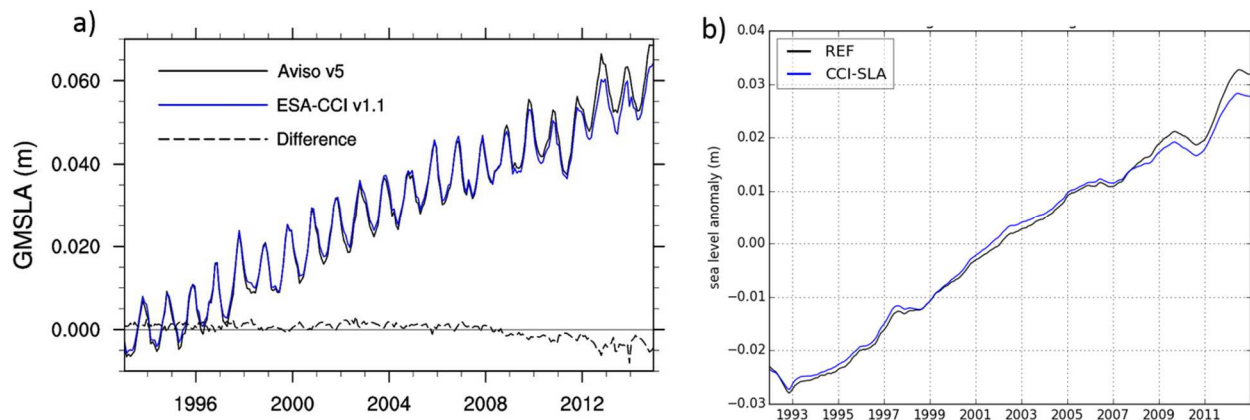


Figure 11: Global mean sea level anomaly. (a) shows monthly anomalies referenced to the beginning of the period for Aviso and CCI-SLA. (b) shows the result of assimilating CCI-SLA instead of Aviso into the ORA system (12-month running mean anomaly referenced to the average over the period).



Assimilating ESA-CCI sea-ice concentration in the ORA system

In the SSMI-derived sea ice concentration product CCI-SIC, spurious sea ice resulting from misinterpreting atmospheric microwave emissions has intentionally not been filtered out. In most other products, so-called weather filters in combination with masks of where sea ice occurrence is plausible are applied to eliminate these spurious sea ice concentrations. However, the application of weather filters and masks potentially removes correctly detected sea ice from the product, when sea ice either appears in unusual locations or under an atmosphere that distorts the microwave signature of sea ice.

The sea ice data assimilation in the ORA system does not check consistency of sea ice observations with other meteorological and oceanographic parameters, and therefore takes the sea ice concentrations in the product at face value. Figure 12 shows annual-mean sea ice concentration in the Arctic (left, north of 70N) and Antarctic (right, south of 50S) in the CCI-SIC data set, in the ORA assimilation experiments. In the Arctic, the excess spurious sea ice in CCI-SIC is not reflected in the assimilation experiment ORA CCI-SIC, presumably because the strong constraint to SST observations is enough to remove any sea ice that is introduced by the assimilation increments. In the Antarctic, however, assimilating CCI-SIC leads to an analysis which closely matches the observational product. As shown earlier, SST in the analysis are less tightly constrained to the observational product in the Southern Ocean, allowing the SIC assimilation to have a stronger effect. It is worth noting that ingesting CCI-SST has almost no impact on sea ice concentration in the Antarctic, which means that CCI-SIC and CCI-SST are not consistent. Trend and interannual variability of sea ice cover are however very similar between the CCI-SIC data set and all assimilation experiments.

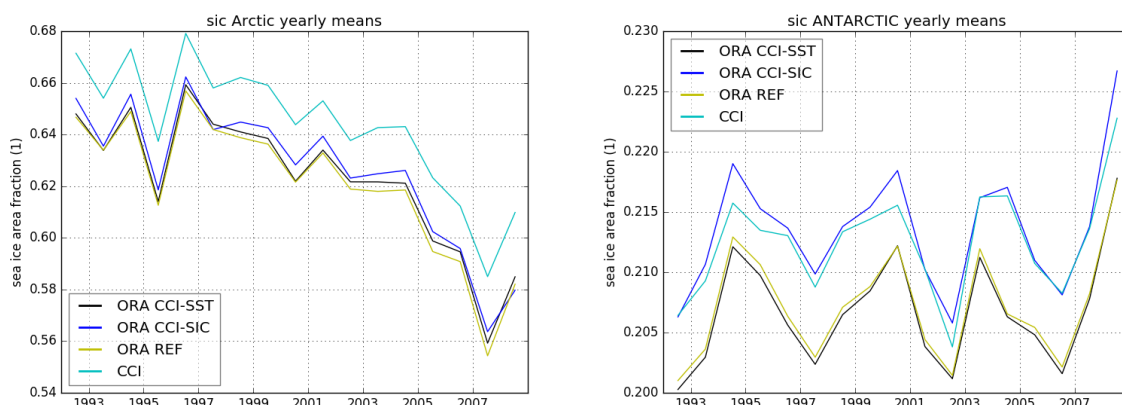


Figure 12: Annual-mean sea ice concentration in ORA assimilation experiments and CCI-SIC. (left) for the Arctic, (right) for the Antarctic.

CMUG Phase 2 Deliverable

Reference: D3.1: Quality Assessment Report
Due date: June 2017
Submission date: 21 December 2017
Version: 4



The varying consistency between CCI-SST and the ORA system, and CCI-SIC and the ORA system is highlighted by the average sea ice concentration assimilation increments in the Arctic (Figure 13). For an unbiased model, the average assimilation increments should be zero. If assimilation increments are consistently positive, the model has a negative bias, and vice versa. In ORA-REF, the average assimilation increment is roughly $1 \times 10^{-8}/s$ (equals 0.1 % per day). When assimilating CCI-SIC, this increases by $\sim 2 \times 10^{-8}/s$, reflecting the fact that the assimilation increments constantly try to bring the model closer to the excess spurious sea ice in the observations. Interestingly, when ingesting CCI-SST into the ORA system, the average sea ice concentration increment is *lower* than in the reference experiment (decrease by $\sim 2 \times 10^{-8}/s$). This indicates that CCI-SST is more consistent than HadISST2 with the sea ice cover in the assimilation experiment. When combining ingesting CCI-SST and assimilating CCI-SIC in experiment ORA CCI-ALL, the two effects cancel out and the average assimilation increment is very similar to ORA-REF.

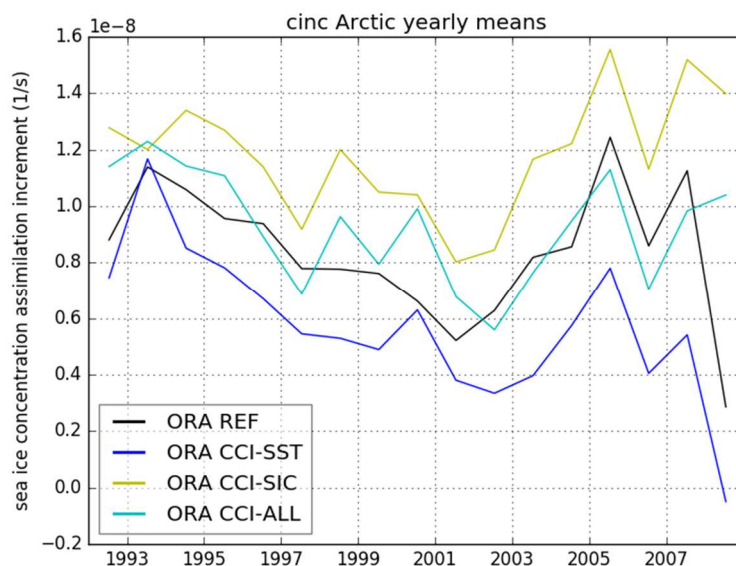


Figure 13: Annual-mean assimilation increments over the Arctic region in different ORA assimilation experiments.

Uncertainties of sea ice concentration provided with the CCI-SIC data are based on two distinct error sources: the algorithmic uncertainty which quantifies the variability of microwave emissivity for sea ice covered surface (Ivanova et al., 2015), and the smearing uncertainty which quantifies the error arising from interpolating brightness temperatures from variable satellite foot prints in the presence of strong spatial gradients. Likewise, if the footprint contains land surface, it is also very difficult to derive reliable ice concentration; this is covered by the smearing uncertainty as well. Figure 14 (left) shows the monthly average of these uncertainties during July 2007 for the Arctic as an example. The uncertainties are very high at the ice edge

CMUG Phase 2 Deliverable

Reference: D3.1: Quality Assessment Report

Due date: June 2017

Submission date: 21 December 2017

Version: 4



and along the coast lines; values larger than 30% occur. Away from the ice edge and coasts, only the algorithmic uncertainty is important, with values of 5% or less.

It is instructive to compare the CCI-SIC uncertainties (Figure 14 left) to the ORA ensemble spread (Figure 14 right). If ensemble spread is taken as a proxy for model uncertainty, then ORA analysis uncertainty is almost zero in the interior of the ice pack, and in areas of open water. The ORA analysis is also very confident about sea ice concentration along the coast lines. Only regions close to the ice edge show elevated levels of analysis uncertainty, but the structure does not match well with the CCI-SIC uncertainty. In summary, uncertainties in CCI-SIC are qualitatively different from uncertainties in the ORA system. This reflects the fundamentally different nature of observation and model errors and is not a problem. To the contrary: with a suitable data assimilation framework, the best fit between observations and model can be calculated using these spatially and temporally varying observation and model errors. This way, an analysis can be found that is superior to both the first guess of the model and the observational estimate, because it exploits the complementary strength of the model and the observations.

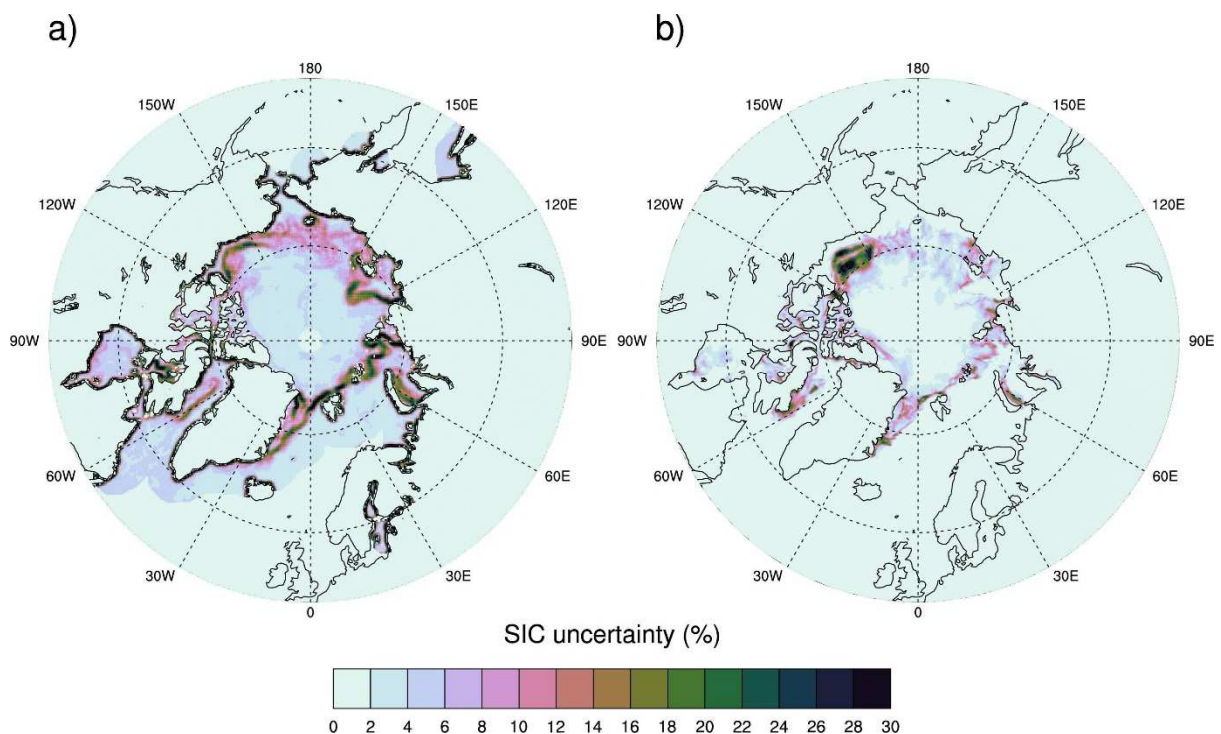


Figure 14: Sea ice concentration uncertainty in July 2007 as represented by (left) ESA-CCI SIC analysis error and (right) ORAS5 ensemble standard deviation. Shown is the monthly mean of daily mean analysis error and ensemble standard deviation, respectively.

CMUG Phase 2 Deliverable

Reference: D3.1: Quality Assessment Report
Due date: June 2017
Submission date: 21 December 2017
Version: 4



Impacts of assimilating ESA-CCI marine ECV on climate indices

As mentioned in the introduction, the value of assessing the marine ECV through assimilation in the ORA system lies in the ability to discuss cross-variable consistency and impact. We chose two indices which represent global modes of variability and climate change, and which are sensitive to changes in the observational data sets: the upper 300m ocean heat content in the tropics (UOHC), and the Northern Hemisphere sea ice volume (SIV).

Figure 15 (left) shows SIV November for 1993-2010 in all the assimilation experiments listed in Table 1. All show a similar strong decreasing trend between 2001 and 2007, with similar superimposed year-to-year variability. Observational estimates of sea ice volume from Kwok et al. (2009) and Tillich et al. (2015) are plotted as well. There are differences of 2000–3000 km³ between the ORA experiments, with ORA REF having the lowest SIV, and ORA CCI-ALL having the highest. There is reasonable agreement with the observational estimates. Overall it seems that ORA REF tends to have too low SIV, ORA CCI-ALL tends to have too high SIV, and CCI-SST and CCI-SIC agree with the observational estimates within the error bars.

For UOHC in the tropics, year-to-year variability and strong increasing trend between 2000 and 2005 are captured similarly by all assimilation experiments (Figure 15 right). During the early period, the different experiments have a larger difference in UOHC than in the later period, a fact that can be explained by the major increase in the density of in-situ observations with the implementation of the network of ARGO floats. In line with the SST differences discussed earlier, the ORA CCI-SST experiment has higher UOHC. Assimilation of SLA in ORA CCI-SLA leads to lower heat content. For both SIV and UOHC, the effect of combining the ingestion of SST and the assimilation of SLA in ORA CCI-ALL seems to be a linear combination of the individual effects.

Finally, it is worth noting that the simulation of major climate indices in the ORA system is not affected by exchanging the reference observational data sets for the CCI marine ECV data sets. Figure 16 demonstrates that there are hardly any discernible changes to monthly mean SST in the North Atlantic and in the Nino3.4 area, nor the Atlantic meridional overturning circulation.

CMUG Phase 2 Deliverable

Reference: D3.1: Quality Assessment Report

Due date: June 2017

Submission date: 21 December 2017

Version: 4

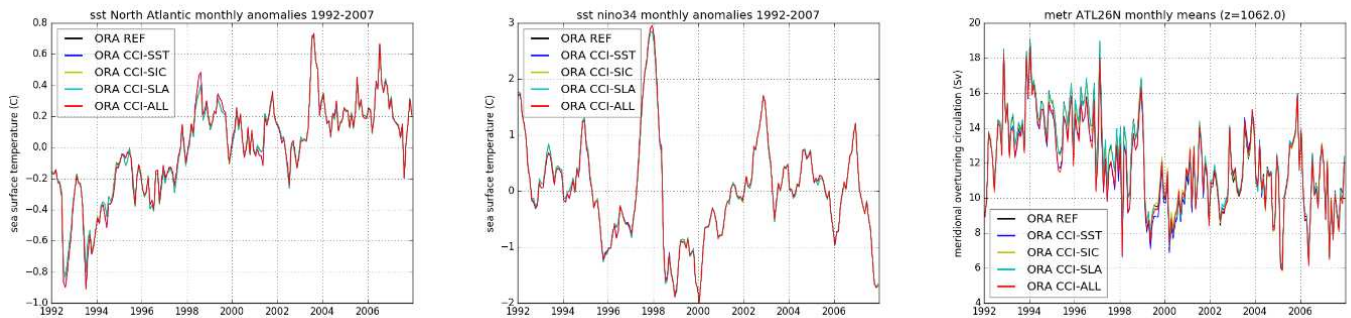


Figure 15: Northern Hemisphere sea ice volume (left), and upper 300m ocean heat content in the tropics (right) in the assimilation experiments.

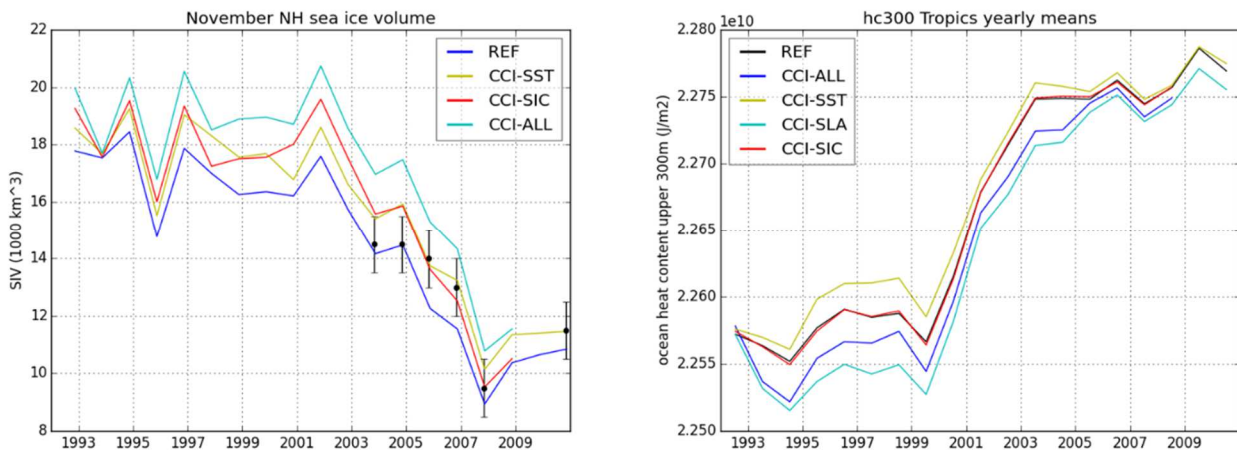


Figure 16: Monthly means of important marine climate indices as simulated by all assimilation experiments for the common period of all data sets. (Left) SST anomalies in the North Atlantic, (middle) SST anomalies in the Nino3.4 region, (right) Atlantic meridional overturning circulation.

Summary

A series of assimilation experiments with the ECMWF ocean reanalysis system has been performed, where standard observational data sets assimilated have been replaced by CCI marine ECV in different combinations. Results indicate that the simulation of large-scale climate indices and trends in the ocean reanalysis is only slightly affected. However, mean-state differences in the data products exist and appear in the reanalysis with some degree of moderation. There is evidence that especially the CCI-SST product has the potential to give positive contributions towards improving the ORA system. The provided uncertainties in the CCI-SIC product are an important improvement, and the overall trend and variability is consistent with earlier products. However, the decision not to mask out spurious sea ice creates

CMUG Phase 2 Deliverable

Reference: D3.1: Quality Assessment Report

Due date: June 2017

Submission date: 21 December 2017

Version: 4



problems with the ORA system, because it is not equipped to treat this properly – it would therefore be preferable to have spurious sea ice filtered out within the data product as much as possible. Assimilating CCI-SLA gives results very similar to the reference experiment, with the noteworthy exception being a lower increase after 2010 due to excluding data from CryoSat2. Combining assimilation of all marine ECVs leads to a combined large-scale result as would be expected from a linear combination of the individual assimilation experiments. The uncertainties provided with the CCI-SST and CCI-SIC look reasonable, and should be very valuable when improving upon the existing ORA assimilation system.

CMUG Phase 2 Deliverable

Reference: D3.1: Quality Assessment Report
Due date: June 2017
Submission date: 21 December 2017
Version: 4



3.3 Assimilation of several L2 ozone products in the ERA system [WP 3.2]

The results presented in this Section were completed in 2016 and there is no update to them in this report.

Aim

The aim of this study is to promote and facilitate the integration of as many O3-CCI products as possible in reanalysis systems in general and in the forthcoming ERA5 production in particular. A number of Observing System Experiments (OSEs) have been designed to provide a detailed assessment of the quality and of the impact of these O3-CCI products. The list of assessed datasets includes seven products encompassing the three lines of production of O3-CCI (total column, profiles from nadir instruments, and profiles from limb instruments).

A set of Round Robin (RR) assimilation exercises for algorithm selection were performed using ozone datasets retrieved alternative algorithms from the same radiance measurements. The aim of the RR exercise was to provide an objective and rigorous assessment of the impact of assimilating similar datasets, thus giving the reanalysis community feedback on which one to use.

By inter-comparison with the results from some of the performed experiments, it is possible to provide user recommendations to space agencies and retrieval teams on the most useful characteristics of future satellite instruments for ozone measurement.

Summary of Results

The results from this study were reported in the CMUG QAR (2015), and briefly summarized as follows:

- The structure of observation uncertainties generally compare well with estimates obtained using the Desroziers method (Desroziers et al., 2005). The differences between estimated and provided uncertainties show up to 60% overestimation in the tropical mid stratosphere for GOME-2 NPO3 (this accounts for less than 4% of the observation values) and up to 100% underestimation in the tropics for the total columns (this difference is about 8% of the global mean total column ozone value).
- All the products exhibit negligible to very small biases.
- All assessed O3-CCI datasets lead to improved ozone analyses.
- Regarding the RR assimilation exercises, with the exception of OMI TCO3, the O3-CCI retrievals seem to better constrain the ozone analyses than retrievals obtained from the same radiances using alternative algorithms.
- The assimilation of the GOME-2 NPO3 show a clear improvement in the internal consistency of the data assimilation system in terms of better fit to the AIRS ozone-sensitive

CMUG Phase 2 Deliverable

Reference: D3.1: Quality Assessment Report
Due date: June 2017
Submission date: 21 December 2017
Version: 4



IR channels that in turn leads to statistically significant reduction (i.e. improvement) in the RMS of the geopotential forecast errors in the tropics.

- Assimilation User Requirements to Space Agencies and retrieval teams:
 - ❖ The comparison of the impact generated by the GOME-2 TCO3 and that of the GOME-2 NPO3 shows that the latter dataset can lead to a greater positive impact on the ozone analyses than the former.
 - ❖ The comparison of the impact generated by the GOME-2 NPO3 and that of the MIPAS LPO3 shows that thanks to its higher vertical resolution limb observations can lead to a greater positive impact in the stratosphere and upper troposphere than the nadir ozone profiles. This is not always the case in the lower troposphere, where despite lacking visibility, the limb observations can still improve the ozone analyses compared to a control experiment if their synergy with other observations (in particular total column ozone products) can be exploited within the data assimilation system.

The recommendations that were formulated on the basis of the results and conclusions summarized above were un-controversially accepted by the C3S reanalysis team, and the following O3-CCI products are being assimilated in the ERA5 reanalysis currently in production: SCIAMACHY TCO3; GOME and GOME-2 NPO3; MIPAS LPO3.

A summary paper, Dragani (2016), was published in Atmospheric Chemistry and Physics.

CMUG Phase 2 Deliverable

Reference: D3.1: Quality Assessment Report
Due date: June 2017
Submission date: 21 December 2017
Version: 4



3.4 Integrated assessment of the CCI Aerosols, GHG, and Ozone datasets [WP3.3]

Aim

WP3.3 aims at providing an integrated assessment of the impact of assimilating ozone, aerosol, and GHG datasets in the global atmospheric composition data assimilation system developed within the ECMWF Integrated Forecasting System (IFS) through a number of FP6, FP7, and H2020 projects (GEMS, MACC, MACC-II, and MACC-III) and currently operated by the Copernicus Atmosphere Monitoring Service (CAMS) to provide NRT monitoring of air quality relevant gases and their reanalyses. The results are expected to feed back into the decision process in preparation for the forthcoming, first reanalysis of the CAMS.

Summary of the results and recommendations

We have performed a set of experiments using the ECMWF Integrated Forecasting System in a configuration with enhanced atmospheric chemistry used routinely by the Copernicus Atmosphere Monitoring Service.

The experiments were designed as integrated runs in which different ozone, aerosol and GHG products retrieved by the corresponding CCI consortia were assimilated in various combinations. The objectives were as follows:

- to assess the impact of each product of each individual ECVs on the corresponding model equivalent; and
- to discuss the level of consistency between the three ECVs.

The impact of assimilating each product was individually assessed through the comparison of the corresponding analyses against independent observations. The results are as follows:

- Ozone: Of the O₃-CCI products, this work focussed on the exploitation of the limb instrument datasets that were not addressed in WP3.2. The results showed that
 - ❖ the SMR limb ozone profiles produce a negligible impact at most latitudinal band but they lead to an improvement of the level of agreement between the ozone analyses and reference data (MLS and ozone sondes) at high latitudes in the SH during winter and spring.
 - ❖ With a few exceptions, the assimilation of both the SCIAMACHY limb and the OSIRIS ozone profiles seem to degrade the analysis fit to MLS (either in the mean or standard deviation) and to the sondes at most upper tropospheric and stratospheric layers in the extra-tropics.
- Aerosols: The assimilation of the SU and ADV datasets was individually assessed as the sole source of aerosol constraint and in combination with MODIS observations. The results

CMUG Phase 2 Deliverable

Reference: D3.1: Quality Assessment Report
Due date: June 2017
Submission date: 21 December 2017
Version: 4



of the comparisons against AERONET show that:

- ❖ The two CCI products have a very similar impact on the aerosol forecasts, with the ADV dataset being only marginally better than the SU one;
 - ❖ Neither of the two AATSR datasets can provide a constraint on the aerosol forecasts as important as that provided by MODIS observations, though the amount of data from the former is latter than that of the former;
 - ❖ The combination of AATSR data with MODIS improves the quality of the aerosol forecasts on that of either AATSR-only or MODIS-only assimilation.
- GHG: The assimilation of several CCI CO₂ and CH₄ products were assimilated in different combinations with and without the LMD IASI CO₂ and CH₄ data used to derive a baseline set of analyses. The results show that:
- ❖ The CO₂ analyses all show very high correlation (>93%) with the TCCON observations. However, the control experiment only constrained by the LMD IASI data is the one with the highest correlation at over 99% and its combination with any of the CCI dataset seems to degrade the analysis agreement with the TCCON data.
 - ❖ Among the two full physics datasets, the SRFP is the one that in combination to IASI CO₂ leads to a larger degradation of the fit to TCCON data than the IASI-only CO₂ analyses.
 - ❖ The assimilation of BESD SCIAMACHY CO₂ in addition to IASI leads to analyses that show only a minor degraded fit to the reference data while the incremental addition of the SRFP dataset produces the CO₂ analyses with the worst fit to TCCON.
 - ❖ For CH₄, the SRON SRFP and SRPR dataset were used to assess the impact of using a datasets produced by an algorithm with detailed physics versus a proxy. The use of the proxy leads to CH₄ analyses that have a 5% lower correlation with TCCON than their equivalent using the full physics product.
 - ❖ On average, either product leads to degraded CH₄ analyses than those from an LMD IASI-only experiment. However, a number of sites showed that the agreement of individual TCCON measurements with their analyses equivalent was higher for the CCI data, particularly during the Aug-Oct period when the IASI-only analyses exhibited a divergent behaviour.
- Cross-ECV consistency: two examples were discussed on the impact of O₃ on aerosols and that of aerosols and GHG together on O₃. In the first case, the assimilation of one additional CCI O₃ dataset leads to a small, but non-negligible positive impact on the aerosols forecasts suggesting a good level of consistency between these two ECVs. The second case is inconclusive as it leads to improvements in some regions of the atmosphere and locations and degradation in others. The degradation found in the GHG analyses after adding the CCI datasets and the limitations of the system in not correcting for the surface fluxes could be the main reason for the degradation promoted in the ozone analyses.

CMUG Phase 2 Deliverable

Reference: D3.1: Quality Assessment Report
Due date: June 2017
Submission date: 21 December 2017
Version: 4



The results of this study show some potential for some of the datasets (e.g. SMR), pose some questions about possible inter-instrumental biases affecting the analyses when combination of datasets are jointly assimilated, suggests that limitations in the data assimilation system can partly explain the limited ability of exploiting some of the considered datasets, and confirm that a proxy dataset cannot provide the same level of constraint of one based on full physics.

Of all the datasets used in this study, the assimilation of the AATSR aerosols in combination with MODIS data can be recommended, that of the SMR ozone profiles could be considered but more experimentation might be needed to determine if more information can be extracted in the summer hemisphere and tropics. Additional work is perhaps needed before the GHG datasets can be efficiently exploited, especially when datasets from different sources are considered for a joint assimilation.

The data assimilation system

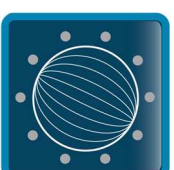
The data assimilation system used in this study consists in the most recent version of the global atmospheric composition data assimilation system operated at ECMWF for the CAMS. This system uses a bin-model for aerosol that includes desert dust, sea salt, organic matter, black carbon and sulphates, as well as the greenhouse gases, allowing assimilation of CO₂ and CH₄. For the chemical reactive species (i.e. O₃, CO, NO₂, SO₂ and HCHO), the IFS data assimilation system was extended to include an integrated chemistry model (referred to as C-IFS), which provides emissions, deposition, and chemical tendencies for the species included in the system. These variables are all constrained by the assimilation of satellite observations, where possible.

The experiment design

The assessment of the three CCI ECVs is performed in both passive and active modes.

To account for the CAMS and CCI requirements, a complex set of experiments was designed. This included six assimilation experiments, and it is presented in Table 4. Experiments **gi91**, **gi92**, **gi93**, and **gi94** (Exp 1 – Exp 4) are used to assess the individual aspects for each of the three ECVs with respect to the Ctrl (**gi90**) while experiment **gi95** (Exp 5) will help to assess the level of consistency between the three ECVs when contrasted with the results from some of the other experiments.

All the experiments started on 1 Jan 2010, and ran until the end of September 2010, with the aim of analysing in detail the NH summer period (May-October 2010) after removing the period affected by spin-up. The experiments ran at a model resolution of T_L255 (about 80 km) on 60 vertical levels – as used in the Copernicus Atmosphere Monitoring Service at the time the experiments were submitted.



The results from the assessment of these experiments are summarized below. We first look at the impact of each ECV on their analysis equivalent, and then we use the data assimilation system to discuss the cross-ECV consistency.

Experiment NAME / ID	Ozone		Aerosol		GHG			
	Passive	Active	Passive	Active	CO ₂		CH ₄	
					Passive	Active	Passive	Active
Control / gi90	SCIA limb OSIRIS SMR ACE-FTS	SBUV SCIA TCO3	SU AATSR	MODIS	BESD SCIA SRFP TANSO	IASI	SRFP TANSO	IASI
Exp 1 / gi91	OSIRIS SMR ACE-FTS	SBUV SCIA TCO3	MODIS	SU AATSR	BESD SCIA	IASI OCFP TANSO	N/A	IASI SRFP TANSO
Exp 2 / gi92	SCIA limb OSIRIS SMR	SBUV SCIA TCO3	N/A	MODIS SU AATSR	BESD SCIA	IASI SRFP TANSO	N/A	IASI SRPR TANSO
Exp 3 / gi93	SCIA limb OSIRIS ACE-FTS	SBUV SCIA TCO3	MODIS	ADV AATSR	OCFP TANSO	IASI BESD SCIA	IASI	SRFP TANSO
Exp 4 / gi94	SCIA limb SMR ACE-FTS	SBUV SCIA TCO3	N/A	MODIS ADV AATSR	N/A	IASI SRFP TANSO	IASI	SRPR TANSO
Exp 5 / gi95	SCIA limb OSIRIS SMR	SBUV SCIA TCO3	ADV AATSR	MODIS	OCFP TANSO	IASI	SRPR TANSO	IASI

Table 4: Experiment design for WP3.3. The CCI data are given in bold. The experiment IDs as used in the following plots are provided in the first column together with their name.

CMUG Phase 2 Deliverable

Reference: D3.1: Quality Assessment Report
Due date: June 2017
Submission date: 21 December 2017
Version: 4



Impact of each ECV on their analysis equivalent:

In this section, the focus is in assessing the impact of each ECV on their model equivalent.

▪ Ozone:

We first look at the impact of the assimilating the CCI limb ozone data on the ozone analyses by comparison with independent ozone observations from the Aura Microwave Limb Sounder (MLS), ozone sondes available at the World Ozone and Ultraviolet Radiation Data Centre (WOUDC). These were used as independent ozone references for the stratosphere and troposphere/lower stratosphere, respectively. In all comparisons, the ozone analyses were spatially co-located with the independent observations allowing a maximum three hour time lag.

The MLS comparisons were performed in two stages. First, the 3D ozone analysis closest in time to the independent observation was interpolated at the observation location. This gives a temporal mismatch of up to 3 hours between the observation sensing time and the analysis valid time. The second stage takes care of the vertical interpolation. This is done by interpolating the profile with the highest vertical resolution to the coarsest grid. In these comparisons, the coarsest grid is represented by that of the MLS data with its vertical resolution of about 3 km. Only the levels spanning the region of the atmosphere encompassed by both datasets are used.

The comparisons with MLS are displayed as the vertical cross-section of the change in the analysis fit to the observations due to the addition of any of the O3-CCI limb data to the reference observing system assimilated in the control experiment. Such a change, Δ , is defined as:

$$\Delta = |\text{STAT}(O_3^{MLS} - O_3^{PERT})| - |\text{STAT}(O_3^{MLS} - O_3^{CTRL})| \quad (1)$$

where $\text{STAT}()$ can be either the mean or the standard deviation. In equation (1), O_3^{MLS} is the ozone observation from MLS, O_3^{PERT} and O_3^{CTRL} are the ozone analyses collocated to the MLS observations from a perturbation and the control experiment (unless otherwise mentioned the control is **gi90**). The perturbation can be any of the other experiments.

For either statistics, a negative value of Δ means that the analyses from a given perturbed experiment fits MLS observations better than those from the control, thus leading to an improvement. In contrast, a positive value of Δ is associated to a degradation in the ozone analyses.

This quantity Δ is showed in figure 17 for the assimilation of the SCIAMACHY limb, the SMR, and the OSIRIS ozone profiles. In the top panels, STAT is the mean; in the bottom panels, it is the standard deviation.

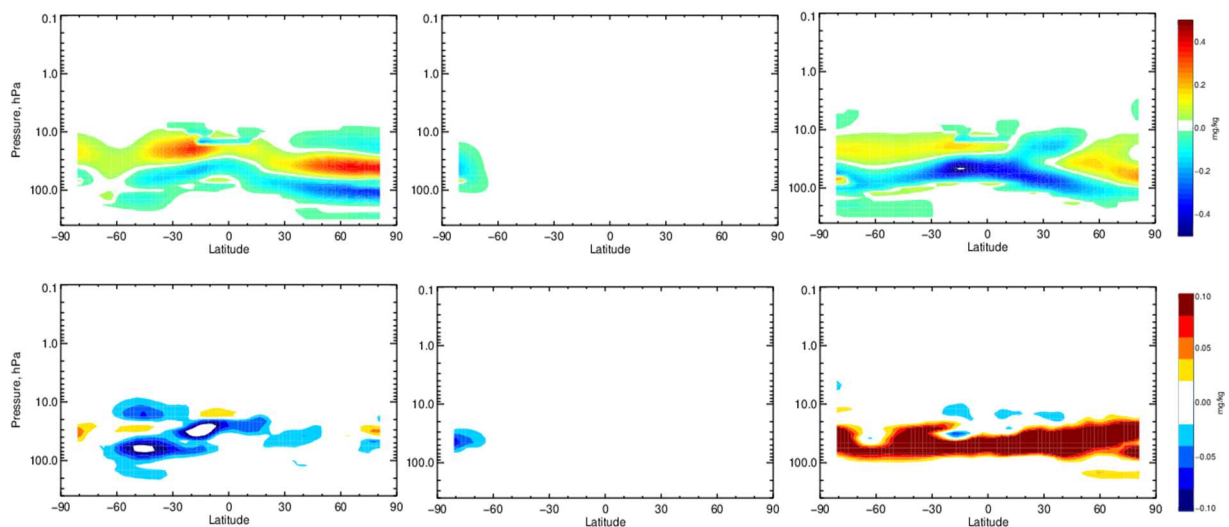


Figure 17: Change in the zonal mean (top panels) and standard deviation (bottom panels) differences between the MLS retrievals and co-located ozone analyses from a perturbation experiment compared to the Exp/Ctrl for May-Oct 2010, computed according to equation (1). The perturbation experiment is the one also assimilating the SCIAMACHY limb data in the left panel, the SMR profiles in the middle panel, and the OSIRIS profiles in the right panel. Negative (positive) values in blue (red) colours indicate a poorer (a better) fit of the control analyses to MLS than their perturbed equivalent, and thus, compared to MLS ozone profiles, an improvement (a degradation) in the data assimilation system due to the new observations. Data are in mg/kg.

Compared to MLS, the assimilation of SCIAMACHY limb data produces a degradation in the analyses mixing ratio around the ozone maximum while the standard deviation of the residuals from the observations is normally improved. In contrast, the assimilation of OSIRIS retrievals (right hand side panels) leads to improvements in the mean analyses but a degradation in the standard deviation of the residuals, implying an increased noise in the ozone analyses. The assimilation of the SMR profiles is the only case in which both the mean state and the standard deviation are improved. However, the impact is only visible at high latitudes in the SH. This is most likely a consequence of the fact that the information provided by the SMR data at latitudes northern than around 60S was also available in the data assimilation system via the assimilation of other ozone observations (namely, total column ozone from SCIAMACHY nadir, and ozone profiles from NOAA-16, -17, and -18 SBUV/2). As these other sources of ozone data are all from UV instruments and those cannot provide measurements at high latitudes in the SH during the polar night (i.e. the period considered here), a positive impact on the ozone analyses is produced by the assimilation of the SMR dataset.

Figures 18 and 19 show the comparisons of four sets of analyses (the control, and three sets of analyses assimilating also the SCIAMACHY limb, the SMR, and the OSIRIS limb profiles from CCI, respectively) and ozone sondes from the WOUDC archive, for May-Jul and Aug-Oct. The comparisons with the ozone sondes are shown in terms of mean RMS residuals, RMSE, between

CMUG Phase 2 Deliverable

Reference: D3.1: Quality Assessment Report

Due date: June 2017

Submission date: 21 December 2017

Version: 4



the sonde profiles and the co-located analyses from the four experiments. Thus the smaller is the RMSE, the better is the analysis fit to the sonde measurements. For plotting purposes, the RMSE are computed and displayed in terms of integrated column quantities.

The comparisons with ozone sondes in May-Jul (figure 18) confirm that the assimilation of SMR data has in general a neutral impact on the ozone analyses, except at high latitudes in the SH (wintertime) where it leads to a slightly better agreement with the independent data than that for the control analyses. With a few exceptions, the assimilation of both the SCIAMACHY limb and OSIRIS seem to degrade the fit to the ozone sondes at most upper tropospheric and stratospheric layers in the extra-tropics during May-Jul 2010.

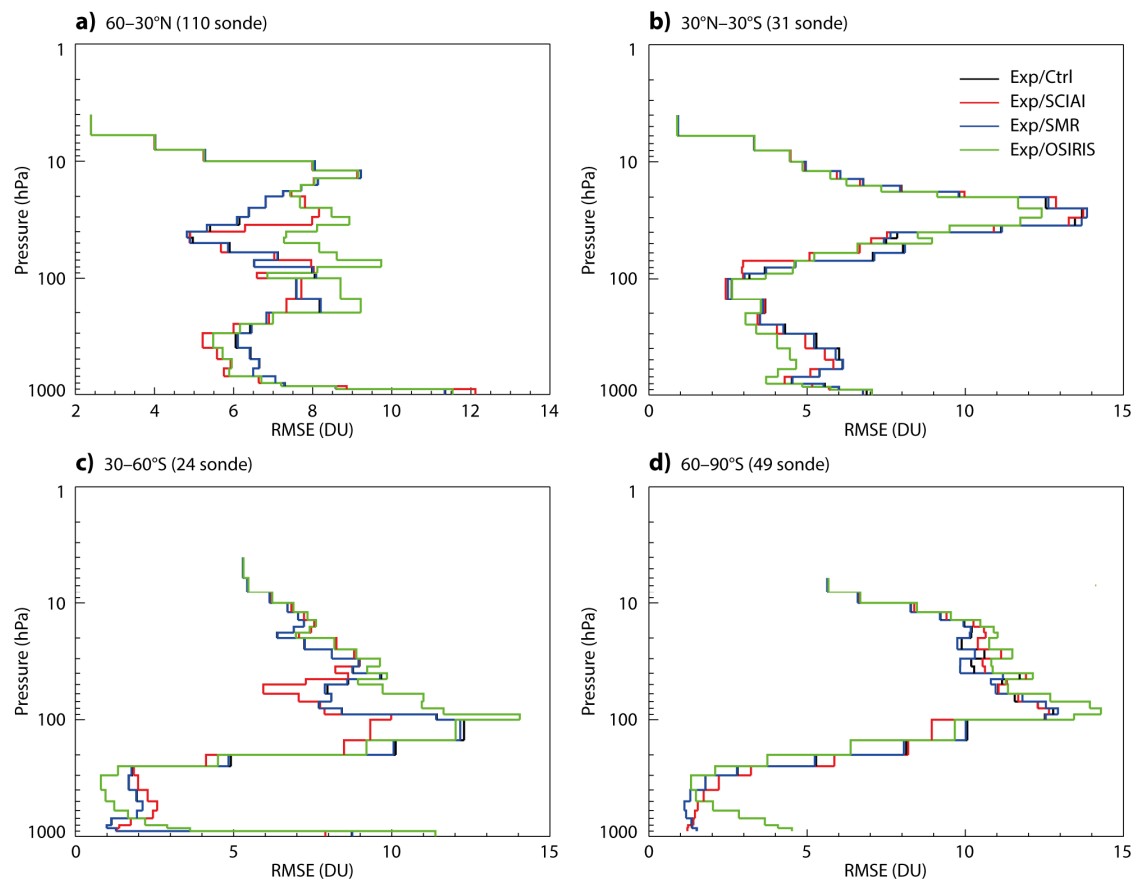


Figure 18: Fit of the ozone analyses from four experiments to ozone sondes given in terms of the RMSE over four latitudinal bands between 90S-60N. The comparisons were computed by averaging over May-Jul 2010. The analyses were taken from the control (black lines), and the experiments assimilating also the SCIAMACHY limb O3 profiles (red lines), the SMR data (blue) and the OSIRIS data all from the O3-CCI. The latitudinal band each panel refers to and the number of ascents included in the average can be found in the corresponding panel title. Data are in Dobson Unit (DU).

CMUG Phase 2 Deliverable

Reference: D3.1: Quality Assessment Report

Due date: June 2017

Submission date: 21 December 2017

Version: 4



In the tropical region, the impact of SCIAMACHY limb data is mostly neutral while OSIRIS has a positive impact in the region of the ozone mixing ratio maximum between 15 and 30 hPa, and as a consequence of the synergy with the total column ozone retrieved from SCIAMACHY (nadir measurements) also at some levels in the troposphere. The reasons why this occurs were discussed in detail by Dragani (2016).

During the period Aug-Oct (figure 19), the assimilation of OSIRIS is at best neutral in the NH and at mid-latitudes in the SH, and from neutral to slightly positive at high latitudes in the SH. The impact of SCIAMACHY limb is in general from slightly positive to positive at most levels and latitudinal bands, with only a few exceptions, for instance the middle stratosphere at mid-latitudes in the SH (bottom left panel of figure 19). As in the May-Jul period, also during the following three months the assimilation of SMR ozone profiles is neutral to slightly positive in the region of the ozone hole.

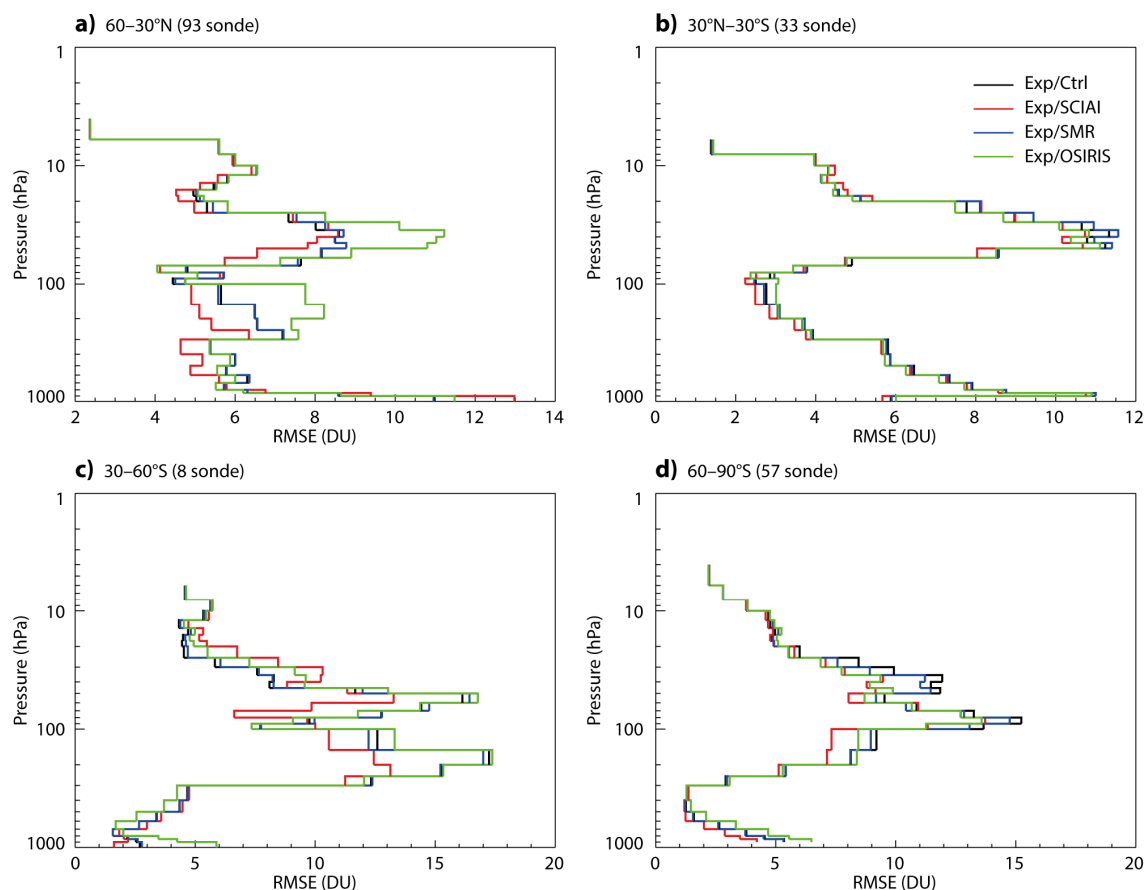


Figure 19: Like in figure 18, but for Aug - Oct 2010.

■ Aerosols:

The CCI aerosol AOD at 550nm produced with the SU and ADV algorithms from the ENVISAT AATSR measurements were each assimilated individually and together with AQUA and TERRA MODIS data. In all cases the impact is assessed against the AERONET dataset used as reference.



An additional experiment, in which only MODIS data are assimilated, is used as a control experiment. It is noted that the two MODIS instruments from AQUA and TERRA provide a larger amount of data than available from the AATSR instrument, thus it should be expected a larger impact of the former on the analyses compared to the latter.

Figure 20 presents a summary of the comparisons. This is presented in terms of the scatter plots of the aerosol forecasts for different experiments against the AERONET observations.

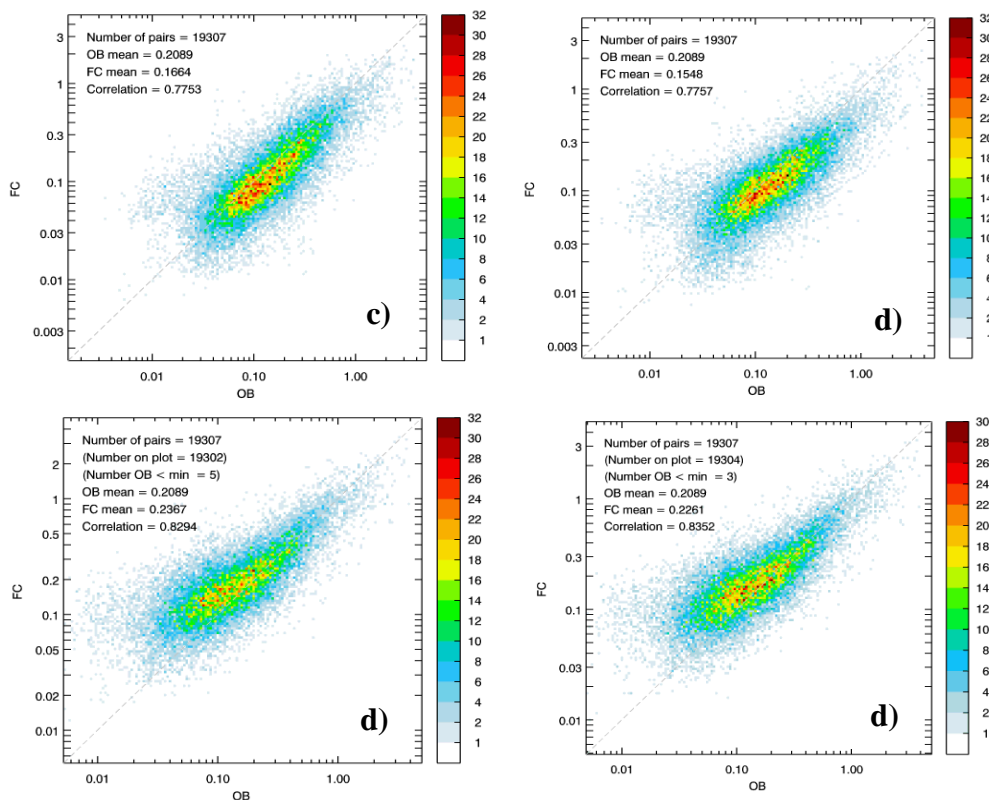


Figure 20: Scatter plot of the Aeronet AOD at 550nm (x-axes) against their forecast equivalent (y-axes) computed for an experiment assimilating the CCI AATSR AOD retrieved with the SU algorithm (a), an experiment assimilating the CCI AATSR AOD retrieved with the ADV algorithm (b), an experiment assimilating the MODIS AOD (c), an experiment assimilating both the CCI AATSR AOD retrieved with the ADV algorithm and the MODIS AOD (d).

Panels a) and b) in figure 20 show that the two CCI AOD products have similar impact on the AOD forecasts. A marginal higher level of agreement can be found in the case of the assimilation of the ADV AATSR dataset (+0.04% higher correlation) compared to the assimilation of the SU AATSR equivalent.

When compared with the assimilation of only MODIS AOD data (panel c)), neither of the two CCI datasets can match the level of agreement that the AOD forecasts reach with the AERONET data. In this case the correlation between observed and forecasted AOD is about 5% higher than

CMUG Phase 2 Deliverable

Reference: D3.1: Quality Assessment Report

Due date: June 2017

Submission date: 21 December 2017

Version: 4



the one computed from AATSR-based forecasts. Nonetheless, the assimilation of both MODIS and either AATSR dataset improves the correlation with AERONET of +0.6% compared with the assimilation of MODIS data alone. This increase in the correlation is a clear indication that the data assimilation system is able to exploit the synergy between the two datasets and transfer that information to the AOD forecast field. When referring to individual locations and regions, the above results are generally confirmed (figure 21).

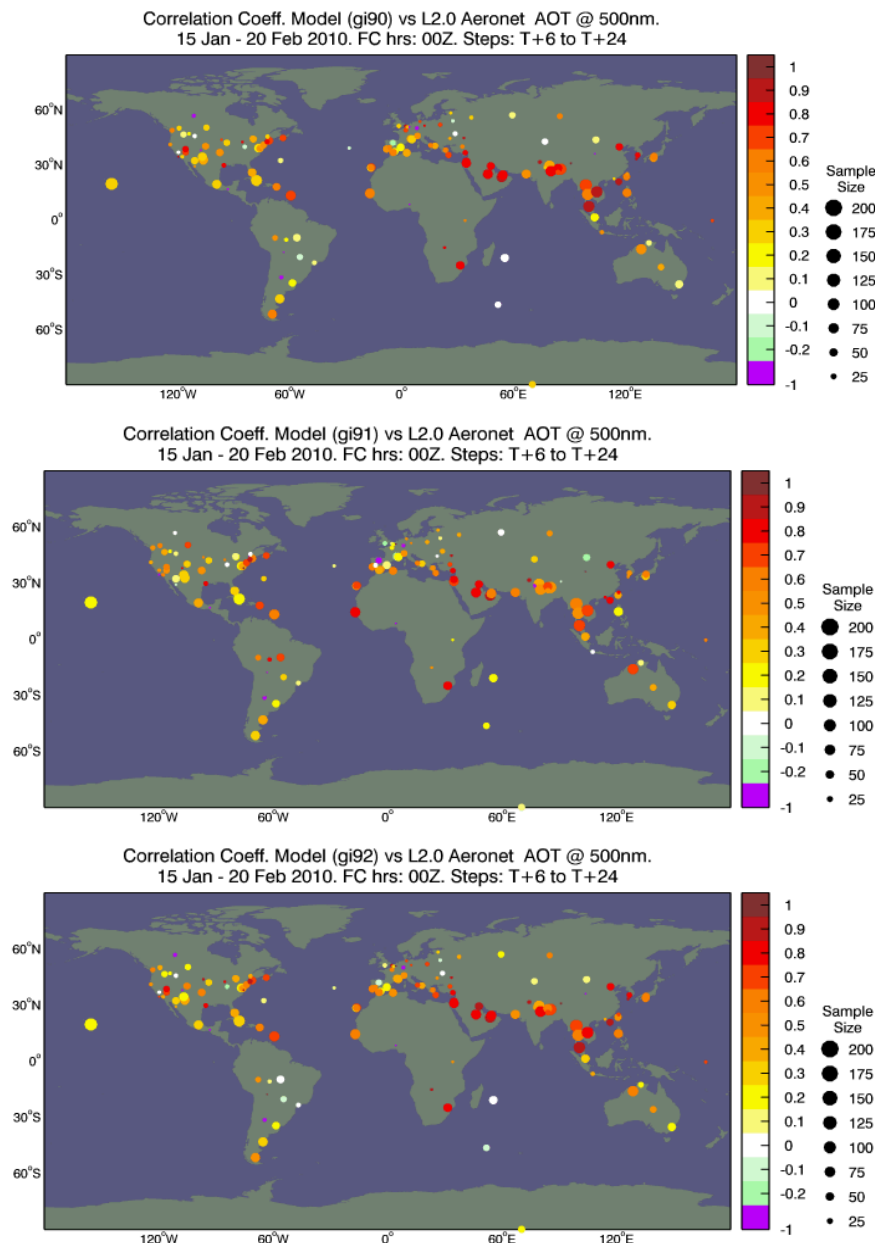


Figure 21: Correlation coefficient between the modelled AOD and the AERONET data at 500 nm at various sites for experiment **gi90** (MODIS only, top panel), **gi91** (AATSR only, middle panel) and **gi92** (MODIS and AATSR, bottom panel). The size of each circle refers to the size of sample used to estimate the correlations.

CMUG Phase 2 Deliverable

Reference: D3.1: Quality Assessment Report
Due date: June 2017
Submission date: 21 December 2017
Version: 4



The correlations between the modelled and AERONET AODs by station for the experiments **gi90** (top panel), **gi91** (mid panel), and **gi92** (bottom panel) show that over the South-East Asia the assimilation of MODIS AOD produces modelled AODs that have higher correlation with the AERONET observations than those constrained with the CCI AATSR retrievals. Some exceptions can be found for a number of station over the South America, over which the latter show higher correlation with the independent dataset than the former.

▪ GHG:

The SCIAMACHY CO₂ and the TANSO CO₂ and CH₄ retrieved with several algorithms from GHG-CCI were assimilated in IFS in a set of experiments detailed in table 4. An experiment assimilating the IASI CO₂ and CH₄ retrievals was also run and used as a control. These IASI observations were retrieved by the Laboratoire de Météorologie Dynamique (LMD) and already available at ECMWF. None of the GHG product was bias corrected in the IFS. The analyses resulting from the set of experiments in table 1 were compared with observations from the TCCON network used as a reference. Not only the comparisons were performed by co-locating the model output with the observed reference but also accounting for the a priori and Averaging Kernels of the CCI data as explained by Massart et al (2016). A summary of the results is presented in figures 22 and 23 for CO₂ and CH₄, respectively.

For CO₂, the experiments were designed to assess the impact of two full physics algorithms, and the incremental impact of two products, one from ENVISAT/SCIAMACHY and the other from GOSAT/TANSO. Figure 22 summarizes the results, and shows the scatter plots between TCCON CO₂ and the CO₂ analysis equivalent for several experiments. Each panel presents with black symbols the scatter plot for the control experiment assimilating only the IASI data. The CO₂ analyses from the control experiment exhibit very high correlation with the TCCON dataset with a level of 99.74% over all the available sites. Compared to this control, the other experiments (**gi91**, **gi92**, **gi93**, and **gi94**) were designed as incremental experiments assimilating one or two datasets from CCI. Overall, the analyses from all experiments show high level of correlation with the TCCON observations, ranging from a minimum of 93.52% to a maximum correlation of 99.74%. Although the correlation is always above 93%, the combination of the IASI data with any of the CCI dataset seems to degrade the level of agreement of the analyses with the TCCON data compared to the assimilation of IASI only data. This could point to inter-instrumental biases between the IASI and the CCI CO₂ retrievals that if uncorrected can deteriorate the resulting analyses.

The CO₂ analyses from experiments **gi91**, and **gi92** were constrained by the IASI CO₂, and by GOSAT TANSO CO₂ data from CCI retrieved using the University of Leicester and SRON full physics algorithms, respectively. These two GOSAT datasets are referred to as the OCFP and SRFP datasets and their scatter plots are shown in the top left and top right panels of figure 22, respectively. The addition of either CCI CO₂ retrievals to the IASI data leads to CO₂ analyses that show a degraded fit to the TCCON observations. The degradation seems to be more important in

CMUG Phase 2 Deliverable

Reference: D3.1: Quality Assessment Report

Due date: June 2017

Submission date: 21 December 2017

Version: 4



the case of the SRFP dataset than in the OCFP case with a reduction of the correlation of 4.23% and 1.7%, respectively.

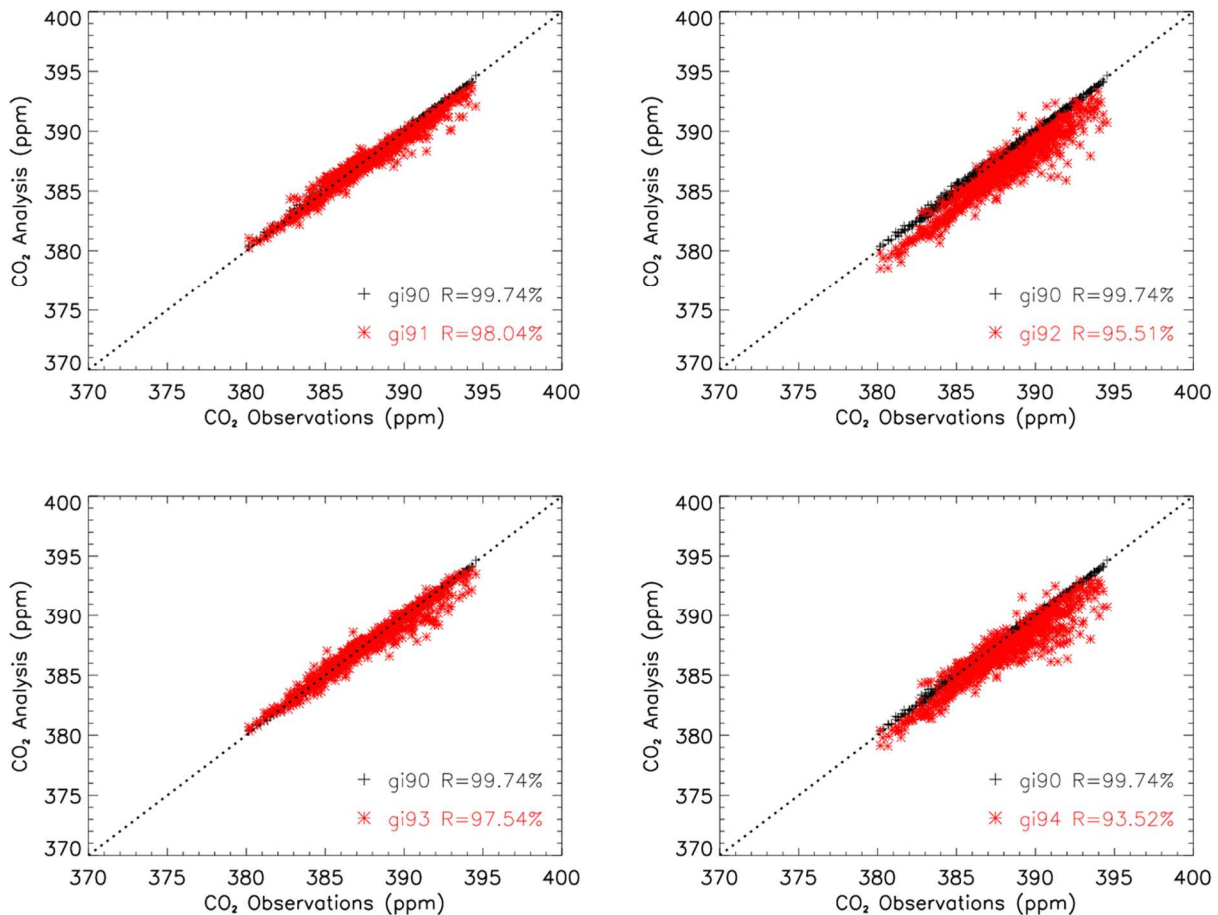


Figure 22: Scatter plot between the TCCON observations and their collocated CO₂ analyses (y-axis) for five experiments: the control experiment (**gi90**, black +), and different combinations of the CCI datasets as given in table X1. For each experiment, the correlation (labelled in the legend of each panel as 'R') is provided in %. All available TCCON data were used.

The bottom left panel of figure 22 refers to the comparisons of the analyses constrained by both the LMD IASI and CCI BESD SCIAMACHY CO₂ data against the TCCON observations. Although lower than for the control using only IASI, the correlation for the **gi93** CO₂ analyses is similar to the one obtained for the **gi91** CO₂ analyses, implying that the two products have a similar impact on the analyses.

The bottom right panel of figure 22 refers experiment **gi94** that assimilated the CCI SRFP GOSAT and BESD SCIAMACHY CO₂ data in addition to the LMD IASI retrievals. The CO₂ analyses

CMUG Phase 2 Deliverable

Reference: D3.1: Quality Assessment Report

Due date: June 2017

Submission date: 21 December 2017

Version: 4



from this experiment is the one that exhibits the lower level of correlation with the TCCON observations at a level of 93.52%.

For CH₄, the experiments were designed to contrast the impact of a dataset retrieved with a full physics algorithm with that of retrievals from a proxy algorithm. In both cases, the impact was evaluated in isolation and in combination with a CH₄ dataset retrieved by LMD from the IASI measurements. The full physics and the proxy data developed by SRON were considered in this case, and referred to as SRFP and SRPR, respectively. Figure 23 summarizes the results, and shows the scatter plots between the TCCON CH₄ and the CH₄ analysis equivalent for several experiments. Each panel presents with black symbols the scatter plot for the control experiment assimilating only the IASI data. The two top panels refer to the experiments using a combination of IASI data and either the SRFP (left panel) or SRPR (right panel) data. The bottom panels refer to the comparisons for the analyses constrained by only one of the CCI datasets.

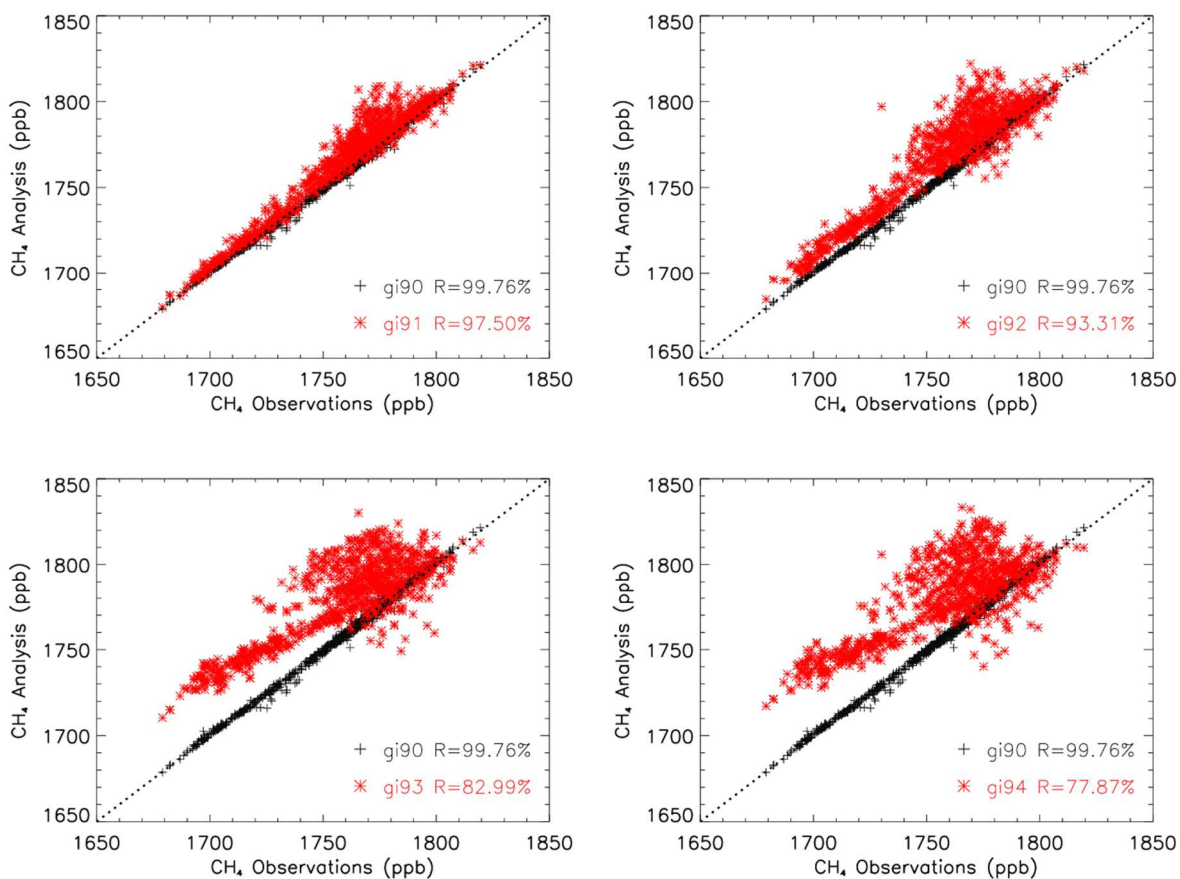


Figure 23: Like figure 22, but the CH₄ analyses and TCCON observations.

CMUG Phase 2 Deliverable

Reference: D3.1: Quality Assessment Report
Due date: June 2017
Submission date: 21 December 2017
Version: 4



On average, the CH₄ analyses from the control experiment exhibit very high correlation with the TCCON dataset with a level of 99.76% over all the available sites. The two GOSAT CH₄ products generate CH₄ analyses that have a lower level of agreement with the TCCON CH₄ data than that from the control experiment. The correlation with TCCON data is about 83% when the data from the full physics algorithm is used, and it decreases of about 5% to less than 78% when the analyses are constrained by the proxy dataset suggesting an advantage in using a product generated using a full physics algorithm compared to a simple proxy (bottom panels of figure 23). This result is confirmed in when the analyses are also constrained by the LMD IASI CH₄ observations, albeit higher correlation values driven by the use of the IASI data.

The level of correlation obtained from all sites over the whole period May-Oct 2010 does not always reflect the level of agreement found over individual sites. In particular, it was noted that during the second half of the considered period the analyses constrained by either the SRFP or SRPR datasets had a better agreement with their TCCON equivalent than those only constrained by the LMD IASI data. Figure 24 shows the time series of the three sets of analyses from **gi90** (IASI only, red), **gi93** (SRFP only, blue), and **gi94** (SRPR only, green) at four selected TCCON stations (as indicated in each panel) against the TCCON observations (black symbols). The red, blue and green symbols show the analysis equivalent of the TCCON data for the three experiments. At these stations, the analyses constrained by IASI-only generally compares better with TCCON data than the other analyses during summertime. Towards the end of the assimilation period, the analyses constrained by the two CCI products are in better agreement with the TCCON measurements over the shown sites while those constrained with the IASI data seem to progressively diverge.

This situation could be related to a model error amplification with observations that are not able to properly correct for the model shortcomings. One of the problems of the system is that the CH₄ concentration is only constrained by the observed CH₄ concentration while no correction is made to the surface fluxes. This suffices to produce sensible analyses in general. However, if in a given location/region and time the CH₄ concentration strongly depends on and is driven by the surface fluxes then errors can result in the analysed fields as the data assimilation system cannot generate increments based on the assimilated data that account or can correct for the missed information in the surface fluxes.

These situations can be exacerbated if the observations have limitation themselves, or when observations from different sources and affected by inter-instrumental biases are assimilated simultaneously without any bias correction.

CMUG Phase 2 Deliverable

Reference: D3.1: Quality Assessment Report

Due date: June 2017

Submission date: 21 December 2017

Version: 4

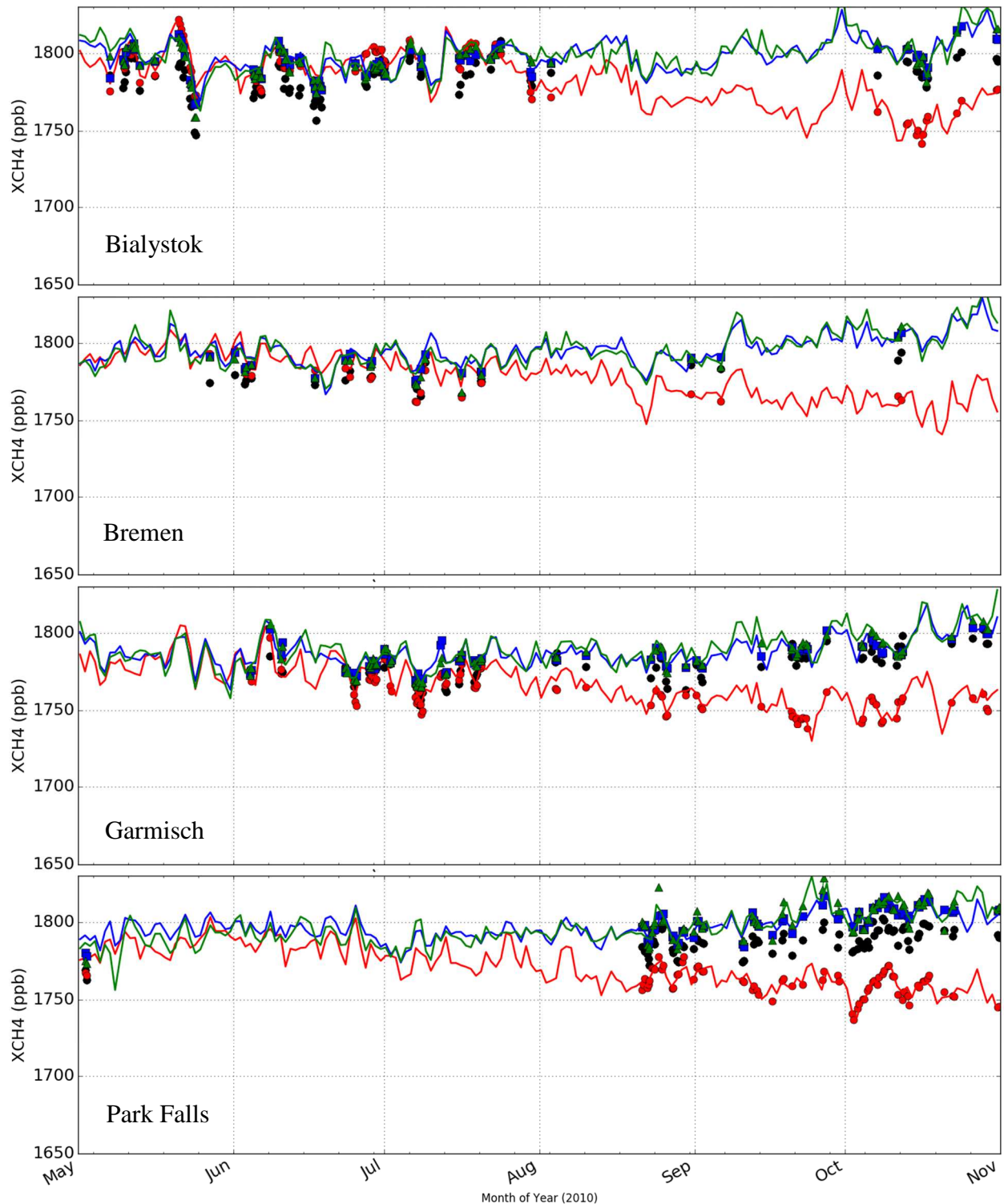


Figure 24: Time series of the *gi90* (red), *gi93* (blue) and *gi94* (green) analyses at four TCCON stations. The TCCON observations are shown by the black symbols. The analysis equivalent of the observations is indicated by the red, blue and green symbols for each of the three experiments.

CMUG Phase 2 Deliverable

Reference: D3.1: Quality Assessment Report
Due date: June 2017
Submission date: 21 December 2017
Version: 4



Assessment of the cross-ECV consistency:

In addition to the impact of each CCI ECV on their model equivalent, the data assimilation system was also used to assess the consistency between the three ECVs. It is important to note that the data assimilation system in its current development allows for little impact across-ECVs. This conservative approach is used to preserve the quality of the corresponding analyses and forecasts avoiding they could be degraded in the event of poor quality observations of a different geophysical variable are mistakenly assimilated. Nonetheless, variational data assimilation techniques, in particular 4DVar, can still provide a weak connection between different ECVs that in some cases can be large enough to be measurable. This is because 3D-Var and 4D-Var multivariate data assimilation schemes make use of explicit background-error correlations and balance relationships. That means that changes to one variable cannot happen in isolation. Thus, an ozone increment due to the assimilation of ozone observations can also be accompanied by an increment in other fields, e.g. aerosols. We show here two examples, the first refers to the impact of ozone data on aerosol forecasts, and the second is the impact of the assimilation of aerosols and GHG on the ozone analyses.

Table 5 lists the data that were assimilated in the experiments **gi90** and **gi95** that are used for the first example. The same aerosols and GHG datasets were used in both experiments. In contrast, the ozone analyses in **gi95** benefitted from the assimilation of SMR data in addition to the SBUV and SCIAMACHY TCO3 that were also used in experiment **gi90**. We now assess the quality of the aerosol AOD forecasts at 550nm for both experiments against the AERONET network.

	OZONE	AEROSOLS	GHG	
			CO2	CH4
gi90	SBUV SCIA TCO3	MODIS	IASI	IASI
gi95	SBUV SCIA TCO3 SMR	MODIS	IASI	IASI

Table 5: Experiments considered in figure 24. The CCI data are given in **bold**. Only the data assimilated in the data assimilation system are listed.

Figure 25 presents the scatter plots of the AERONET AOD data and their model equivalent for the experiments **gi90** and **gi95**. Albeit small, it shows that the correlation of the aerosol forecasts to AERONET increases from 82.94% to 83.11%, i.e. +0.17%, when the SMR ozone profiles are also assimilated. This is a clear indication that there is a consistency cross-ECV

CMUG Phase 2 Deliverable

Reference: D3.1: Quality Assessment Report

Due date: June 2017

Submission date: 21 December 2017

Version: 4



It should be reminded that the assimilation of SMR ozone profiles has limited impact on the ozone analyses and that impact, albeit positive, is only measurable at high latitudes in the SH. One could argue that if a more significant positive impact was found in the ozone analyses, this could have triggered in turn a larger change also in the quality of the aerosol forecasts.

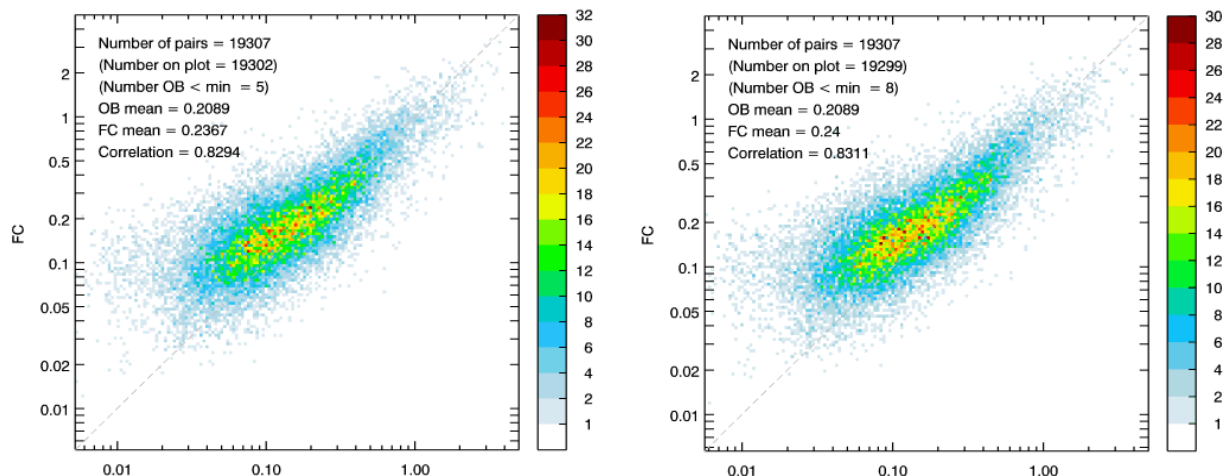


Figure 25: Scatter plot of the Aeronet AOD at 550nm (x-axes) against their forecast equivalent (y-axes) computed for **gi90** (left) and **gi95** (right) as defined in table 2.

The second example refers to the impact aerosols and GHG on the quality of the ozone analyses. The considerations made above regarding the limited interaction allowed within the data assimilation system are also valid here, thus only a small impact should be expected. The experiments considered are **gi93** and **gi94**, and as a reminder table 6 provides the list of datasets assimilated for each of the three ECVs.

	OZONE	AEROSOLS	GHG	
			CO2	CH4
gi93	SBUV SCIA TCO3 OSIRIS	ADV AATSR	IASI BESD SCIA	SRFP TANSO
gi94	SBUV SCIA TCO3 OSIRIS	ADV AATSR MODIS	IASI BESD SCIA SRFP TANSO	SRPR TANSO

Table 6: Like in table 2, but for experiments **gi93** and **gi94**.

CMUG Phase 2 Deliverable

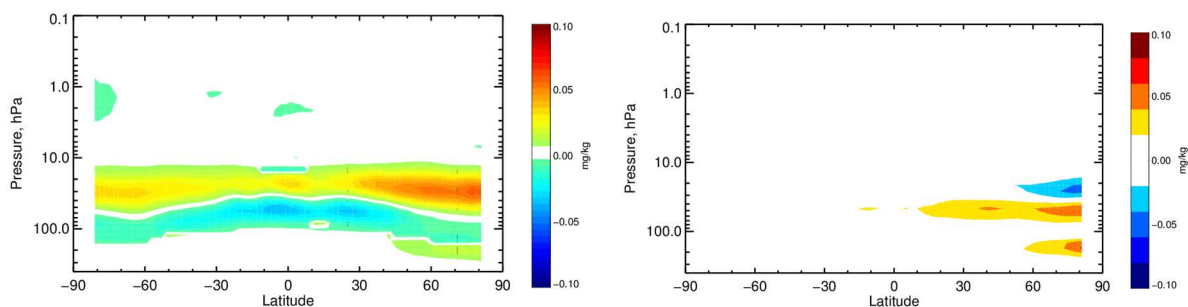
Reference: D3.1: Quality Assessment Report
Due date: June 2017
Submission date: 21 December 2017
Version: 4



Figure 26 shows the rate of change in the agreement of the ozone analyses to MLS computed as in equation (1) for the two experiments in table 6, using **gi93** as reference. In the plot, negative values in either the mean (left panel) or the standard deviation (right panel) means that the changes inferred improve the ozone analyses (in the sense of the agreement to the MLS data used as a reference).

Figure 26 shows that both in the mean and standard deviation the ozone analyses are degraded at some levels and regions and improved in others. Because of the way the experiments had to be designed interpreting the impact on the ozone analyses of changes in the aerosols and GHG observing system is not trivial, in particular to disentangle the relative weight of aerosols and GHG.

One could speculate that perhaps the degradation found in the GHG analyses when adding the CCI datasets and the limitations of the system in not correcting for the surface fluxes could be the main reason for the degradation in the ozone analyses, but a clean demonstration of the linkages of each of the two ECVs on ozone is required. If the above speculation was confirmed, then it would also confirm the ability of a complex data assimilation system to assess the cross-ECVs' consistency and to exploit it.



*Figure 26: Change in the zonal mean (left panel) and standard deviation (right panel) differences between the MLS retrievals and co-located ozone analyses from experiment **gi94** compared to **gi93** for May-Oct 2010, computed according to equation (1). Negative (positive) values in blue (red) colours indicate a poorer (a better) fit of the control analyses to MLS than their perturbed equivalent, and thus, compared to MLS ozone profiles, an improvement (a degradation) of the **gi94** ozone analyses compared to those from **gi93**. Data are in mg/kg.*

CMUG Phase 2 Deliverable

Reference: D3.1: Quality Assessment Report
Due date: June 2017
Submission date: 21 December 2017
Version: 4



3.5 Integrated assessment of CCI terrestrial ECVs impact in the MPI-ESM [WP3.4]

Aim

WP3.4 includes an integrated assessment of the terrestrial ECV variables available in the CCI with a joint analysis of the ECVs land cover, fire, soil moisture, and greenhouse gases (GHG). The ECVs were used to optimize uncertain parameters in the MPI-M ESM fire model process formulations using an optimum estimate framework, to make use of the uncertainty information provided with the ESA CCI datasets. The overarching questions to be addressed were:

- Are the four CCI data-sets consistent with each other and with model data so that modelled and observations data can be used directly for model validation and data assimilation?
- How can CCI data records be used to improve fire emission modelling in an earth system model?
- Do simulated carbon emissions improve using CCI datasets?

Summary of Results

3.5.1 Fire model optimization

SPITFIRE-JSBACH simulations were performed for the time period 1850 to 2010 in which burned area and fire carbon emissions are interactively simulated. Simulations were run with the standard model setup as described in detail in Lasslop et al., 2014. In addition, simulations were performed with a modified representation of the Nesterov-Index in SPITFIRE following Groisman et al. 2007. The modified version served as a first test case to use ESA CCI data in the evaluation of the SPITFIRE-JSBACH model. Simulated, FIRE_CCI burned area as well as burned area reported in GFEDv3/GFEDv4 based on MODIS (Giglio et al., 2006, Giglio et al., 2010) for the time period 2006-2008 are compared in Figure 27.

Contrasting the burned area with soil moisture reported from CCI_SM, we find a distinct relationship between burned area and soil moisture with low burned area for low soil moisture (fuel limitation) and low burned areas for high soil moisture (moisture limitation). The comparison shows that all products have a very similar distribution. The CCI-MERIS product peaks at a higher soil moisture compared to GFED products and the distribution is wider. Both versions of JSBACH-SPITFIRE peak at a too high soil moisture and the distribution is too wide.

CMUG Phase 2 Deliverable

Reference: D3.1: Quality Assessment Report

Due date: June 2017

Submission date: 21 December 2017

Version: 4

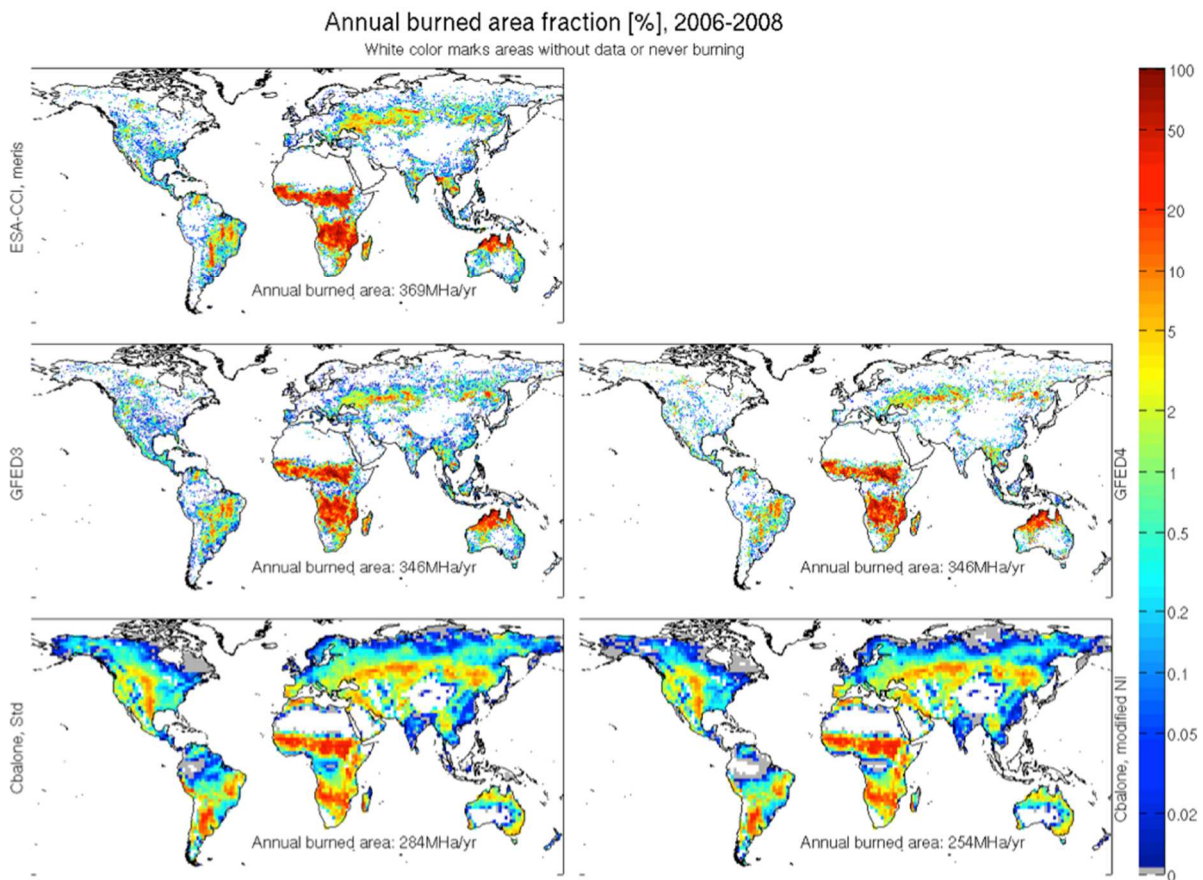


Figure 27: Burned area averaged for the years 2006-2008. FIRE_CCI (upper row), GFEDv3 and GFEDv4 (middle row), SPITFIRE-JSBACH standard and modified (lower row).

We identified two parameters (conversion soil moisture to fuel moisture and ignition rate) in SPITFIRE-JSBACH that are not well constrained by observations, which we systematically varied over a reasonable parameter space to optimize width and peak position of the soil moisture / burned area relationship. JSBACH-SPITFIRE was optimized to run a large number of experiments with varying parameter settings in a reasonable amount of time. Figure 28 shows the deviations in peak position and distribution width for 70 experiments with CCI-MERIS as reference. The optimized parameters do form the new standard values for JSBACH-SPITFIRE and are applied in the ongoing MPI-ESM CMIP6 simulations.

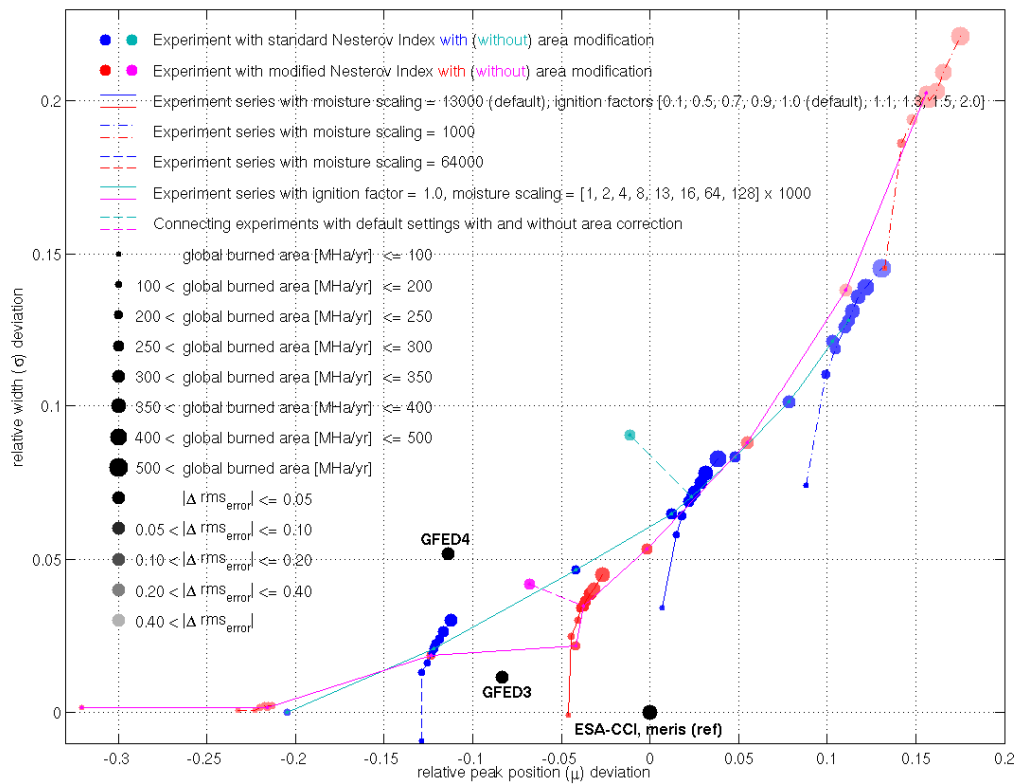


Figure 28: Relative difference in peak position and width of the burned area – soil moisture relationship for 70 experiments performed with JSBACH-SPITFIREv1/v2 compared to GFEDv3/v4 and CCI MERIS (reference).

The Fire Model Intercomparison Project (FIREMIP, Hantson et al. (2016) allowed us to perform similar analysis for a range of state-of-the-art global fire models. Figure 29 shows the relationship between burned area and soil moisture for four fire models. The models all show rather different relationships, which might partly explain the very different distributions of burned area simulated in the FIREMIP models. The relationship between soil moisture and burned area will be included in the benchmarking scheme developed for FIREMIP including ESA CCI burned area data.

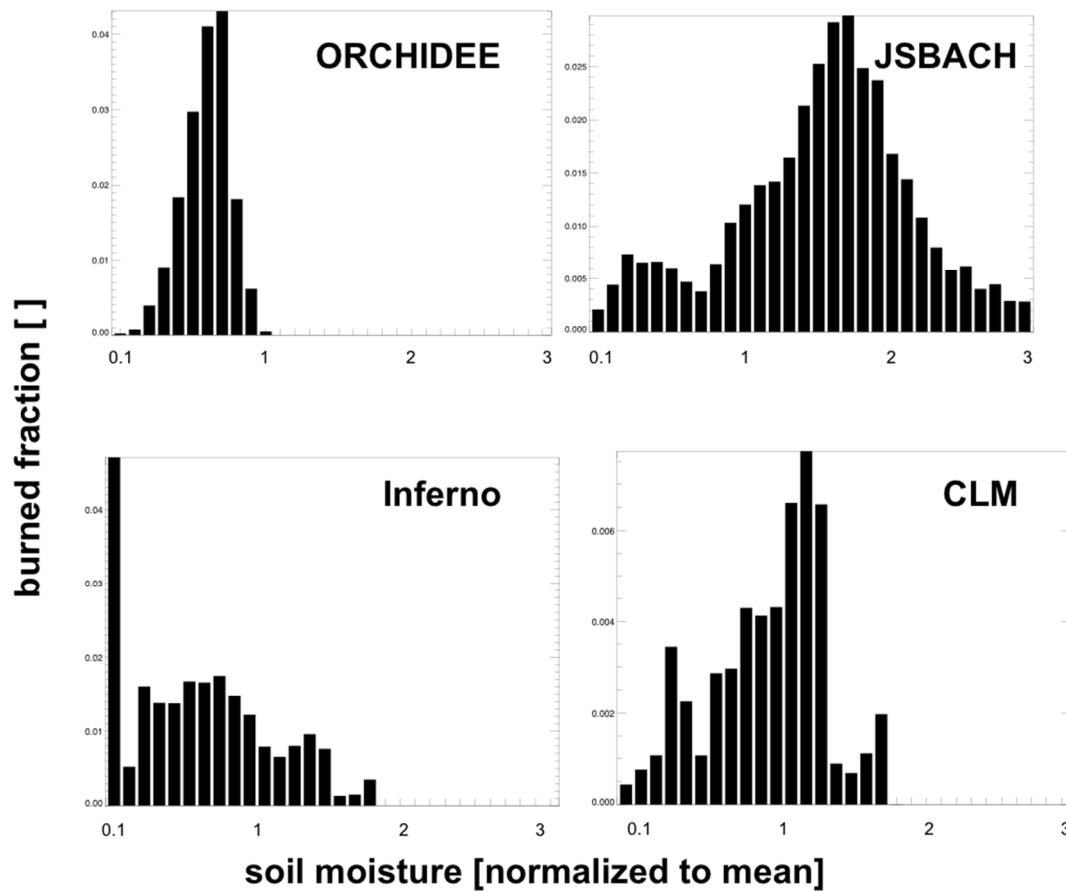


Figure 29: burned area – soil moisture relationship in four global fire models participating in FIREMIP.

3.5.2 Fire carbon emissions

With the release of the FIRE CCI data version 4.1 in July 2016 the longer time period covering the year 2005 to 2011 allowed us to prescribe the burned area data as boundary condition in JSBACH. Prescribing burned area in a global vegetation model as boundary condition to derive related fire carbon emissions still requires parameterizations of a range of processes including fire history, fuel consumption and mortality rates. Here we followed the approach applied in GFEDv3 (van der Werf et al., 2010). Figure 29 shows on the left hand side the Fire CCI burned area data and on the right and side the simulated fire carbon emissions using Fire CCI burned area data as boundary condition. Globally the mean annual burned area of 346 Mha for the time period 2005 to 2011 results in the emissions of 2.19 PgC/year. This compares well to the most recent GFEDv4s estimates (van der Werf et al., 2010 and updates) in which a global MODIS based burned area of 402 Mha results in fire carbon emissions of 2.18 PgC/year.

CMUG Phase 2 Deliverable

Reference: D3.1: Quality Assessment Report
Due date: June 2017
Submission date: 21 December 2017
Version: 4



The fire CCI data are reported with an uncertainty range for the global burned area of +/- 28%. Applying the uncertainty range for the prescribed burned area data in JSBACH results in +15% and -19% difference in the simulated fire carbon emissions.

A crucial parameter for the fire carbon emissions is the prescribed landcover distribution, which defines which vegetation type burns. Next to the standard JSBACH landcover distribution (Raddatz et al., 2007) we applied CCI LC product. Landcover classes reported in ESA CCI were converted into plant functional types used in JSBACH following Poulter et al., 2015. Using ESA CCI LC results in global fire carbon emissions of 1.85 PgC/year which is 4% lower than using the standard JSBACH landcover distribution.

Quality relevant outcomes

In WP3.4, only the gridded FIRE_CCI products were used. The FIRE_CCI gridded products from phase I were only available for a 3 year period (2006-2008), which limited their applicability for climate studies. To test the functional relationships, such as the relationship between burned area and soil moisture, global data coverage was available, reducing the dependency on having a long time series. Further assessment for fire model development will require categorization by land cover type to optimize land cover dependent parameters, which will benefit from a longer time series.

The CCI-MERIS product shows a very similar distribution of soil moisture dependency compared with the MODIS based GFEDv3/GFEDv4 product, which was applied in previous studies. These findings agree with the analysis of the FIRE CCI team reported in the Product Validation Report II and the Climate Assessment Report. The temporal stability of the product was not assessed due to the limited time period covered by the global product.



3.6 Cross assessment of clouds, water vapour, aerosols, ozone, GHG, SST, radiation and soil moisture impact on global climate variability and trends [WP_O3.4]

Aim

The aim of this WP is to make an integrated assessment of ESA-CCI ECVs and other observations studying climate variability by investigating relationships between co-varying variables and evaluate the same processes, such as ENSO, in global climate models. The uncertainty information for the CCI data sets are used when comparing to other observational data sets and the associated model-generated variability. The scientific questions are:

- How are the observed ECV's related and what is the robustness of associated mechanisms across different observational data sets (section 3.6.2)
- Can the models capture the relations between ECVs and the variability seen in observations for ENSO? (section 3.6.3)

Key Outcomes of CMUG Research

- Assessments of the CCI observations
 - CCI SST and clouds spatial and temporal mean and variability agree well with other independent observations. Cloud CCI cloud fraction (CLT) has higher variability for tropical ocean high pressure regions than the other AVHRR datasets possibly linked to an underestimation of low level clouds. CCI SST, Cloud cover, sea level and ocean colour all capture the ENSO variability consistently.
 - The CCI SST mean uncertainty is smaller than the difference compared to other observations. CCI total cloud cover uncertainty is larger than the difference compared to similar observations. The assumption on pixel independent cloud fraction errors over estimates the uncertainty, this should be improved in the next Cloud_cci v3 product.
 - Some CCI data issues: CCI AVHRR cloud products have inconsistency in their timeseries due to NOAA satellites scanning motor problems in 2000. This has been amended for in the Cloud-CCI v2.0 dataset, although some features remain and should be communicated to end users. The aerosol early AOD products were not stable across the satellite changes, improvements have been made for the latest versions.
- Evaluation of AMIP5 atmospheric simulations forced with observed monthly SST

CMUG Phase 2 Deliverable

Reference: D3.1: Quality Assessment Report
Due date: June 2017
Submission date: 21 December 2017
Version: 4



- All four models, have despite prescribed SST, cold biases and too small variability in their two meter temperatures (T2M's) over the tropical Pacific Ocean especially for the western part. These T2M biases are similar to the biases found for SST for coupled models, except there is no warm bias for the eastern Pacific Ocean. This suggests that the atmospheric models affect the well known cold tongue bias but has less influence on the eastern warm bias.
- The AMIP5 model spread in mean cloudiness is large. Two of the models capture the longitudinal variation of the mean and variability and the time variation associated with ENSO for both CLT and Top of the Atmosphere Outgoing Longwave Radiation (OLR).
- Evaluation of CMIP5 atmosphere-ocean coupled simulations
 - All four CMIP5 models present day simulations have too cold SST's over most of the Pacific Ocean except for warm biases at the eastern edge, as found in previous studies. The SST variabilities are too small with a peak in standard deviation (STD) around 240-250°E contrary to the observed flat profiles. Towards the end of the century all models mean tropical Pacific Ocean SST increase by 1-2°C and the variability increase for most models, retaining the erroneous peak in STD.
 - The CMIP present day cloudiness biases and variabilities are similar to the AMIP simulations except over the Eastern Pacific where the models have larger underestimates of CLT in accordance with their positive biases in SST. Three of the models show small increases in cloudiness towards the end of the century and their longitudinal pattern remain. While the fourth model has a small decrease in cloudiness. The changes in CMIP cloudiness between present day and future are smaller than difference between AMIP and CMIP present day simulations.

Summary of Results

3.6.1 Introduction

The El Niño Southern Oscillation (ENSO) is the most important coupled ocean-atmosphere phenomenon affecting global climate variability on seasonal to inter-annual time scales. It is an irregularly periodical variation in winds and sea surface temperatures (SST) over the tropical eastern Pacific Ocean, affecting much of the tropics and subtropics. The warm (El Niño) phase is associated with large positive SST anomalies in eastern to central Pacific occurring on 3-7 years times-scales and the cold phase (La Niña) occurring every 2-4 years is less intense but longer lasting. The phases can be classified by calculating SST anomalies for different regions of the Equatorial Pacific, most typically the Niño3.4 region (190E-240E, 5S-5N). Figure 30 shows the correlation between CCI SST Niño3.4 index and CCI global cloud cover. The warm El Niño phases are accompanied with deep convective clouds in the central or eastern Pacific and reduced cloudiness in the western Pacific. The maximum positive correlation is for the mid Pacific shifted west of the Niño3.4 box. More recently other variables, top of the atmosphere outgoing long-wave

CMUG Phase 2 Deliverable

Reference: D3.1: Quality Assessment Report
Due date: June 2017
Submission date: 21 December 2017
Version: 4



radiation and clouds have also been used to classify the ENSO events giving new perspective of the ENSO phase distributions (Chodi and Harrison 2010, Chodi and Harrison 2013, L'Heureux et al 2015).

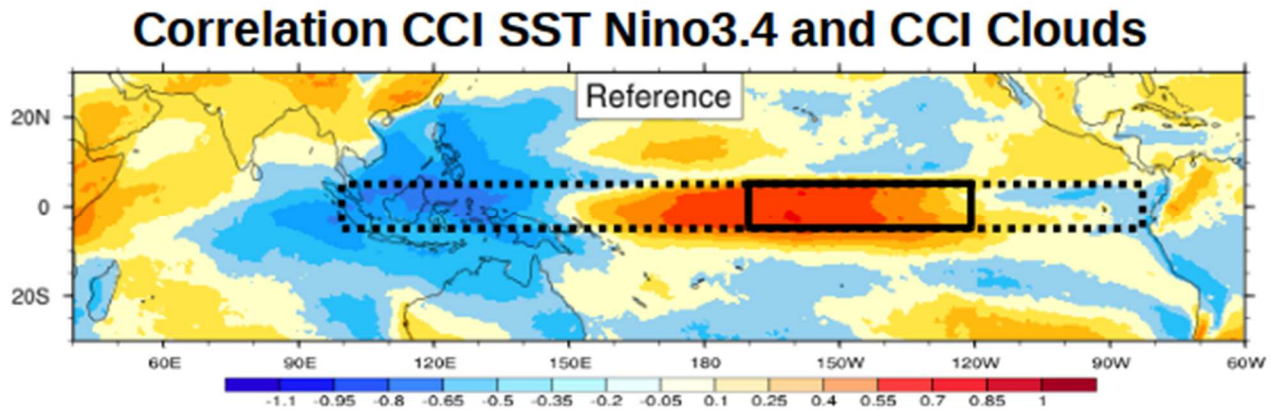


Figure 30: Correlation between CCI SST Niño 3.4 SST time series and CCI global Cloud cover for 1992-2008. The boxes show the Niño3.4 region (170W-120W, 5S-5N, full black box) and the Hovmöller region (100E-80W, 5S-5N, hatched box).

Outgoing Longwave Radiation (OLR) at the top of the atmosphere variability is a good proxy for the deep atmospheric convection in the tropics that generates atmospheric heating anomalies which force local and remote atmospheric circulation anomalies (Lau et al 1997). Negative (positive) OLR anomalies are indicative of enhanced (suppressed) convection and hence more (less) cloud coverage typical of El Niño (La Niña) episodes. The tropical Pacific deep atmospheric convective activity spreads eastward during the transition to El Niño state as found for satellite-measured OLR (Chodi and Harrison 2010). Unfortunately the existing directly measured OLR satellite datasets are short, only 15 years or less, while there exist multiple cloud satellite datasets with long time records. We investigate if the cloud dataset can be used to complement the OLR datasets when evaluating ENSO in observations and models.

The relative short time scale, large amplitude and multiple ECV's affected by ENSO makes it an ideal natural forcing to focus on for cross-assessment of multiple satellite records as the CCI data sets, albeit the records are too short for sampling the full ENSO diversity and the decadal ENSO variability. Climate models capture the basic ENSO features but the amplitude, life cycle and frequency are not properly reproduced and most models variability extends too far into the Western Pacific. To further understand model performances and biases, evaluating models with observational constraints derived from multiple variables as described in this research, can give new perspectives.

CMUG Phase 2 Deliverable

Reference: D3.1: Quality Assessment Report
Due date: June 2017
Submission date: 21 December 2017
Version: 4



We examine the tropical Pacific Ocean variability and ENSO in the following satellite observations, CCI SST (Merchant et al 2014 a,b), sea level (Quartly et al 2017), ocean colour (Valente et al 2016) and clouds (Stengel et al 2015, 2016), PATMOS-X (Heidinger et al 2014), CLARA-A2 (Kaspar et al 2009), HadISST (Rayner et al 2003), CERES OLR (Loeb et al 2012), NOAA OLR (Liebmann and Smith 1996) as well as the corresponding variables from climate models from the CMIP dataset (Taylor et al 2012) and ERA-Interim (Dee et al 2011).

3.6.2 Cross assessment of the observations

For the CMUG cross-assessment and to find alternative ENSO indices, we investigate the variability for all CCI variables for the equatorial Pacific Ocean, by calculating normalized anomalies (5°S to 5°N) for all longitudes and months for CCI SST, Sea level, ocean colour (chlorophyll) and cloud cover. The results are shown in Hovmöller diagrams (Figure 31), where the positive and negative values show the deseasonalised monthly anomalies as function of longitude and time. For all variables we see the strong El Niño event 1997/1998 and the following longer La Niña period as well as other weaker El Niño's peaking further west. We note that the largest variability for the different ECV's occur at different longitudes.

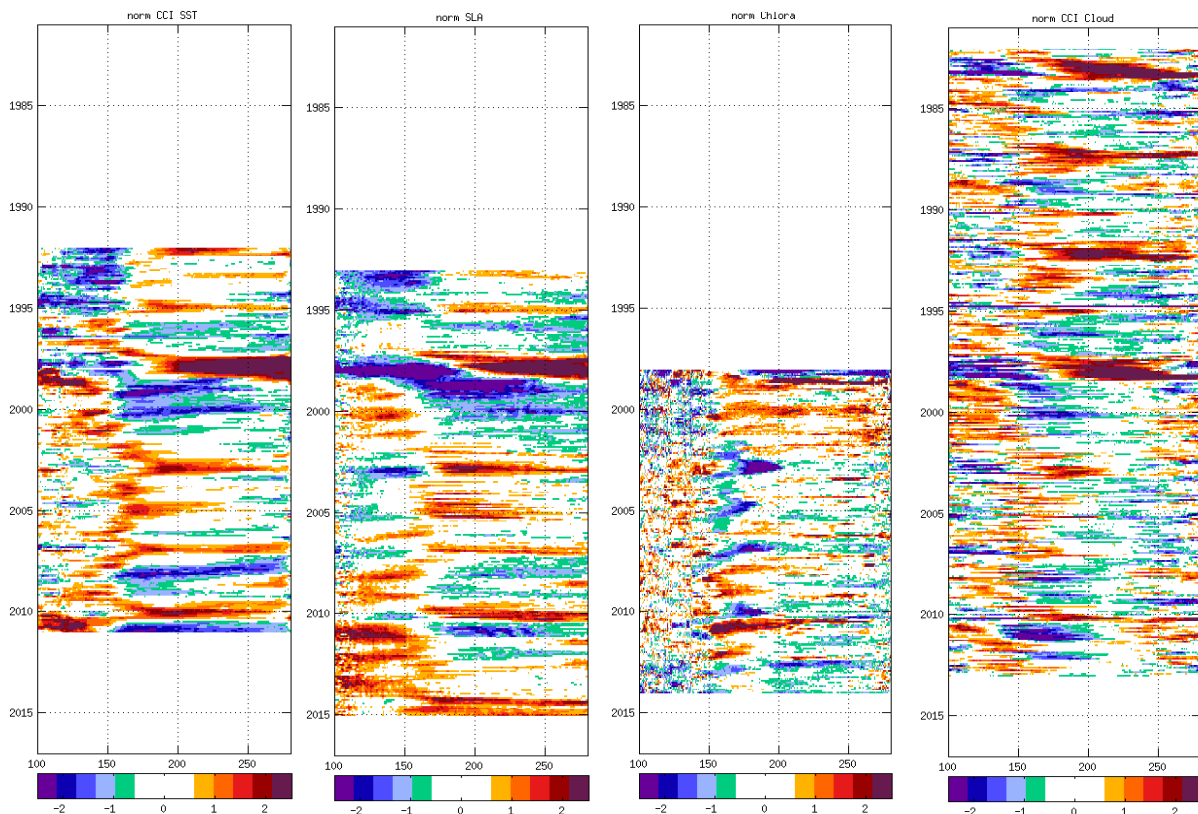


Figure 31: Hovmöller diagrams for Pacific Ocean 5S-5N normalized anomalies for CCI SST, Sea Level, Chlorophyll and Cloud cover as function of time and longitudes between 100E to 270E.

CMUG Phase 2 Deliverable

Reference: D3.1: Quality Assessment Report

Due date: June 2017

Submission date: 21 December 2017

Version: 4



For the rest of this WP we concentrate on SST, clouds and OLR. Observed and simulated ENSO characteristics is thought to depend on the mean state in the tropical Pacific Ocean as well as the variability in time and space. We compare the ECV's mean values (left column) and variability (right column) to other observations and ERA-Interim as a function of longitude in Figure 32. The CCI SST varies from 30°C over the western warm pool decreasing over the cold tongue region to 25°C of the South American coast (Fig 32a). CCI SST is very similar to HadISST data but somewhat warmer, 0.5°C, for the western part. We also show the CCI SST uncertainty plotted around the mean. It is too small ($\sim 0.1^\circ\text{C}$) to be clearly visible but we note it is smaller than the difference compared to HadISST mean value.

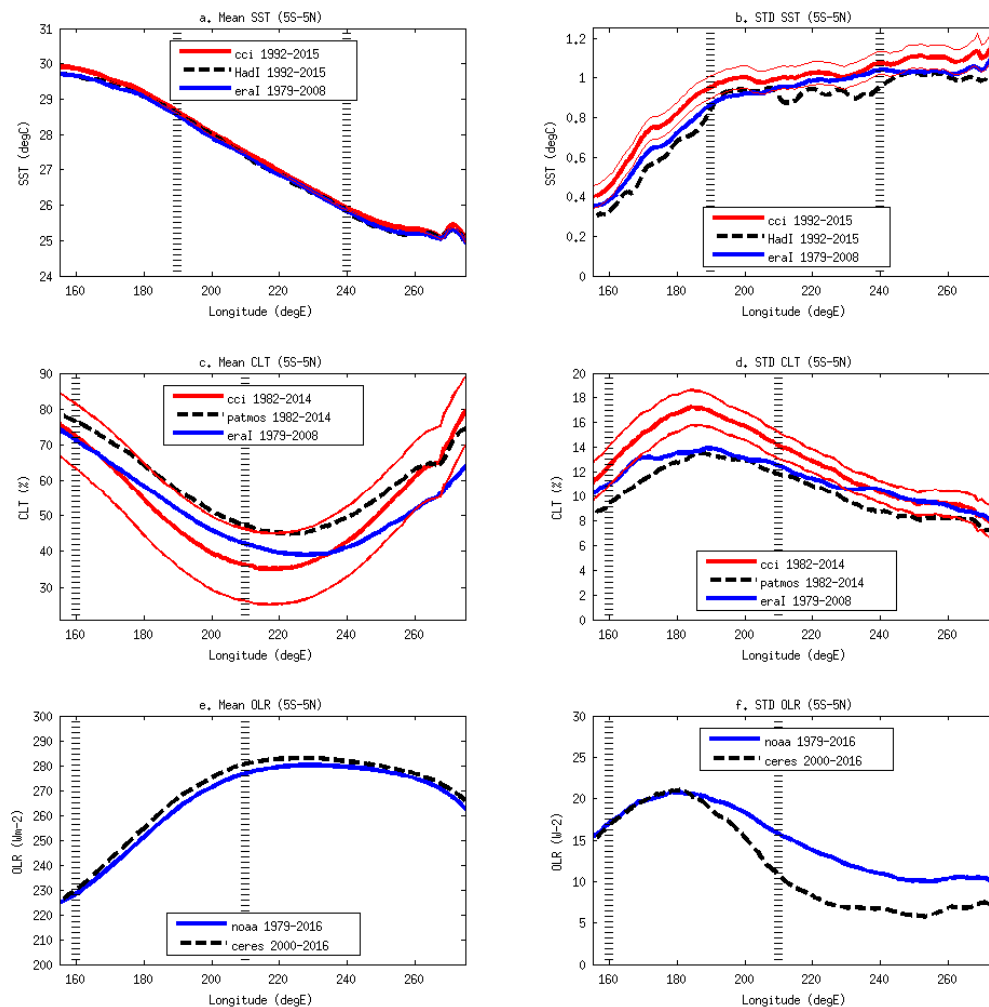


Figure 32: Mean (left column) and STD (right column) values across the tropical Pacific Ocean (5S-5N) for SST (a and b) CCI 1992-2015 (red lines mean and uncertainty), HadISST 1992-2015 (black hatched lines) and ERA-Interim 1979-2008 (blue lines), for Cloud cover (c and d) CCI 1982-2014 (red lines mean and uncertainty), PATMOS-x 1982-2014 (black hatched lines) and ERA-Interim 1979-2008 (blue lines), for OLR (e and f) NOAA 1982-2015 (blue lines) and CERES 2001-2016 (black hatched lines).

CMUG Phase 2 Deliverable

Reference: D3.1: Quality Assessment Report
Due date: June 2017
Submission date: 21 December 2017
Version: 4



The mean cloudiness across the Pacific Ocean is U-shaped, all cloud data sets have high values (~70%) for the western convective region, minima (35-40%) over the mid Pacific Ocean and high values (~70%) for the eastern stratocumulus region off the South America coast and (Fig 32c). The CCI cloud minima is 5% smaller than for the other data sets. The CCI uncertainty (red thin hatched lines in Fig 32c) is unrealistically large ~10%, i.e. larger than the differences compared to PATMOS-x and other AVHRR datasets (not shown). The CCI cloud mask uncertainty is based on hit rate scores against measurements from the Cloud-Aerosol Lidar with Orthogonal Polarization (CALIOP) not taking into account co-dependent pixel errors. This will be improved in the next CCI release v3.0. For most other CCI cloud variables such as liquid and ice water path, the uncertainty estimates are based on optimal estimation theory.

OLR is low over the western convective region for both NOAA and CERES as expected for the high clouds emitting at lower temperatures, while OLR is high for the mid Pacific where on average less high clouds shield the surface and for the western stratocumulus region with low clouds emitting at higher temperatures (Fig 32e). CERES provides direct measurements of OLR although data is only available from year 2000. NOAA OLR is derived from AVHRR data from 1979 and onwards and has a coarse resolution of $2.5^\circ \times 2.5^\circ$ and therefore not ideal.

We examine the variabilities across the Pacific Ocean to find the optimum region to characterize ENSO for each ECV. As noted before the largest variability for the different ECV's occur at different longitudes as seen for the deseasonalised monthly standard deviations (STD's) (right column, Figure 32). SST has a wide flat peak in STD (and wide gradient in mean SST) over the Pacific cold tongue region (enclosing the Niño3.4 region), which is the standard region for classifying the ENSO phases. In contrast the cloud and OLR variabilities have peaks in their STD distributions just east of the dateline (~190E) in the Niño4 region (160E-210E) where their mean values have sharp gradients (Fig 32c).

The CCI SST variability is larger than for the other observations which likely due to the high horizontal resolution (0.25°) than for the HadISST and ERA Interim datasets (1.0°). CCI CLT has higher variability than PATMOS-x and ERA-interim for the warm pool region, which appears to be due to less CCI cloudiness during La Niña time periods compared PATMOS- and CLARA-A2 (not shown). The reason for CCI AVHRR detecting fewer low and mid clouds common for La Niña is unknown, but it has been communicated to the Cloud CCI team. For OLR we note that CERES has much lower STD values than NOAA east of the dateline (Fig 32d), this is due to the short CERES time record, 2001-2016, which does not include the major El Niños over the central and eastern Pacific during the 80's and 90's (see Fig 33c).

Next we investigate the time variabilities for the ECV's by calculating indices for the different regions with the highest variability. The deseasonalised monthly anomalies normalized by the mean standard deviation are shown in Fig 33 for the Niño3.4 region. The CCI SST timeseries is

CMUG Phase 2 Deliverable

Reference: D3.1: Quality Assessment Report

Due date: June 2017

Submission date: 21 December 2017

Version: 4



almost identical to HadISST and show the ENSO phases. The cloud index (Fig 33b) covary with the SST index especially for the positive ENSO phase. OLR is anti-correlated with SST and Clouds (Fig 33c), i.e. less emitted OLR for high convective clouds associated with El Niño and the opposite more OLR when convection is suppressed during La Niña.

The scatter plots in Figure 43 show the relations between the SST indices and CLT (top row) and OLR (bottom row) indices, respectively. For the Niño34 region (left column) the relationships are stronger for El Niño, high positive values, than for La Niña, negative values, for SST and CLT. For the Niño4 region (right column) the relationship between the indices is skewed towards negative values, capturing the La Niña phase better.

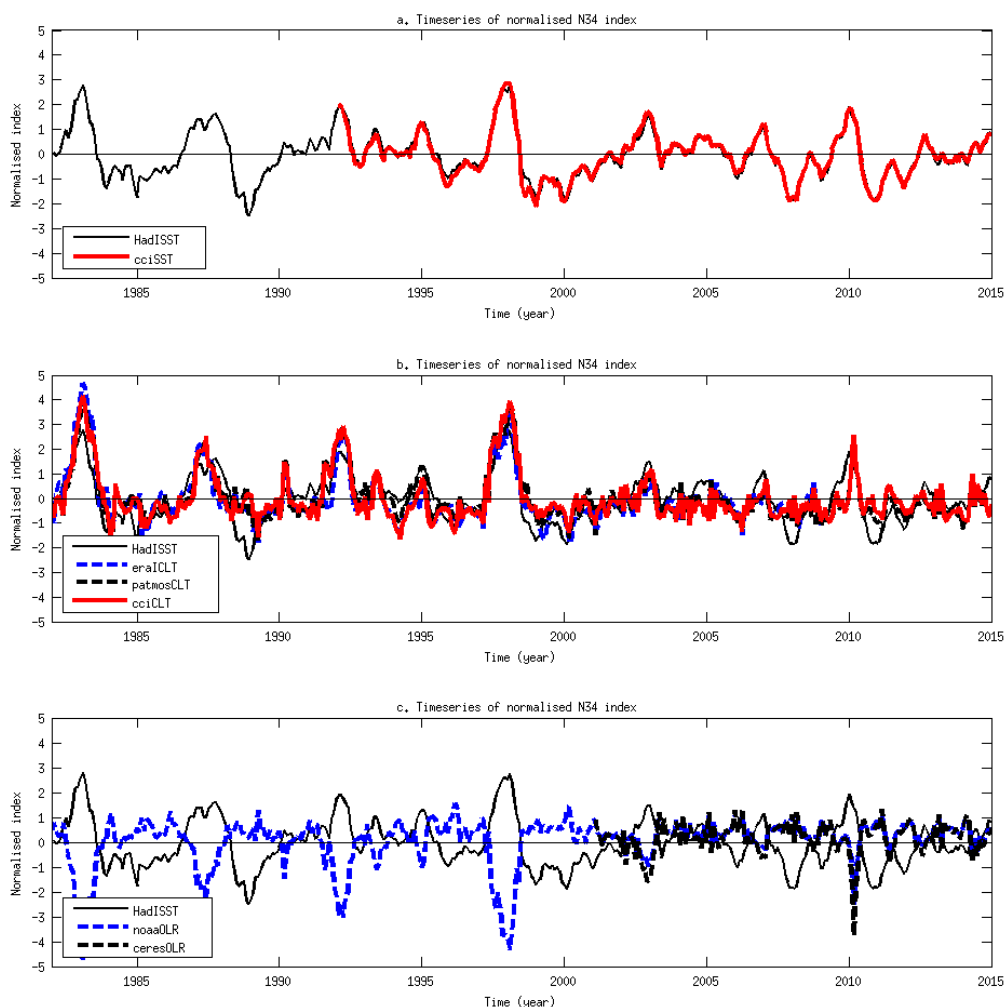


Figure 33: Timeseries of Niño3.4 indices for a. SST HadISST (black thin line, repeated in all 3 panels) and CCI SST (red line), b. CCI CLT (red line) and PATMOS-x CLT (black hatched line), and c. NOAA OLR (blue hatched line) and CERES OLR (black hatched line).

CMUG Phase 2 Deliverable

Reference: D3.1: Quality Assessment Report

Due date: June 2017

Submission date: 21 December 2017

Version: 4



The CLT-SST (Fig 34a and d) relations are similar to the OLR-SST relations (Fig 34b and d) that has been used to characterize ENSO phases (L'Heureux et al 2015). The CLT-OLR relationships for the different regions are close to linear (Fig 34e and f) especially for the Niño4 region. The existing direct measured OLR satellite datasets are short, only 15 years or less, while there exist multiple cloud satellite datasets with long time records. From these comparisons we therefore suggest using satellite cloud dataset to complement the OLR datasets when evaluating observed ENSO. The relationships in Fig 34 can be viewed as the ENSO relation between the ocean part (SST) and the atmospheric part (OLR or CLT), next step is to evaluate these relationships in the models.

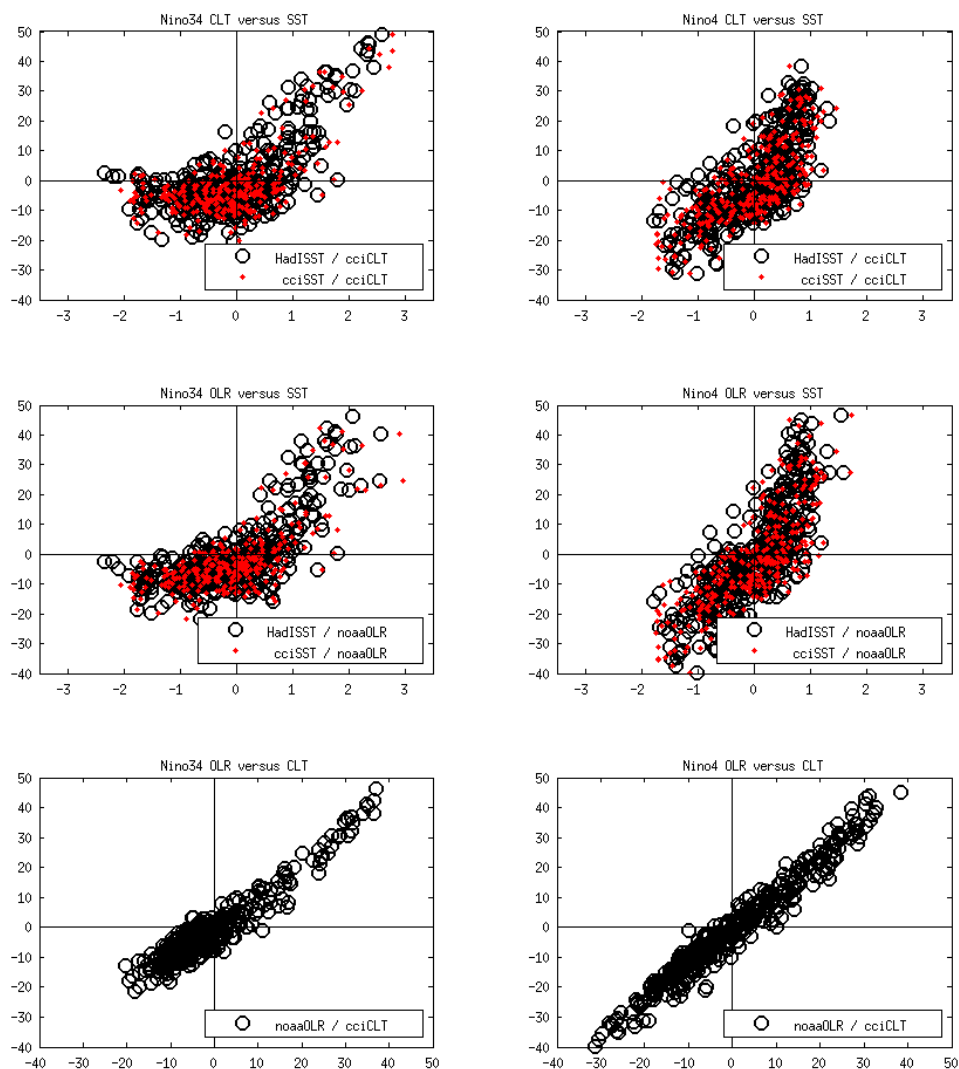


Figure 34: Scatter plots of the Niño3.4 (left column) and Niño4 (right column) timeseries indices for CLT versus SST (top row), CCI SST vis CCI CLT (red dots), HadISST vis CCI CLT (black circles), for OLR versus SST (middle row), CCI SST vis NOAA OLR (red dots), HadISST vis NOAA OLR (black circles) and for CLT versus OLR (bottom row), CCI CLT versus NOAA OLR (black circles).

CMUG Phase 2 Deliverable

Reference: D3.1: Quality Assessment Report
Due date: June 2017
Submission date: 21 December 2017
Version: 4



3.6.3 Evaluation of ENSO in climate models using CCI and other observations.

We now examine the ENSO variability in climate models evaluating SST, T2m, Clouds and OLR from climate models. Most CMIP5 coupled atmosphere-ocean models have cold SST biases in the western equatorial Pacific for the cold tongue region and warm SST biases in the far eastern Pacific (east of 260E) where stratocumulus clouds are underestimated (Bellenger et al 2014). To evaluate the climate models, we first analyse AMIP simulations, with prescribed observed monthly SST at the lower boundary, thereby isolating the atmospheric part of the model and capturing the present day ENSO through the SST variations. Thereafter we evaluate the corresponding CMIP5 historical simulations for present day and RCP4.5 scenarios for end of the 21st century. The models presently used are CNRM-CM5 (1.4°x1.4°, L31, Voltaire et al. 2013), EC-Earth (1.1°x1.1°, L62, Hazeleger et al 2010), HadGEM2-AO (1.9°x1.3°, L60, Collins et al 2011) and IPSL-CM5A-MR (2.5°x0.6°, L39, Hourdin et al. 2013), the data were obtained from the World Climate Research Programme's (WCRP) CMIP5 data archive made available through the Earth System Grid Federation.

All four AMIP5 models, have 1-3°C colder two meter temperatures (T2m's) than the prescribed SST's for the tropical Pacific Ocean, especially for the western part as seen in Figure 35a. These T2m biases are similar in magnitude and shape to the well known western Pacific cold SST bias mentioned above. The other common coupled model problem, the warm SST bias for the eastern Pacific Ocean, is not present in the T2m's. The SST STD (Fig 35b) are close to HadISST, plotted for the same time period 1979-2008. The T2m variability is smaller than the prescribed observed SST STD for the western Pacific. The cold two meter temperatures and small variability over the cold tongue region suggests that the atmospheric models in this study are contributing to the cold tongue coupled model SST bias, but for the eastern warm bias the ocean play a larger role.

The AMIP5 model spread in mean CLT is large (-10 to +20% biases compared to observations for mid Pacific Ocean Fig 35c). Two of the models (EC-Earth and HadGEM) capture the longitudinal variation of the mean and variability for both CLT and OLR. CNRM underestimate clouds for the eastern Stratocumulus region and has a peak in variability too far east. IPSL CLT mean and variability do not change much across the Tropical Pacific Ocean but it has a maxima for the stratocumulus region. Both CNRM and IPSL OLR have maxima further east than observed thereby underestimating OLR for the western part and overestimating for the eastern part, still their OLR variability peaks for the Niño4 region as observed.

The results for the coupled atmosphere-ocean simulations are show in Figure 36. All four CMIP5 models SST's for present day are too cold over most of the Pacific Ocean except for warm biases at the eastern edge, as found in previous studies and mentioned above. The present day variabilities are too small compared with observations and there are peaks in STD around at 240E-250°E, contrary to the observed flat structure. Towards the end of the century all models mean tropical

CMUG Phase 2 Deliverable

Reference: D3.1: Quality Assessment Report

Due date: June 2017

Submission date: 21 December 2017

Version: 4



Pacific Ocean SST increase by 1-2°C and the SST STD increase for most models. All four models retain the longitudinal pattern with the erroneous peak in STD around 240-250°E.

The CMIP present day cloudiness biases compared to the observations are similar (in shape) to the AMIP simulations biases except over the Easter Pacific where the models have larger underestimates of CLT in accordance with their positive bias in SST. The CMIP CLT present day variabilities are smaller than the AMIP variabilities and have a flatter structure. The variabilities become slightly larger towards the end of the century, except for eastern parts where they remain fixed.

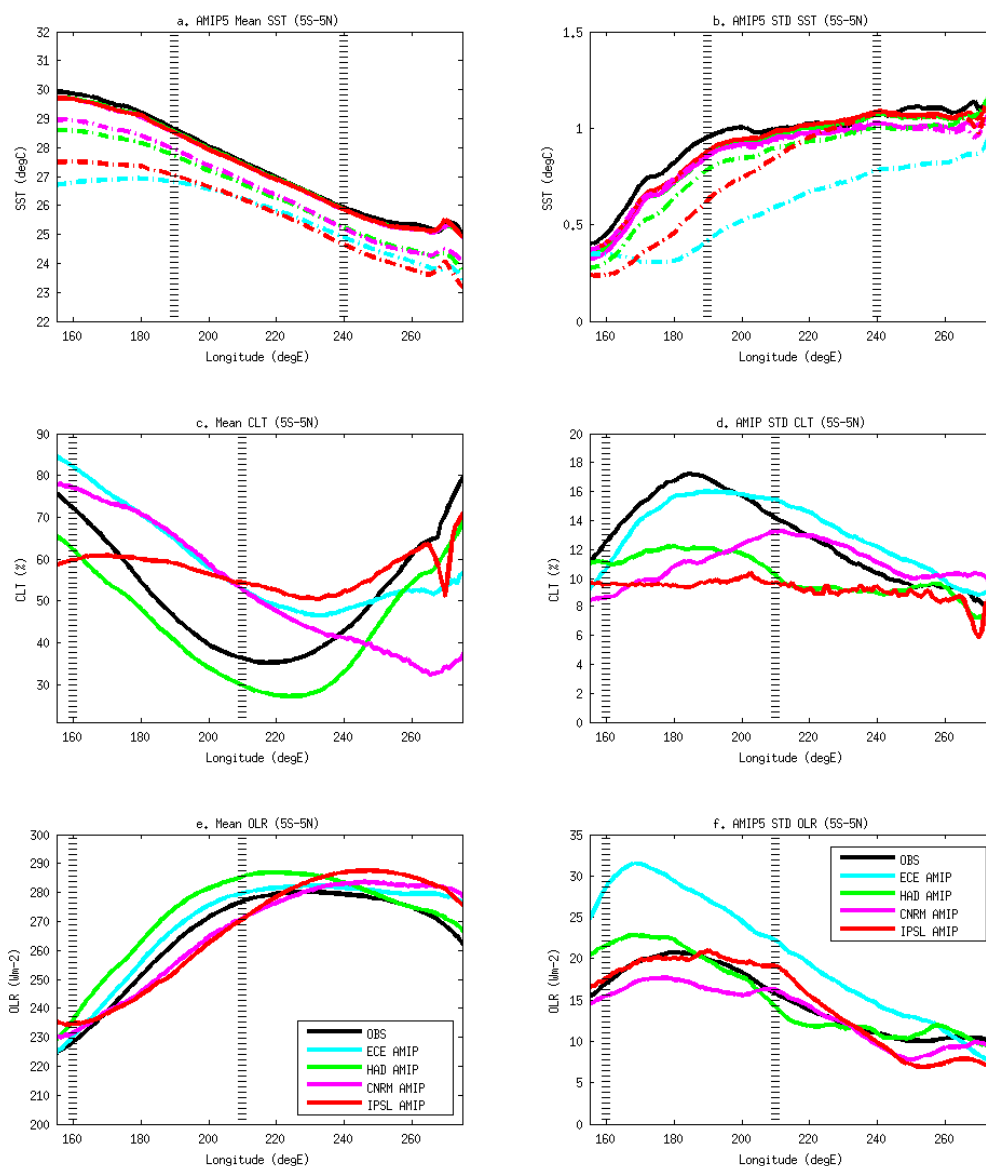


Figure 35: AMIP5 1979-2008 simulations. Mean (left column) and STD (right column) values across the tropical Pacific Ocean (5S-5N) for SST (a and b, observations HadISST, full lines SST, hatched lines T2m), CLT (c and d, observations CCI) and OLR (e and f, observations NOAA) for EC-Earth (cyan), HadGEM (green), CNRM (magenta) and IPSL (red).

CMUG Phase 2 Deliverable

Reference: D3.1: Quality Assessment Report

Due date: June 2017

Submission date: 21 December 2017

Version: 4



Three of the models have a small increase in cloudiness towards the end of the century (2-5%) and their longitudinal pattern remain. While the fourth model, IPSL, has a small decrease in cloudiness (3%). The changes in cloudiness between CMIP present day and future are smaller than difference compared to the AMIP cloudiness.

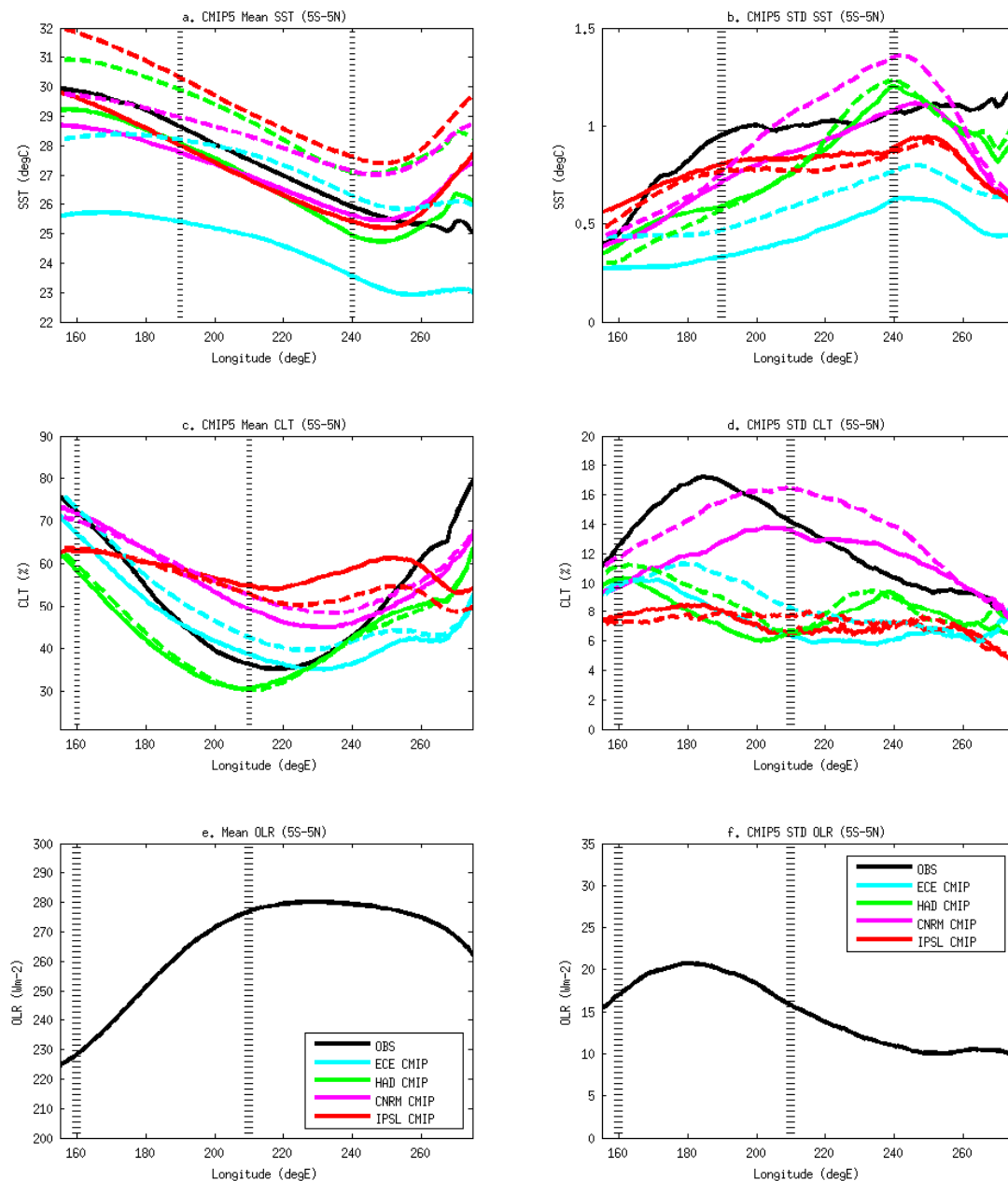


Figure 36: CMIP5 1979-2008 (full lines) and CMIP5 2070-2099 (hatched lines). Mean (left column) and STD (right column) values across the tropical Pacific Ocean (5S-5N) for SST (a and b, observations HadISST), CLT (c and d, observations CCI) and OLR (e and f, observations NOAA) for EC-Earth (cyan), HadGEM (green), CNRM (magenta), IPSL (red). (The model OLR will be added to e and f)

CMUG Phase 2 Deliverable

Reference: D3.1: Quality Assessment Report

Due date: June 2017

Submission date: 21 December 2017

Version: 4



The ENSO relationships between the AMIP SST indices and clouds and OLR indices are shown for the Niño34 region in Fig 37. The models relationship for SST-OLR are close to the observations, while for SST-CLT only HadGEM and EC-Earth are (fairly) similar to the observations. This confirms that the two models, CNRM and IPSL, have cloud fraction that are not radiatively consistent with their OLR. In order to properly compare model CLT with observations we need to use a cloud satellite simulator.

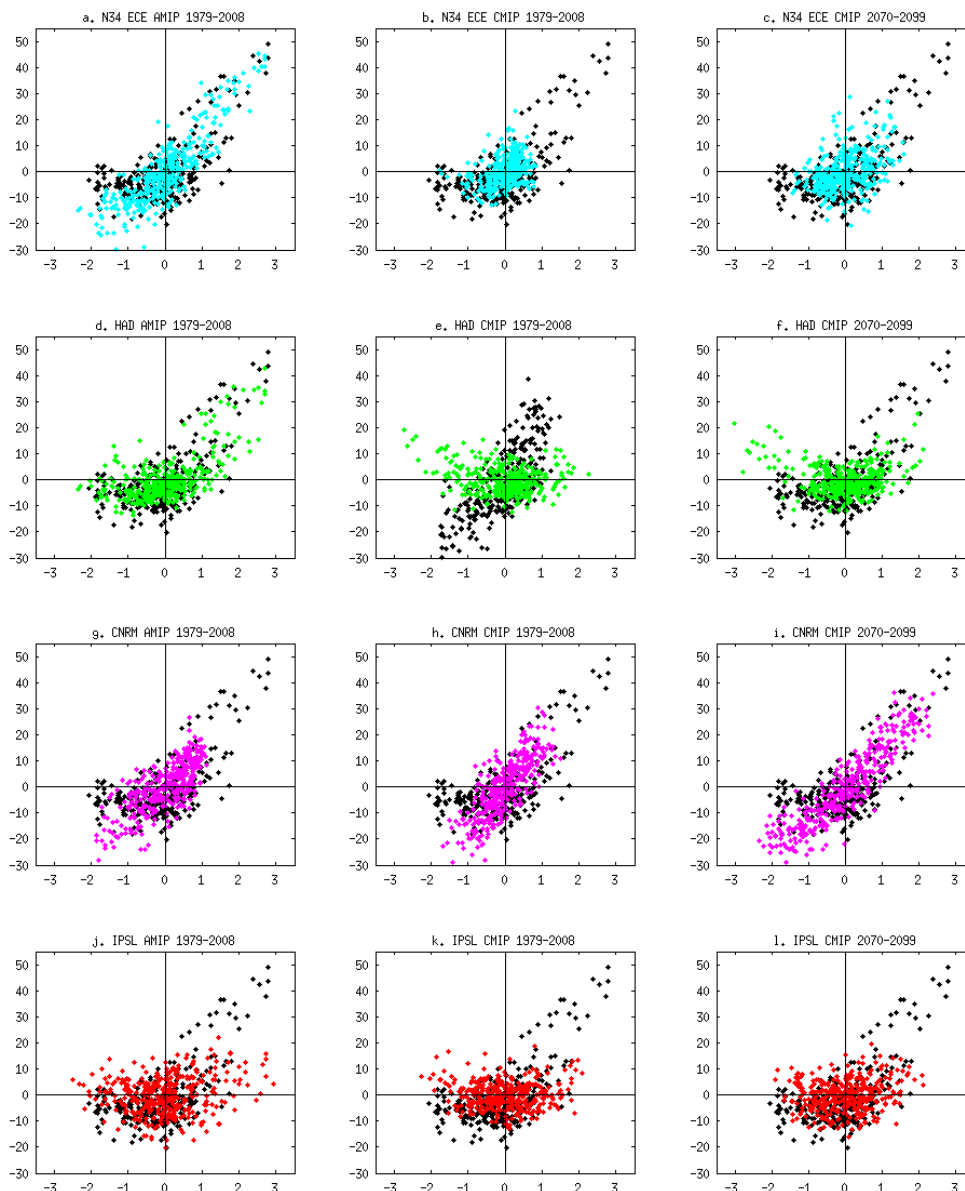


Figure 37: Scatter plots of the Niño3.4 AMIP5 (left column), CMIP5 1979-2008 (middle column) and CMIP5 2070-2099 (right column) timeseries indices for CLT versus SST, CCI CLT versus NOAA OLR (black dots), EC-Earth (cyan dots), HadGEM (green dots), CNRM (magenta dots) and IPSL (red dots).

CMUG Phase 2 Deliverable

Reference: D3.1: Quality Assessment Report

Due date: June 2017

Submission date: 21 December 2017

Version: 4



However, since most CMIP5 and CMIP6 historical and scenario simulations are run without simulators, except for a number of specific CFMIP experiments, an alternative would be to calculate an effective radiative cloudiness from CLT, LWP and IWP since those variables are standard CMIP output. This will be tested as well as the difference using EC-Earth CLT without and with Cloud_cci simulator.

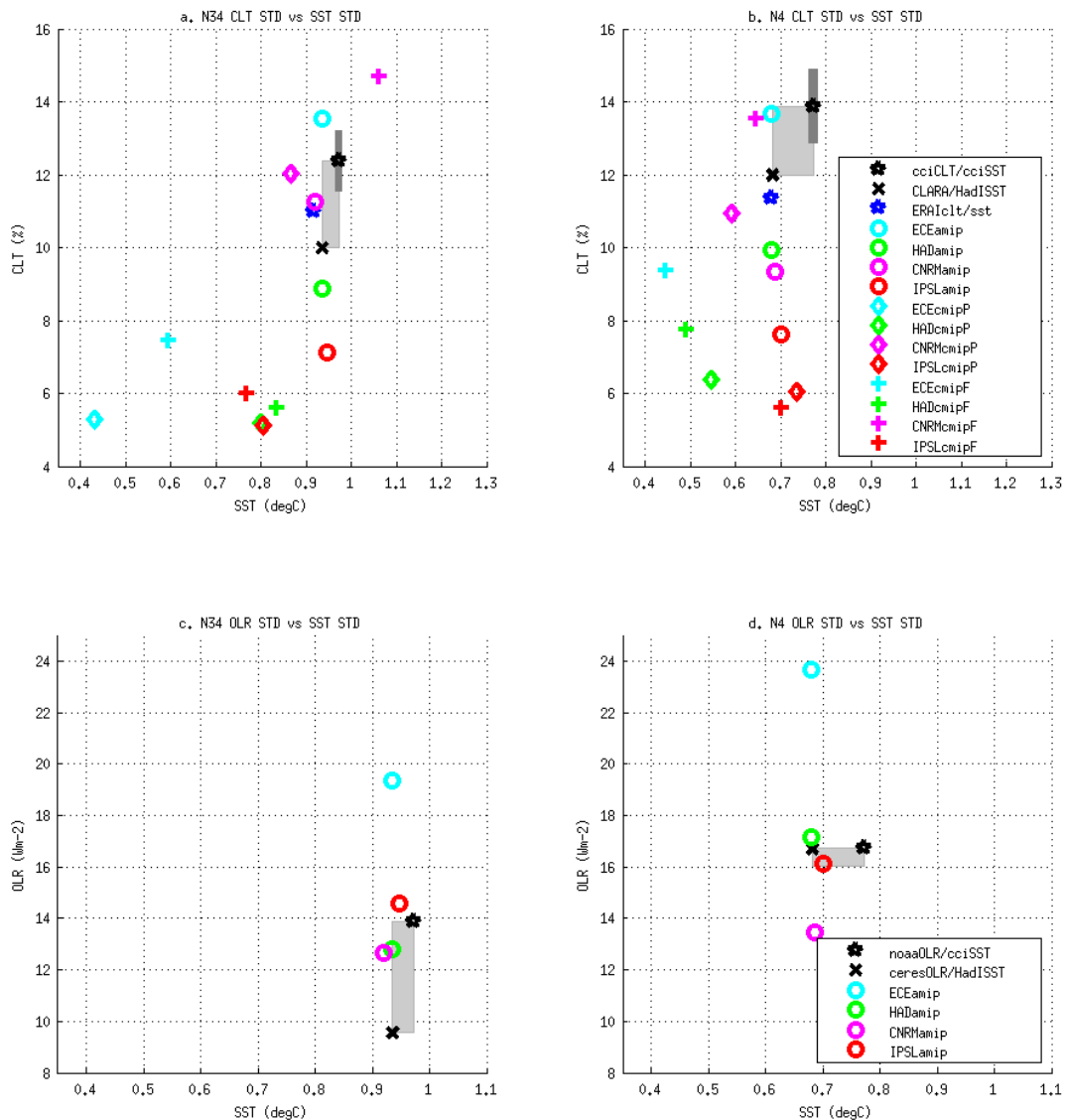


Figure 38: Relationships between CLT and SST (top row) and OLR and SST (bottom row), for Niño3.4 (left column) and Niño4 (right column). Observations black markers and models coloured markers, EC-Earth (cyan), HadGEM (green), CNRM (magenta) and IPSL (red). The grey box shows the observed spread and the dark grey the cci uncertainties.

CMUG Phase 2 Deliverable

Reference: D3.1: Quality Assessment Report

Due date: June 2017

Submission date: 21 December 2017

Version: 4



From this CMUG study we aim to derive observational relations that can be used for evaluation of models and possibly for obtaining observational constraints. By comparing the covarying SST and CLT or OLR variabilities for the different regions we get measures of the ENSO amplitude, and the covariation of the ocean and atmosphere. The preliminary Figure 38 show these relationships for the two Niño regions. For CLT the models show a large spread as previously discussed we need to use satellite simulators for the model data as will be done using the Cloud_cci simulator as well as the simplified simulator using the CMIP model output. For OLR we can compare directly which will be done when the CMIP5 data have been obtained.

3.6.4 Feedback to the ECV teams

This CMUG process study revealed issues for some of the CCI ECV's which have been communicated to the teams. Three examples are described here. We found inconsistencies in the Aerosols ECV AOD550 time series, they were not stable across the ATSR2 and AATSR satellite change, adjustments of the jump in timeseries have since been made in their latest versions. We also noted that the Cloud_cci v2 cloud fraction uncertainties were unrealistically large, due to assumption of independent cloud fraction pixel errors, which should be improved for Cloud_cci version 3.

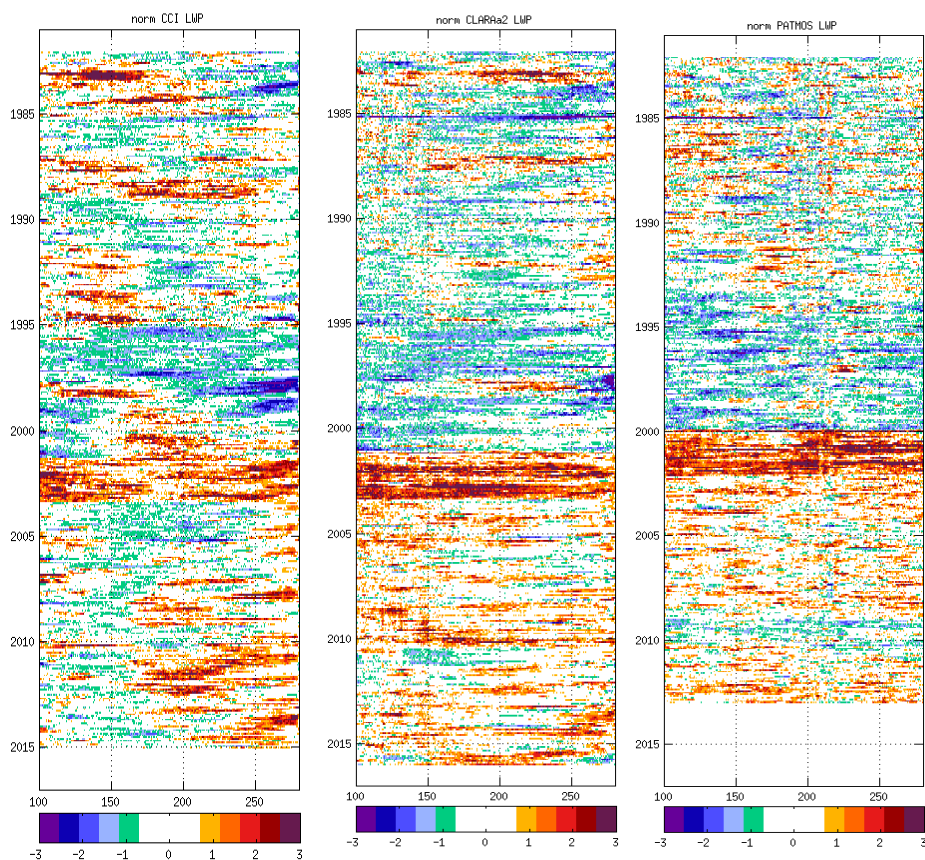


Figure 39: Hovmöller diagrams for CCI, CLARA and PATMOS-x LWP, anomalies for 5S-5N as a function of time and longitude, 100E-270E.

CMUG Phase 2 Deliverable

Reference: D3.1: Quality Assessment Report
Due date: June 2017
Submission date: 21 December 2017
Version: 4



For other CCI cloud products we found inconsistencies in the timeseries due to hardware problems for the NOAA satellites as shown in Figure 39. The Hovmöller diagrams for liquid water path (LWP) for Cloud-CCI, CLARA and PATMOS-x show unrealistic high values for the anomalies after year 2000. This is due to problems with the scanning motor on-board the NOAA satellites. The Cloud-CCI and CLARA team were aware of this problem but it was not clear on how it could affect the ECV's. In the latest Cloud CCI data v2.0 corrections have been made that mitigated the issue but some features remain, which should be communicated to end users.

3.6.5 Outlook

This study will be updated with the final CCI ECV's products, SSH and ocean colour, covering the full time records when available in 2017. Other satellite datasets such as ISCCP cloud and radiation products and water vapour will be added to the analysis as well as additional reanalysis products. We will also add products missing for the climate models such as OLR and include several more models from the CMIP5 and CMIP6 archives.

We will continue the analysis on how to compare satellite observed cloudiness with model simulated cloud fraction, using Cloud_cci simulator but also trying simplified versions that can be used to derive model satellite clouds from standard CMIP output. The impact on the ENSO characteristics for EC-Earth simulations of different horizontal and vertical resolution is also ongoing. A paper is in preparation in collaboration with the ECV teams on this ENSO evaluation using multiple ECV's. Thereafter the new ENSO diagnostics will be implemented into the ESMValTool

CMUG Phase 2 Deliverable

Reference: D3.1: Quality Assessment Report
Due date: June 2017
Submission date: 21 December 2017
Version: 4



3.7 Coupled climate model assessment [WP3.5]

Key Points:

- Comparison of satellite derived products for Soil Moisture and Evaporations exhibit huge differences. It is not possible to say which one is closer to the reality.
- Partitioning combined SW surface radiation and evaporation data with respect to 4 soil-moistures quartiles at regional scale allow to derive consistent diagnostics on the land-atmosphere coupling.
- These diagnostics can be used to better constrain parameterization implemented in climate models.

3.7.1 Introduction

The strength of the coupling between the soil-moisture and surface atmospheric variables has important implications for regional climate simulations as well as for climate projections Cheruy et al. (2014), Orth and Seneviratne (2017). It is controlled by the boundary layer turbulence, the radiation at the surface, the precipitation and the state of the soil. The observation and/or the numerical simulations of processes like cloud-radiation interactions, boundary layer-turbulence, precipitation that control the coupling are still challenging. The soil-moisture itself is a quantity poorly observed at scales consistent with the numerical models requirements. In this work we explore conjointly various state-of-the-art satellite or site-observations upscaled products for evaporation, soil moisture and radiation in order to derive guidance for the development of parameterizations relevant for the soil-moisture atmosphere coupling in the IPSL-CM.

3.7.2 Materials and Methods

Observations

We used site-observations Jung et al. (2011) upscaled product for evaporation and, satellite estimation of evaporation and soil moisture through data assimilation process Martens et al. (2017) and ESA-CCI Blended Active and passive microwave retrieval of surface soil moisture Dorigo et al. (2017) and CERES-EBAF for surface shortwave radiation Kato et al. (2013). For the sake of manageability of the comparison with model outputs, we used monthly mean values and we apply to the products derived from the observations a first-order conservative remapping on a common longitude-latitude grid identical to the one of the model simulations. The period analysed last over 10 years from 2001 to 2010, where all sets of data are available.

Numerical Simulations

We used the atmosphere-land component of the IPSL-CM (Dufresne et al 2011). LMDZ is the atmospheric General Circulation Model (GCM) that has been developed for about thirty years at

CMUG Phase 2 Deliverable

Reference: D3.1: Quality Assessment Report
Due date: June 2017
Submission date: 21 December 2017
Version: 4



the Laboratoire de Meteorologie Dynamique. The model resolution for this study is 2.5 degree (latitude) by 1.25 degree (longitude) with 79 vertical levels. The physical parameterizations originally implemented in the version used here are described in (Hourdin et al., 2011) , (Rio et al., 2010) and (Jam et al., 2013). The Land Surface is the ORCHIDEE model (Krinner et al., 2005). The parameterization of the soil hydrology allows for a physically-based description of vertical water fluxes, using Richards equation (De Rosnay et al., 2002; d'Orgeval et al., 2008). This work has been conducted during a phase of intense activity on the parameterizations in view of the Coupled Model Intercomparison Project Phase 6 (CMIP6) (Taylor et al., 2012) and the combined evaporation/radiation/soil-moisture dataset has been used to assess the impact of new developments of the hydrology module implemented in ORCHIDEE (paper in preparation) on the realism of the simulated soil-moisture atmospheric coupling. A reference simulation and three sensitivity experiments relying on the new developments of the hydrology module have been performed with the LMDZOR model. The sensitivity experiments are designed to test a modification of the vegetation map and of the back-ground albedo (a), in addition to (a) a modification of the stress function for the transpiration (b), in addition to (c) the implementation of a resistance for the bare soil evaporation. Each experiment follows the Atmospheric Model Intercomparison Project (AMIP) protocol where the AGCM is constrained by realistic sea surface temperature and sea ice, the runs cover the period 2001-2011. The large-scale atmosphere dynamics is constrained towards prescribed atmospheric conditions using a nudging approach (Coindreau et al. (2007)). This method has been successfully used to evaluate the parameterizations related to the land-surface/atmosphere coupling (Cheruy et al. (2013)). The simulated global wind fields (zonal u ; meridional v) are nudged with the ECMWF reanalyzed winds by adding a linear restoring term with a 6-hour relaxing time (τ_{nudge}).

Method

The global dataset is split into regions in order to insure homogeneous climate conditions to prevail. The Koeppen Geiger climate classification system is adopted. We focus on three regions where the soil-moisture/atmospheric coupling is strong: the Mediterranean coasts (region 15), the South Great Plains (SGP) in United States (06) and the western Europe (21) depicted in figure 1.

For each region, histograms of the soil-moisture and of the evaporation have been produced with the various datasets and compared for the whole period. They are reported on figure 2 and 3 for the Mediterranean coasts and Western Europe.

For the evaporation (Figure 2), the histogram of the GLEAM product has a much larger amplitude than the one of the Jung's product, but the form of the histograms are similar. Concerning the surface soil moisture, differences exist in both the amplitude and the form of the histograms, especially for the Western-Europe and the SGP (not shown) regions where the GLEAM histogram is much skewed to the downside than the CCI-SM one. Note that GLEAM produces the highest values of both the surface soil-moisture and of the evaporation, this is consistent with the use of a retrieval algorithm that is based on a water budget approach. For the surface soil-moisture retrieval the ESA-CCI approach uses an heuristic evaluation of the driest and wettest reference values where

CMUG Phase 2 Deliverable

Reference: D3.1: Quality Assessment Report

Due date: June 2017

Submission date: 21 December 2017

Version: 4



the saturated conditions for the soil moisture may not be always captured (Algorithm Theoretical Baseline Document: http://www.esa-soilmoisture-cci.org/sites/default/files/documents/ATDB/CCI2_Soil_Moisture_DL2.1_ATBD_v3.2_01_Executive%20Summary.pdf), this can explain the smaller amplitude of the histograms. In this work we used the combined ESA-CCI product which results from blended ACTIVE and PASSIVE merged products.

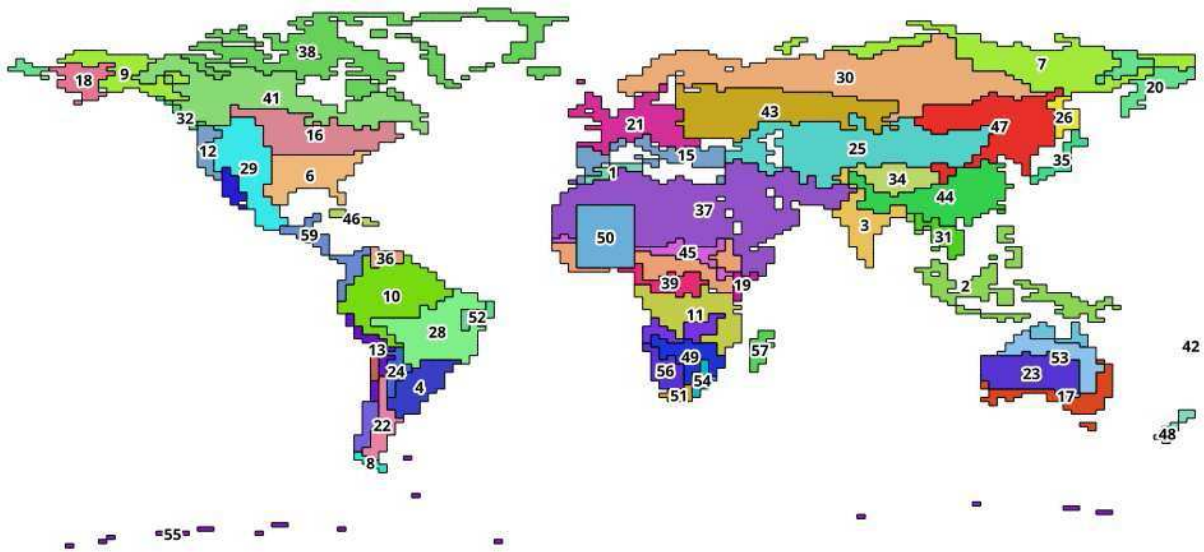


Fig. 1. Regions used for the stratification of the data. The Köppen Geiger climate classification system is used.

CMUG Phase 2 Deliverable

Reference: D3.1: Quality Assessment Report

Due date: June 2017

Submission date: 21 December 2017

Version: 4

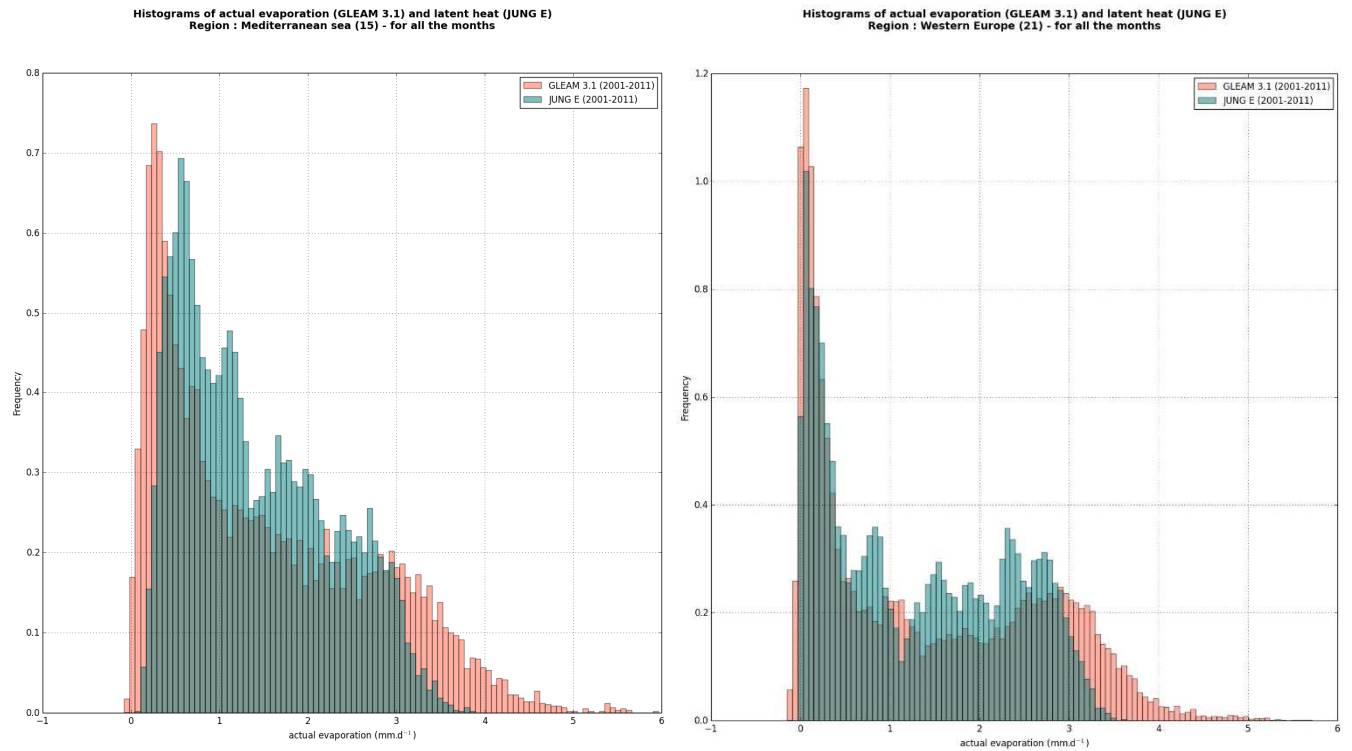


Fig. 2. Regional histogram for the evaporation (GLEAM.3.1 and Jung products) for the Mediterranean coasts and the western Europe region.

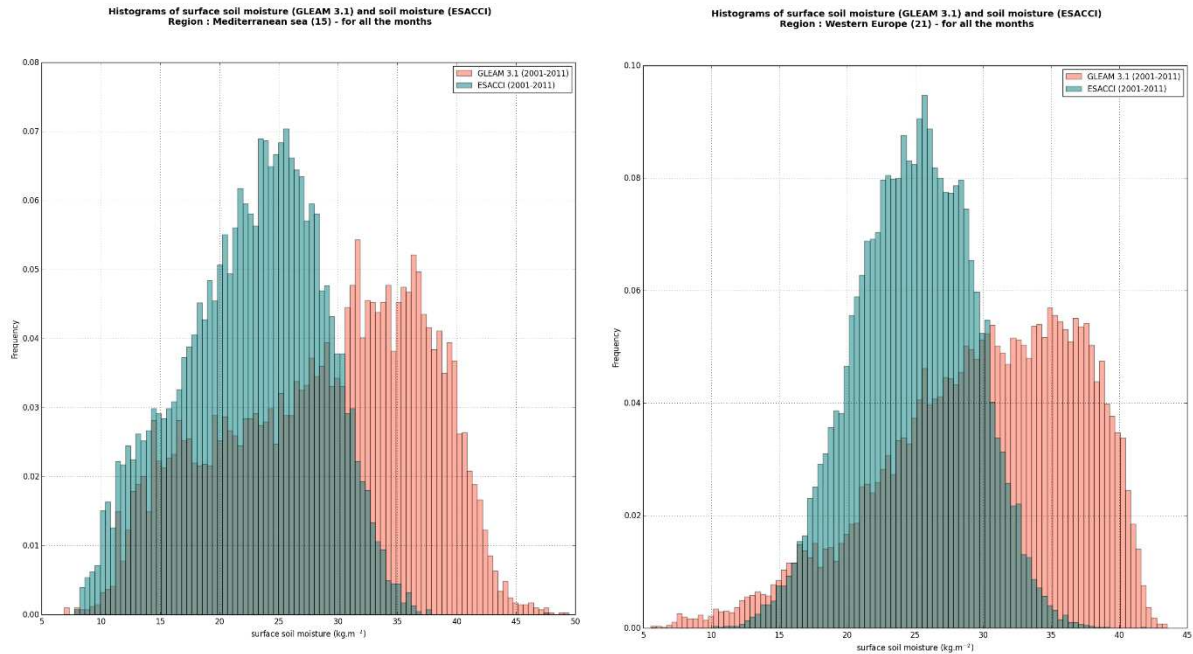


Fig. 3. Regional histogram for the surface soil moisture (GLEAM.3.1 and ESA.CCI Combined products) for the Western Europe.

In the merging process, since the passive and active products have different dynamical range they have to be rescaled. This is done with the help of GLDAS- Noah land surface model Rodell et al. (2004). This approach rises the questions of the nature of the surface soil moisture observations and on how much the observational product is independent of the model used to rescale the observations. This issue requires additional investigation which is out of the scope of the present work.

From these results, it is difficult to say if one dataset is closer to the reality than another. This makes the straightforward use for evaluation purpose complicated. However, we notice that the agreement is more satisfying for the evaporation than for the soil moisture. This suggests to look for robust information combining the available datasets and giving less weight to the absolute values of the soil-moisture.

The surface soil moisture for GLEAM as well as for ESA-CCI is expressed in $m^3.m^{-3}$ which is consistent with a volumetric soil moisture. We converted it in a soil moisture content in the first 10 cm of soil in order to compare them to the similar simulated quantity (expressed in $kg.m^{-2}$).

CMUG Phase 2 Deliverable

Reference: D3.1: Quality Assessment Report
Due date: June 2017
Submission date: 21 December 2017
Version: 4



3.7.3. Characterizing Soil-moisture - Evaporation Regimes using the observational products

The way the respective role of soil moisture and radiant energy at surface impact the evaporation is poorly constrained at scales representative of the grid-boxes of a climate model. This induces significant dispersion in the response of the evapotranspiration in a changing climate (e.g. Boie and Terray (2008)) with consequences on the possible impacts of climate change. The above described datasets can be used to better document this process. According to the previous findings, we now use the soil-moisture information to discriminate between very dry, moderately dry, moderately moist and highly moist soil and investigate the links between evaporation and net SW radiation at the surface for each class of soil moisture. More than absolute values of the evaporation or of the soil moisture, we look for information on the strength of the response of the evaporation to the net SW radiation available at the surface. For each region and all the possible combinations of data, bi-dimensional histograms for simultaneous (at the monthly time scale) estimations of evaporation and net shortwave radiation have been plotted for each of the 4 quartiles of the soil moisture distribution. In order to get information of the impact of the uncertainties of the observational products on the robustness of the diagnostics, we constructed the histograms for all possible combination of data. This gives sets of histograms for a particular region.

Whatever the combination used, the scatter plots exhibit robust behaviours for each soil moisture quartile. When the soil moisture is not too low, the relation between radiation and evaporation is almost linear. A straight line depicting a linear regression is super-imposed on the plots. For all datasets and all regions the intersection with x-axis occurs for positive values of the SW radiations, meaning that below a certain threshold of incoming energy, the evaporation is not triggered. This threshold is lower when Jung product is used to estimate the evaporation but it is almost insensitive to the choice of the soil moisture product. For the Mediterranean and the SGP and for the lowest values of the soil moisture the linear relation almost vanishes. In dry regions (figures 6, 5) and during the dry season radiation has hard time to trigger the evaporation. When it is triggered, it is a yes-or-no process and the evaporation rates can vary over a large range of values. The highest values of the evaporation rates occur for the intermediate values of the soil moisture and the highest values of the net SW radiation. For the moistest quartile (figures 6, 5, 7) the values of the SW radiation and of the evaporation are relatively low. In this case the surface layer is probably too moist to allow available soil moisture to evaporate and the radiation is lowered because of clouds.

CMUG Phase 2 Deliverable

Reference: D3.1: Quality Assessment Report

Due date: June 2017

Submission date: 21 December 2017

Version: 4

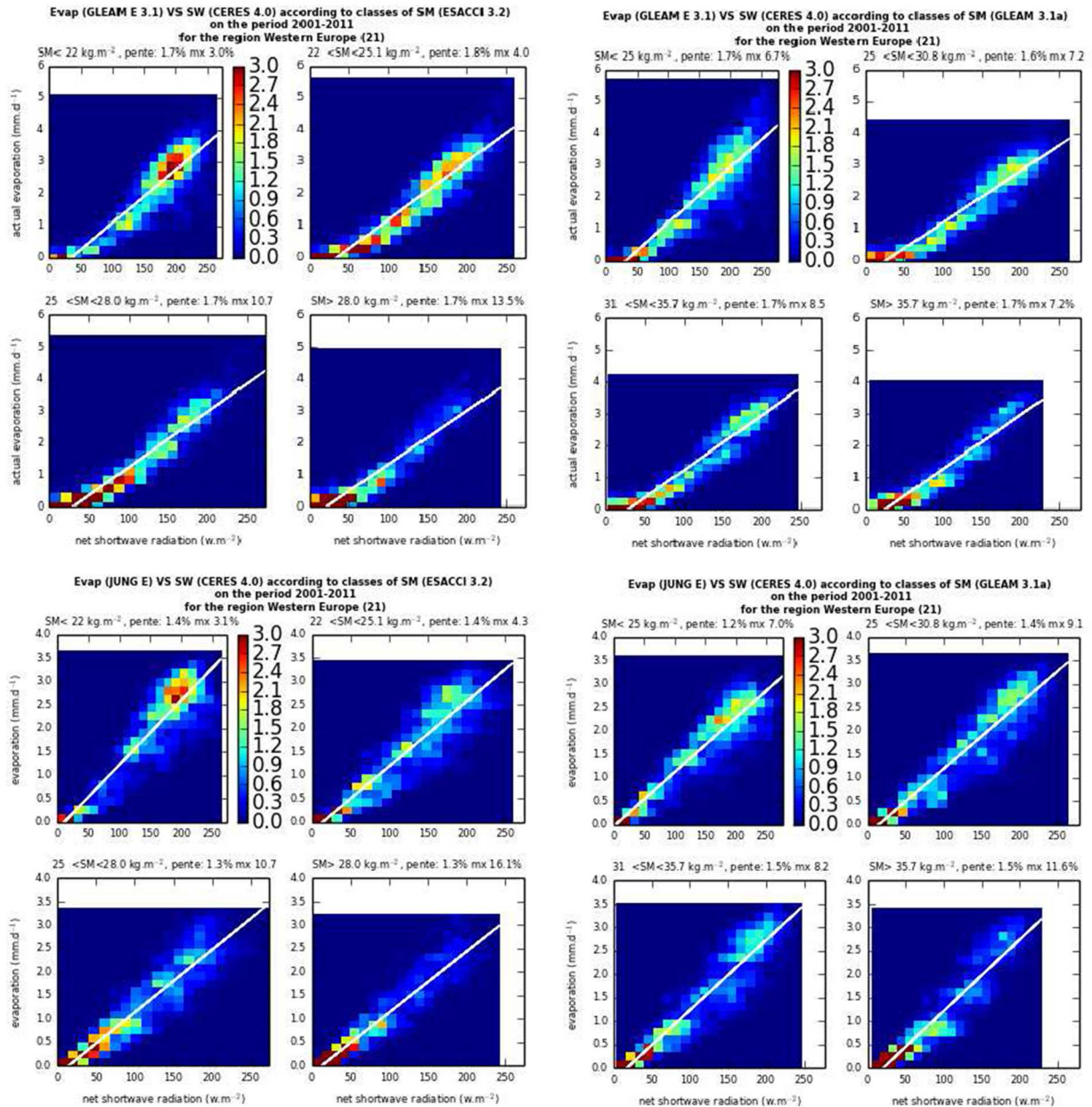


Fig. 4. Bi-dimensional histograms of the occurrence of pairs of (Evaporation, SW_{net} radiation) values binned into 20 intervals and for each quartiles of the soil moisture distribution for the Western-Europe and for 10 years. The colour scale indicates the percentage of the total population with particular (SW_{net} , Evaporation) binned values. The scale is bounded at 3%, the values outside the range are set to the maximum and minimum. The maximum value is indicated in the title of each histogram. The datasets used are indicated in the title of each set of histograms.

CMUG Phase 2 Deliverable

Reference: D3.1: Quality Assessment Report

Due date: June 2017

Submission date: 21 December 2017

Version: 4

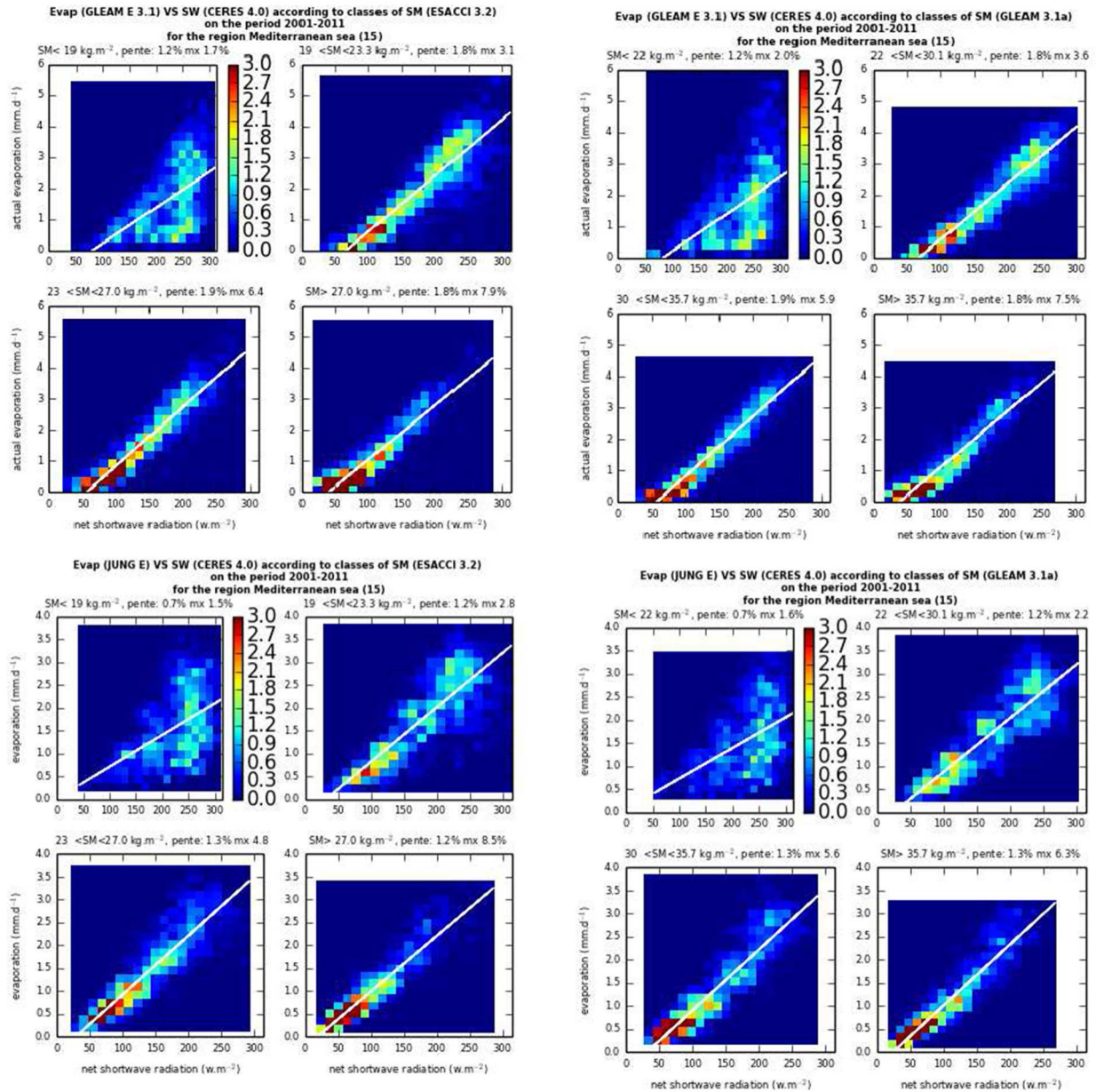


Fig. 5. Two dimensional histograms of the occurrence of pairs of (Evaporation, SWnet radiation) values binned into 20 intervals and for each quartiles of the Soil moisture distribution for the Mediterranean coasts and for 10 years. The colour scale indicates the percentage of the total population with particular (SWnet, Evaporation) binned values. The scale is bounded at 3%, the values outside the range are set to the maximum and minimum. The maximum value is indicated in the title of each histogram.

CMUG Phase 2 Deliverable

Reference: D3.1: Quality Assessment Report

Due date: June 2017

Submission date: 21 December 2017

Version: 4

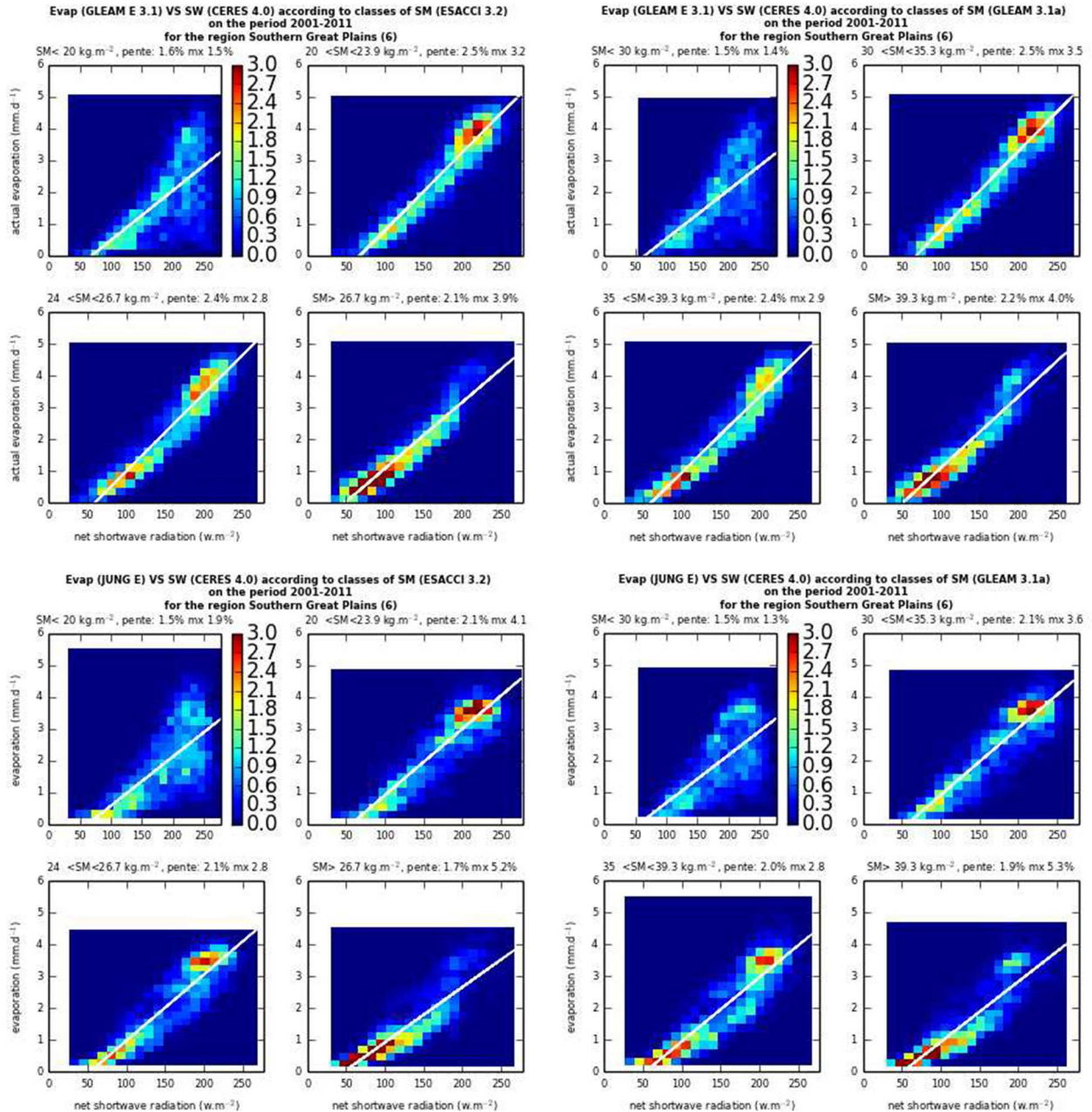


Fig. 6. Bi-dimensional histograms of the occurrence of pairs of (Evaporation, SWnet radiation) values binned into 20 intervals and for each quartiles of the Soil moisture distribution for the Southern Great Plains and for 10 years. The colour scale indicates the percentage of the total population with particular (SWnet, Evaporation) binned values. The scale is bounded at 3%, the values outside the range are set to the maximum and minimum. The maximum value is indicated in the title of each histogram.

CMUG Phase 2 Deliverable

Reference: D3.1: Quality Assessment Report

Due date: June 2017

Submission date: 21 December 2017

Version: 4

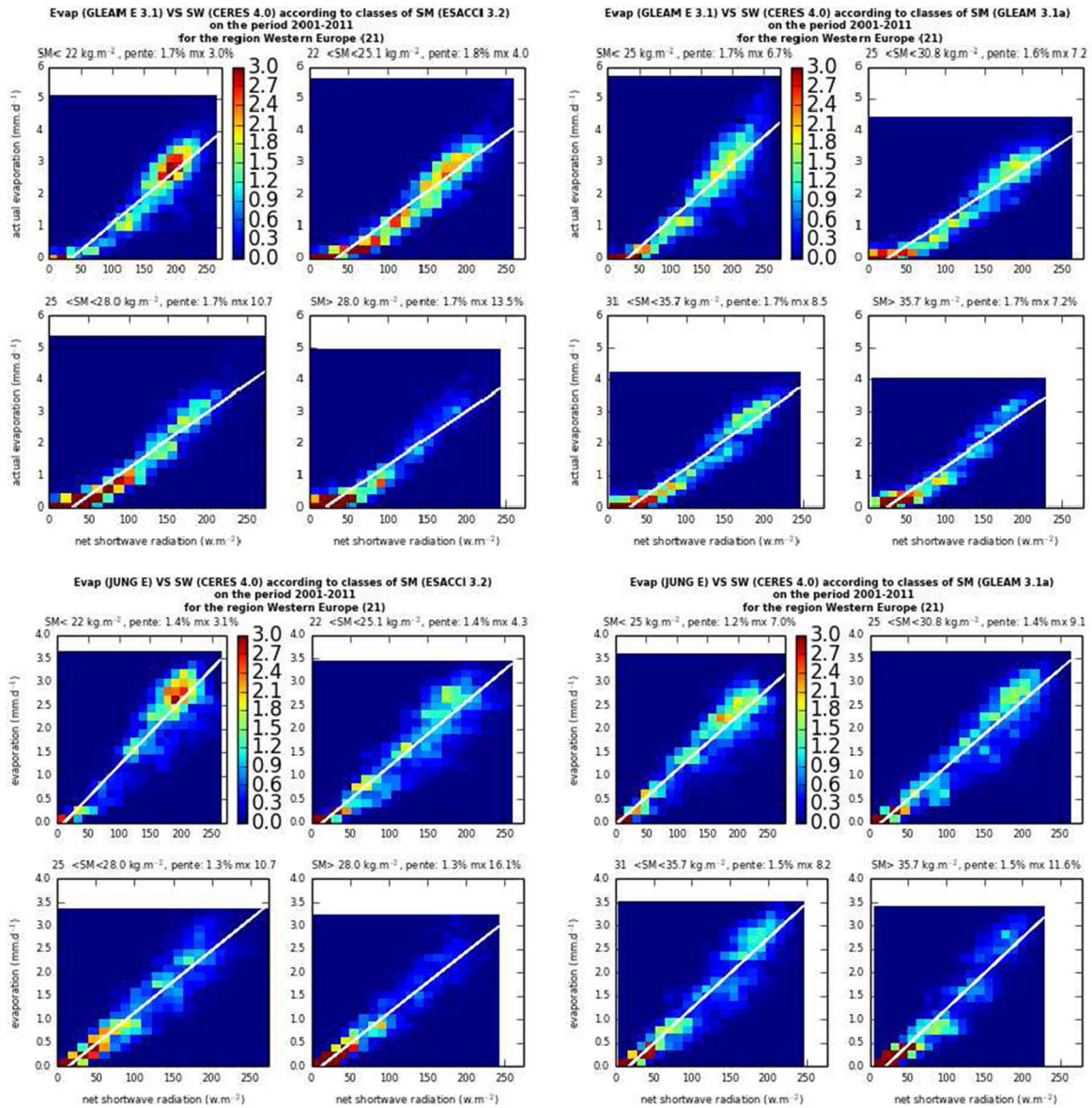


Fig. 7. bi-dimensional histograms of the occurrence of pairs of (Evaporation, SWnet radiation) values binned into 20 intervals and per each quartiles of the Soil moisture distribution for the Western Europe and for 10 years. The colour scale indicates the percentage of the total population with particular (SWnet, Evaporation) binned values. The scale is bounded at 3%, the values outside the range are set to the maximum and minimum.

CMUG Phase 2 Deliverable

Reference: D3.1: Quality Assessment Report

Due date: June 2017

Submission date: 21 December 2017

Version: 4

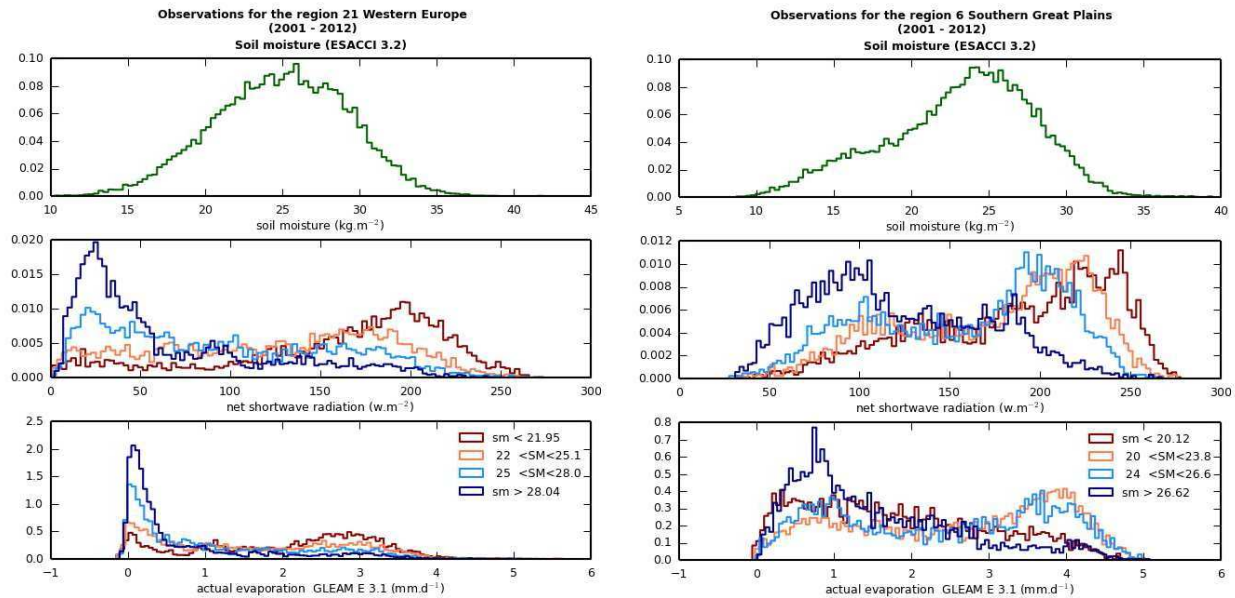


Fig. 8. Soil moisture distribution for Western Europe and Southern Great Plains, and histograms of the distribution of the evaporation and SWnet radiation binned into 20 intervals for each quartile of the soil moisture and for 10 years.

Figure 8 gives an even clearer picture of the indirect impact of the soil moisture on the SW radiation. The histogram of the SW radiation and the evaporation have been plotted for each quartile. The blue line which corresponds to the moister upper soil layer peaks at low values of both SW radiation and evaporation. The occurrence of high evaporation rate is more frequent in the driest quartile.

3.7.4 Comparison with the model simulations

Discussion of the bi-dimensional histograms

We produced bi-dimensional histograms similar to the ones produced with the observations but for the reference simulation and the 3 sensitivity experiments. All these sensitivity experiments potentially impact the radiation and the evapo-transpiration. The model produces more regular distribution than the observations (e.g. figure 9). The difficulty to trigger the evaporation when the soil is dry is captured by the model. When the soils are moister, the almost linear behaviour of the evaporation-radiation relationship is also captured by all experiments. The results of the reference experiment and the first 2 sensitivity experiments are similar (not shown). When the soil is dry (first 2 soil moisture quartiles), the model appears to be slightly more efficient to evaporate for the high values of the net SW radiation. It is remarkable that the intersection of the regressed straight line with x-axis occurs for negative values of the SW radiation. This indicates that evaporation can

CMUG Phase 2 Deliverable

Reference: D3.1: Quality Assessment Report

Due date: June 2017

Submission date: 21 December 2017

Version: 4



occur even when the SW radiation is very low in contradiction with the observations. This behaviour is corrected when the resistance to the bare soil evaporation is activated in the simulations. Note that this modifies the distribution of the SW radiation for all quartiles as well. For intermediate values of the SW radiation, the evaporation rates are lower, in better agreement with the histograms obtained with the products derived from observations. This is particularly true for the Mediterranean area and the Southern Great Plains. The maximum value of the SW radiation, is often higher in the numerical simulations compared to the CERES derived observations.

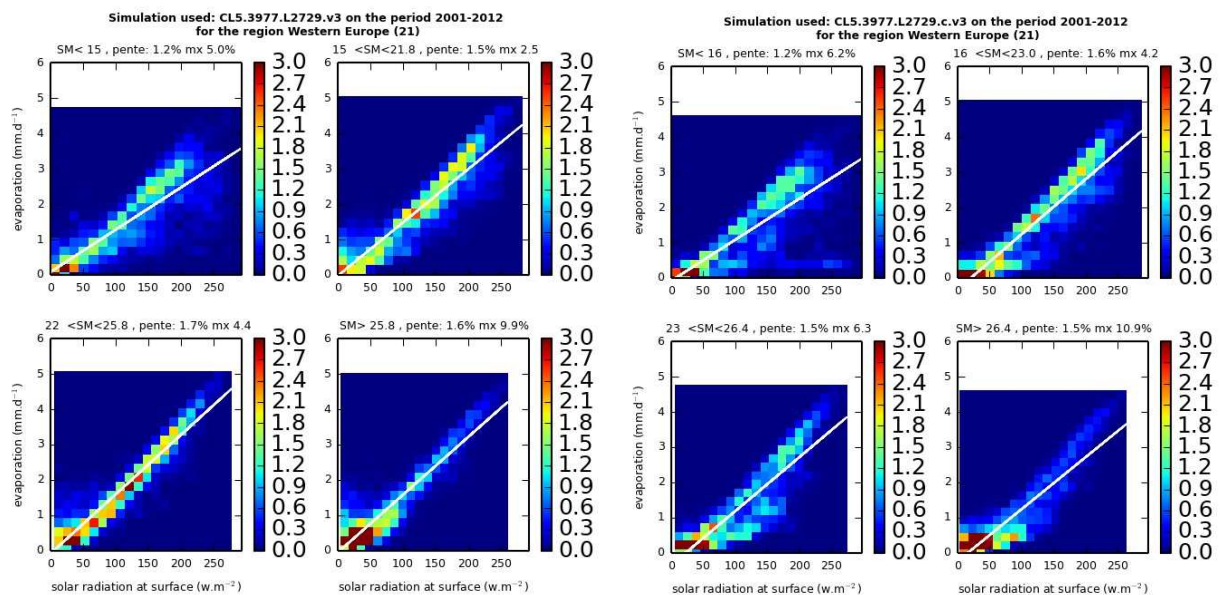


Fig. 9. 2D-histograms of the simultaneous (evaporation, net SW radiation) pairs for each quartile of the soil moisture distribution for the Western-Europe. The values outside the range are set to the maximum and minimum. The left hand side histograms corresponds to the reference experiment, the right hand-side plot corresponds to the sensitivity experiment where the resistance to the bare soil evaporation is implemented (v3.c).

CMUG Phase 2 Deliverable

Reference: D3.1: Quality Assessment Report

Due date: June 2017

Submission date: 21 December 2017

Version: 4

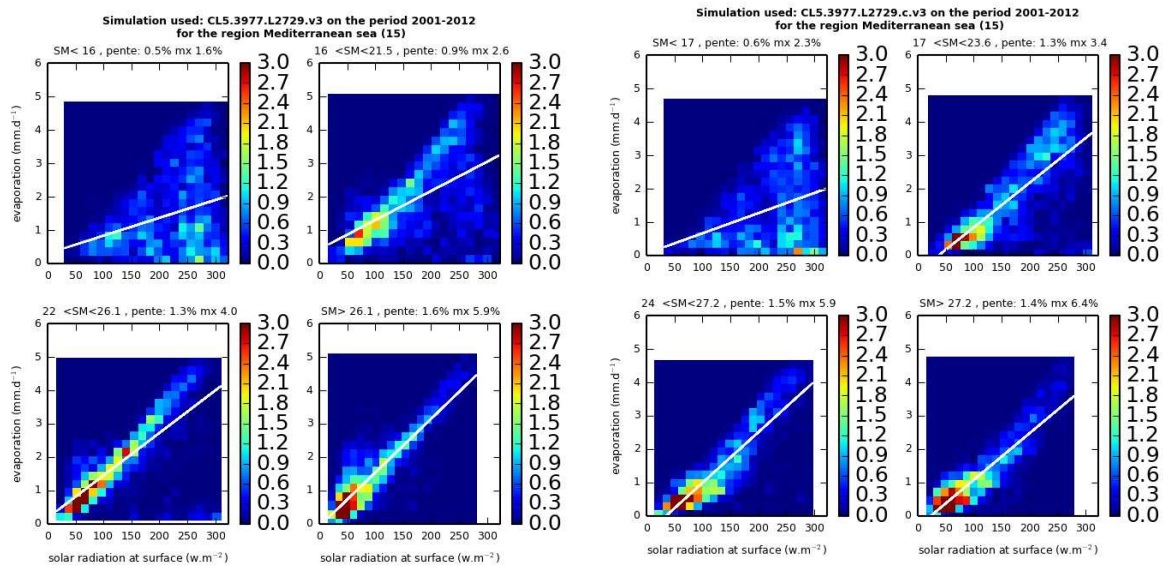


Fig. 10. 2D-histograms of the simultaneous (evaporation, net SW radiation) pairs for each quartile of the soil moisture distribution for the Mediterranean area. The values outside the range are set to the maximum and minimum. The maximum value is reported in the title of each histogram. The left hand side histograms corresponds to the reference experiment, the right hand-side plot corresponds to the sensitivity experiment where the resistance to the bare soil evaporation is implemented (v3.c).

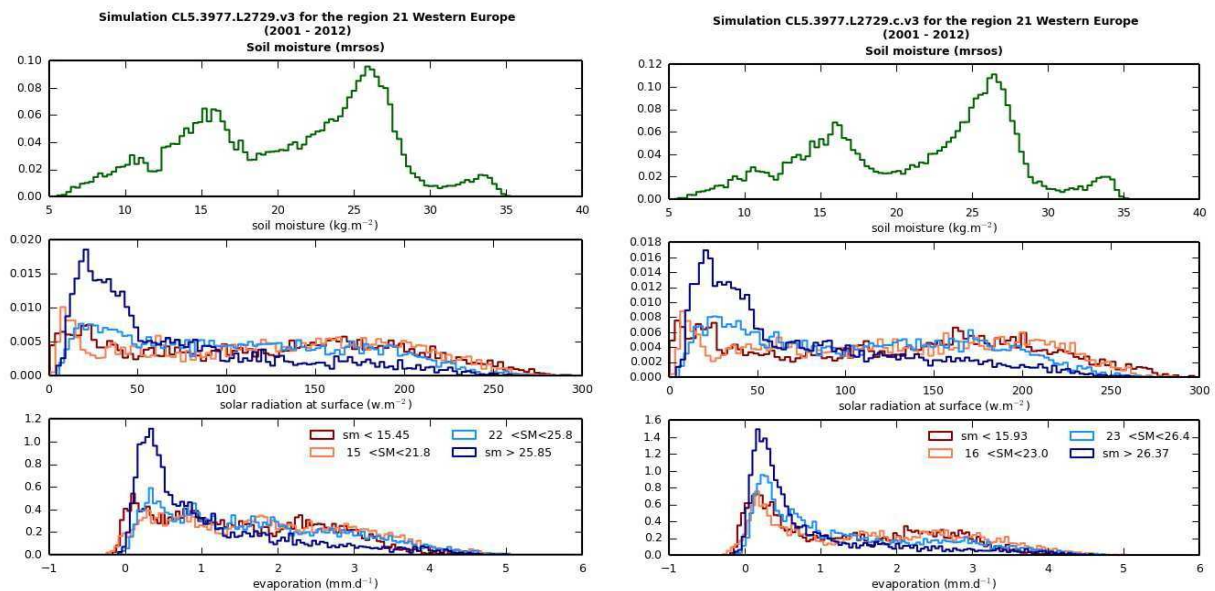


Fig. 11. upper panel: histogram of the surface soil moisture for the Western Europe area, middle panel : histograms of the SW net radiation for each soil moisture quartile, lower panel: histogram of the evaporation for each soil moisture quartile. The left hand-side panels correspond to the reference numerical experiment, the right hand-side one to the sensitivity experiment where the resistance to the bare-soil evaporation is turned on.

CMUG Phase 2 Deliverable

Reference: D3.1: Quality Assessment Report
Due date: June 2017
Submission date: 21 December 2017
Version: 4



Figure 11 and 12 (lower 2 panels) show the histograms of the evaporation and the SW radiation for each soil moisture quartile and for the reference numerical experiment and when the resistance to the bare soil evaporation is turned on. For the first 3 quartiles, the histograms of the evaporation and of the SW Radiation are very similar, contrarily to the observations. In Western Europe (figure 4.1), the model shows very low values (less than 10 W.m^{-2}) of the SW radiation for the dry quartiles in contradiction with the observations. When the resistance of the evaporation for the bare soil is turned on the frequency of the low evaporation rates is increased in the moister quartile (blue curve). Negative values of the evaporation (down to -0.3 mmd) are simulated during winter over Western Europe they corresponds to condensation processes.

Revisiting a long lasting bias

Most state-of-the art climate models contributing to CMIP5 shared a strong summer- time warm bias in mid-latitude areas, especially in regions such as the Southern Great Plains where the coupling between soil moisture and atmosphere is effective. The most biased models overestimate solar incoming radiation, because of cloud deficit and have difficulty to sustain evaporation. These deficiencies are also involved in the spread of the summer temperature projections among models in the mid-latitudes Cheruy et al. (2014) Near surface simulated temperatures are compared to the $0.5^\circ \times 0.5^\circ$ CRU-TS3.10 2- m temperature dataset (Mitchell and Jones, 2005) and the 2D histograms of the (SW radiation, temperature bias) couples are calculated for each of the soil moisture quartiles. The results are displayed on Figure 13.

Whatever the quartile, the bias is stronger for the highest values of the SW radiation. An interesting result here is that the bias exists even for last quartile, where soil moisture is available for evaporation. When the resistance to bare soil evaporation is activated, the bias increases more rapidly with the SW radiation (the slope of the linear regression depicted by the white straight line on the plots increases from 0.6% to 1.2 %). This is consistent with insufficient evaporation rates contributing to the bias and in this model difficulty to evaporate occurs even when enough soil moisture and radiation are available. Evaporation is made of bare soil evaporation and transpiration by the plants that take the moisture from deeper layer in the soil. It is possible that in this case an under-estimation of the transpiration is responsible for the too elevated temperature.

CMUG Phase 2 Deliverable

Reference: D3.1: Quality Assessment Report

Due date: June 2017

Submission date: 21 December 2017

Version: 4

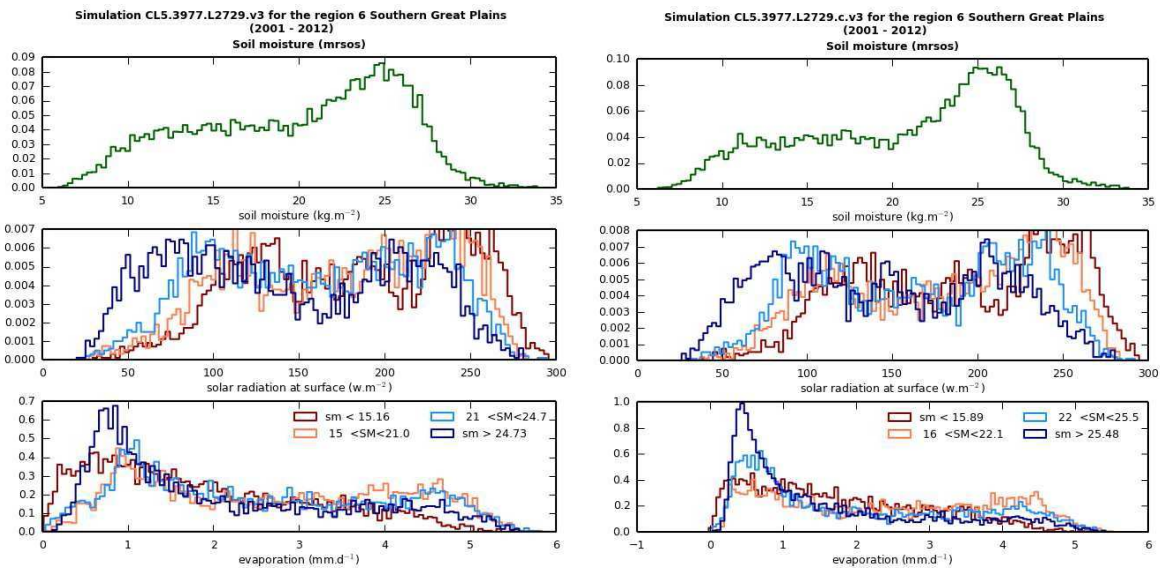


Fig. 12. Upper panel: histogram of the surface soil moisture for the Southern Great Plains area, middle panel : histograms of the SW net radiation for each soil moisture quartile, lower panel: histogram of the evaporation for each soil moisture quartile. The left hand-side panels correspond to the reference numerical experiment, the right hand-side one to the sensitivity experiment where the resistance to the bare-soil evaporation is turned on.

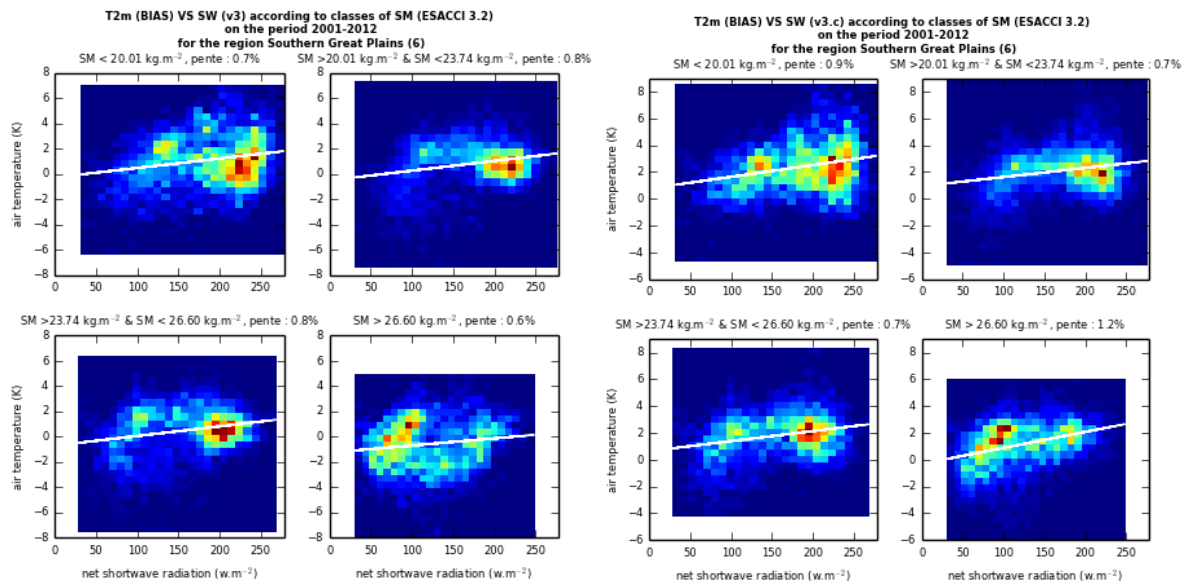


Fig. 13. Bi-dimensional histograms of the occurrence of pairs of (surface air temperature bias, SWnet radiation) values binned into 20 intervals and for each quartiles of the surface Soil moisture distribution for the Southern Great Plains and for 10 years. The colour scale indicates the percentage of the total population with particular (SAT bias, SWnet) binned values. The bias is evaluated against CRU data. The scale is bounded at 3%, the values outside the range are set to the maximum and minimum. The maximum value is indicated in the title of each histogram.

CMUG Phase 2 Deliverable

Reference: D3.1: Quality Assessment Report
Due date: June 2017
Submission date: 21 December 2017
Version: 4



Soil Moisture Histograms

The upper panels in Figure 4.1 and 12 show the histograms of the soil moisture for the Western Europe and the Southern Great Plains. The histograms of the soil moisture are significantly different, especially for Western Europe, where they show a tri-modal distribution. While in the real world a large number of texture is present and is mixed in each model grid box, the soil hydrology module works with the predominant soil texture in each only the predominant soil texture is selected for the description of the water fluxes by the soil hydrology module ; the tri-modal structure of the histogram reveals the signature of the three different textures present in the Western Europe region according to the USGS-produced soil property maps (<http://soils.usda.gov/use/worldsoils/mapindex/>) used in the numerical experiments. This rises several questions on both the retrieved and the simulated surface soil moisture and on the approach to compare them.

- The tri-modal structure of the simulated soil moisture histogram might shows that it is necessary to improve the representation of the variations of the pedotransfer function with the soil grain size distributions (e.g Schaap et al. 2001).
- Underlying hypothesis in the numerical model and in the retrieval algorithms (e.g. dependency of the wilting point and field capacity with the soil grain size distribution) might leads to inconsistent estimation of the soil moisture content. This can lead to misleading conclusion when directly comparing simulated and retrieved soil moisture content.
- Greater care should be taken in order to allow meaningful comparison. This requires more detailed description of the underlying hypothesis in the retrieval algorithm in order to allow to construct and compare normalized histograms Koster et al. (2009) with rely on similar hydrological properties related to the soil texture.

3.7.5. Summary

We showed that satellite derived products for evaporation and surface Soil Moisture exhibit strong differences. It is not possible to say which one is closer to the reality. This is particularly true for the surface soil moisture. Nevertheless the partitioning of combined SW surface radiation and evaporation data with respect to 4 soil-moisture quartiles at regional scale and on a monthly basis allowed to derive consistent diagnostics which can be used to better document the soil-moisture atmosphere coupling and as a guidance for the development of the parameterizations implemented in the climate model. A better description of the underlying hypothesis used to derive surface soil moisture from satellite observations is critical to better assess the nature of the soil moisture observations and to reinforce the robustness of these diagnostics. Instrumented sites such as the

CMUG Phase 2 Deliverable

Reference: D3.1: Quality Assessment Report
Due date: June 2017
Submission date: 21 December 2017
Version: 4



ARM site located in the Southern Great Plains provide quality checked observations of the surface radiation budget, the boundary layer turbulence and the soil-moisture which might help to assess the robustness of the diagnostics as well. In addition, we investigated the behaviour of a long lasting warm bias which exists in most of the climate models over Central North America in summer. For each soil moisture quartile, 2D-histograms of combined SW radiation, temperature bias have been constructed. While this bias is attributed to insufficient evaporation, these histograms show that the bias is present even when surface soil moisture is not a limitation to the evaporation. We propose that the transpiration of the vegetation, which can rely on the moisture present at deeper levels into the soil, can play a role. Finally we identified a spurious behaviour in the histograms of the simulated surface soil moisture when compared to the satellite product. This behaviour can be related to the restricted number of soil textures implemented in the hydrological module. The consequences on the soil-moisture/atmosphere coupling have to be investigated and improvement in the hydrological module of the LSM are foreseen.

CMUG Phase 2 Deliverable

Reference: D3.1: Quality Assessment Report
Due date: June 2017
Submission date: 21 December 2017
Version: 4



3.8 Improved process understanding from Arctic and Antarctic cross ECV assessment [WP3.6]

ESA-CCI sea ice and sea surface temperature data products

We assess here the quality of sea ice concentration and sea ice thickness datasets compiled by the ESA Sea Ice CCI (SICCI) team, and perform a polar ECV cross assessment between ESA-CCI ice concentration and sea surface temperature datasets. To analyse the quality of the sea ice concentration and thickness products we assimilated these datasets into the Max Planck Institute Earth System Model (MPI-ESM; Stevens et al., 2013). In order to evaluate the SICCI ice concentration dataset we assimilated only SICCI ice concentration data into the model, and compared the performance of the simulated sea ice behaviour with identical experiments where ice concentration data from the National Snow and Ice Data Center (NSIDC) was assimilated. To evaluate the quality of the SICCI ice thickness dataset, we assimilated both SICCI ice concentration and thickness data into the model, and compared the simulated sea ice volume to other observational datasets as well as to the ice volume derived from the experiment where only ice concentration was assimilated. For the polar ECV cross assessment ESA-CCI sea ice concentrations and sea surface temperatures were assimilated into the model. For each of the two ECVs the assimilation run was repeated with a reference data product.

The assimilation technique we apply in our model system is Newtonian relaxation (or “nudging”), and besides sea ice also atmospheric and oceanic observations are assimilated into the model. In the atmosphere vorticity, divergence, temperature and surface pressure data provided by ERA-Interim reanalyses (Dee et al., 2011) are assimilated, while ocean temperature and salinity are nudged with ORA-S4 reanalysis data (Balmaseda et al., 2013). Relaxation times applied when data was assimilated into the model vary from 1 day for atmospheric nudging to 10 days for ocean nudging, and 20 days for nudging of sea ice. When only sea ice concentration is assimilated into the model, sea ice thickness is updated proportionally to sea ice concentration updates (Tietsche et al., 2013).

Results of our performance analysis for both SICCI sea ice concentration and thickness datasets, as well as for the polar ECV cross assessment, are given below.

3.8.1 ESA-CCI sea ice concentration dataset (version 1.1, daily data, 1991-2008)

A comparison of SICCI and NSIDC sea ice concentration products shows that the Arctic sea ice area computed from SICCI data lies between NASA-Team (Cavalieri et al., 1984) and Bootstrap (Comiso, 1995) datasets from NSIDC. While NASA-Team data shows lower Arctic sea ice area than SICCI, the Arctic sea ice area derived from Bootstrap data is larger than for SICCI. The difference between NASA-Team and Bootstrap products lies in the selection of tie points for

CMUG Phase 2 Deliverable

Reference: D3.1: Quality Assessment Report

Due date: June 2017

Submission date: 21 December 2017

Version: 4



brightness temperatures representing “fully ice-covered” grid boxes. In the Bootstrap retrieval algorithm 100% ice cover is obtained already for lower brightness temperatures compared to the NASA-Team algorithm. From computed Arctic sea ice areas we infer that the SICCI algorithm gives intermediate ice concentrations in the Arctic. This result also holds for simulated Arctic sea ice area in assimilation experiments with the different ice concentration datasets.

The Antarctic sea ice area derived from both the SICCI ice concentration dataset and the assimilation run performed with SICCI ice concentrations shows that in the Antarctic the SICCI product resembles the NSIDC Bootstrap product, while the NASA-Team product shows about 10% less sea ice area.

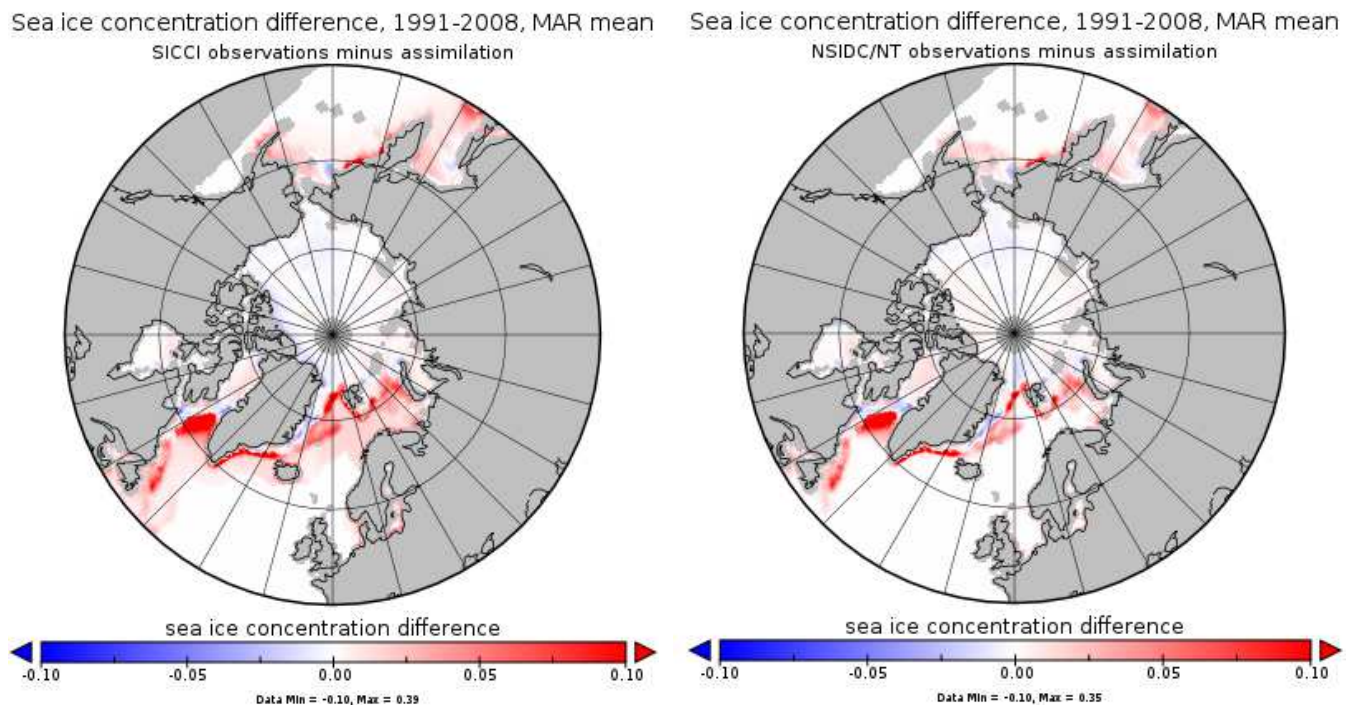


Figure 40: Sea ice concentration differences between observations and the associated assimilation runs are presented for SICCI (left) and NSIDC/NASA-Team (right) data products. March-mean values over the period 1991 to 2008 are shown.

A regional evaluation of the correspondence of the assimilated sea ice data product with the model physics indicates, however, a clear difference between SICCI and NSIDC data products. In many regions, especially in the Norwegian and Labrador Sea, low ice concentrations (< 3%) are obtained by the SICCI algorithm in grid boxes where observed sea surface temperatures as well as NSIDC ice concentration products indicate ice-free waters (see Figure 40). These spurious ice concentrations occur, because consciously no weather filter was applied in the SICCI algorithm. In NSIDC ice concentration products these low ice concentrations, which originate from the

CMUG Phase 2 Deliverable

Reference: D3.1: Quality Assessment Report
Due date: June 2017
Submission date: 21 December 2017
Version: 4



contribution of clouds to brightness temperatures recorded by the satellite, are removed by a weather filter. However, since it is not feasible to objectively distinguish between the origins of possible brightness temperature sources, weather filters are likely to filter out also contributions of actual sea ice. Thus, although not using a weather filter introduces spurious ice concentrations in the open ocean, it provides a more objective view on the satellite data, since no actual ice concentrations are removed and it is left to the user to discard spurious low ice concentrations over open waters, if intended.

The regional investigation of the assimilation performance also showed that a notable amount of sea ice in the marginal ice zone melts directly after assimilation into the model. The most prominent area for this to happen is the Davis Strait (see Figure 40). Sea ice observations show that in a few years (e.g. 1993) this area is largely covered by sea ice in March, however, model physics does not allow here for sea ice to exist. The model physics in a grid box where both sea ice and sea surface temperature are assimilated can be described as follows:

In a model grid box the temperature of the uppermost ocean layer needs to be at freezing point to allow even for small amounts of sea ice to exist. Thus, assimilated sea ice cannot persist if the heat content in a certain ocean model grid box plus the sum of heat contributions from the assimilated sea surface temperature and the assimilated sea ice adds up to an ocean surface temperature above freezing.

In many regions inconsistencies with the assimilated SST data also play an important role (see also Section 3.7.3).

In summary, we consider the SICCI sea ice concentration data product as adequate for use in climate modelling, and of comparable quality as NSIDC data products. A major advantage of the SICCI product with respect to other datasets is its error characteristics. The different types of uncertainties provided with the dataset allow for more accurate studies, e.g., on the evaluation of model physics.

3.8.2 ESA-CCI sea ice thickness dataset (version 0.9, Arctic-only, monthly data for October to March, 2003-2008)

A comparison of the SICCI ice thickness product with other data products derived from observational time series reveals a substantial positive bias in SICCI data. When besides sea ice concentration data also SICCI ice thickness data is assimilated into the model, the March-mean Arctic sea ice volume exceeds the ice volume derived from the assimilation run where only ice concentration is nudged by almost 100% (see Figure 41).



Reduced Arctic sea ice volume, MAR mean

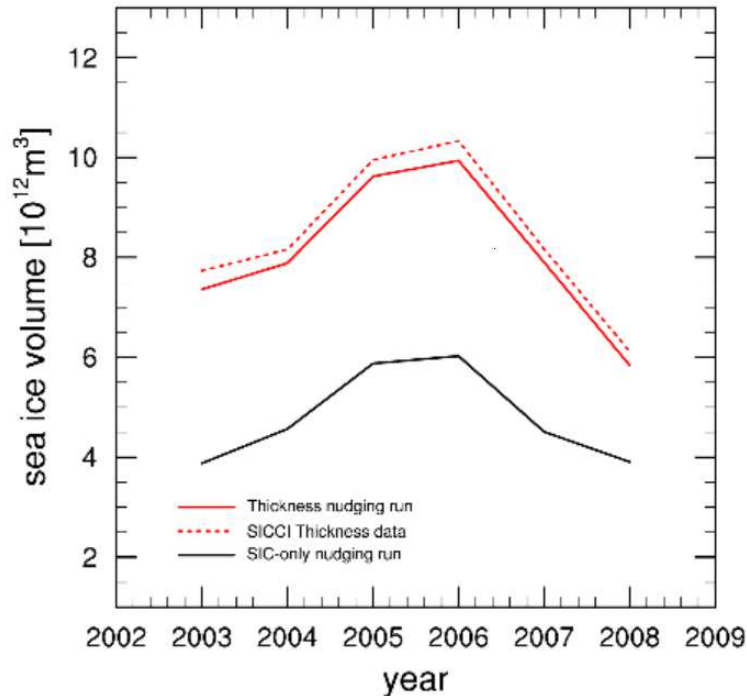


Figure 41: March-mean reduced Arctic sea ice volume over 2003-2008, as derived from SICCI ice thickness data (red dotted line), the combined SICCI ice thickness/concentration assimilation run (red solid line), as well as the SICCI ice concentration-only assimilation run (black line), is shown. The term “reduced” is introduced here, since only grid boxes, where the SICCI ice thickness dataset contains non-missing non-zero values, are considered.

A side effect of assimilating high SICCI ice thicknesses into the model is that almost no assimilated sea ice in the marginal ice zone is lost directly after assimilation due to sea surface temperatures above freezing (see section on SICCI ice concentration data). The additional cooling of the system due to the positive bias in assimilated ice thicknesses prevents assimilated sea ice from being melted. However, we find the positive bias in the SICCI sea ice thickness dataset to be too large to allow for the data product to be of adequate quality for climate modelling studies. Error characteristics were not provided with the SICCI ice thickness data product.



3.8.3 Cross assessment ESA-CCI sea surface temperature and ice concentration (SST data version 1.1, daily data, 1992-2008)

A comparison between ESA-CCI sea surface temperature (SST) and sea ice concentration (SIC) datasets reveals that inconsistencies among the data products exist in many regions close to the ice edge. Figure 42 shows the ESA-CCI sea surface temperature for March 1998 in all grid boxes where the ESA-CCI ice concentration is larger than 5%. Particularly in the Denmark Strait, but also in other regions such as the Baltic Sea, sea surface temperatures exceed 2°C over large areas, although ice concentrations above 5% are found in the same grid boxes. This result does not change qualitatively in other years.

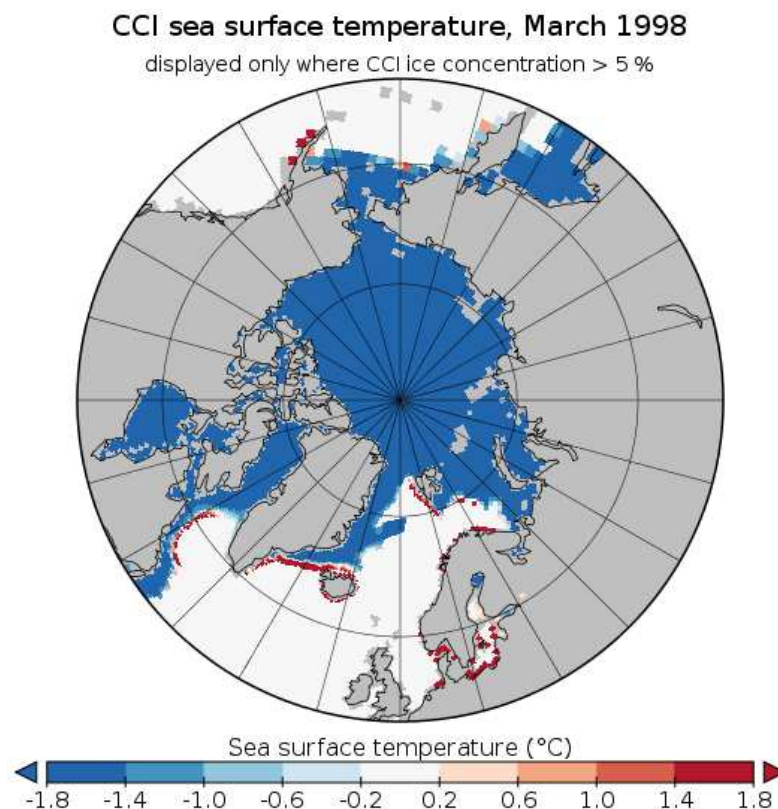


Figure 42: ESA-CCI sea surface temperatures are shown for March 1998. Grid boxes with less than 5% ice concentration were set to 0°C.

The reason for these inconsistencies is likely that for the compilation of the ESA-CCI SST product another sea ice dataset, the OSI-SAF SIC product, was used to determine the exact position of the ice edge. Thus, ESA-CCI SST and SIC datasets are two independent data products, each showing the location of the ice edge as retrieved from the respective algorithm.

In order to test how MPI-ESM model physics agrees with both ESA-CCI SST and SIC data, we assimilated both datasets simultaneously into the model. To assess the quality of the correspondence between the model and the data products, we repeated the assimilation run once

CMUG Phase 2 Deliverable

Reference: D3.1: Quality Assessment Report
Due date: June 2017
Submission date: 21 December 2017
Version: 4



with ERA-Interim (instead of ESA-CCI) SST data, and once with NSIDC/Bootstrap (instead of ESA-CCI) SIC data. For reference, we also performed an assimilation run without any ESA-CCI data by using the respective SST and SIC reference products.

The impact of the assimilated SST data product on the simulated total Arctic sea-ice area is almost undetectable. Figure 43 shows that both SST products assimilated into the model give very similar Arctic sea-ice area. This result holds, independent of the SIC product assimilated simultaneously. The total Arctic ice area reduces, however, after assimilation into the model. This reduction is slightly higher for the ESA-CCI compared to the NSIDC/Bootstrap SIC product, and is generally more prominent in March than in September (see Figure 43). The cause for this reduction is twofold. On the one hand, SSTs above freezing overlapping with the marginal ice zone cause ice melt in the respective regions (compare Figure 42). On the other hand, in regions such as the Davis Strait MPI-ESM model physics does not allow for ice being formed. The reduction is higher for ESA-CCI SIC than NSIDC/Bootstrap sea ice data, since the ESA-CCI algorithm does not apply a weather filter, so that clouds over open water are interpreted as ice concentrations by the algorithm (compare Figure 40).

The general offset between ESA-CCI and NSIDC/Bootstrap SIC data is likely to originate from a different setting of the ice tie points in the different retrieval algorithms.

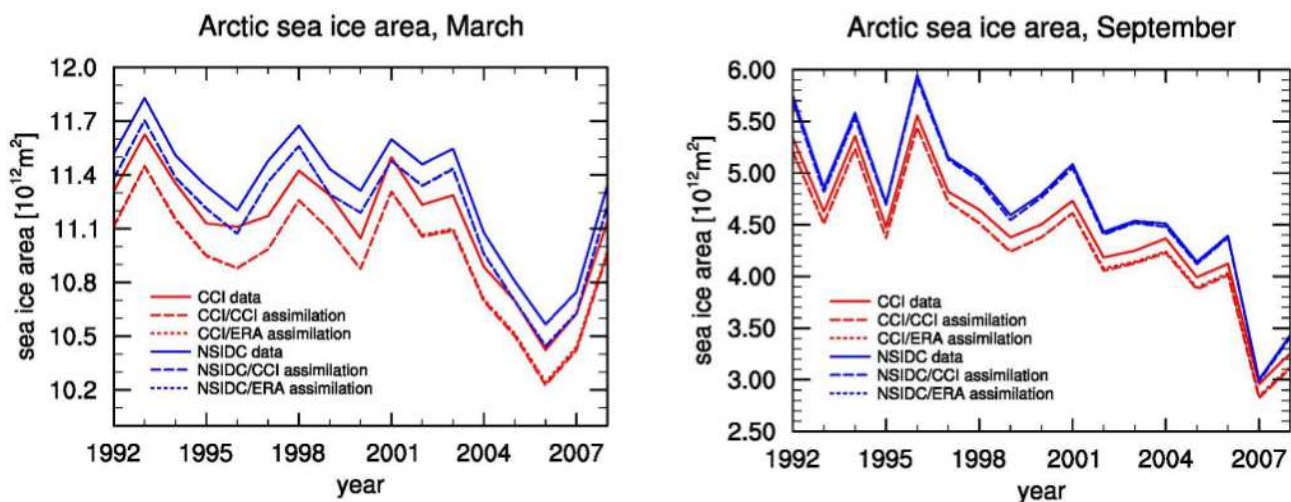


Figure 43: Arctic sea-ice area in March (left) and September (right) as derived from observational datasets (solid lines) and assimilation runs (dashed and dotted lines). Only grid boxes with non-missing values in all datasets were considered for the computation.

CMUG Phase 2 Deliverable

Reference: D3.1: Quality Assessment Report
Due date: June 2017
Submission date: 21 December 2017
Version: 4



3.8.4 Update on CCI Sea-ice concentration data set Version 2.0

In spring 2017, an updated version of the CCI sea-ice concentration data set was published. There are four main differences compared to the earlier version of this product.

First, many of the algorithms and processing steps have been improved in this version 2.0. Noticeably, the calculation of dynamic tie-points, the tuning of the sea ice concentration algorithm, and the mitigation of land spill-over effects were all revised.

Second, the product comes at three distinct resolutions: A high-resolution product at 12.5 km resolution, a medium-resolution product at 25 km resolution and a low-resolution product at 50 km resolution. The 12.5km product is deemed more experimental and for internal evaluation only. It is not at present made available to the scientific community.

Third, the product now only covers the period 2002 to 2015, with a gap of several months in 2011.

Fourth, the product now comes with a filtered version where artefacts possibly arising from weather influence for example have been removed, and an unfiltered version that all values as they are reported by the algorithm. This includes values above 100 % and below 0 % ice concentration.

In the following, we will discuss the impact of these changes from a climate-model perspective.

For doing so, we first repeated our analysis for the previous product version as we have moved on to a new version of our Earth-System-Model, namely MPI-ESM-LR V 1.1. Using that version, we in particular found that much of the spurious ice directly at the ice edge that we had identified with the previous version of our model has disappeared (Fig. 44 a vs. b). This might be a reflection of changes in the oceanic mixing scheme that more realistically distributes the nudged sea-surface temperature distribution, causing a better representation of the observed ice edge in the assimilation simulation.

Regarding the changes between SICCI 1 and SICCI 2, a major improvement of the compatibility of the SICCI product with model physics comes about by the improved algorithms of SICCI2. This is visible by comparing in particular the difference between the assimilation simulation and SICCI data for SICCI 1 unfiltered versus SICCI 2 unfiltered (Fig. 44 b vs. d), both evaluated against our new model version MPI-ESM-LR 1.1. SICCI 1 contained large areas where sea-ice concentration was clearly incompatible with model physics, for example in between Svalbard and Scandinavia. In contrast, in SICCI 2, the unfiltered version shows far less differences between the model simulations and the satellite record. These are usually located along coast lines and near the ice edge, where issues such as grid interpolation become important. The 50 km resolution SICCI 2 product contains a band of sea ice between Greenland and Iceland that is not compatible with model physics. This band of sea ice is absent in the 25 km resolution product. Other than that, the difference between the low-resolution and the medium-resolution product are small. We have not been able yet to successfully assimilate the 12.5 km unfiltered product into our model.

The provision of a version containing both filtered and unfiltered version came about in response to feedback from CMUG that the unfiltered, original product contains sea ice in areas where no sea ice can be found on physical grounds. While such sea ice would usually not affect the use of the data for climate-model evaluation or initialisation studies, it nevertheless made the earlier product appear less reliable than comparable products. This is despite the fact that this apparent

CMUG Phase 2 Deliverable

Reference: D3.1: Quality Assessment Report
Due date: June 2017
Submission date: 21 December 2017
Version: 4



lack of reliability indeed came along with a more honest representation of the possible limitations of the underlying algorithms. In particular, the unfiltered product contains values for sea-ice concentration that lie outside of the physical bounds from 0 to 100 %, which allows data-assimilation schemes a possibly more reliable representation of the model-data mismatch.

In comparing the simulation with our new model version for the old and the new product of CCI sea-ice concentration, we see comparably little overall long-term impact of the filtering (middle row versus bottom row in Fig. 44). Some ice is removed by the filter along coast lines, and the band of spurious ice between Greenland and Iceland is removed in the 50 km product. Other than that, on the multi-year average that we consider here, the filtering is of limited impact. Note, in particular, that the filtering might for individual time steps remove actually existing ice for example near the ice edge, such that use of the filtered data in climate-model application might give misleading results. Hence, as stated above, from a climate-research perspective we very much welcome the inclusion of the unfiltered data, which the experienced user can then combine with the filtered data according to their own needs.

Regarding resolution, the different products show a different distribution of observational uncertainty, with a clear tendency to higher uncertainty for the high-resolution 12.5 km product. This is probably related to the fact that this product includes information from the 89 GHz channel of the AMSR satellites, which is significantly affected by weather noise. The products at 25 km and 50 km resolution at first sight show a fairly similar distribution of observational uncertainty. There does not seem to be a distinct advantage of the 50 km product, despite its use of a 6 GHz channel that should be quite insensitive to atmospheric noise. Our model at present cannot fully exploit the information content of the 12.5 km and the 25 km product, as our model grid resolution usually is below these values. We can hence not reliably evaluate a possible advantage of the higher-resolution product for higher-resolved model simulations.

Regarding the shorter observational period, this came about by an agreement between ESA and EUMETSAT that the ESA CCI product will be based on the AMSR satellites, which only cover the period from 2002 onwards, with a gap of several months during the shift from AMSR to AMSR-2 in 2011. EUMETSAT provides data based on the SMMR and SSMI satellites in their OSI-SAF project, covering the period from 1979 until today. Note that many of the insights gained during the ESA-CCI project have informed the development of the recent OSI-SAF product, which hence profited substantially from the ESA-CCI developments. However, from a climate-research perspective the much shorter time series of the official ESA CCI product severely limits its usefulness. Indeed, except for use as initialisation data in seasonal prediction studies we currently do not believe that the higher reliability of the CCI sea-ice concentration time series can compensate for the drawbacks that stem from its short length, at least not for the rather coarse model resolution that is typical for most current climate models. This will likely lead to rather limited use of this time series by the climate-model community in the foreseeable future, until models become standard that employ the higher native resolution that underlies the SICCI product. Note, in particular, that the native resolution of OSI-SAF is around 50 km, which is then upsampled to 25 km. In contrast, the native resolution of the SICCI 25 km product is indeed 25 km. For the time being, however, because of the greater length of the OSI-SAF product, it is well possible that the major impact of the SICCI work on current climate research will not carry the SICCI name in it, but will be hidden behind the label OSI-SAF.



3.8.5 Update on CCI sea-ice thickness product

At the time of writing in May 2017, no new CCI sea-ice thickness product is available.

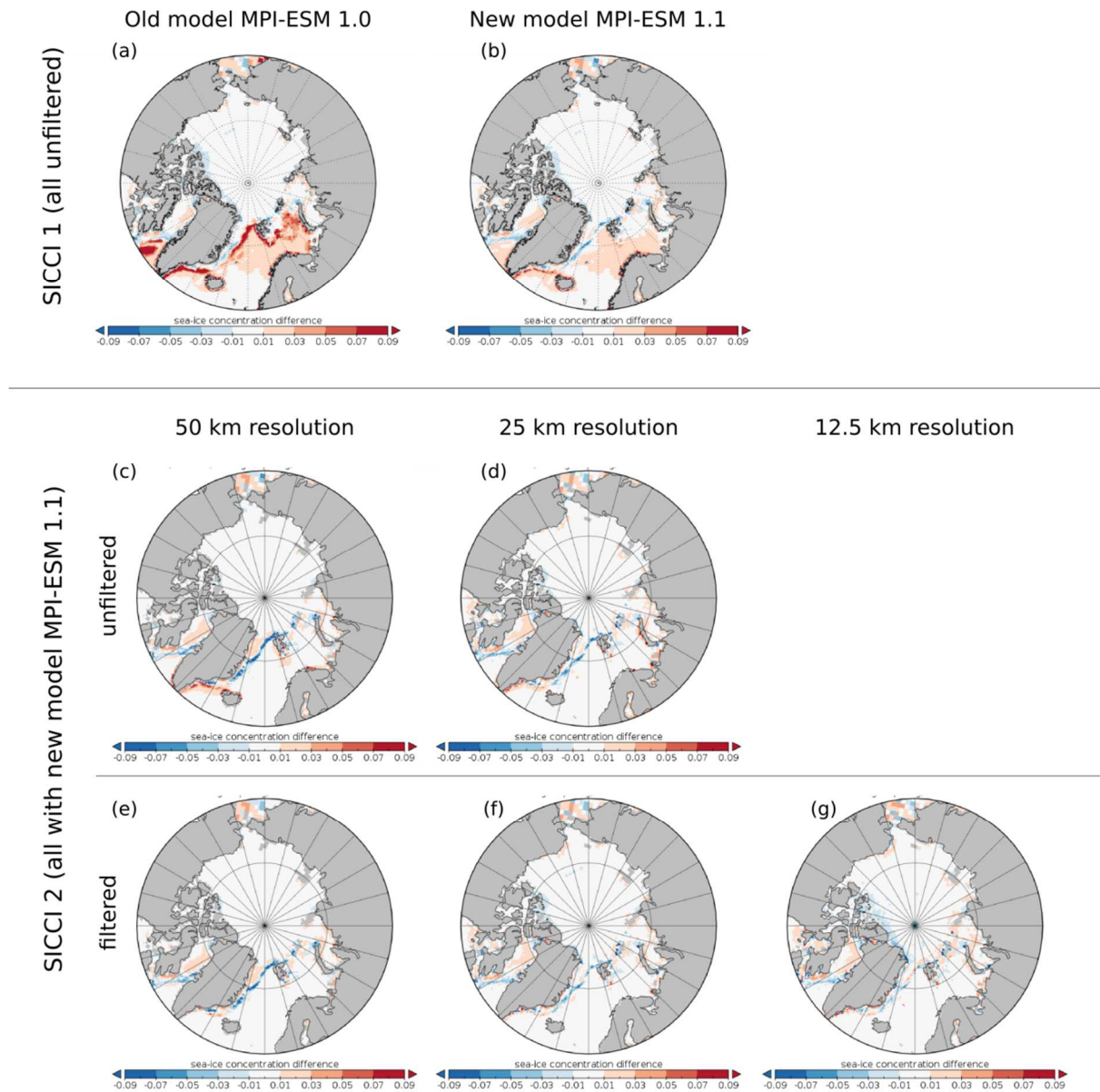


Fig 44: Difference in March sea-ice concentration between the model assimilation and the satellite retrieval. Negative (blue) values indicate that the satellite retrieval contains less ice than the model simulation. The panels show the multi-year mean difference of March sea-ice concentration for the period 2003 to 2008.

CMUG Phase 2 Deliverable

Reference: D3.1: Quality Assessment Report
Due date: June 2017
Submission date: 21 December 2017
Version: 4



3.9 Cross-Assessment of Aerosols, Cloud and Radiation CCI ECVs [WP3.7]

The results presented in this Section were completed in 2016 and there is no update to them in this report.

Aim

The aim of this work package is to complement the work of the Aerosol CCI Climate Research Group by providing a cross-assessment in the ESA CCI ECVs and in the CMIP5 climate models. We also aim at providing an improved process understanding by performing additional, more-detailed studies with the global aerosol model EMAC. The following scientific questions shall be addressed:

- What is the interrelation between different aerosol, cloud and radiation ECVs in CCI data and Earth System Models?
- How do the CMIP5 models perform in comparison to a more detailed aerosol global model (EMACMADE) in the representation of processes related to aerosol-radiation and aerosol-clouds interactions?

Summary of Results

A first working version of the EMAC model, coupled with a new version of the aerosol sub-model MADE (MADE3) has been set up. The MADE3 sub-model is able to simulate the main aerosol microphysical processes, such as nucleation, condensation and coagulation, as well as the equilibrium between the gas and the aerosol phases. In the current version of EMAC-MADE3, it is also possible to calculate aerosol optical properties using the aerosol quantities calculated by MADE3 (particle number, mass and radius) combined with pre-calculated lookup tables of optical parameters. This allows us to couple MADE3 to the radiation scheme of the model. An additional coupling of MADE3 to the cloud scheme (including aerosol interactions with liquid, mixed-phase and ice clouds) is currently being developed and will be used to perform the planned experiments if a working version is available by the end of the project.

Several test simulations have been conducted with the new model system. Using the ESMValTool, which is being developed within WP5.1, the model has been extensively evaluated by comparison with several observational datasets, including the ESA-CCI aerosol products for aerosol optical properties. In particular, we compared the simulated aerosol optical depth (AOD) at 550 nm against the ESA-CCI satellite products (Figure 45). The simulated AOD is higher than that derived from ESA-CCI satellite measurements, especially over the southern oceans, which may indicate too high sea spray emissions, and in East Asia, where an incorrect estimate of the input emissions may play a role. As mentioned in the previous quarterly report, however, differences exist also in the observational data, e.g. when comparing the ESA product with MODIS. Furthermore, deviations

CMUG Phase 2 Deliverable

Reference: D3.1: Quality Assessment Report

Due date: June 2017

Submission date: 21 December 2017

Version: 4



in the simulated AOD compared to measurements are common also in other models. The relative error of MADE3 in this experiment is comparable to or smaller than those of other global models.

In order to perform a full transient simulation with EMAC-MADE3 and to compare its performance to that of the CMIP5 models, a similar emission setup has been developed, covering the period 1950-2010. It makes use of the MACCity inventory, which builds on the original CMIP5 emission data, but considers yearly-resolved emissions (using a linear interpolation between the decades) and a sector-specific seasonal cycle based on RETRO. This should allow a more precise representation of the emissions with respect to the CMIP5 models, which is particularly important for aerosol and aerosol precursors given the relatively short lifetime of these species.

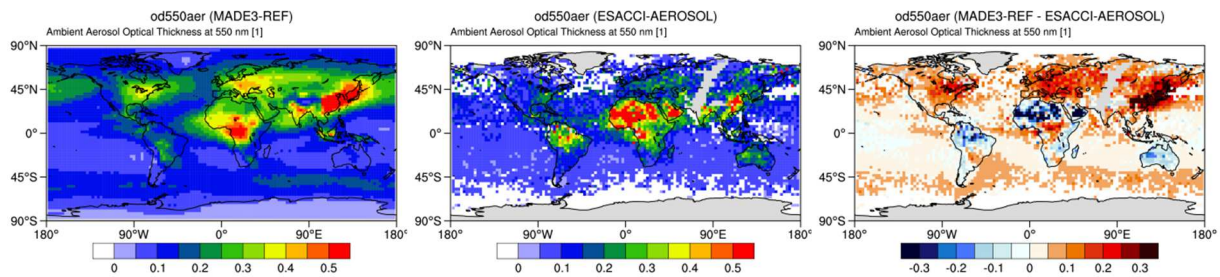


Figure 45: aerosol optical depth at 550 nm ($od550aer$) as simulated by EMAC-MADE3 (left panel) and from the ESA-CCI satellite product (middle panel). The right panel shows the difference model minus observations. Average values for the year 2001 are depicted in all panels.

CMUG Phase 2 Deliverable

Reference: D3.1: Quality Assessment Report
Due date: June 2017
Submission date: 21 December 2017
Version: 4



3.10 Cross assessments of clouds, water vapour, radiation, soil moisture for regional climate models [WP3.8]

The results presented in this Section were completed in 2016 and there is no update to them in this report, subsequent research in this area was redirected to WP 3.14.

Aim

The aim of this work package is to make an integrated assessment of ECV's related to regional moisture processes - clouds, soil moisture, precipitation and water vapour, to assess their consistency for African monsoons and European rainfall as simulated by regional climate models. The assessment will include an estimation of the usability of the corresponding CCI uncertainties. It will address the following scientific questions:

- How do the CORDEX regional climate models simulate cloudiness and soil moisture for the African and European regions?
- Are observed soil moisture and extreme precipitation relationships captured by regional climate simulations at different horizontal resolutions?
- Investigate moisture related feedbacks in observations which are important in the African monsoon development. This involves local feedback mechanisms, lagged regional correlations in time and space and large scale forcing.
- Identify key processes in regional climate models affecting the simulated rainfall and monsoon systems that can lead to improvements in their representations in the climate simulations.

Key Outcomes

For Europe,

- The observed variabilities of CCI cloud cover, CCI soil moisture (SM) and EOBS precipitation are consistent over Europe and suitable for climate model evaluations. The regional model anomalies are of similar magnitude as the observed anomalies.
- The climate model output (SM and Clouds) differ in absolute values compared to the observations. For SM it is due to difference in what is possible to compare, for cloudiness it is due to observational and model errors, as listed in the 3 points below.
- SM-CCI absolute values representing the top 2cm cannot be compared directly to model fields (see SM FAQ <http://www.esa-soilmoisture-cci.org/node/136>). However, comparisons of absolute values can help to identify seasonal model shortcomings. For comparisons with models, the model data should be sampled in time and space according to the availability of the satellite data (also stated in SM FAQ).
- Cloud-CCI prototype data v1.4 cloud cover is overestimated over North Atlantic and Mediterranean Sea. Feedback to the Cloud-CCI team has led to changes in thresholds for the cloud mask, which has improved the cloud cover in the final v2.0 data.

CMUG Phase 2 Deliverable

Reference: D3.1: Quality Assessment Report
Due date: June 2017
Submission date: 21 December 2017
Version: 4



- ERA-Interim underestimate cloud fraction in southern Europe. The regional climate model HCLIM agrees better with the satellite observations.

For Africa,

- The observed variabilities of CCI and other satellite datasets and surface based observations are consistent over Africa and suitable for climate model evaluations.
- Cloud-CCI and other cloud satellite data reveal that cloud cover in the CRU surface observations have “country shaped” errors.
- CCI Cloud prototype data v1.4 overestimate cloud cover over sea for latitudes north and south of 20°, here the Mediterranean Sea and Southern Ocean (improved for v2.0).
- RCA4 overestimate clouds over seas compared to the satellite observations, for regions with thin clouds as the stratocumulus region off the African west coast and cloudiness over sea East of Africa horn.

Summary of Results

The work so far for WP3.8 include evaluation of cloudiness, soil moisture and precipitation simulated by two Regional Climate Models (RCMs) utilizing the ESA CCI data soil moisture remote sensing product (Wagner et al., 2012) and CCI-clouds (prototype v1.4, Stengel et al 2013) and EOBS precipitation (Haylock et al 2008). In addition we use satellite cloud data from CLARA-A1 (Caspar et al 2009) and PATMOS-x (Heidinger et al 2014) and land surface based cloud data from CRU (Haylock et al 2008). Simulations were performed using two different RCM systems, the Rossby Centre Regional Climate model (RCA4) and a climate version of the non-hydrostatic meso-scale modelling system HARMONIE (HCLIM). Both models are driven by ERA-Interim (ERA-Interim, Dee and co-authors, 2011) lateral boundary fields of winds, temperature and humidity and sea surface temperature, every six hours.

All comparisons have been made for monthly mean values. Since the CCI-SM data is available on daily bases with spatial and temporal gaps, we used a simplistic simulator interpolating the regional models daily values of soil moisture to the observational grid. A daily mask represented by the grid boxes which have valid CCI-SM values was applied to the interpolated model SM fields. From these daily values monthly mean values were calculated for the RCM's and CCI-SM, respectively.

HCLIM over Europe

The aim is to evaluate moisture processes for Europe in the high resolution model HCLIM for a 30 year, 6km horizontal resolution simulation (work not yet completed). Here, we show preliminary results from a four year (2003-2007) HCLIM simulation at 15km horizontal resolution over Europe (Figure 46). An example of the co-variability of the moisture related variables is shown for the Mediterranean region in Figure 47. Time series of absolute values (left column) and de-seasonalised anomalies (monthly mean removed, right column) are shown for cloudiness, precipitation and soil moisture.



ESA CCI SM monthly mean May 2003

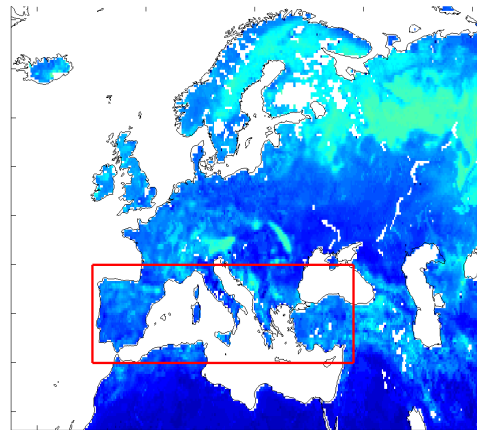


Figure 46: Map of the HCLIM area, the red box show the region for the time series in Figure 32.

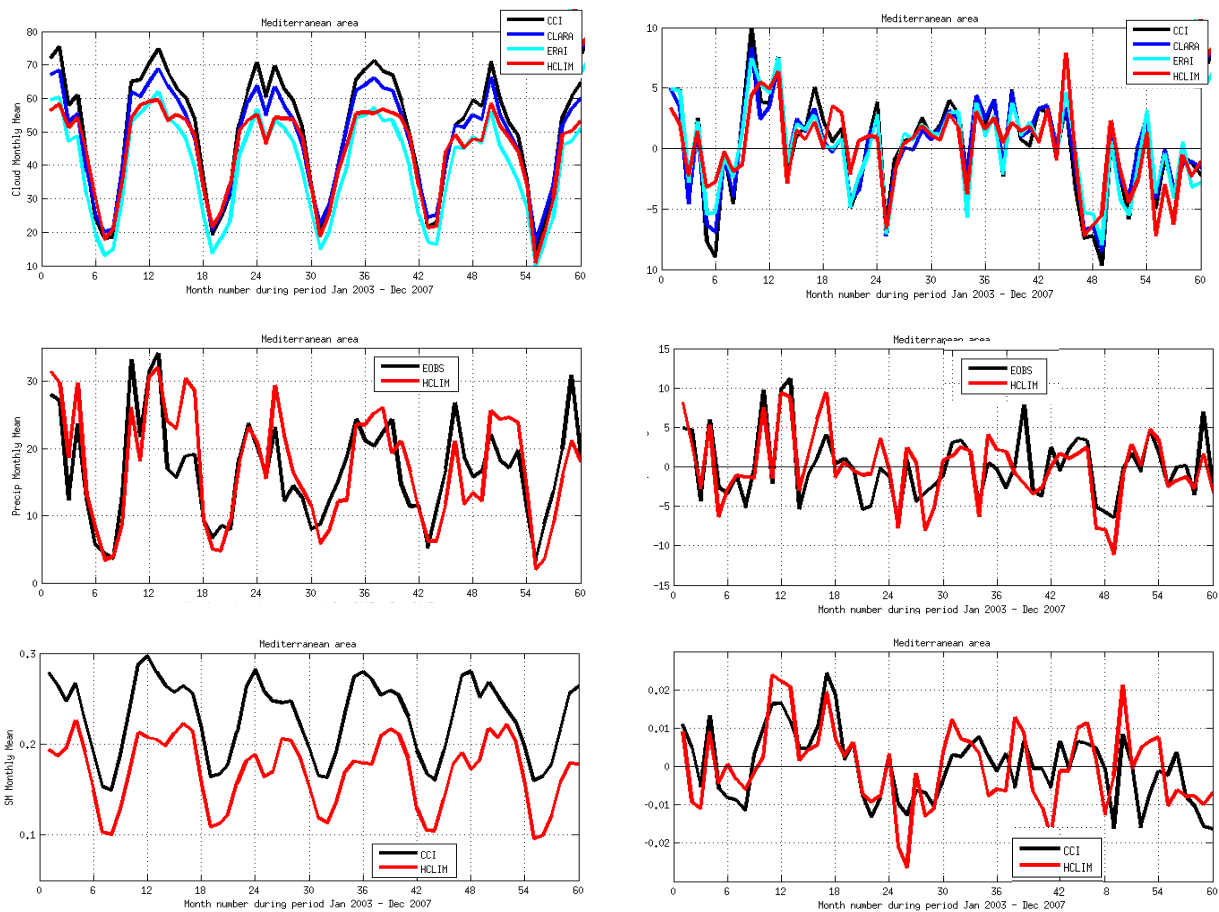


Figure 47: Monthly mean time series 2003-2007 for the Mediterranean region marked in the previous figure. Left column show absolute values for clouds (top), precipitation (middle) and soil moisture (bottom). Right column shows de-seasonalised anomalies for clouds (top), precipitation (middle) and soil moisture (bottom). Black lines CCI data, red lines HCLIM, blue lines CLARA data and cyan lines ERA-Interim.

CMUG Phase 2 Deliverable

Reference: D3.1: Quality Assessment Report
Due date: June 2017
Submission date: 21 December 2017
Version: 4



The different observations show consistent variations in time with higher cloud fraction, precipitation and soil moisture in winter and lower values in summer (left column). The regional model anomalies are of similar magnitude as the observed anomalies (right column). Both observations and model anomalies have the wettest winter 2003/04 and the driest 2006/07.

ERA-Interim underestimate cloud cover all year but especially in autumn to spring (top left), as also found in other studies for Southern Europe (Calbó et al 2016). HCLIM is similar to ERAI and does not manage to produce more clouds than ERAI, except in summer when the regional model is less influenced by the inflow from the lateral boundaries. Both HCLIM and ERAI reproduce the observed cloud monthly variability (right top panel) but HCLIM has smaller variations than observed. Cloud-CCI v1.4 overestimate cloud cover over the Mediterranean Sea compared to CLARA and PATMOS-x data (top left) and over the Atlantic (not shown). This issue was reported to the Cloud-CCI team and was found to be due to too low thresholds over sea in the Neural Network cloud mask. In the latest v2.0 Cloud-CCI data the cloud cover bias over sea has been reduced.

HCLIM surface scheme has three layers of soil moisture, here we used the top 1cm to compare with the satellite observation. SM-CCI absolute values representing the top 2cm cannot be compared directly to models as known (<http://www.esa-soilmoisture-cci.org/node/136>). However, comparisons of absolute values can help to identify seasonal model shortcomings. As an example we note SM-CCI has a peak value each December while the simulated SM peaks later during the spring (lower left panel). This model SM bias can be explained by an overestimation of precipitation in spring as seen in the middle left panel in Figure 47. Further analysis into the moisture ECV's relationships will be made for the longer simulation.

CORDEX RCA4 simulations over Africa

The analysis of African monsoon and relationships between clouds, precipitation and soil moisture, in observations and CORDEX (Coordinated Regional Climate Down-scaling Experiment) simulations is ongoing. Here, we show examples comparing cloud cover from different observational data sets and RCA4 (Strandberg et al., 2014) run at 50 km horizontal resolution for the time period 1982-2010 driven by ERA-Interim and different CMIP5 models at the lateral boundaries.

The East African Monsoon is associated with the ITCZ moving south of the equator. The so-called long rains prevail during spring (MAM) and the short rains during autumn (OND). The transition season (JFM) bring most rainfall and cloudiness to East Africa. Figure 48 show the mean cloud fraction for January to March for the satellite observations, Cloud-CCI, CLARA, PATMOS-x and land surface observations CRU and three reanalysis datasets (ERAI, MERRRA2 and JRA25). For now, we use CLARA as the reference cloud data set, since the Cloud-CCI prototype data v1.4 has some known errors, the analysis will be remade for the final phase 2 Cloud-CCI v2.0 dataset. All

CMUG Phase 2 Deliverable

Reference: D3.1: Quality Assessment Report

Due date: June 2017

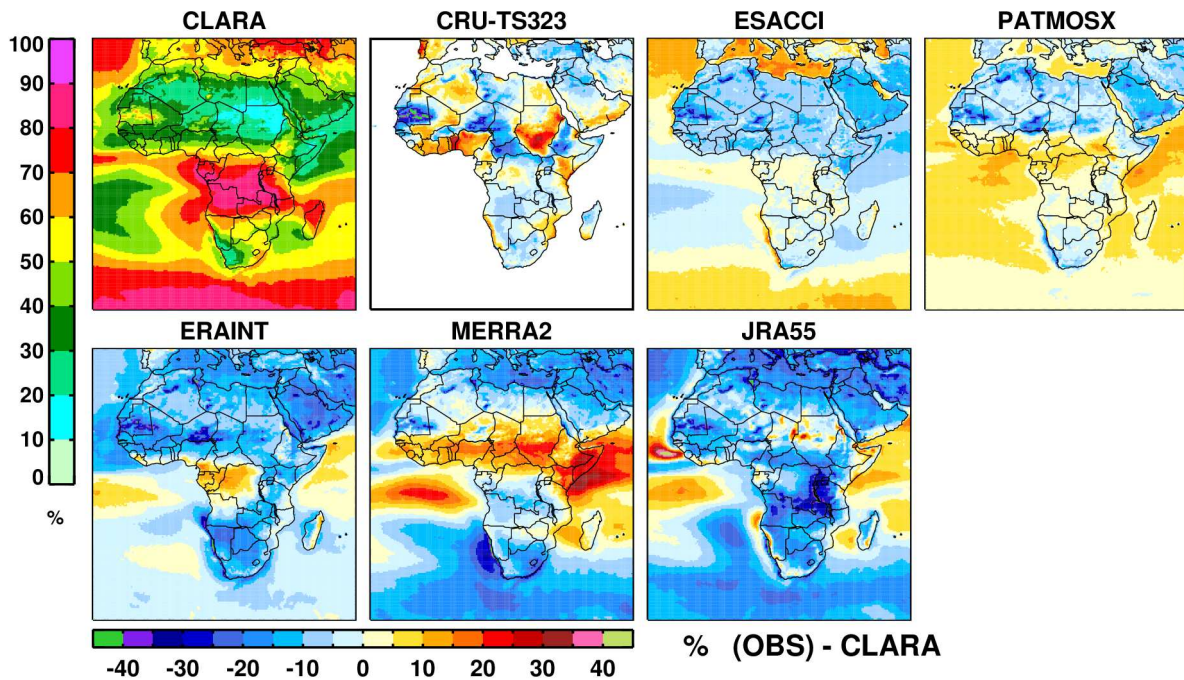
Submission date: 21 December 2017

Version: 4



observational datasets have a maximum in cloud cover over East Africa consistent with the region of large amounts of rainfall. The reanalysis models underestimate the East-African cloud cover maxima, ERAI being closest to the observations.

Cloud Fraction (clt) | JFM | 1982-2012 | AFR-44



Cloud Fraction (clt) | JFM | 1982-2012 | AFR-44

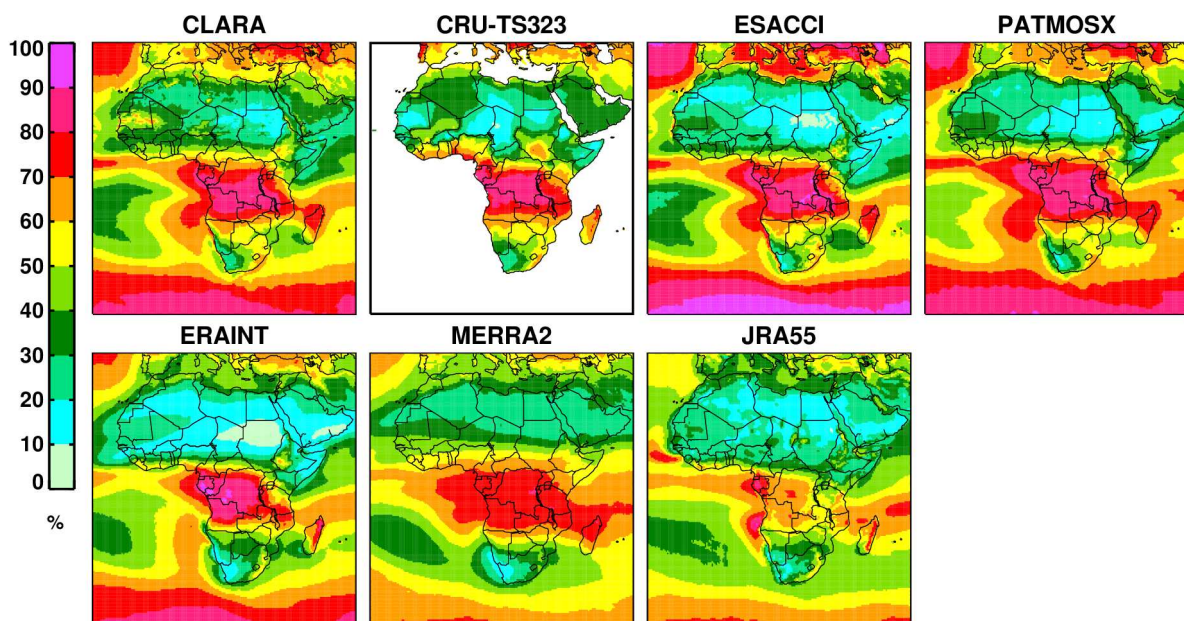


Figure 48: Top panel: Cloud fraction for observations and reanalysis over Africa. Bottom panel: CLARA cloud fraction and differences for satellite and reanalysis data compared to CLARA. All figures for January-March 1982-2012 (%).

CMUG Phase 2 Deliverable

Reference: D3.1: Quality Assessment Report
Due date: June 2017
Submission date: 21 December 2017
Version: 4



We note some problem regions for CRU, Cloud-CCI and CLARA cloud fraction. CRU surface observations have “country shaped” differences compared to CLARA (Fig 48 lower panel) and compared to the other satellite and reanalysis data sets (not shown). CCI Cloud prototype data v1.4 overestimate cloud cover over sea for latitudes north and south of 20°, as seen here over the Mediterranean Sea and Southern Ocean. The biases have been reduced in the latest Cloud-CCI v2.0 datasets. CLARA cloud cover is about 10% smaller than Cloud CCI, PATMOS and the reanalysis over Sahel and the desert regions in North Africa. This could be due to problems over-detecting clouds over desert surfaces for CLARA.

Figure 49 (top panel) show the cloud fraction for CLARA and the bias for RCA4 driven by ERA-Interim and 10 CMIP5 GCM models (resolution 200-300km) at the lateral boundaries. RCA4 overestimate clouds over sea; for the stratocumulus region off the African west coast and for seas East of Africa horn, the biases are very similar for all RCA simulations indicating problems with RCA thin cloud formation over sea that needs to be looked into. RCA4 driven by ERAI has the smallest bias over land compared to RCA4 driven by the atmosphere-ocean coupled CMIP5 models and the highest correlation compared to the observations (lower panel). This is expected since the coupled model climate do not reproduce the climate of a certain year, for coupled models other statistics is needed. To compare directly with the observations we will evaluate RCA4 driven by CMIP5 AMIP simulations (GCM's driven by observed SST and Sea-Ice at the lower boundary) which can reproduce the climate natural variability. We will also extend this study to include all moisture variables and other CORDEX RCM's for the final CMUG QAR report.

Quality relevant outcomes (updates from CMUG QAR 2015)

We found from these preliminary results assessing CCI SM and cloud cover that both variables are of “climate quality”. CCI clouds and soil moisture are consistent on a regional scale. Listed below are some remarks and recommendations for the individual variables and some general thoughts on observed versus modelled soil moisture.

Cloud-CCI Quality

The Cloud-CCI prototype data v1.4 was obtained directly from the Cloud-CCI team in December 2015, some issues were found and are listed below. These issues have been corrected and reduced in the final version that will be available summer 2016 from ftp://ftp-cmsaf-projects.dwd.de/ESA_Cloud_CCI/CLD_PRODUCTS/L3C/.

- Cloud-CCI prototype data had too much cloud fraction over sea compared to other satellite data (CLARA, PATMOS) and models (ERA-Interim, EC-Earth) as communicated to the Cloud-CCI team and since improved in the latest v2.0 dataset.
- For the NOAA satellites there are overlapping L3C data for same time periods. What is the Cloud-CCI recommendation on how to make one single time series, to minimize the drift and any artificial trend?

CMUG Phase 2 Deliverable

Reference: D3.1: Quality Assessment Report
 Due date: June 2017
 Submission date: 21 December 2017
 Version: 4

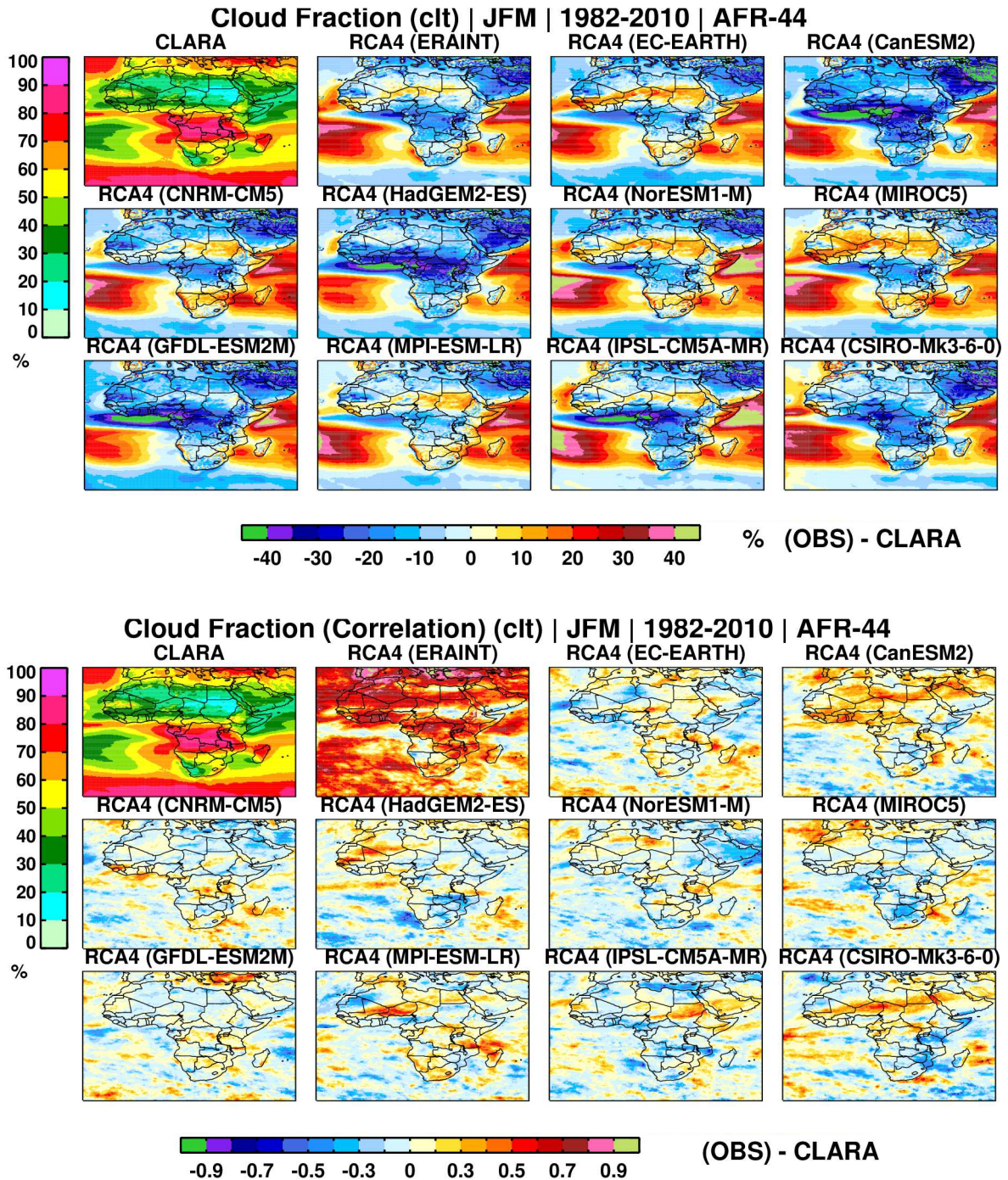


Figure 49: Top panel: Cloud fraction for CLARA and differences RCA4 (driven by ERA-Interim and 10 CMIP5 models) - CLARA. Bottom panel: CLARA cloud cover and correlation CLARA and RCA4 cloud cover. All figures for January-March 1982-2010 (%).

CMUG Phase 2 Deliverable

Reference: D3.1: Quality Assessment Report
Due date: June 2017
Submission date: 21 December 2017
Version: 4



SM-CCI Quality

The Frequently Asked Questions on the SM website (<http://www.esa-soilmoisture-cci.org/node/136>) was very useful. **It is recommended that a FAQ page be set up for all CCI ECVs, and any bugs can be listed under known issues/errors.** The following points should be added to the SM FAQ to avoid misuse under ‘Do’, ‘Don’t’ or ‘Data usage in models’.

- Do not compare (or take care when comparing) your model total SM directly with these products, the satellite observes the top ~2cm”.
- Any model data should be masked (“simplistic simulator approach”) when compared to the observations. This is indirectly implied in the spatial and temporal availability SM FAQ's. It was less important in this study but for other regions and time periods the differences can be much larger. Any user comparing with model data should strongly be recommended to do mask the model data.
- It would be useful to have a presentation similar to that presented at the CMUG 5th integration meeting available at the FAQ link or somewhere else at the website.

General thoughts on satellite and model soil moisture comparisons

The CCI-SM represents a very shallow layer corresponding to approximately the top two centimeters of the soil, however, the observed depth depends on the soil moisture content (deeper for drier soils). It is not easy to characterize this top soil layer but in many regions it is some combination of active or dormant vegetation mixed by some dead vegetation material mixed with mineral soil. In the model, depending on the exact parameterization applied, the top SSM layer may be purely mineral soil or some weighted value between mineral soil, soil carbon and vegetation material.

As stated on the CCI-SM web page “the statistical comparison metrics like root-mean-square-difference and bias based on our combined dataset are scientifically not meaningful. However, the CCI SM products can be used as a reference for computing correlation statistics or the unbiased root-mean-square-difference”. This would support the anomaly analysis of SM in the 2015 CMUG Quality Assessment Report (CMUG 2015), although the absolute simulated SM values are sometimes at the uncertainty limit of the CCI-SM. The most important soil moisture in models is represented by the layer occupied by roots since this is the soil moisture limiting the transpiration. Methods do exist which can be used to integrate CCI-SM in time to reach a soil moisture representing a thicker layer but assumptions, sometimes difficult to control, are needed for such methods. CCI-SM can be nudged or assimilated in a land-surface model to compile a deep soil moisture product but such a product will always be model dependent and must be used carefully when compared to other models. **A soil moisture product representing the degree of saturation rather than volumetric soil moisture would limit, or even exclude, any model dependence. We argue that such a product is preferable.** The SM team at the CMUG 5th integration meeting informed that such products are planned to be made, we support that work.

CMUG Phase 2 Deliverable

Reference: D3.1: Quality Assessment Report
Due date: June 2017
Submission date: 21 December 2017
Version: 4



3.11 Cross assessments of ESA CCI glacier, land cover and sea level data for hydrological modelling of the Arctic Ocean drainage basin [WP3.9]

Aim

The aim of this study is to assess the use of the CCI Glacier and Land cover data in hydrological modelling of the Arctic Ocean drainage basin. The main underlying question is if the use of CCI Glacier and Land cover can improve hydrological models and simulated river runoff to the Arctic Ocean. The current assessment is focused on the usefulness of the data as input for model parameterization, initialization, and evaluation compared to pre-cursor datasets, as well as on the 'climate quality' of the products in terms of understanding long term trends and seasonal variation in the Arctic hydrological system. In addition, we evaluate the suitability of ESA – CCI Land cover data to derive the location of irrigated areas for hydrological modelling at global scale.

Use of Land cover and Glacier data in the Pan-Arctic hydrological model Arctic-HYPE

A pan-arctic application of the hydrological model HYPE (Hydrological Predictions for the Environment) developed by SMHI (e.g. Lindström et al., 2010; Arheimer et al., 2012) is used in the analysis. The model is based on a semi-distributed multi-basin approach, with each river basin divided into sub-basins, and each such sub-basin divided into a set of soil-type/land-cover classes. The model domain includes the land area draining into the Arctic Ocean (excluding Greenland) and covers 23 million km², divided into 32,599 sub-basins with an average size of 715 km² (see further on). The model simulates processes including for instance accumulation and melt of snow and glaciers, evapotranspiration, surface runoff, and drainage from individual soil layers, routing in lakes and rivers, and accumulated water discharge through the mouth of each sub-basin. Arctic-HYPE version 2.5 was developed without any CCI data using GlobCover 2004-2006. A first model version 3.0 based on CCI data was developed during 2015-2016 including information from CCI Land cover (v1.4) and CCI Glacier (Randolph Glacier Inventory, RGI v4.0). Included in the current analysis is also some initial assessments of CCI Land Cover v1.6 and RGI v5.0.

Land cover information is used in the partitioning of the hydrological model sub-basin areas into the runoff-generating sub-units representing unique combination of soil types and land cover types. The original land cover data is re-classified to a smaller number of classes in order to represent only the most important hydrological responses and processes. The current land cover classes in Arctic-HYPE are: lake, glacier, urban, wetland, crops, forest, open vegetation, and bare soil. This may be a oversimplification, since we know for instance that different types of forest tend to grow in different hydrological and permafrost conditions (deciduous needle leaf and evergreen needle leaf, respectively). It should be noted that land cover classes are fixed and their areal extent cannot be changed during the HYPE model simulation. The exception is the glacier land cover class, for which the glacier covered areal fraction is calculated based on the glacier ice volume (see further below). **Lakes and rivers** are given special attention in HYPE: surface water area can be separated

CMUG Phase 2 Deliverable

Reference: D3.1: Quality Assessment Report

Due date: June 2017

Submission date: 21 December 2017

Version: 4



into rivers, lakes on the main river course, and internal lakes connected to the main river through local rivers. The outlet of the major lakes are used in the delineation of the river network and sub-basins, and their position is thus crucial for the basic understanding of the hydrological system. The internal lakes are important for the runoff from the sub-basin areas to the main river network, and characterization of the number of lakes and their size distribution can be further used for analysis of variation in hydrological response. However, none of the land cover data used in Arctic HYPE (neither GlobCover nor CCI land cover) contains information to separate surface water area into rivers and lakes. Lake polygons from the Global Lake and Wetlands Database (GLWD) are used to identify the major lakes situated on the main river network, whereas the remaining water area from the land cover data is considered as internal lakes in the model sub-basins. To illustrate the impact of this assumption, the river area is separated from the internal lake area by a simplified approach based on a buffer zone around the Hydro1k and HydroSHEDS flow lines.

Irrigation plays a crucial role in water management around the world. According Portmann et al. (2010) at 25% of the global harvest areas are irrigated. Therefore, many hydrological models including HYPE (e.g. Lindström et al., 2010; Arheimer et al., 2012) has specific parameterizations to simulate the role of irrigation on the water cycle, where water is extracted from surface water bodies or ground water aquifers and applied in the irrigated areas depending on the simulated plant water demand or pre-defined schemes. CCI land cover (v1.6) provides a specific class for irrigation: land-cover 20 “Cropland, irrigated or post-flooding” (Figure 50, blue). The CCI data on irrigated areas is assess using data from the Global Map of Irrigated areas (GMIA, Seibert et al, 2005), the Global Water Surface Explorer (Pekel et al, 2016) and USDS.

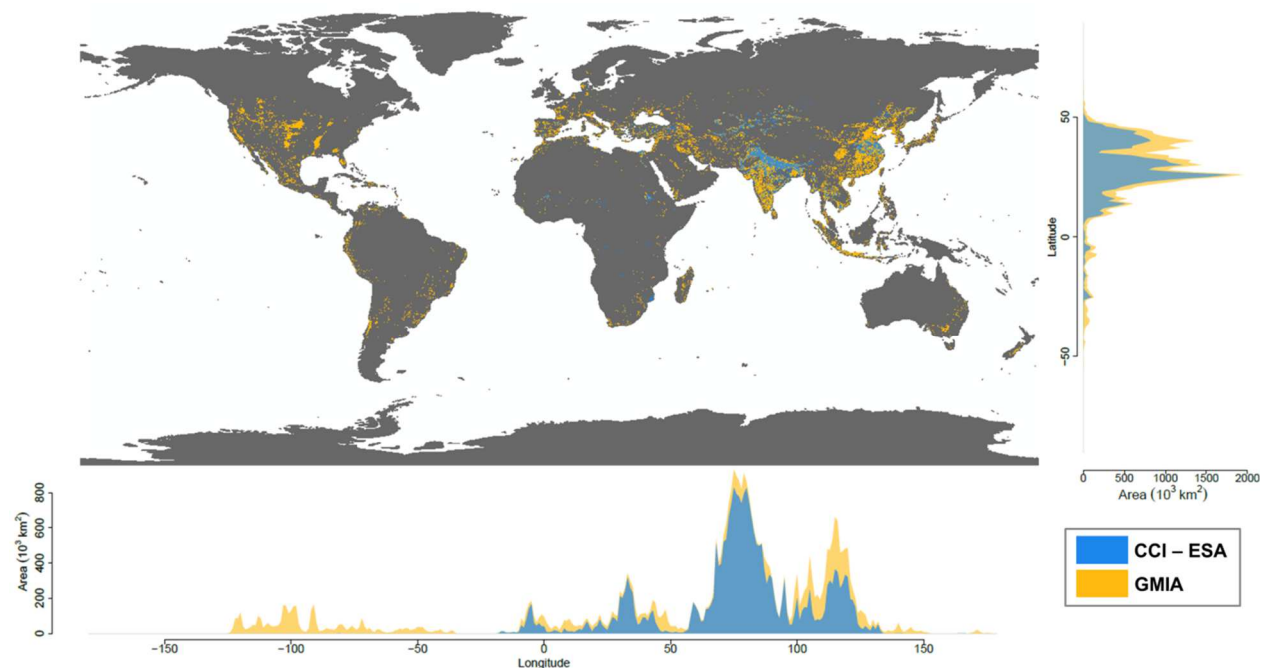


Figure 50. Global map with the location of ESA CCI v1.6 land-cover 20 “Cropland, irrigated or post-flooding”(blue) and GMIA (yellow.)

CMUG Phase 2 Deliverable

Reference: D3.1: Quality Assessment Report
Due date: June 2017
Submission date: 21 December 2017
Version: 4



The distribution of irrigated areas in the CCI land cover data compares well with GMIA over all continents except America where irrigated areas are completely lacking in the CCI product. The irrigated area is also larger in GMIA than in the CCI data in specific regions in India and China. However, there is also large areas where irrigation is missing the GMIA data compared to the CCI data, for instance along the Yangtze and Ganges rivers. More results of this analysis is given in the summary section below.

Glacier information is used to initialize and parameterize a simplified glacier area and mass balance sub-model in HYPE, representing all glaciers within a hydrological model sub-basin by a single storage of ice. **Total glacier area** within each sub-basin is the main input information, whereas the **total glacier volume** is the main state variable in the model. Glacier area and volume is related using area-volume relationships following Bahr et al. (2015). The initial volume is calculated from the input glacier area, whereas during the simulation, the glacier area is updated as a function of the simulated glacier volume. In summary, there are at least 4 major issues related to glacier modelling in HYPE that has been assessed using the CCI Glacier data:

- The use of glacier area-volume scaling is actually not intended for dynamic modelling of individual glaciers, but rather for volume estimates of populations of glaciers. It has been suggested by the CCI Glacier scientific leader to instead use glacier models or glacier volume estimates by Huss and Farinotti (2012). On the other hand, the more simple area-volume scaling models might still be motivated for large-scale hydrological models, since the interest is mass balance and runoff generation of the population of glaciers within a river basin and not of individual glaciers. As a compromise for Arctic-HYPE v3 and later, the linear coefficients in the area-volume relationships are calibrated by fitting the total glacier volume per RGI zone to the values reported in Huss and Farinotti (2012). The glacier type data field in the RGI v4 was used to separate into glaciers and ice caps.
- When area-volume scaling is used, it should be applied on the individual glacier areas; otherwise the total volume will be different due to the non-linear properties of the scaling-functions. This poses a problem for the lumped model structure in HYPE where smaller glaciers within the same sub-basin are lumped together, and larger glaciers and ice caps covering several sub-basins are divided in smaller sections. This problem was solved using the RGI v4 glacier outlines by deriving sub-basin-specific corrections of the linear area-volume coefficients. The exponential coefficients are kept constant with different values for glaciers and ice caps, as discussed by Bahr et al., 2015).
- In previous versions of Arctic-HYPE (version 2.5 and earlier), the glacier area was derived from GlobCover's land cover class "Permanent snow and ice". First of all, this land cover class largely overestimate the glacier area (both using GlobCover and CCI Land Cover; Figure 51; Table 5), and obviously, land cover data does not provide information on individual glacier basis, which is needed for the area-volume coefficient estimations as described above - only the total area of (permanent snow and) ice.

CMUG Phase 2 Deliverable

Reference: D3.1: Quality Assessment Report
Due date: June 2017
Submission date: 21 December 2017
Version: 4



- A major issue is the problem of: How to initialize glacier area and volume for historical time periods? The mean year of the RGI v4 glacier outline source data is 1996 and the CCI land cover data is representing the period 1998-2012, whereas we would like to start model simulations around 1960. The World Glacier Monitoring Service (WGMS) provide annual glacier mass balance from a large number of glaciers, but still that information need to be generalized through some sort of modelling in order to be applied on all glaciers in the RGI database. The following method was developed solve this problem for the Arctic-HYPE model:
 - Used annual mass balance data from 74 WGMS glaciers within the Arctic-HYPE model domain (Figure 52). The data was used to derive statistical models for the annual glacier mass balance at any point in the Arctic-HYPE model domain as a function of a) a 9 year centered running mean of all annual mass balance data points within the same RGI zone plus b) a linear regression model for the annual deviation from the regional running mean taking into account annual precipitation and temperature
 - An example of the statistical annual glacier mass balance model from the RGI zone Scandinavia is shown in Figure 53.
 - The annual mass balance was integrated backwards to 1961 from the RGI source data year, for each glacier in the model to obtain the initial ice volume. In total over the Arctic-HYPE model domain, the initial ice volume increased only by 2% by this procedure. But there were large regional differences: For the regions Iceland, Svalbard and Western Canada/US the initial glacier volume increased by 5%, 10%, and 30% respectively, whereas for Scandinavia and North Asia the initial glacier volume decreased by 17% and 36%, respectively.

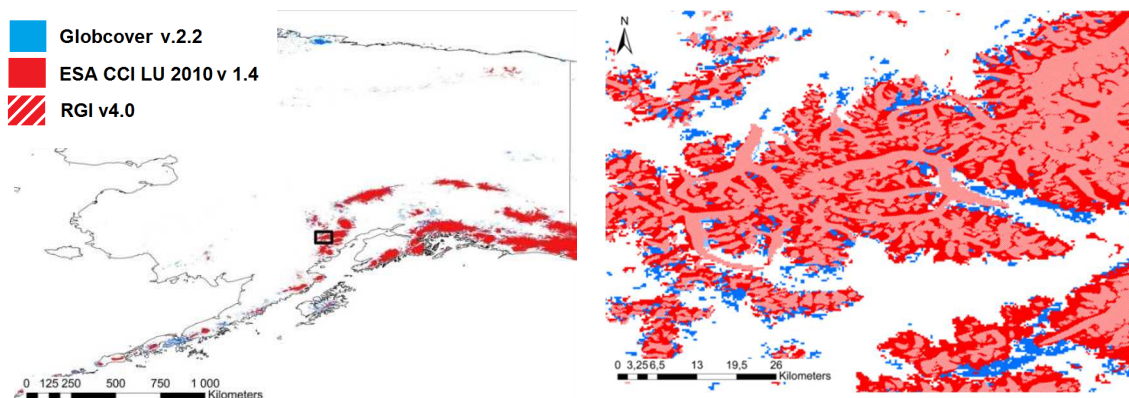


Figure 51: Comparison of glacier area in Alaska derived from CCI land cover and ESA GlobCover 2004-2006 (permanent snow and ice) and the glacier outlines from CCI Glacier (RGIv4).

Table 5: Glacier area in the Arctic-HYPE model per RGI region, comparing data from CCI glacier (RGI v4), Huss and Farinotti (2012), and estimations based on the land cover class “permanent snow and ice” in CCI land cover v1.4 and GlobCover 2004-2006.

CMUG Phase 2 Deliverable

Reference: D3.1: Quality Assessment Report

Due date: June 2017

Submission date: 21 December 2017

Version: 4



RGI region	All glacier areas		ArcticHYPE model domain			
	RGIv4	HF2012	Based on RGIv4		Based on LCv1.4	Based on GlobCover
	km2	% of RGIv4	km2	% of region	% of area based on RGIv4	
01 Alaska	86723	104%	10346	12%	140%	157%
02 Western Canada/US	14559	100%	2151	15%	325%	1711%
03 Arctic Canada North	104873	100%	104716	100%	123%	240%
04 Arctic Canada South	40883	100%	40875	100%	159%	265%
06 Iceland	11060	100%	11060	100%	101%	208%
07 Svalbard	33959	100%	33458	99%	117%	165%
08 Scandinavia	2851	100%	2268	80%	157%	131%
09 Russian Arctic	51592	100%	50844	99%	121%	229%
10 North Asia	3435	82%	1613	47%	235%	860%
Total	349934	101%	257330	74%	130%	242%

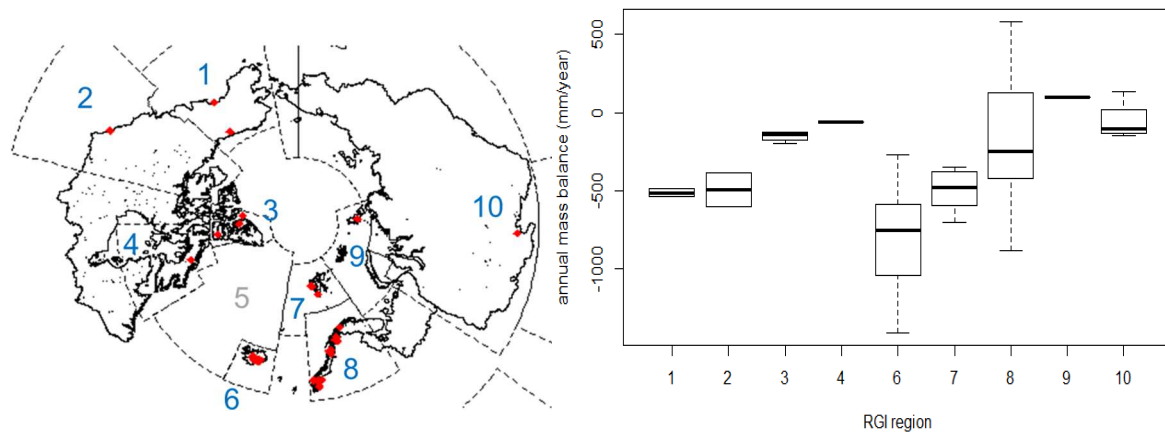


Figure 52: Left: Location of 74 WGMS glaciers with mass balance data within the Arctic-HYPE model domain and RGI regions 1-10 (Greenland zone 5 excluded from the model), Right: average annual glacier mass balance per RGI region.

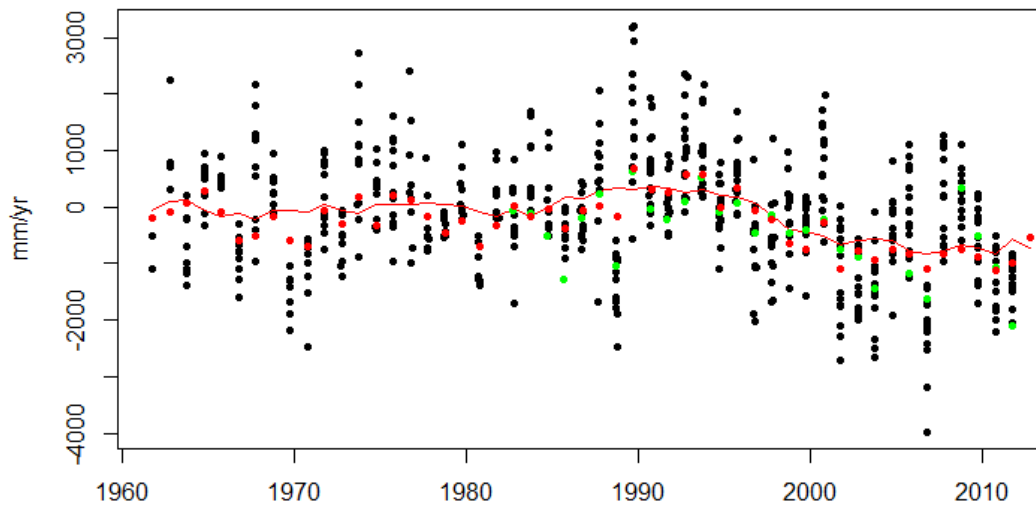


Figure 53: Annual glacier mass balance data from WGMS database for all glaciers in RGI zone 8 (black dots) (Scandinavia), simulated and observed for one of the glaciers (green and red dots, respectively) and the centered running average using a 9 year window (red line).

Summary of Results

CCI Glacier

CCI Glacier data (Randolph Glacier Inventory, RGI v4 and v5) was found to be very useful for evaluating and improving the setup of the glacier sub-model in the Arctic-HYPE model, especially in combination with additional information from other data on glacier mass balance (WGMS) and glacier volume (Huss and Farinotti, 2012):

1. The use of CCI glacier data drastically changed the total area of glaciers compared to previous model versions. Glacier area estimated from the class “permanent snow and ice” from CCI Land cover v1.4 and GlobCover 2004-2006 was found to overestimate the glacier area derived from RGIv4 by 30 % and 140 %, respectively (Figure 51; Table 5).
2. The individual RGI (v4) glacier areas and glacier type information were used to calibrate the area-volume scaling parameters used in the Arctic-HYPE model, by fitting the total glacier volume per RGI region in the Arctic area versus regional glacier volume estimates from Huss and Farinotti (2012).
3. Furthermore, the RGI data enabled the derivation of basin specific corrections of the area-volume scaling coefficients to correct for errors in the volume estimation when lumping or dividing individual glaciers by the hydrological model sub-basin delineation.
4. Compared to estimates with the scaling parameters used in Arctic-HYPE version 2.5, the new scaling parameters implies a decreased glacier volume by 8% when applied on the individual RGI glacier areas for all glaciers in the arctic RGI regions (Table 6). However, when applied on the total glacier area within the Arctic-HYPE sub-basins, the area-volume

CMUG Phase 2 Deliverable

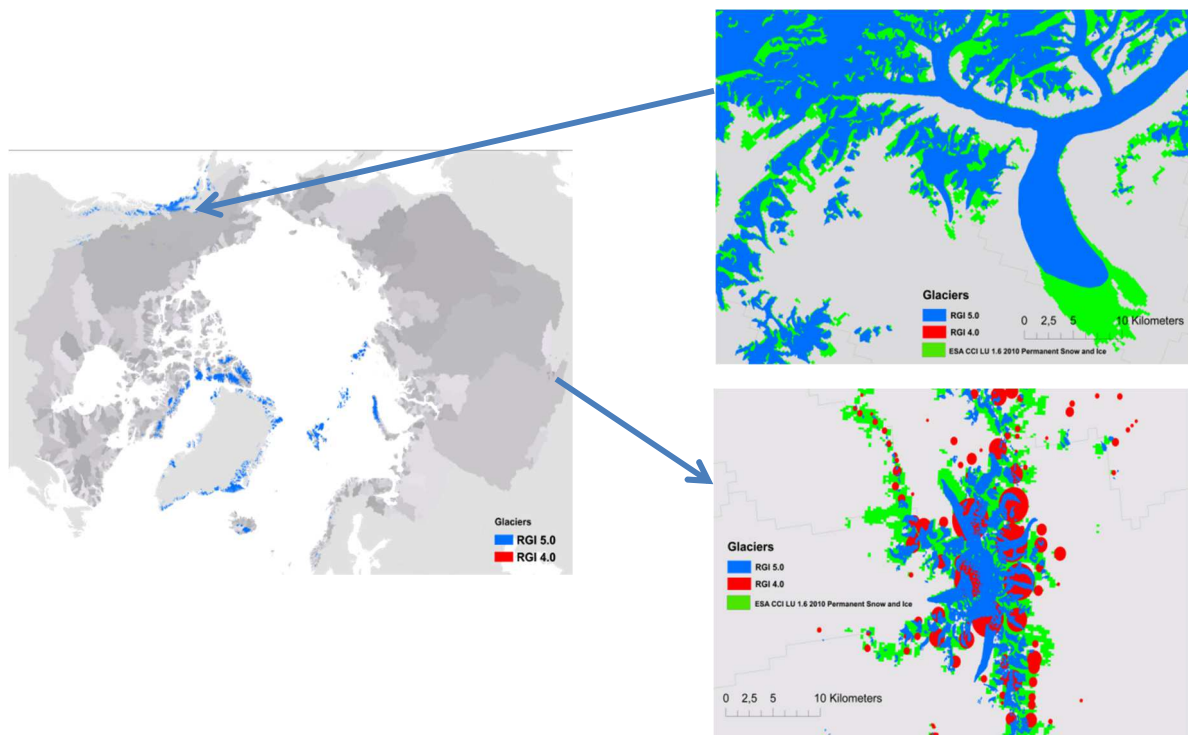
Reference: D3.1: Quality Assessment Report
Due date: June 2017
Submission date: 21 December 2017
Version: 4



scaling resulted in a 37% overestimation of the total glacier volume if the new sub-basin corrections without the scaling parameters.

5. If the overestimation of glacier area in previous model version is also taken into account, the total overestimation of glacier volume in previous model version was even larger (44%, Table 4).
6. RGI glacier outlines could probably also be further used for improving sub-basin delineation following the glacier outlines. The data also includes additional information that could be further used to improve the glacier sub-model parameterizations: mean, maximum and minimum elevation, slope and length, as well as the detailed hypsography, but none of these potential values of the CCI glacier data have been assessed yet.

A first preliminary analysis of RGI v5 showed substantial improvements in North Asia, where previously many glaciers were only marked by a circle area without a real outline (Figure 54). Previous glaciers outlines were also improved and many of them shifted laterally in this region – some glaciers rather large shifts. It has not been not assessed if these updates have been adopted in the CCI Land cover data v1.6.



CMUG Phase 2 Deliverable

Reference: D3.1: Quality Assessment Report
Due date: June 2017
Submission date: 21 December 2017
Version: 4



Figure 54: Comparison of Glacier area derived from CCI Glacier (RGI v4 and v5) and CCI Land cover 'permanent snow and ice' v 1.6. Glaciers with unknown outline but known existence and known area were represented by circles in RGI 4.0 (example in lower right panel from upper part of River Ob basin).

CMUG Phase 2 Deliverable

Reference: D3.1: Quality Assessment Report
 Due date: June 2017
 Submission date: 21 December 2017
 Version: 4



Table 6: Glacier volume estimated for RGI regions in the arctic region and in the Arctic-HYPE model per RGI region, comparing data from Huss and Farinotti (2012) with data estimated by area-volume scaling with glacier areas based on CCI glacier (RGI v4), CCI land cover v1.4 and GlobCover 2004-2006.

RGI region	All glacier areas			Arctic-HYPE model domain			
	HF2012	Area-volume scaling based on RGI v4		Area-volume scaling Based on RGI v4			Based on Land Cover v1.4
		Calibrated parameters	Reference parameters	calibrated	calibrated	reference	reference
	km3	% of HF2012		subbasin corrected	uncorr.	uncorr.	uncorr.
	km3	% of sub-basin corrected		km3	% of sub-basin corrected		
01 Alaska	20402	99%	118%	2112	153%	182%	212%
02 Western Canada/US	1025	96%	115%	109	298%	356%	1463%
03 Arctic Canada North	34399	101%	94%	34705	123%	114%	127%
04 Arctic Canada South	9814	97%	79%	9476	134%	114%	210%
06 Iceland	4441	103%	61%	4555	104%	62%	74%
07 Svalbard	9685	95%	80%	9015	166%	140%	155%
08 Scandinavia	256	99%	78%	216	200%	148%	276%
09 Russian Arctic	16839	99%	74%	16516	158%	112%	133%
10 North Asia	140	118%	141%	71	288%	344%	922%
Total	97001	99%	92%	76777	137%	116%	144%

CCI Land cover

CCI land cover v1.4 was compared to the precursor data GlobCover 2004-2006 with regard to differences in land cover distribution. The “climate quality” of the information in the land cover time series (2000, 2005, 2010) was of special interest, since the on-going changes in the Arctic regions (mainly climate related) are expected to be expressed for instance in the distribution of vegetation, surface water, and snow and ice. Furthermore, a initial assessment was made comparing CCI land cover v1.4 and v1.6 for the Arctic region.

Results to date:

- More surface water area in CCI Land cover data sets compared to the pre-cursor GlobCover 2004-2006):
 1. Arctic-HYPE water surface area based on CCI Land cover v1.4 increased with about 6-20% compared to the precursor based on GlobCover 2004-2006 (Figure 55), with ranges depending on how the land cover data was combined with the GLWD lake vector data. This is a very important improvement for understanding Arctic hydrology which is dominated by large rivers and a large number of small and large lakes. The total water body area in the Arctic domain further increased with about 1% from v1.4 to v1.6.

CMUG Phase 2 Deliverable

Reference: D3.1: Quality Assessment Report

Due date: June 2017

Submission date: 21 December 2017

Version: 4



2. More realistic distribution and higher resolution of water bodies in CCI Land cover v1.6:
3. CCI Land cover v1.6 includes a new water body mask with higher spatial resolution (150m), which represented small lakes and river outlines much realistically than v1.4.
4. The new 150 m resolution water mask has also been re-sampled in the v1.6 300 m land cover products with similar improvements in the representations of water bodies compared to v1.4 (Figure 56).
5. By vectorizing the water body pixels, statistics on number of lakes and lake size distribution within the hydrological model sub-basins were further used to regionalize lake runoff generating parameters, which was helpful for improving the river discharge simulations in the model.

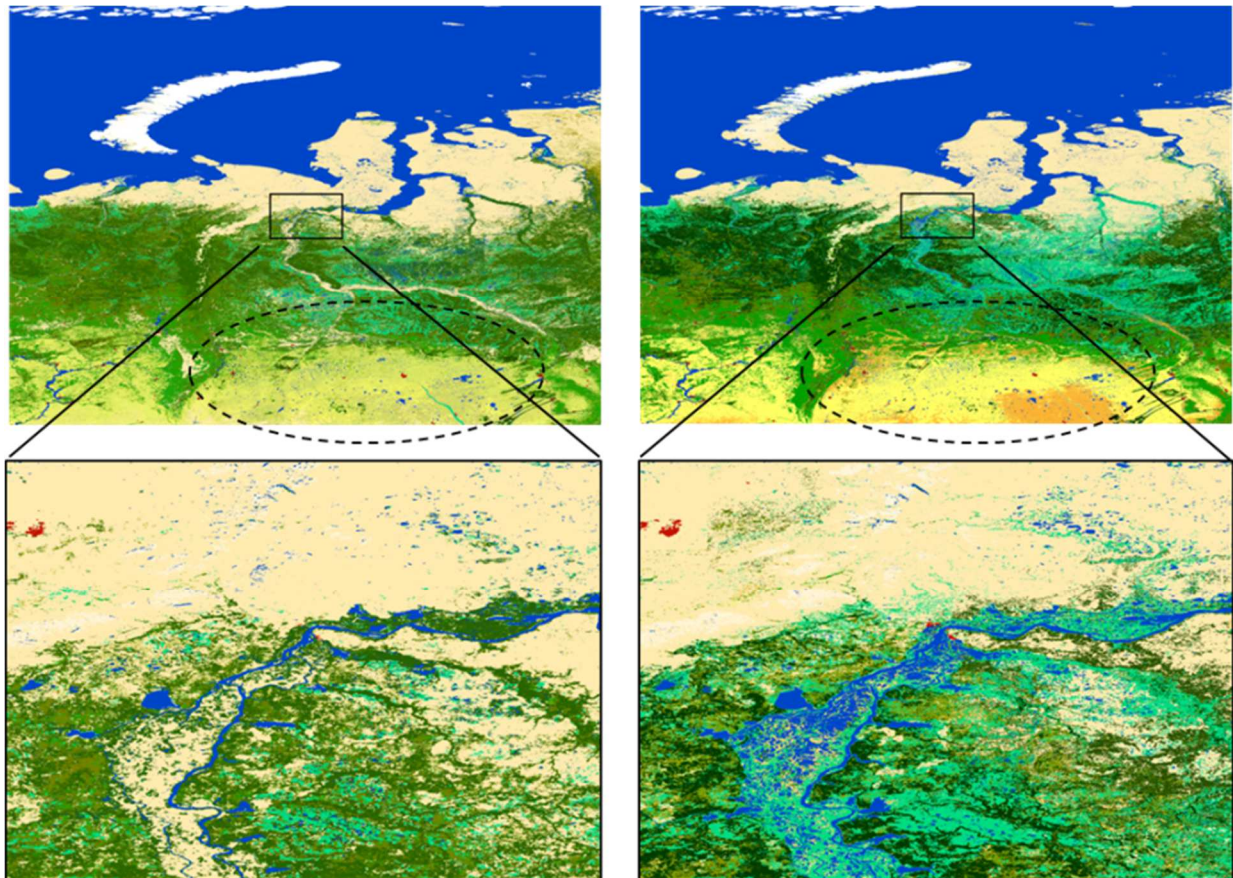


Figure 55: Land cover data from the area around the Ob River showing a clear increase in surface water area from Left: GlobCover to Right: CCI land cover.

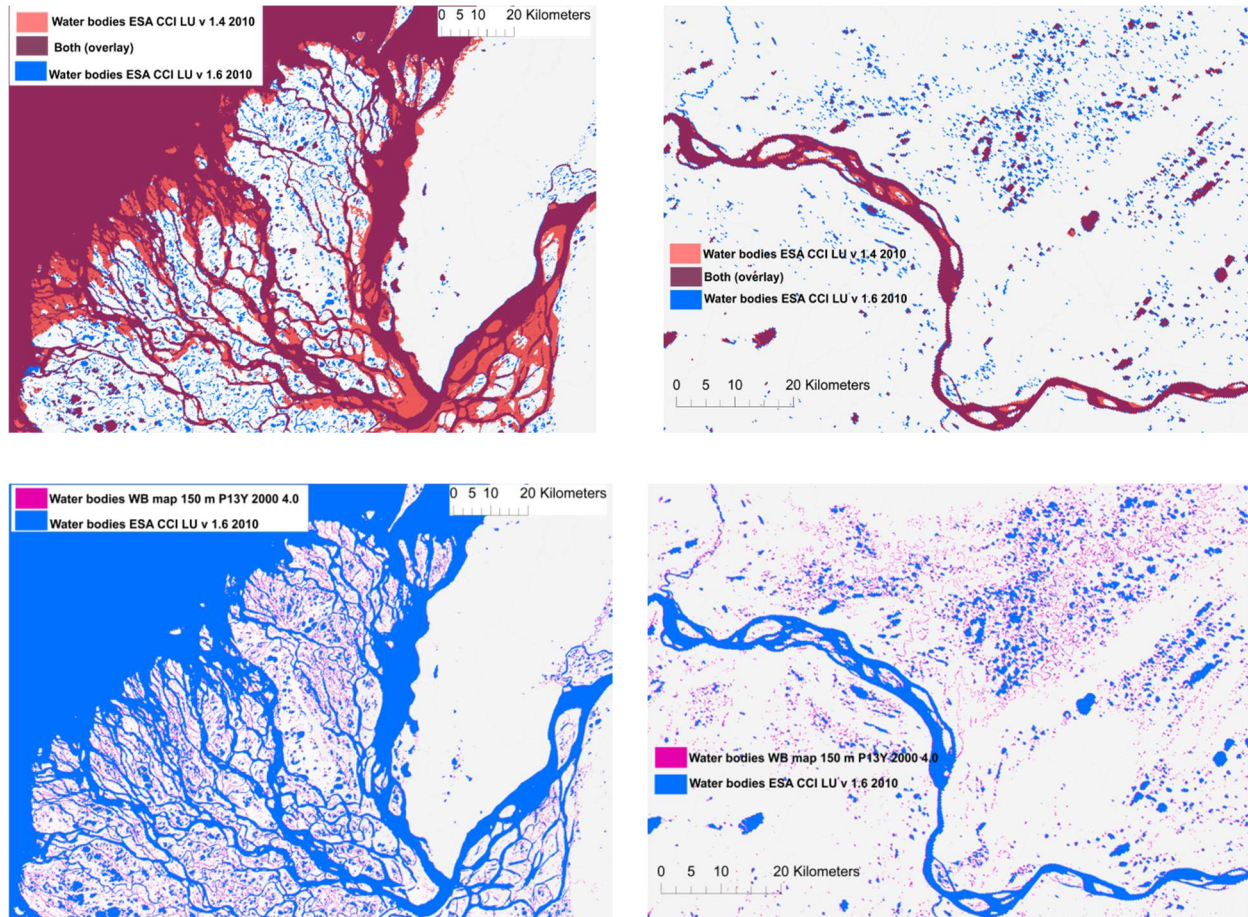


Figure 56: ESA CCI Land Cover Water bodies 2010 showing the difference between (top panels) v1.4 and (bottom panels) v1.6, as well as the difference between the 150 m resolution water body mask (ESACCI-LC-L4-WB-Map-150m) and the 300m land cover product in v1.6 (ESA CCI LU v 1.6), with examples from the Lena River delta (left panels) and the Mackenzie River (right panels).

- The class “water bodies” is constant throughout the three epochs and water bodies are not included in the seasonal products.
 1. From a “climate quality” perspective, it would be interesting to get information on the trends and seasonal variation in the spatial distribution of surface water. Variation in small water bodies is a relevant ECV related to permafrost melting, which is of highest interest in the Arctic region.
- The fraction of deciduous needle leaf trees was reduced in the latest epoch (2008-2012) compared to previous periods in eastern Siberia (based on v1.4, still to be evaluated in v1.6).
 1. Field observations suggest that this might be due to increasing precipitation during the period.

CMUG Phase 2 Deliverable

Reference: D3.1: Quality Assessment Report

Due date: June 2017

Submission date: 21 December 2017

Version: 4



2. This will affect the ‘climate quality’ of the land cover time-series data.
3. Analysis of relation to observed and simulated river discharge still to be analyzed.
4. Improved distribution of lichens and mosses in v1.6 compared to v1.4:
5. In Land cover v1.4 there was no lichens and mosses in the Eurasian part of the Arctic region. In v1.6 this is improved (Figure 56), mainly by replacing sparse vegetation and bare soils. Summarized over the entire Arctic-HYPE model domain, water bodies and lichens and mosses increased by 1% and 2% respectively, between v1.4 and v1.6, whereas sparse vegetation and bare soil classes were reduced by 1.5% and almost 1% respectively. There were also minor reductions in forests and other remaining classes (Figure 57).

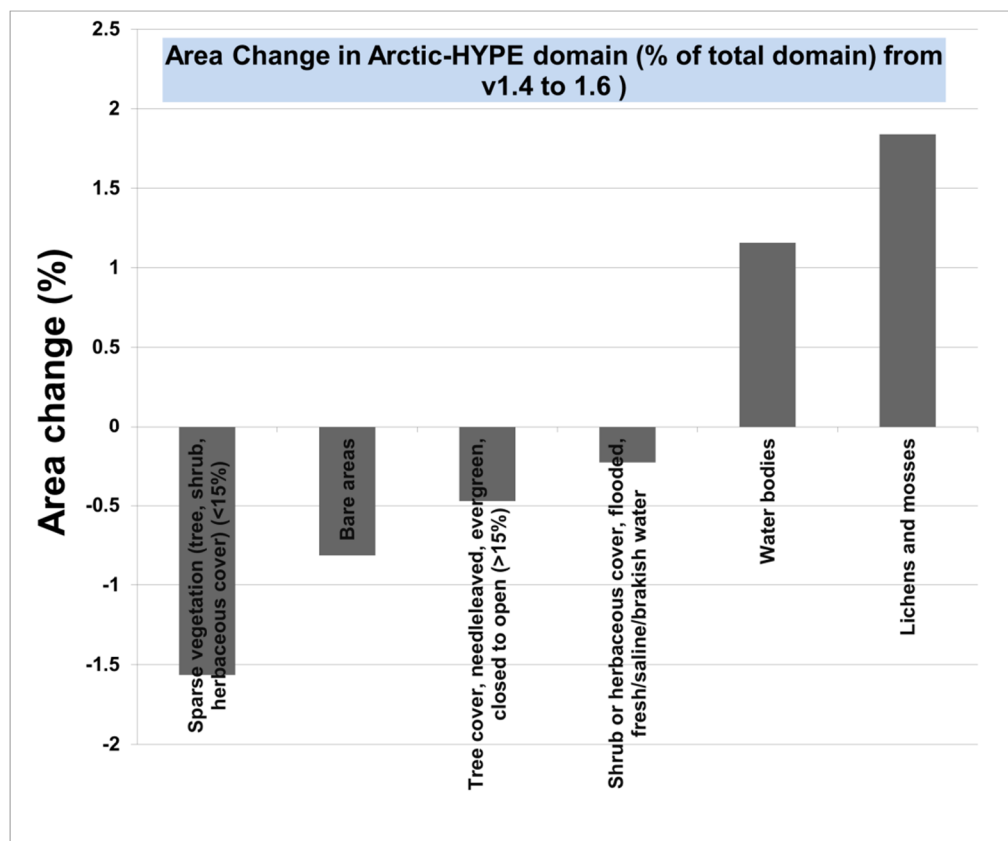


Figure 57: Changes in some aggregated land cover classes between CCI land cover v1.4 and v1.6, summarized over the Arctic-HYPE model domain.

CCI Land cover – Irrigated areas

The CCI land cover data on irrigated areas (“Cropland, irrigated or post-flooding”) was initially assessed versus the Global Map of Irrigation Areas (GMIA) published by Seibert et al (2005) (Figure 50). GMIA was developed by combining irrigation statistics for 10 825 sub-national statistical units and geo-spatial information on the location and extent of irrigation schemes and provides irrigated area on a 5 arc minute by 5 arc minute grid. The CCI data was upscaled to the GMIA resolution for quantitative comparison (Figure 58).

CMUG Phase 2 Deliverable

Reference: D3.1: Quality Assessment Report

Due date: June 2017

Submission date: 21 December 2017

Version: 4

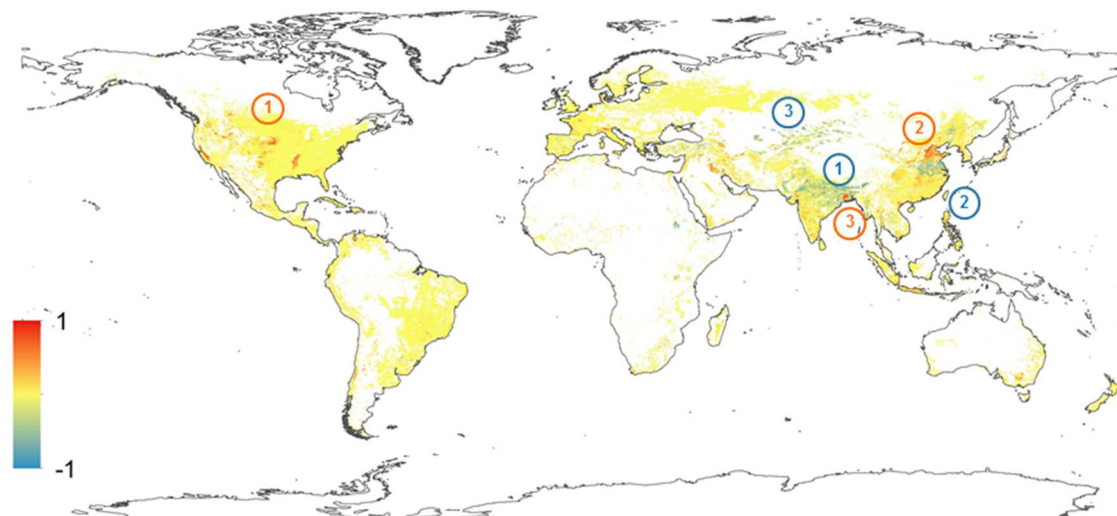


Figure 58: Global map with the differences between GMIA and “Cropland, irrigated or post-flooding” - CCI Land cover v1.6. Red pixels shows areas where irrigation from GMIA is greater than those proposed by CCI Land cover v1.6 and vice versa. Numbered circles indicate the location of the areas with the highest differences.

In many areas of the world, the difference between GMIA and the CCI Land cover irrigated areas is small, however there are some areas with large discrepancies indicated by numbered circles in Figure 43 and summarized in Table 7.

Table 7 Location of the mainly areas with high mismatches between irrigated area derived from CCI Land cover (v1.6) and GMIA.

	CCI-ESA > GMIA	GMIA > CCI-ESA
1	Riverbank of Ganges River	USA fields crops
2	Yangtze River mouth	Yellow River Mouth
3	Central Asia (Naryn River Basin)	Ganges Delta

Irrigation overestimation by CCI Land cover (v1.6) compared to GMIA

The tree selected areas where CCI land cover (v1.6) overestimates irrigation compared to GMIA are located in the surrounding of big rivers in Asia (Ganges, Yangtze and Naryn). Additional data for assessing this discrepancy was taken from the recently published Global Surface Water Explorer data (Pekel et al, 2016), which is based on the analysis of Landsat imagery 1984-2015.

CMUG Phase 2 Deliverable

Reference: D3.1: Quality Assessment Report

Due date: June 2017

Submission date: 21 December 2017

Version: 4

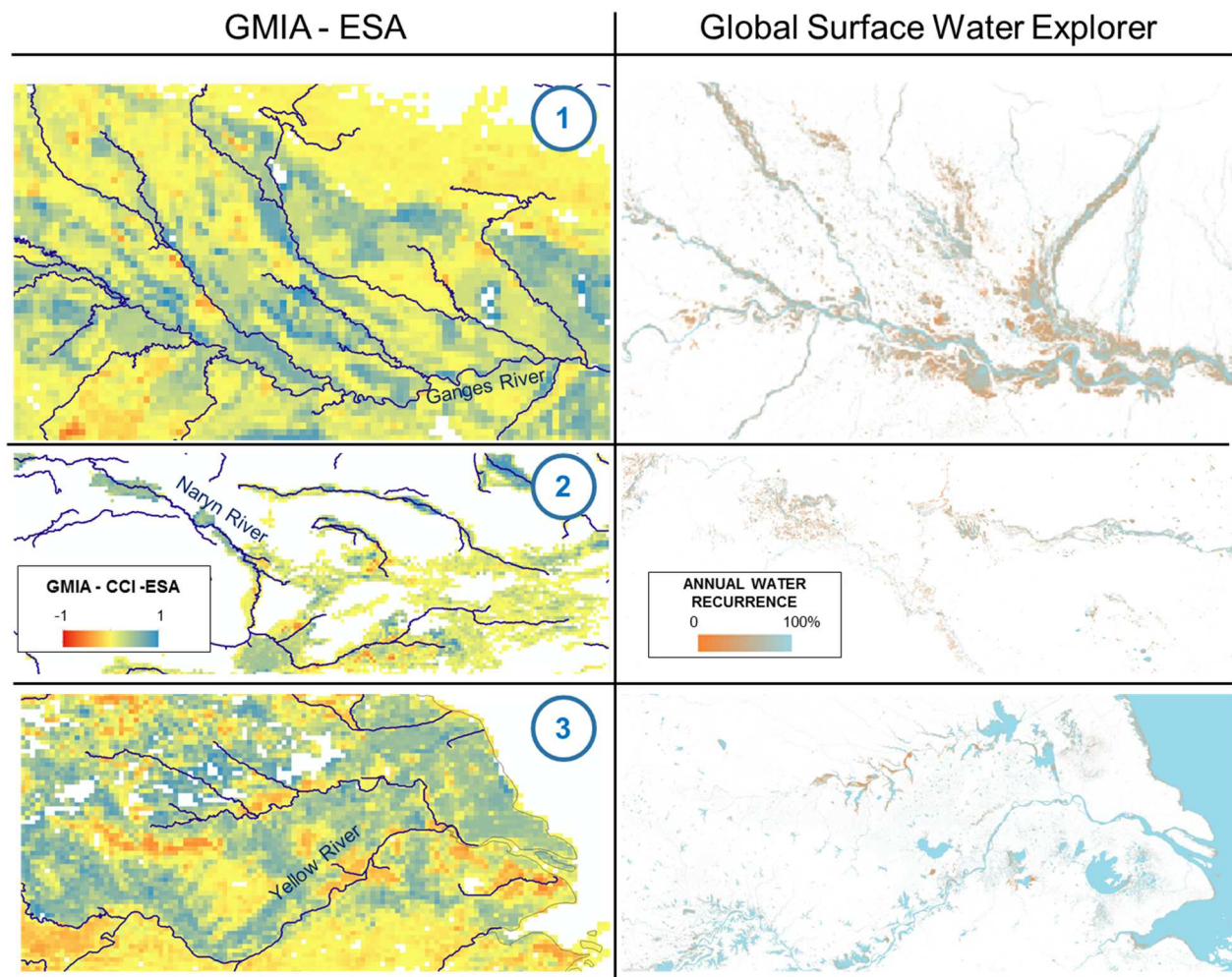


Figure 59: Comparison between the overestimation in irrigation in CCI-ESA (right column) compared with the annual water recurrence (Pekel et al., 2016) (left column) on the three selected areas.

Figure 59 compare the location of the selected areas where irrigated areas in CCI Land cover is larger than GMIA with the water annual recurrence product from the Global Surface Water Explorer (Pekel et al., 2016). In cases 1 and 2 there is a clear relation between these areas and areas where water is recurrently present according to the Global Surface Water Explorer. This can be explained by the fact that the CCI land cover (v1.6) in fact includes both post-flooding and irrigated areas in the same category. In case 3, the study region is one of the main Chinese rice producers between 10000 and 20000 thousand of ton in 2014 (Clauss et al., 2016). Rice is a crop that usually grows in post-flooded areas. However, the Global Water Surface Explorer does not indicate the same amount of recurrent water presence in this area as in area 1 and 2.

Irrigation underestimation by CCI land cover compare to GMIA

The underestimation of irrigated areas in CCI Land cover compared to GMIA is located in agricultural areas of USA, China and India. In the two first cases, there are indicators that probe that they are irrigated areas (Census of Agriculture reported by USDA 2013, Clauss et al., 2016,

CMUG Phase 2 Deliverable

Reference: D3.1: Quality Assessment Report
Due date: June 2017
Submission date: 21 December 2017
Version: 4



respectively). Over the areas is also common to find in satellite images the characteristic circular and gridded patterns of irrigated fields. In the case of India there is not a clear understanding that why there is these mismatches between the two sources.

Quality relevant outcomes

- Disagreement between CCI Glacier and CCI Land cover:
 - The CCI Land cover class “permanent snow and ice” is larger than the glacier area derived from the glacier outlines in CCI Glacier - in total over the Arctic-HYPE model domain 30% too large (Figure 51; Table 5).
 - The CCI Land cover documentation reveals that the CCI Glacier outlines have been used to assign “permanent snow and ice” to all land cover pixels within the outlines – however, areas outside of the CCI Glacier outlines classified as “permanent snow and ice” have not been reset to “unclassified” or any other land cover class. In addition, the latest version of land cover (v1.6) does not seem to be updated to the latest version of glacier data (RGI v5).
 - Previous discussions with Science Leaders from CCI Glacier and Land cover confirmed that CCI glacier area was added to “permanent snow and ice”. It was suggested to include a sub-class under “permanent snow and ice” separating pixels under ice and other snow pixels. But as we can see, it has not been implemented yet in CCI LandCover v1.6.
- No ice thickness in CCI Glacier data (RGI v4 or v5):
 - Glacier thickness is not included in RGI even though estimates of each glacier exist based on modelling and observations (Farinotti and Huss, 2012).
 - The model estimates can be requested from the CCI Glacier team on request. However this information is not yet clear in the CCI Glacier documentation.
- No temporal information in CCI Glacier (RGI v4 or v5):
 - The RGI data provide the date of the source data, but information is still needed for proper initialisation of glacier models for previous time periods. Recommended practices on how to model historical glacier extents and volumes would be useful as an extension of the CCI Glacier.
- The need for a CCI Hydrography
 - Hydrography data (river network, sub-basin delineation, lake and water delineation, flow directions, man-made and natural diversions, dams, etc) is one of the most important inputs for hydrological models. Arctic-HYPE uses a polygon based partitioning of the landscape into sub-basins derived from digital elevation data (Hydro1K), vectorised lake delineation (GLWD) and discharge station metadata (location and upstream area). Other models uses gridded hydrography (Flow directions), but the importance for model development and evaluation is nevertheless essential. The most used datasets on the global scale are the USGS Hydro1K (1km² resolution) and only available below 60°N HydroSheds (90 m²

CMUG Phase 2 Deliverable

Reference: D3.1: Quality Assessment Report

Due date: June 2017

Submission date: 21 December 2017

Version: 4



resolution), which both provide hydrologically constrained digital elevation and flow direction data.

- Just like land cover, the river and lake network may change as a result of hydrological, climatological, morphological and anthropogenic processes. Both river morphology, flow directions, number and extend of lakes is changing in the Arctic region and in other regions of the world.
- The CCI Land Cover mask include excellent information of water bodies and the latest version 1.6 provide a major improvement of identified water bodies and spatial detail. However, water pixels are not linked to lakes and river network data. For instance, separating water pixels into lake and river pixels would be a important first step towards and improved usefulness of the CCI water mask data in hydrological modelling. The ultimate goal of a CCI Hydrography could be to contribute to a global high resolution hydrography dataset, including lakes and river outline data, and gridded hydrologically constrained elevation and flow direction data.

CMUG Phase 2 Deliverable

Reference: D3.1: Quality Assessment Report
Due date: June 2017
Submission date: 21 December 2017
Version: 4



3.12 Cross-assessment of CCI-ECVs over the Mediterranean domain [WP3.10]

Aim

The activity within the context of this Work Package is in some respect in the continuity of the Météo-France activity in the context of CMUG Phase 1. Its first main objective is to evaluate the performances (mean climate, variability and trends) of the Med-CORDEX regional climate system models (RCSMs) over the Mediterranean domain with a sub-set of atmosphere, marine and surface CCI-ECVs. A second objective is the evaluation of the consistency between CCI-ECVs through the analysis of a climate specific event (the 2006 heat wave) observed with the CCI-ECVs and possibly reproduced by a RCSM. Two scientific questions to address are the following: are the state of the art RCSMs able to reproduce observed Mediterranean climate trends and variability over the last decades? What are the potential coupled mechanisms between atmosphere, ocean and land that play a role on the characteristics of a climate specific event like a Mediterranean heatwave?

Summary of results

Sea level variability and trends

During CMUG Phase 1, the SSH simulated by the so-called CNRM-RCSM4 coupled regional climate model (Sevault et al., 2009) developed at CNRM and applied in the Med-CORDEX international simulation exercise, was confronted with the CCI Sea Level ECV and its precursor over the 1993-2010 period (see Phase 1 deliverable 3.1). Some results of this confrontation have been recently published in the scientific literature as part of a presentation of the evaluation of the ocean component of the CNRM-RCSM4 model (Sevault et al, 2014).

One main conclusion from this confrontation was that the CCI SSH is suitable for regional climate studies over the Mediterranean basin, even at a scale of a few tens of kilometres. The results of the model concerning trends of sea level change are encouraging. It also let some open questions concerning the way to facilitate the comparison between the modelled and observed sea levels. These questions come from the fact that climate models are not directly calculating the contributions to sea level changes that are due to mass changes implied by glaciers and ice sheet melting or by changes in continental water storage. In addition, in the specific case of regional climate models simulating the Mediterranean domain, the contribution to mass change in the Mediterranean Sea due to the mass flux at the Gibraltar Strait need also to be carefully taken into account.

Since the beginning of CMUG Phase 2, thanks to the development of a new version of the Mediterranean Sea model, and thanks to the availability of a new ocean reanalysis, it was possible to improve the comparison between the modelled and the satellite-derived SSH.

CMUG Phase 2 Deliverable

Reference: D3.1: Quality Assessment Report
Due date: June 2017
Submission date: 21 December 2017
Version: 4



The operational ocean reanalysis system (ORAS4; Balmaseda et al., 2013) has been implemented at ECMWF and it spans the period 1958 to the present. This makes this reanalysis suitable for MedCORDEX simulations since it can be used to constrain the oceanic component of a regional climate model in the Atlantic buffer zone over the ERA-Interim period (1980-2013). Contrary to the so-called COMBINE reanalysis previously used, ORAS4 assimilates satellite-derived SSH anomalies from the AVISO dataset (the precursor used in Phase 1). It also includes sea level contributions from ice sheet mass loss, glaciers ice melt, changes in land water storage and global thermal expansion. This makes great difference because this potentially allows to account for sea level changes due to mass changes in the simulated Mediterranean sea level through the boundary condition applied in the Atlantic buffer zone (see Phase 1 deliverable 3.1). The results presented below confirm that this is indeed the case.

The new version of the Mediterranean Sea model is NEMOMED12, a regional version of NEMO v3.2 model simulating the free surface evolution associated to the convergence of the oceanic current and to the fresh water flux at the ocean surface, as this was the case for NEMOMED8 used during Phase 1. Compared to this last, the resolution is improved on the horizontal ($1/12^\circ$ versus $1/8^\circ$) and on the vertical (75 vertical levels versus 43). The model was integrated over the period 1980-2013 with an atmospheric forcing from ALDERA (a dynamical downscaling of ERA-Interim using the ALADIN-Climat regional climate model) and a relaxation toward ORAS4 in the Atlantic buffer zone of the model (3D for temperature and salinity, 2D for SSH). However, since ORAS4 underestimate the mean seasonal cycle of the SSH over the basin (see Figure 60), it has been previously corrected in the Atlantic buffer zone in order to reproduce on average the mean annual cycle obtained from the CCI-ECV over the 1993-2010 period. This correction also applies before the satellite observing period.

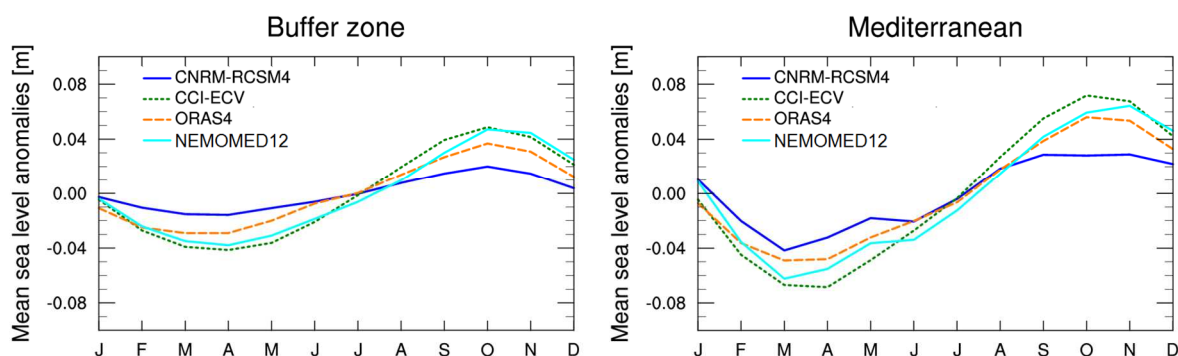


Figure 60: Seasonal cycle of mean sea level anomaly over the buffer zone (left) and over the Mediterranean Sea (right) for the CCI sea level (green dotted line), ORAS4 ocean reanalysis (orange dashed line), the coupled regional climate system model CNRM-RCSM4 (dark blue line) and the Nemomed12 Mediterranean sea model (light blue line).

The results presented in Figure 61 show that the NEMOMED12 model reproduces correctly the mean seasonal cycle from the CCI-ECV over the buffer zone, small differences coming from the

CMUG Phase 2 Deliverable

Reference: D3.1: Quality Assessment Report

Due date: June 2017

Submission date: 21 December 2017

Version: 4



fact that the relaxation coefficients toward the corrected ORAS4 are decreasing in the eastern part of this zone. But NEMOMED12 also reproduces fairly well the Mediterranean Sea mean sea level inferred from the CCI-ECV, and with a much better agreement than the CNRM-RSCM4 free surface (in Phase 1 Deliverable 3.1, CNRM-RSCM4 sea level was presented after adding the thermosteric component of sea level inferred from the simulated temperature changes only over the basin to account for missing terms in the model equations).

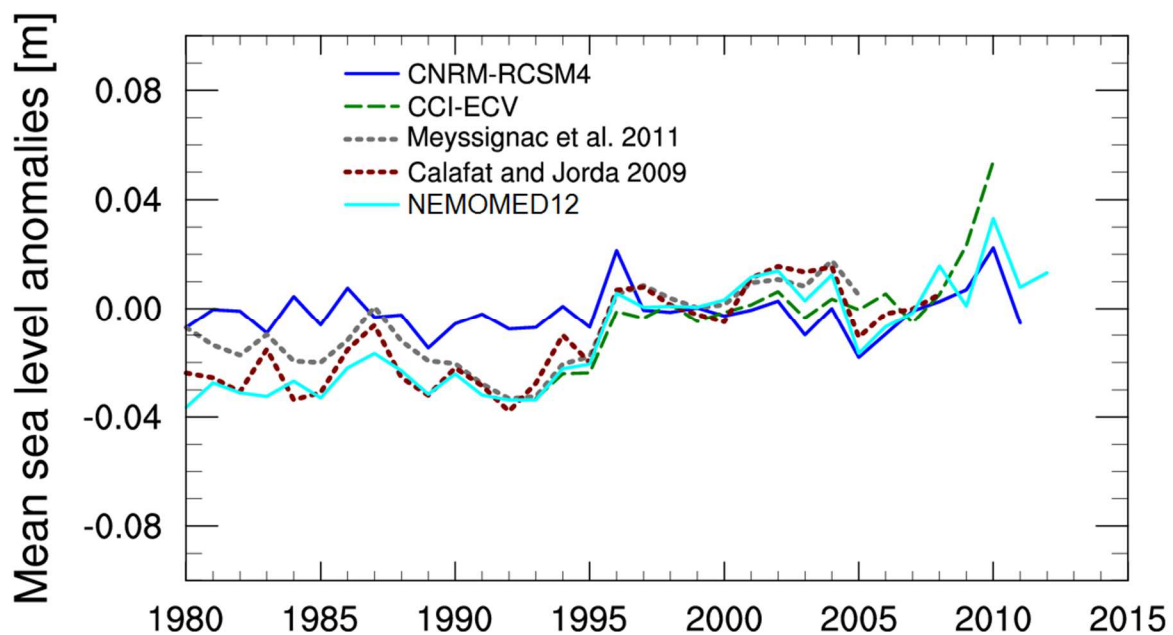


Figure 61: Time series of mean sea level anomalies averaged over the Mediterranean Sea over the period 1980-2013 for the CCI sea level (dashed green line), the tide gauge derived sea level reconstructions of Meyssignac et al. (dotted grey line) and Calafat and Jordà (dotted brown line), for the coupled regional climate system model CNRM-RCSM4 (dark blue line) and the Nemomed12 Mediterranean sea model (light blue line).

The positive impact of the assimilation of satellite-derived sea level in the ocean reanalysis used to constrain the ocean model in the Atlantic is also illustrated in Figure 61 showing the time series of mean sea level over the Mediterranean Sea. NEMOMED12 is indeed able to reproduce the sea level change over the period as observed from tide gauges and by the CCI-ECV. This also illustrates that the mean sea level change in the Mediterranean Sea mainly depends on the mass flux change at the Gibraltar Strait. Here again, without the thermosteric term contribution, the CNRM-RCSM4 model has low performance due to the absence of SSH assimilation in the COMBINE reanalysis used to constrain the model in the Atlantic.

This analysis of the added-value of the CCI Sea Level ECV using the CNRM regional climate coupled and uncoupled models was completed by a multi-model intercomparison, considering two

CMUG Phase 2 Deliverable

Reference: D3.1: Quality Assessment Report

Due date: June 2017

Submission date: 21 December 2017

Version: 4



additional coupled regional climate system models used within the context of the Med-Cordex project (Adloff et al., 2017). The first one is the so-called LMDZ-MED model (L'Hévéder et al., 2013) coupling the LMDz4 regional atmospheric component with the NEMOMED8 regional configuration of the NEMO ocean model with a horizontal resolution of 9 to 12km. For this model, the mean sea level in the Atlantic buffer zone is kept constant. The second is the MORCE-MED model (Lebeau-pin-Brossier et al., 2013) coupling the WRF atmospheric model with NEMOMED12. As for the CNRM-RCSM4 and the NEMOMED12 models, the simulated SSH is here relaxed toward a reference dataset in an Atlantic buffer zone. Over the period 2002-2008, it comes from the GLORYS-1 reanalysis (Ferry et al., 2010) which assimilates the AVISO satellite sea level. Over the period 1989-2001, the reference SSH varies seasonally but not interannually.

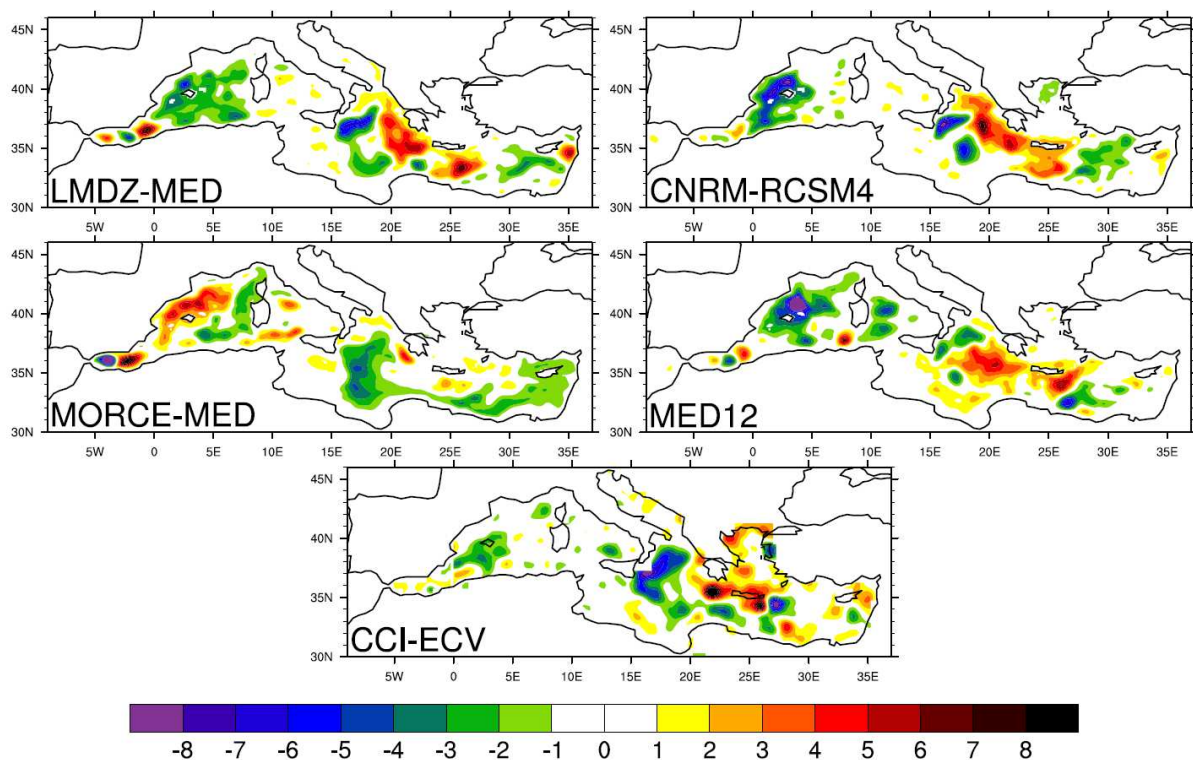


Figure 62: Trends in mm/year of Mediterranean sea surface height anomalies with respect to basin average over the period 1993-2008 for the three coupled regional climate system model (CNRM-RCSM4, LMDZ-MED and MORCE-MED), the NEMOMED12 Mediterranean Sea model (MED12) and the CCI Sea Level (CCI-ECV).

We have also reproduced in Figure 62 the simulated and observed sea level trends anomalies with respect to basin average, for the 16-year of the simulations common period (1993-2008). For the three coupled models, to account for the imperfect boundary conditions applied to the sea level in the Atlantic buffer zone, the reproduced trends are calculated as the sum of the calculated dynamic component and a spatially constant thermosteric component of the sea level change. This consists

CMUG Phase 2 Deliverable

Reference: D3.1: Quality Assessment Report
Due date: June 2017
Submission date: 21 December 2017
Version: 4



in neglecting the contribution of salinity changes in the computation of modeled sea level change at the Mediterranean basin scale as justified by previous analyses (see Phase 1 deliverable 3.1). However, whatever the hypothesis made to correct the trend averaged at the basin scale, the spatial trend variability reproduced in Figure 62 only results from the simulated dynamical processes and sea surface fresh water fluxes.

Here CNRM-RCSM4 and NEMOMED12 display very similar performances because the different boundary conditions have little impact on the spatial trend variability. But this also proves that this variability is not too much affected by the coupling between the atmosphere and the Mediterranean Sea. The LMDZ-MED model also shows important similarities with the observations, showing that the spatial variability of the local trends is not significantly affected by the specification of the lateral boundary conditions. The difficulties of the models to reproduce the observed trends in the western part of the Mediterranean basin can be attributed to their difficulty to reproduce the circulation in the Alboran region (Adloff et al., 2017). The patterns are differently reproduced by the different models in this region. The patterns are better reproduced in the eastern part of the basin and in particular due to their ability to reproduce the recovery following the so-called “Eastern Mediterranean Transient” (EMT) anomaly. There is thus a model dependence of the results and the CCI-ECV can be used to assess the performances of the models.

In addition, the level of agreement between the models and the CCI-ECV observations shows that the uncertainty on local trends first estimated to be 3mm/yr (Error Report v1.1 dated 9 April 4 2013), might have been overestimated by the CCI Sea level team. The new error estimate presented as a map in their last error report (Error Characterization Report v2.2 dated 29 July 2016) are now of the order of 1 to 2 mm/yr over the Mediterranean Sea and are consistent with the model results. The modelled trends are indeed close to the observations in many regions but the differences are the most often higher than this estimated error. This finding has however to be confirmed through a more quantitative approach.

Cross-assessment of a subset of CCI-ECVs

The consistency of the CCI-ECVs is here evaluated through the analysis of a climate specific event that can be as well observed with the satellite-derived products as potentially reproduced in RCSM simulations. In this work we focus on the July 2006 heat wave that affected the western part of the Mediterranean continental and marine area. The model is the so-called CNRM-RCSM5 model close to the CNRM-RCSM4 model as it couples a version of the ALADIN-Climat atmospheric component with a 50km horizontal resolution and the NEMOMED8 Mediterranean model with a 1/8° horizontal resolution, but including a prognostic aerosol scheme for desert dust, sea salt, organic, black-carbon and sulfate particles (Nabat et al., 2015). The CNRM-RCSM5 model was integrated from May to July 2006 with application of a spectral nudging towards the ERA-Interim reanalysis (hereafter referred to as SN simulation). In addition to the surface pressure, the atmospheric temperature, wind vorticity and divergence, and specific humidity are nudged above

CMUG Phase 2 Deliverable

Reference: D3.1: Quality Assessment Report

Due date: June 2017

Submission date: 21 December 2017

Version: 4



the 700 hPa level (relaxation zone between 850 hPa and 700 hPa). An additional simulation with the same model but no spectral nudging (hereafter referred to as NSN simulation) and covering the period 1992-2010, is used to infer the model climatology.

In order to analyse the development of the 2006 heat wave both with satellite-derived observations and with the model outputs, we calculate for different climate variables the differences between their July and June monthly means. We first reproduce in Figure 63 these differences for the SST. It reveals that, with SST differences of 4 to 7°C in the western part of the basin, the year 2006 appears to be singular compared to the 1992-2010 climatology that exhibits differences of only about 3.5 degree in this region. It also shows the fairly good agreement between the simulated SST and the CCI-SST (version v02.0) as well for the NSN 1992-2010 climatology (spatial correlation coefficient of about 0.76) as for the 2006 SN simulation (correlation coefficient of about 0.9). This shows that the application of the spectral nudging method in our simulation allows reproducing the effect of the 2006 heat wave event on the Mediterranean surface temperature with a proper chronology.

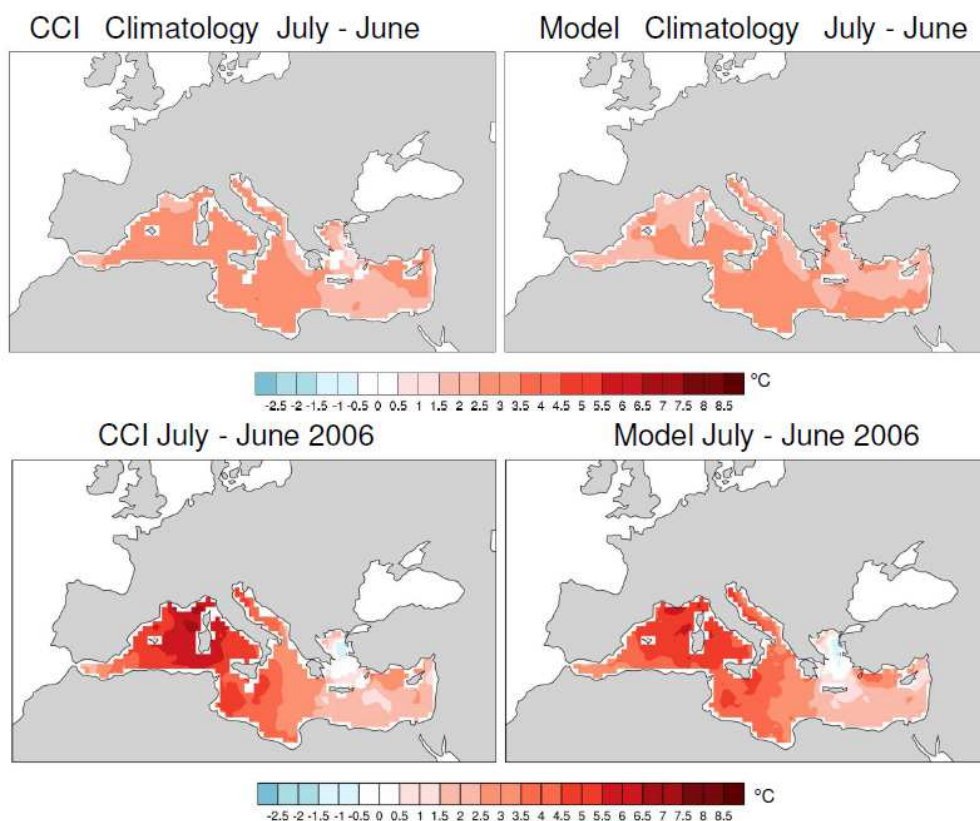


Figure 63: Climatological differences between July and June over the 1992-2006 period for CCI SST (top left) and for CNRM-RCSM5 NSN SST (top right); differences between July and June 2006 for CCI SST (bottom left) and for CNRM-RCSM5 SN SST (bottom right).

CMUG Phase 2 Deliverable

Reference: D3.1: Quality Assessment Report
Due date: June 2017
Submission date: 21 December 2017
Version: 4



Afterwards the consistency between the simulated and the CCI aerosol optical depth (AOD) is examined. Three algorithms are available to infer the CCI long-term total column AOD datasets from European Earth Observation sensors: the Oxford RAL Aerosol and Cloud retrieval (ORAC), the Swansea University AATSR retrieval (SU) and the AATSR dual-view (ADV). The spatial correlation coefficients between the SN AOD and the satellite-derived AOD (CCI, MODIS and AMSR) over the whole Euro-Mediterranean area (see the domain in Figure 46), at the daily and monthly time scale for June and July 2006, are presented in Table 7. The satellite product giving the highest correlations with the simulation is the CCI AOD determined through the Swansea University (SU) algorithm. This is consistent with Holzer-Popp et al. (2003) showing better results for this algorithm over northern Africa and the Mediterranean region.

Table 7: Spatial correlation coefficient between SN simulated aerosol optical depth and different satellite products.

Satellite product/Algorithm	CCI/ADV		CCI/ORAC		CCI/SU		MODIS		MISR	
	July	July	June	July	June	July	June	July	June	July
Daily	0.48	0.36	0.76	0.74	0.85	0.83				
Monthly	0.19	0.23	0.65	0.74	0.84	0.82	0.81	0.78	0.56	0.67

We thus choose this product to illustrate the development of the 2006 heat wave on the AOD (Figure 64). Compared with the CCI climatology over the 1992-2010 period, the observed distribution of AOD change between the two months shows specificities for 2006 that are fairly well simulated by the model. A further investigation of geopotential and wind at 850 hPa from ERA-Interim reanalysis corroborates an impact of the circulation change, associated to an increase of geopotential over Maghreb, on the transport of dust from the African continent towards Western Europe. The same circulation change between June and July 2006 also appears to be partly at the origin of the cloud change pattern over Western Europe (not shown) that is trapped by the model simulation with a spatial correlation of about 0.9 between the SN and the CCI total cloud changes. It is worth noting that this high correlation is obtained in spite of a negative bias of the simulated cloud having no impact on the correlation.

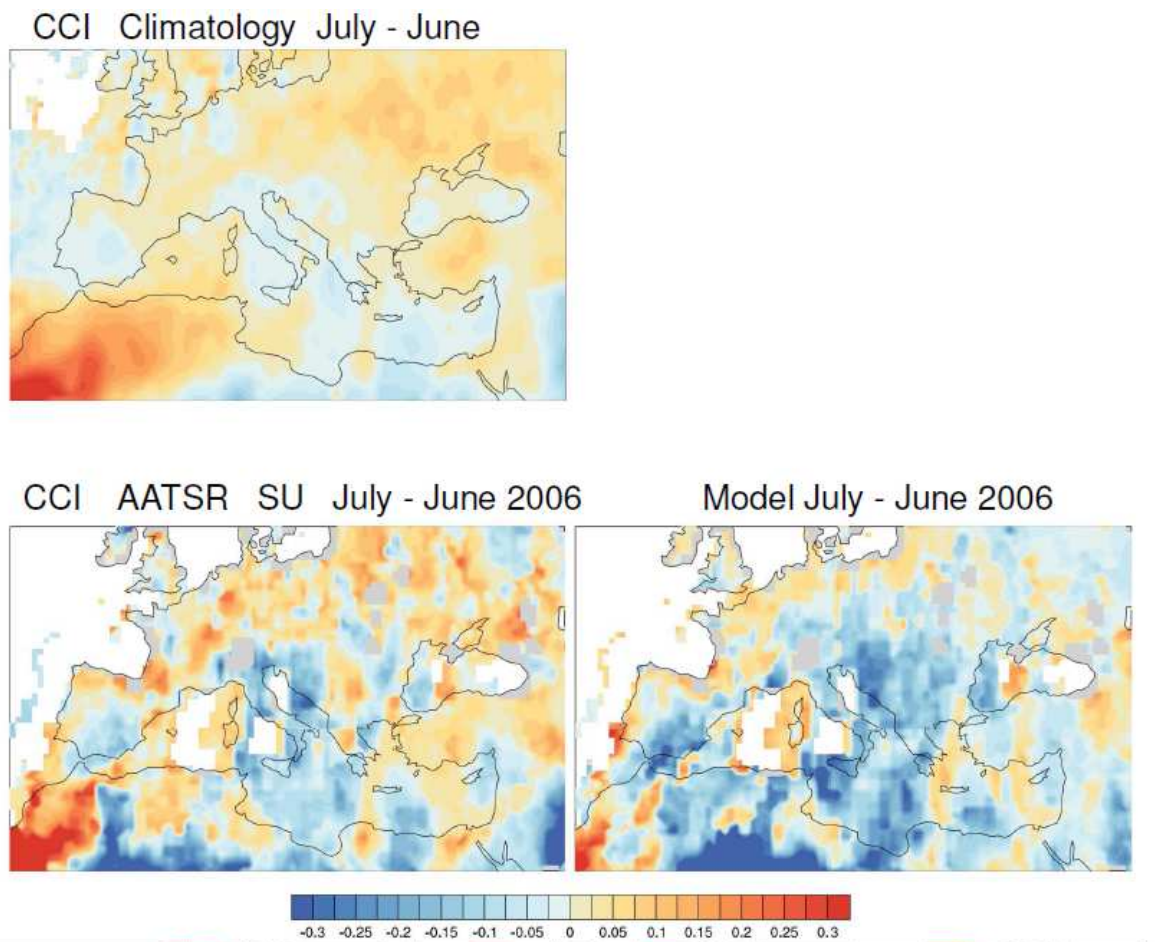


Figure 64: Climatological differences between July and June over the 1992-2006 period for CCI AOD (top left); differences between July and June 2006 for CCI SU AOD (bottom left) and for CNRM-RCSM5 SN AOD (bottom right).

In addition, the analysis of the CCI soil moisture shows that 2006 is also much drier in July than in June compared to the 1992-2010 climatology (not shown). This is particularly the case in North-Western Europe and this is also well trapped by the SN soil moisture with a correlation coefficient of about 0.8 between the modelled and the CCI ECV changes. This drying is an expected impact of the heat wave amplification between June and July, a mechanism that has been identified in previous studies. Reversely, the heat wave development has no clear impact on the sea level change that is dominated by an internal dynamical variability at the scale of the oceanic mesoscale eddies (10 to 100km).

As a conclusion, the application of the spectral nudging method at the mid and upper atmospheric levels towards the ERA-Interim reanalysis allows to simulate the right chronology of the 2006 heat wave. For all the ECVs considered except sea level, the correlations between the model and the satellite-derived observations are very high showing the ability of the model at reproducing the

CMUG Phase 2 Deliverable

Reference: D3.1: Quality Assessment Report
Due date: June 2017
Submission date: 21 December 2017
Version: 4



patterns of change. As shown by an analysis of complementary simulated atmospheric fields, the development of the heat wave is consistent with a circulation change that likely impacts the aerosol and cloud distribution changes. The drying of the upper surface is moreover an expected effect of the heat wave development that is simulated by the model. The agreement between the model and the satellite-derived observations during the 2006 heat wave thus allows concluding in the consistency between the different analysed ECVs over the region for this specific event. An additional learning is the significant effect of the choice of the algorithm that is used to infer the AOD satellite product, revealed by the comparison to the modelled field. The choice of the best algorithm is however regionally dependent.

Quality relevant outcomes

Some key outcomes of the CMUG research activity on this topic are that:

- The CCI ECVs considered in this study (Sea level, SST, aerosol, soil moisture, cloud) are adequate to assess the performance of the state of the art regional climate models over the Mediterranean basin.
- There is a significant positive impact of the assimilation of the CCI Sea Level ECV in the ocean reanalyses that are used for the Atlantic lateral boundary conditions of the Mediterranean regional climate models.
- The new uncertainty estimate on the Sea Level ECV local trends seems now to be consistent with the models results.
- The analysis of the consistency between the simulated model aerosol optical depth and the corresponding ECV products reveals the importance of the choice of the algorithm used to infer this variable from the satellite observations.
- The analysis of a climate specific event simulated by a RCSM reveals the consistency between several ECVs over the Mediterranean domain.

CMUG Phase 2 Deliverable

Reference: D3.1: Quality Assessment Report
Due date: June 2017
Submission date: 21 December 2017
Version: 4



3.13 Assessment of sea ice concentration observational uncertainty from a data assimilation point of view [WPO3.11]

Sea ice concentration (SIC) is arguably one of the longest remotely-sensed and most essential climate variables (ECV) at high latitudes. Global SIC records date back to the late 1970s (Cavalieri et al, 1996), which makes them crucial for climate studies. In addition, SIC is an essential term in the sea ice mass budget and is the primary information on which the skill of contemporary climate models is estimated in polar regions (e.g. Guemas et al, 2014). However, satellites do not measure SIC directly. Rather, they sense sea surface brightness temperature; since water and ice have different passive microwave signatures at a certain frequency, it is possible to estimate the relative amount of sea ice in a grid cell (that is, sea ice concentration) given the brightness temperature information. This conversion between brightness temperature and SIC is associated with a number of assumptions which, added to the instrumental uncertainty, make SIC products intrinsically uncertain. The comprehensive review by Ivanova et al. (2016) documents advantages and pitfalls of different algorithms for SIC retrieval and discusses these issues in detail.

By contrast, sea ice thickness (SIT) is a very demanding variable to observe in-situ or remotely at any scale, although it is thought to carry a significant share of sea ice predictability, at least for the summer season. Indeed, thin ice melts more easily, so that SIT anomalies are directly related to SIC anomalies a few months later, with possible re-emergence up to a year later (Guemas et al., 2014). Defining SIT anomalies is not trivial, given the sparsity and intermittency of existing records. Efforts from many projects, including ESA-CCI, to make these products routinely available are therefore more than welcome, given the valuable information that they represent for the climate community.

The quality of observational sea ice products is critical for accurate initialization of climate predictions. Within the CMUG Phase 2, the Earth Sciences Department of the Barcelona Supercomputing Center (BSC-ES) has implemented a sophisticated method of data assimilation for SIC, namely the Ensemble Kalman Filter (EnKF; Evensen, 2003, 2007). The EnKF works in two steps: (1) a forecast step, during which an ensemble of N climate simulations is forwarded in time, each element (“member”) of the ensemble being subject to a perturbation and (2) an analysis step, during which all members are updated based on new information available from observations (Figure 55).

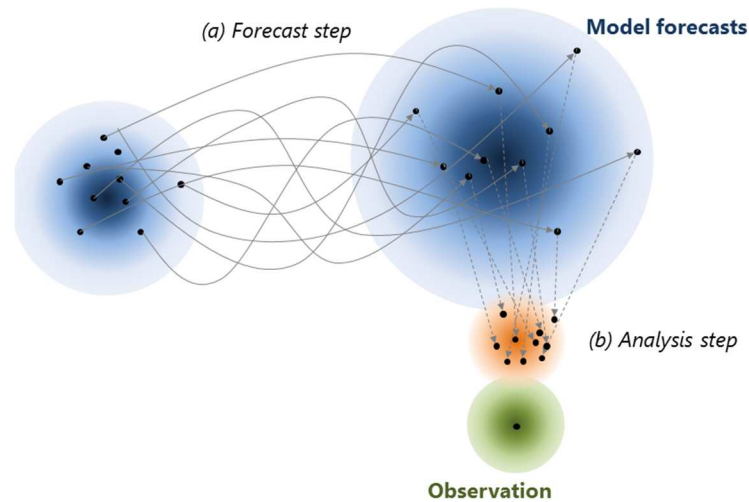


Figure 55: Principle of the ensemble Kalman Filter (EnKF). During the forecast step, model error is explored by integrating N model versions, each subject to a perturbation. The ensemble is then updated during the analysis step. The update is proportional to the misfit of forecasts to the observation, and is weighted by the relative uncertainties in observations and forecasts. A new forecast cycle is then started using the result of the analysis step as initial conditions for the new forecast step.

The EnKF is an advanced data assimilation method which propagates the model updates from observed variables to non-observed variables through the error covariance matrix which appears in the gain matrix formulation, the latter being used to update the model. When assimilating observational data through the EnKF, partial observations can therefore have a global impact. For example, the observation of SIC alone can lead to a substantial correction of SIT but also sea surface temperature, salinity or even currents. The other strength of the EnKF is the fact that this filter accounts for both model and observational uncertainties. In regions where the model is relatively confident (e.g., the interior of the Arctic sea ice pack in winter), updates will be minor; while they will be larger in the marginal ice zone where the position of modelled ice edge is usually uncertain. At the same time, updates will be large where observations are relatively confident. An accurate estimation of SIC uncertainties is therefore essential for an efficient data assimilation with the EnKF.

In the previous quarterly report in 2017, we validated our sea ice reanalysis performed with the NEMO3.6-LIM3 model assimilating the ESA CCI SIC product through the EnKF at standard resolution over the 1993-2009 period. We illustrated the performance of assimilating ESA SIC through a comparison with a NEMO3.6-LIM3 free run (i.e. without sea ice data assimilation) and OSI-SAF SIC. We showed that the assimilation of ESA CCI SIC improves the representation of extreme events (e.g., September 2007 in Arctic) as well as the mean state (especially in the Southern Ocean where the free-running model exhibits larger biases than in the Arctic). In this final report we illustrate new results about:

1. Assimilating ESA CCI SIC data in coupled mode at standard resolution (about 1 degree in the ocean and 80km in the atmosphere)

CMUG Phase 2 Deliverable

Reference: D3.1: Quality Assessment Report
Due date: June 2017
Submission date: 21 December 2017
Version: 4



2. Initializing coupled climate predictions from the standard resolution sea ice reanalysis produced for the previous quarterly report

Key results of CMUG research on SIC assimilation in coupled mode within Ec-Earth3.2 at standard resolution

We use the EC-Earth3.2.0 coupled climate model in T255L91 (about 80km atmospheric horizontal resolution and 91 levels) ORCA1L75 (about 1 degree oceanic horizontal resolution and 75 levels) configuration to assimilate the ESA CCI sea ice concentration (SIC) product using the Ensemble Kalman Filter (EnKF) with 25 members. The assimilated SIC has a direct impact on the sea ice and ocean variables through the EnKF updates at monthly intervals, but not on the atmosphere and land variables by construction, because our primary focus is on monthly and longer climate timescales. We assume that the atmospheric potential shocks, right after the EnKF updates of the ocean and sea ice states which could become inconsistent with the atmospheric variables, are statistically indistinguishable from typical weather noise governed primarily by synoptic processes.

In the Northern Hemisphere (NH), the assimilation of SIC reduces both the summer minima and the winter maxima of sea ice extent (SIE) by more than 1 million square km with respect to a free-running simulation (Figure 56). In late spring and early summer, the Arctic SIE is also substantially reduced. These EnKF corrections are suspected to correspond to a compensation for misrepresented surface thermodynamics sea ice processes, such as melt ponds and multi-layer snow, which are particularly important during the melting period.

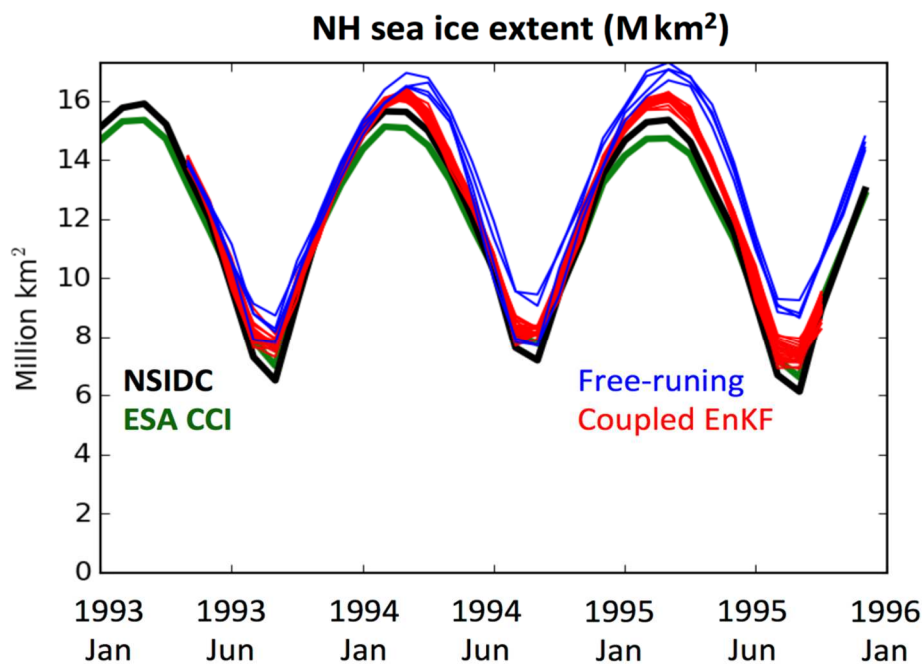


Figure 56: Northern Hemisphere sea ice extent in millions square km. The black (green) line shows the NSIDC (ESA CCI) monthly mean observations. The blue (red) lines show a free-running (EnKF) ensemble of EC-Earth3.2.0 reconstructions.

CMUG Phase 2 Deliverable

Reference: D3.1: Quality Assessment Report
Due date: June 2017
Submission date: 21 December 2017
Version: 4



Figure 57a shows the ensemble mean SIC of a free-running simulation which tends to overestimate the NH SIC in the marginal zones during the winter maximum in March 1994 (with respect to observed conditions in Figure 57d). The SIC tends to be reduced in these regions when assimilating ESA SIC data (Figure 57c). Our EnKF approach uses the SIC and its uncertainty from ESA (Figure 57b illustrates the SiC uncertainty that was used for the EnKF update on 1 March 1994). The SIC reduction is large in regions of low SIC uncertainties such as the Labrador and Irminger seas, but comparatively moderate in regions of large SIC uncertainties such as in Fram Strait.

Figure 58 shows the equivalent fields for the summer maximum in September 1994 (including Figure 58b that shows the SIC uncertainty that was used for the EnKF update on 1 September 1994). Overall, these results show some substantial improvements in the NH SIC conditions thanks to our data assimilation approach, the EnKF larger corrections matching regions of low SIC uncertainty. This is the case for example in the Baffin Bay, in the Chukchi and Beaufort Seas. Surprisingly, in some other regions such as along the Euro-Asian continental shelf, the reanalysis does not necessarily match better the observations than the free-running simulation despite a low SIC uncertainties. A robust correction of the SIC in this region would probably require more successive updates.

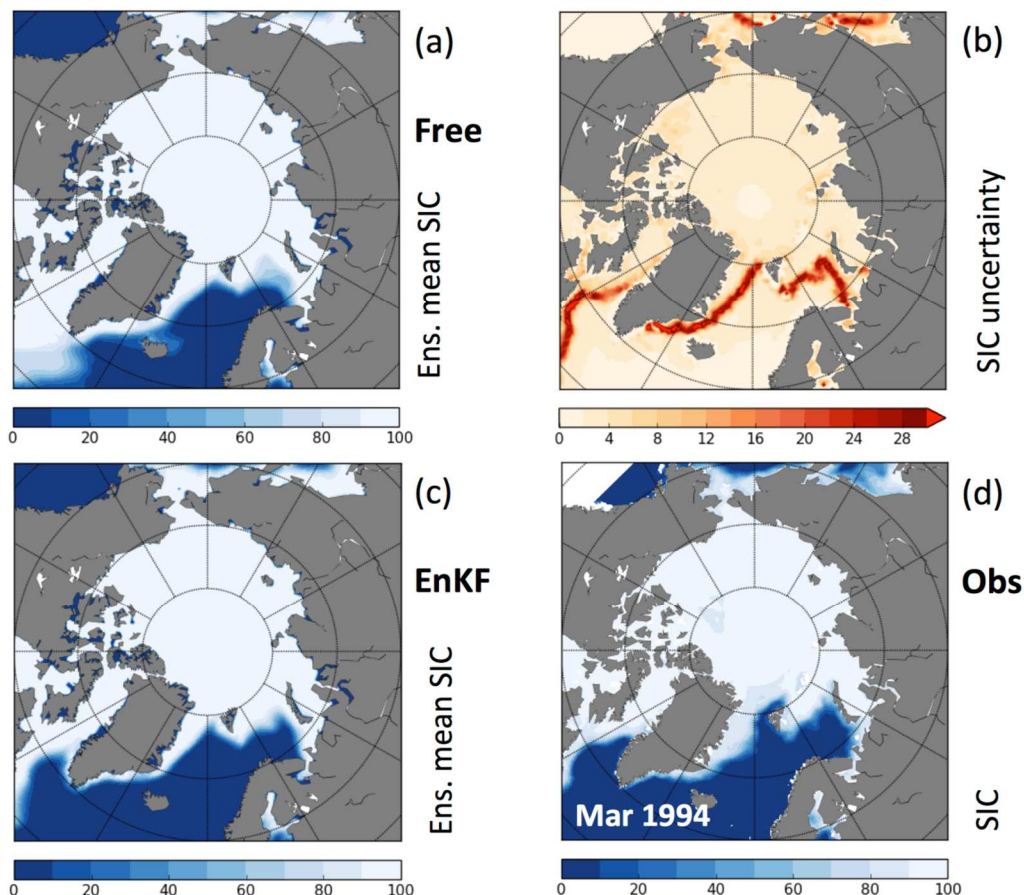


Figure 57: The upper (lower) left panel shows the ensemble-mean SIC of a free-running simulation (EnKF analysis) in March 1994. The upper (lower) right panel shows the NH SIC uncertainty on 28 February 1994 in the ESA-CCI SIC data used for the EnKF update (in March 1994 in NSIDC data). The units of SIC and SIC uncertainty are %.

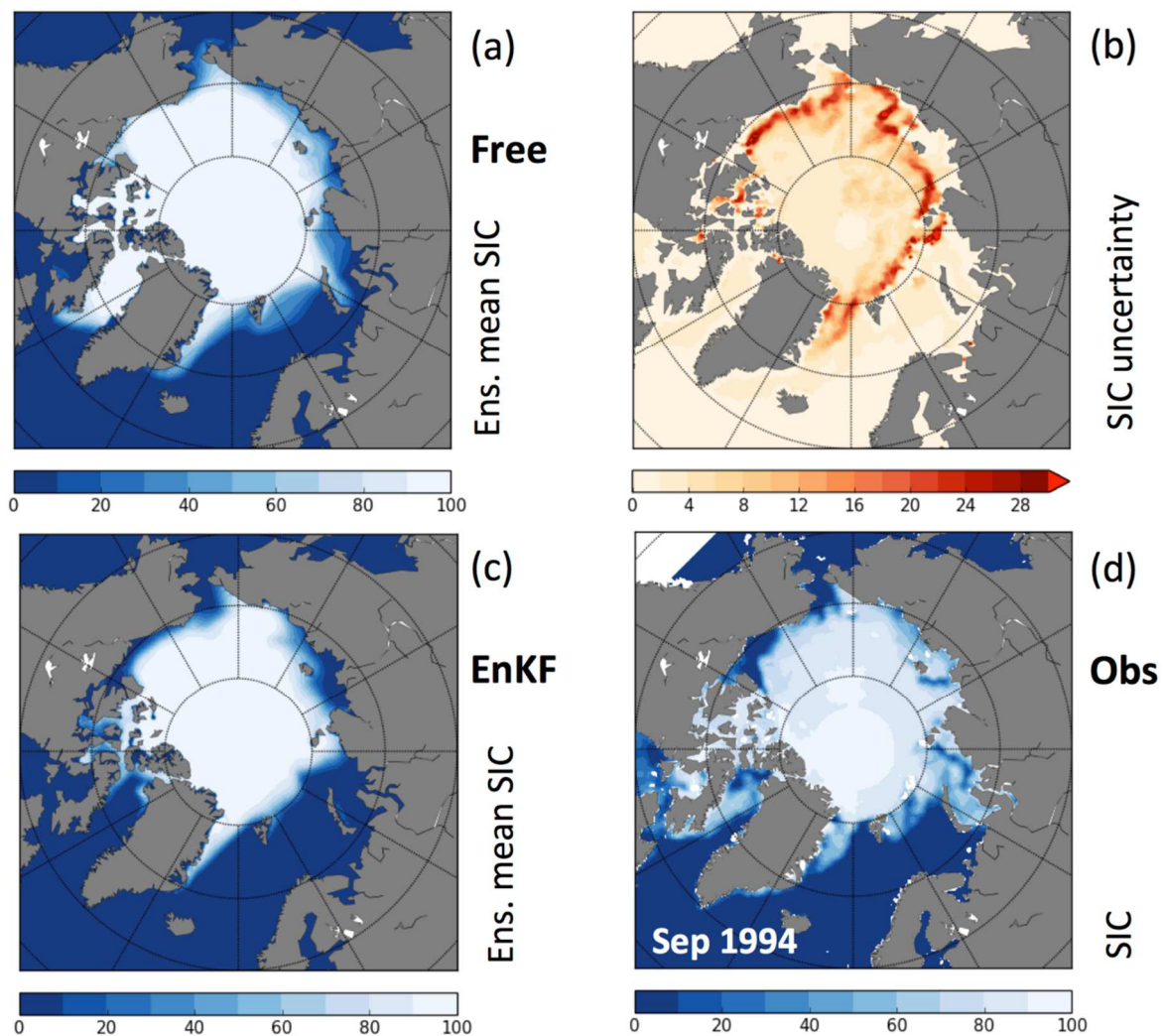


Figure 58: The upper (lower) left panel shows the ensemble-mean NH SIC of free-running (EnKF analysis) in September 1994. The upper (lower) right panel shows the NH SIC uncertainty on 31 August 1994 in ESA data used for the EnKF update (in September 1994 in NSIDC data). The units of SIC and SIC uncertainty are %.

In the Southern Hemisphere (SH), the assimilation of ESA-CCI SIC allows for a substantial reduction of the SIE and its ensemble spread so that the simulated SIC becomes statistically indistinguishable from the observations (Figure 59). The observed SIC uncertainties tend to be confined to narrower zones in the Southern Ocean as illustrated by the comparison between Figures 60b and 61b with Figures 57b and 58b, and the model ensemble spread tend to be larger in the Southern Ocean as illustrated by the comparison between Figures 56 and 59 which both contribute to larger EnKF updates toward observational data, the second factor being the dominant one.

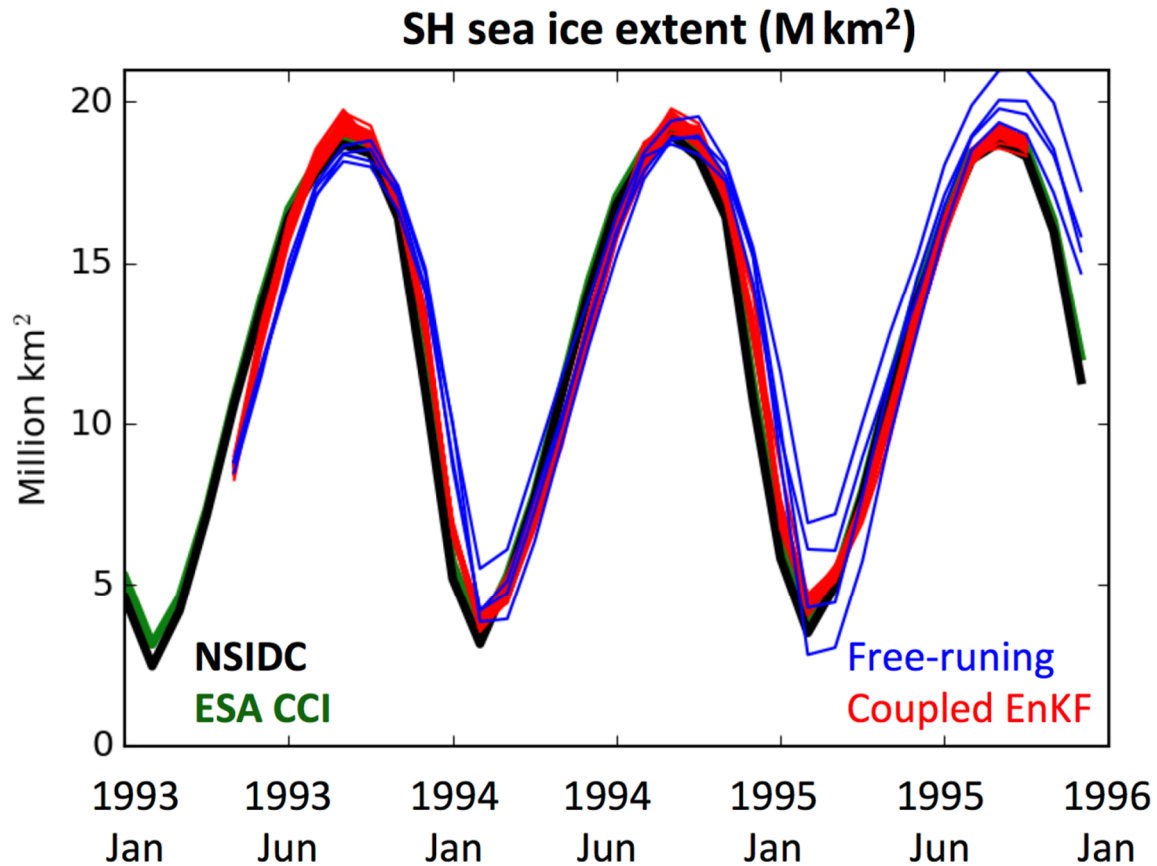


Figure 59: Southern Hemisphere sea ice extent in millions square km. The black (green) line shows the NSIDC (ESA CCI) monthly mean observations. The blue (red) lines show a free-running (EnKF) ensemble of EC-Earth3.2.0 reconstructions.

The SIC from our reanalysis shows on average in the SH a better agreement with the observations than in the NH at the sea ice minimum during the austral summer (March) in most seas around the Antarctica (Figure 60). A reasonably good agreement between the reanalysis and satellite data is also obtained during the austral winter maximum (Figure 61). A regional comparison of the EnKF corrections (Figures 60c and 61c) and the SIC uncertainty from the ESA data (Figures 60b and 61b) around the Antarctic indicates that the Southern Ocean sea ice cover has not been as effectively updated in the regions with relatively higher SIC uncertainty as in the regions with lower uncertainty. For example, the EnKF corrections during austral summer in the middle of the Ross Sea close to the Ross Ice Shelf could be economically important for the planning of the transportation of people and material to numerous nearby research stations.

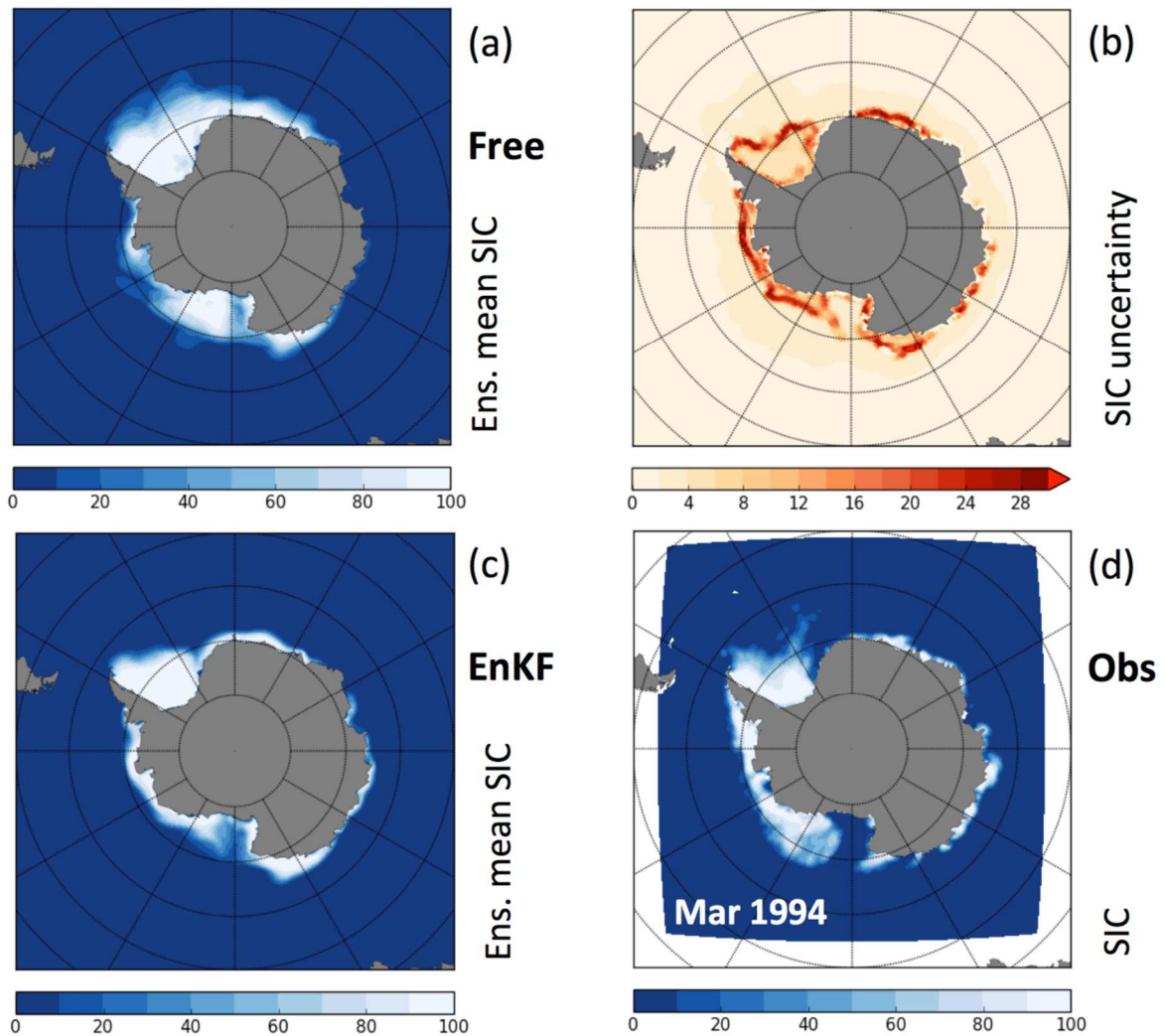


Figure 60: The upper (lower) left panel show the ensemble-mean SH SIC of free-running (EnKF analysis) in March 1994. The upper (lower) panel show the SH SIC uncertainty on 28 February 1994 in ESA data used for EnKF update (in March 1994 in NSIDC data). The units of SIC and SIC uncertainty are %.

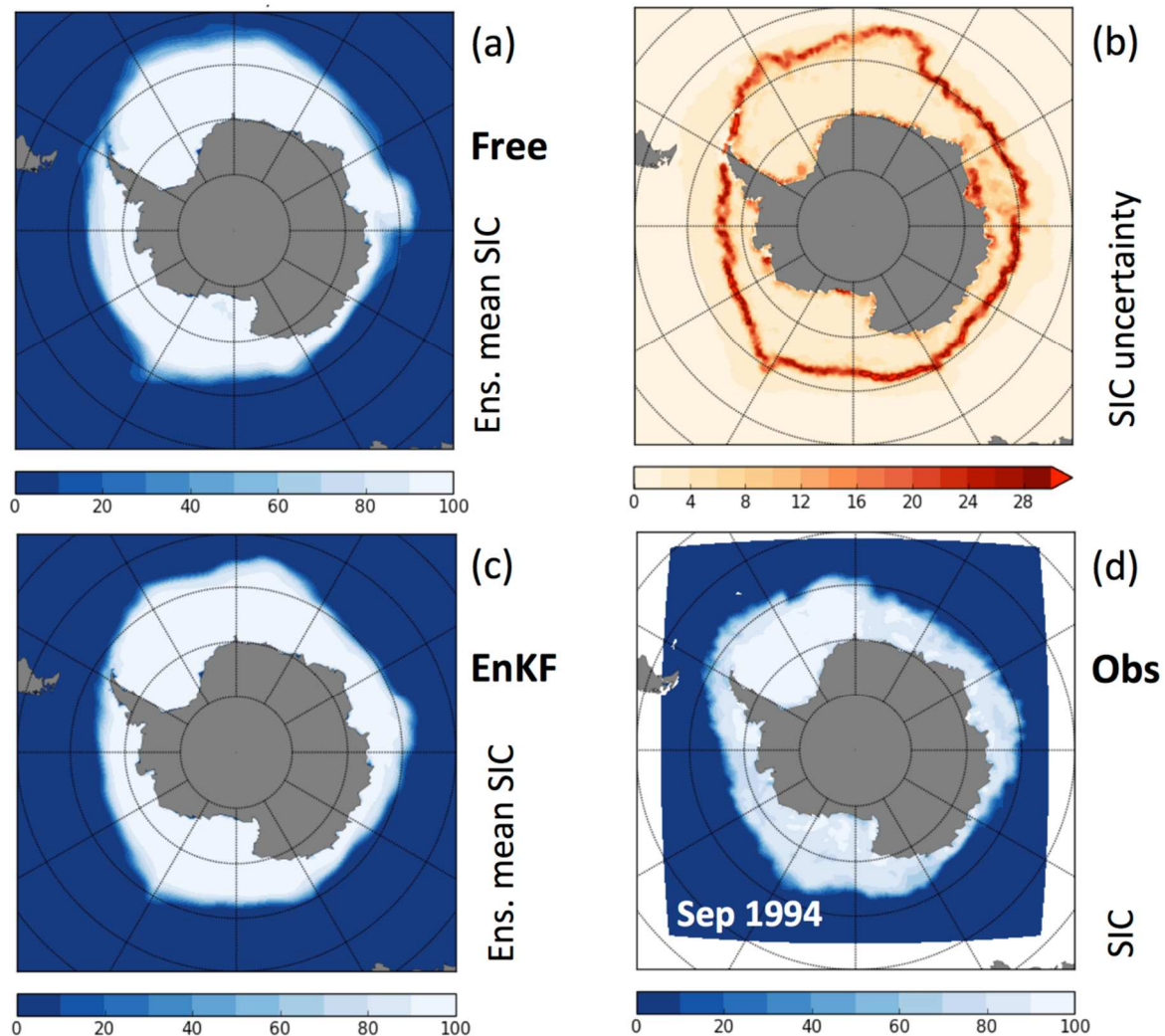


Figure 61: The upper (lower) left panel show the ensemble-mean SH SIC of free-running (EnKF analysis) in September 1994. The upper (lower) panel show the SH SIC uncertainty on 31 August 1994 in ESA data used for EnKF update (in September 1994 in NSIDC data). The units of SIC and SIC uncertainty are %.

Key results of CMUG research on initializing climate predictions from a reanalysis assimilating ESA SIC at standard resolution

Coupled seasonal forecasts were carried out for the period 1993-2008 with the T255L91 ORCA1L75 configuration of the EC-Earth3.2.2 climate model (about 80km horizontal resolution and 91 levels in the atmosphere and about 1 degree horizontal resolution and 75 levels in the ocean). The model was initialized on every 1st of May and every 1st of November and integrated until seven months into the future. Two identical sets of seasonal forecasts were conducted except for their sea ice initial conditions (IC). Each set consists of five ensemble members. For the atmospheric IC, we used the ERA-Interim reanalysis, and for the oceanic IC ORAS4 reanalysis, the sea ice was initialized from the BSC reconstruction without SIC data assimilation, while the other experiment used the EnKF data assimilation of ESA CCI sea ice concentration for the initial

CMUG Phase 2 Deliverable

Reference: D3.1: Quality Assessment Report
Due date: June 2017
Submission date: 21 December 2017
Version: 4



conditions. These sources of sea ice initial conditions, i.e. a sea ice reanalysis assimilating ESA CCI at standard resolution and a free-run simulation were illustrated in the last quarterly report. The 5 members were generated through the introduction of singular vector perturbations in the atmosphere and the use of 5 different members of the ORAS4 and sea ice reconstructions/reanalysis for the ocean and sea ice respectively.

Figures 62 through 66 display the added value of initializing the SIC with data assimilation (1993-2008) for the Pan-Arctic sea ice extent and sea ice volume forecasts. All figures display the predictive skill evaluated through correlation coefficients (left) and root mean square errors (right) against the NSIDC satellite observations.

Predictions initialized in May with SIC assimilation show a decrease in predictive skill during the boreal summer months (June to September) in terms of sea ice extent (Fig. 62) compared to predictions which did not assimilate ESA CCI data. Sea ice volume skill is slightly improved in the autumn (Fig. 63) by SIC assimilation on the other hand. The root mean square error (RMSE) of sea ice extent indicates a better performance of the model initialized without assimilation, but a worse performance if sea ice volume is considered.

The SIC assimilation improves to a larger extent the forecast quality when those are initialized in November (Figs. 64 and 65). Both sea ice extent and volume are systematically better predicted when the forecast system is initialized with assimilated SIC for both correlation coefficient and RMSE. Although the ocean is thought to be the main driver of sea ice predictability during the freezing season (Chevallier and Salas-Melia, 2012; Guemas et al 2016), these results demonstrate that SIC assimilation has a clear added-value for the initialization of seasonal forecast in November.

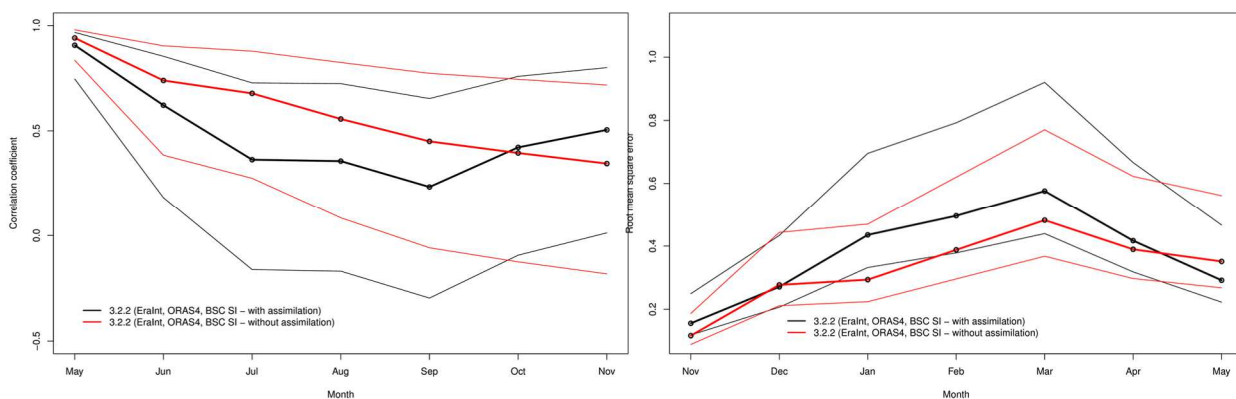


Figure 62: Prediction scores (thick lines with circles) for the Arctic sea ice extent as a function of the forecast month for simulations initialized in May. The scores shown are the correlation coefficient between the EC-Earth3.2.2 forecast system and NSIDC observations after linearly detrending the anomalies (left figure) and the root mean square error (right figure). The 95% confidence intervals are shown in thin lines. The red lines show results from simulations initialized with ERA-interim reanalysis for the atmosphere, ORAS4 reanalysis for the ocean and BSC reconstruction for sea ice. The black lines show results from simulations initialized with ERA-interim reanalysis for the atmosphere, ORAS4 reanalysis for the ocean and BSC reanalysis for sea ice. Root mean square error in millions of square kilometers.

CMUG Phase 2 Deliverable

Reference: D3.1: Quality Assessment Report
 Due date: June 2017
 Submission date: 21 December 2017
 Version: 4

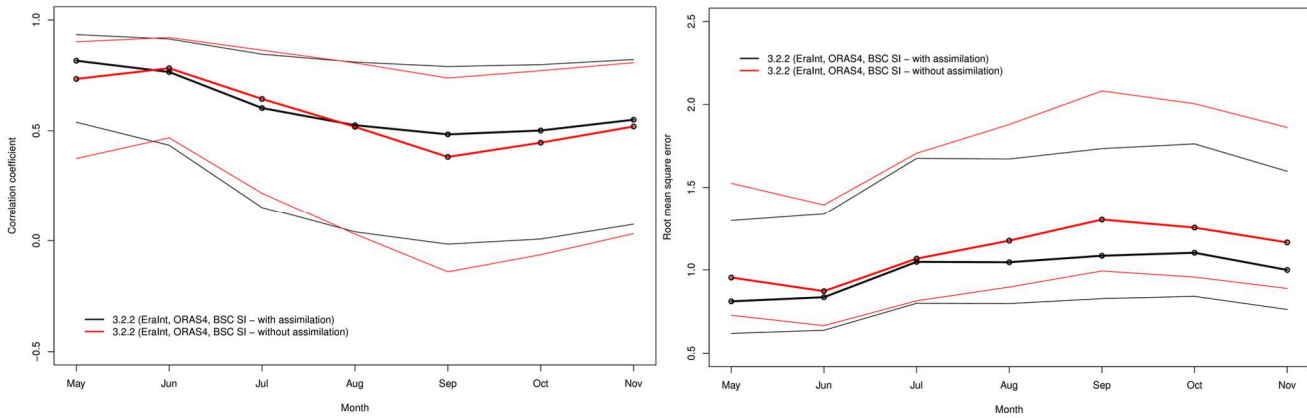


Figure 63: Prediction scores (thick lines with circles) for the Arctic sea ice volume as a function of the forecast month for simulations initialized in May. The scores shown are the correlation coefficient between the EC-Earth3.2.2 forecast system and PIOMAS observations after linearly detrending the anomalies (left figure) and the root mean square error (right figure). The 95% confidence intervals are shown in thin lines. The red lines show results from simulations initialized with ERA-interim reanalysis for the atmosphere, ORAS4 reanalysis for the ocean and BSC reconstruction for sea ice. The black lines show results from simulations initialized with ERA-interim reanalysis for the atmosphere, ORAS4 reanalysis for the ocean and BSC reanalysis for sea ice. Root mean square error in thousands of cubic kilometres.

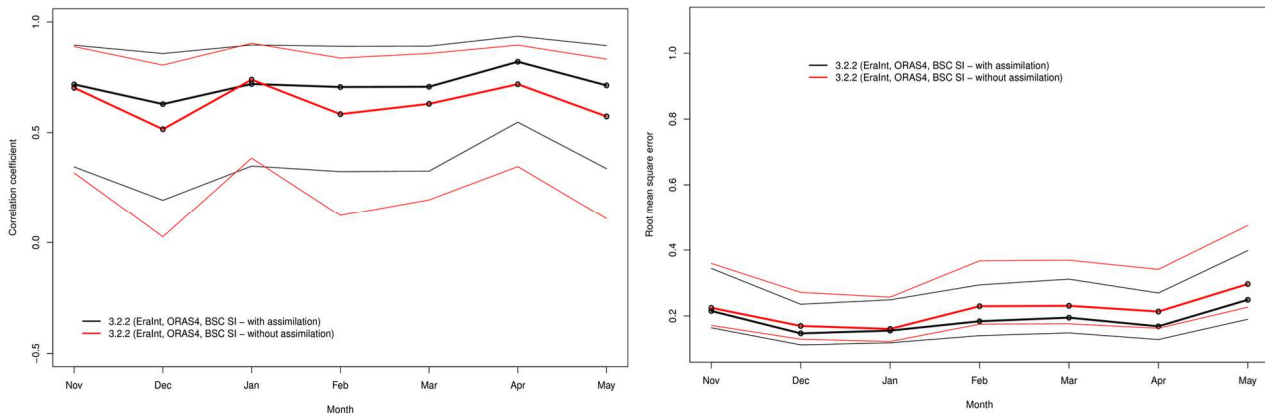


Figure 64: Same as Figure 62, but for predictions initialized in November.

CMUG Phase 2 Deliverable

Reference: D3.1: Quality Assessment Report

Due date: June 2017

Submission date: 21 December 2017

Version: 4

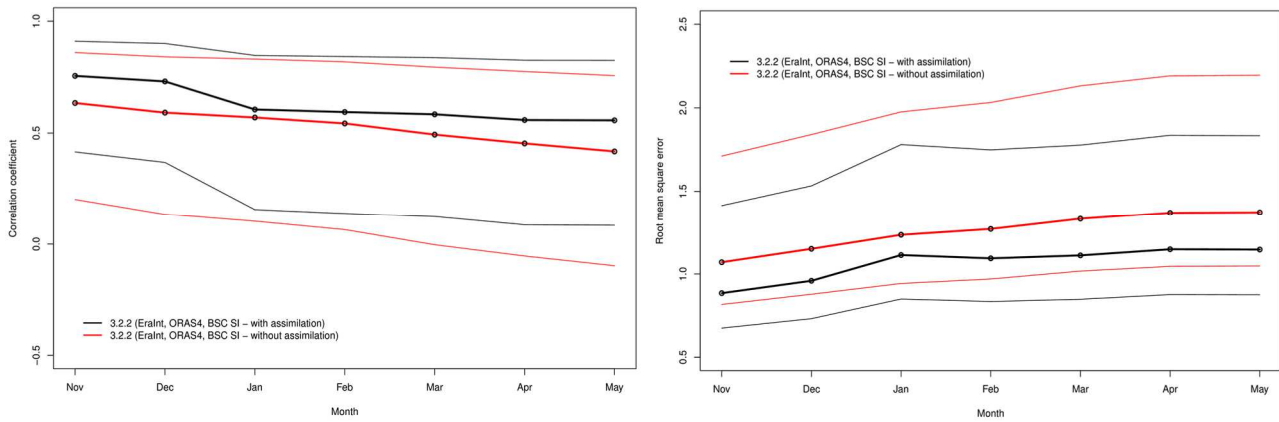


Figure 65: Same as Figure 63, but for predictions initialized in November.

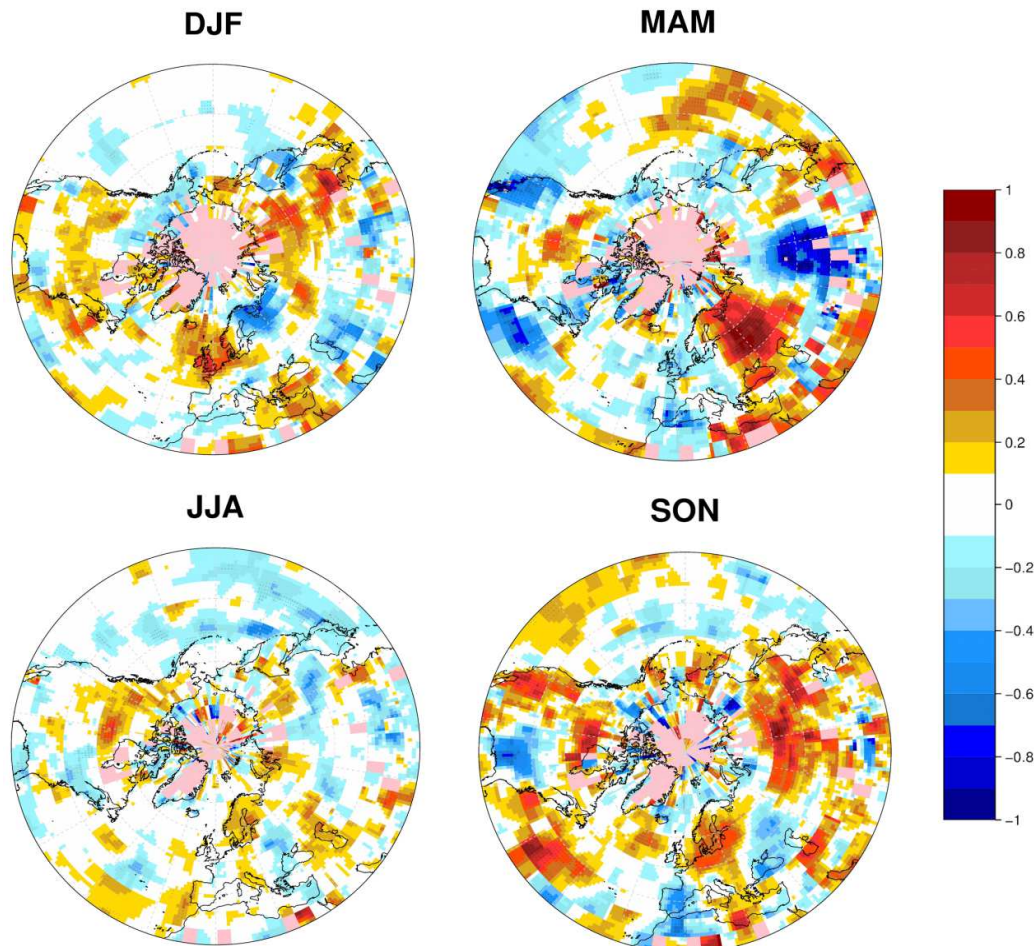


Figure 66: Added value (as a difference in correlation coefficient) from using ESA SIC data assimilation to initialize the model in seasonal predictions. Maps showing scores for the northern hemisphere surface temperature for simulations initialized in November (top) and May (bottom). Red means more skilful model, blue less skilful. Stippling indicates statistical significance at the 95% confidence. Model comparison against HadCRUT_V4.



Figure 66 displays the added value of initializing the forecast system with SIC data assimilation for predicting the mean seasonal surface temperature in the northern hemisphere mid- to high-latitudes. There is a general increase in predictive performance for the boreal winter (DJF) over Siberia and the North Atlantic and spring (MAM) seasons over Europe. Results are mitigated for the summer (JJA) and autumn (SON) seasons in predictions initialized in May, in agreement with the mitigated added-value of SIC assimilation for the sea ice conditions.

Figure 67 displays the added value of initializing the forecast system with SIC data assimilation for predicting mean seasonal surface precipitation in the northern hemisphere mid- to high-latitudes. Only boreal winter (DJF) precipitation skill shows significant improvement over parts of North-eastern Eurasia and Western Europe. This together with the improvement in temperature skill suggests that improved sea ice initialization leads to better climate representation during boreal winter at Eurasian mid-latitudes.

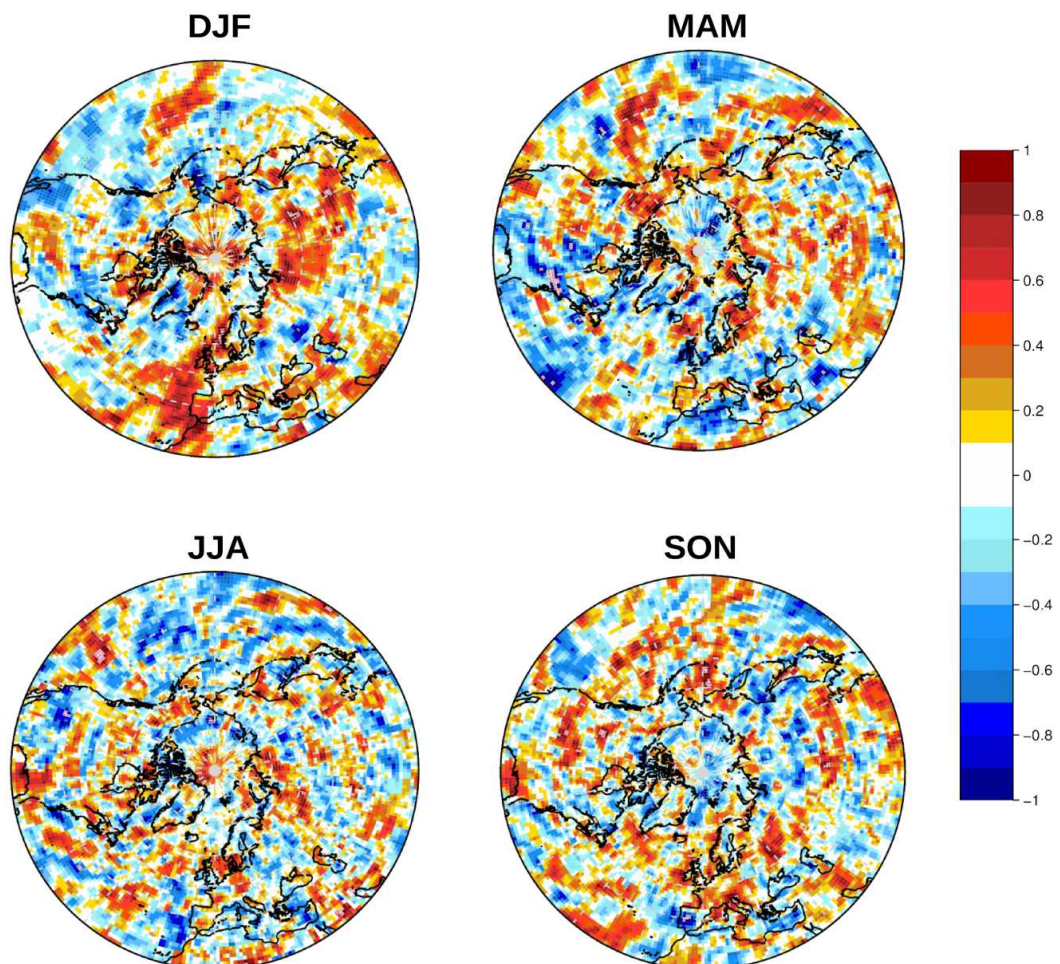


Figure 67: Added value (as a difference in correlation coefficient) from using sea ice data assimilation to initialize the model in seasonal prediction. Maps showing scores for the northern hemisphere surface precipitation for simulations initialized in November (top) and May (bottom).

CMUG Phase 2 Deliverable

Reference: D3.1: Quality Assessment Report
Due date: June 2017
Submission date: 21 December 2017
Version: 4



Red means more skilful model, blue less skilful. Stippling indicates statistical significance at the 95% confidence. Model comparison against GPCP V2.

Summary of work

The assimilation of ESA-CCI SIC data within a coupled climate reconstruction performed with EC-Earth3.2 leads to large improvements of the sea ice condition representation at high latitudes in both hemispheres with respect to the free-running model. In particular, the SIE is substantially reduced in the Northern Hemisphere during both the summer and winter seasons. The largest corrections induced by the EnKF correspond in general to regions of low SIC uncertainties as provided by the ESA-CCI product. A puzzling feature is the relatively small update obtained in summer along the Euro-Asian continental shelf in spite of low SIC uncertainties as given by ESA and prescribed into the EnKF. Longer experiments should be carried out to investigate whether successive EnKF updates correct this feature. In the SH, the EnKF corrections are comparatively larger than in the NH, mainly due to the larger model uncertainties (large model spread). The SIE ensemble after the EnKF updates becomes statistically indistinguishable from the observations. This study illustrates the substantial added-value of the ESA-CCI product as an observational reference for data assimilation since this product comes with an associated uncertainty which can be prescribed. Future lines of investigation include the exploration of the sea ice thickness and snow cover over ice products as additional sources of information to generate sea ice reanalyses. Indeed, both variables have been suggested to play a key role in the sea ice variability and predictability (Chevallier and Salas-Melia, 2012)

The assimilation of ESA-CCI sea ice concentration into the initial conditions of the EC-Earth forecast system improves the seasonal prediction capability in the northern hemisphere, particularly during the boreal winter. The model predictive capability for pan-Arctic sea ice extent and volume, surface temperature and precipitation increases in the predictions starting in November. For predictions starting in May the performance is mitigated. This result is puzzling given that sea ice predictability is thought to originate mostly from initial sea ice conditions in summer and initial ocean conditions in winter (Chevallier and Salas-Melia, 2012; Guemas et al, 2015; Guemas et al 2016).

Quality relevant outcomes

The SIC uncertainties which come with the ESA product makes it an optimal product for assimilation purposes where these uncertainties can be directly prescribed into the assimilation algorithm and balanced with the model uncertainties to compute an optimal model update. These uncertainties need however to be translated into the spatio-temporal timescales of the model to be adequately used. Refining techniques for this spatio-temporal adaptation of ESA product uncertainties will be one of the objectives of WP4 of the next ESA CMUG project. An unsuitable adaptation of these SIC uncertainties could explain the mismatch between the SIC after assimilation and in the observations along the Euro-Asian continental shelf. Information about how observational uncertainties are correlated in space and time, i.e. the off-diagonal terms of the covariance matrix could also be beneficial to the SIC assimilation. Another explanation for the Euro-Asian continental shelf mismatch would be that more successive updates or a higher resolution would be necessary to reach a better model-observation agreement. This last hypothesis will be tested within the WP3 of the next ESA CMUG project.

CMUG Phase 2 Deliverable

Reference: D3.1: Quality Assessment Report
Due date: June 2017
Submission date: 21 December 2017
Version: 4



The decrease in sea ice extent forecast quality when assimilating the ESA-CCI SIC product into the initial conditions of the EC-Earth forecast system whereas the sea ice volume forecast quality increases highlights forecast errors confined to the sea ice edge. These forecast errors could originate from different sources: 1. a misspecification of the observational errors at the sea ice edge which would reduce the quality of the reanalysis sea ice extent and therefore the prediction skill for sea ice extent (but not necessarily for sea ice volume dominated essentially by the central Arctic contribution), 2. an initial shock at the initialisation time due to the use of a sea ice reanalysis which is not fully consistent with the atmosphere initial state, 3. an inaccuracy of the forecast error estimate themselves at the sea ice edge because they do not account for observational uncertainty. The first explanation should be tested though the comparison of the observational error provided with the ESA-CCI SIC product with observational uncertainties obtained through other techniques (Bellprat et al 2017), which is one of the objectives of WP4 of the next ESA CMUG project. The second explanation should be tested through the initialisation of climate predictions from the EC-Earth simulation assimilating ESA-CCI SIC product in coupled mode which is validated above in this report, this activity being one of the objectives of WP3 of the next ESA CMUG project. The third explanation should be tested through the development of forecast quality estimates accounting for observational errors, which is one of the objectives of WP4 of the next ESA CMUG project.

CMUG Phase 2 Deliverable

Reference: D3.1: Quality Assessment Report
Due date: June 2017
Submission date: 21 December 2017
Version: 4



3.14 Assessment of Antarctic ice sheet ECVs for modelling [WP3.12]

Aims

We assess the consistency of an Antarctic ice sheet ECV within the framework of an Antarctic ice sheet model. This type of model simultaneously handles the simulation of both the grounded ice sheet and its downstream extension, the floating ice shelf that is in contact with the ocean, along with their mutual interactions. More specifically, from a modelling point of view, we assess the quality of the ECV IV (Ice Velocity, product that is not officially available yet in the CCI) through its possible use for initialising ice sheet models. This is applied to the Amundsen sea sector, where currently the most rapid ice-dynamical changes of the West Antarctic ice sheet are observed, with significant contribution to current sea level rise (Shepherd et al., 2012).

We discuss the assets of this product compared to the equivalent data that are currently being used by the ice sheet modelling community. We highlight some of the difficulties and give a series of recommendations on how this product could be improved for ice-sheet modelling purposes.

Changes with respect to the original deliverable

Our initial goal (starting in June 2016) was to apply an Antarctic wide model and a regional model to a part of Dronning Maud Land in East Antarctica, to (i) initialise the model using the ECV IV for different years over the satellite era (the last three decades), (ii) hindcast the evolution of the ice sheet, starting from the older initial state until today, in order to compare the model results to the ECV SEC (Surface Elevation change) and the GMB (Grace Mass Balance) and (iii) perform future predictions starting from the different initial states. The most important phase is the initialisation of the ice sheet, which highly determines the quality of further predictions.

The IV data for the 1990s and the 2000s appeared to be either too sparse or lacking, respectively, to enable both Antarctic wide and regional (for Dronning Maud Land) initialisations. The last decade (or the 2010s) IV data processed from the Sentinel 1 satellites by the ENVEO team were also lacking some crucial areas for initialisation purposes. For instance, the presence of data gaps (means no data at all for various reasons: proximity to the grounding line, signal coherence...) near major ice streams, such as the Jutulstraumen ice stream, did not enable to initialise the regional model with sufficient accuracy. Also, for the global model to be applied to the last decade IV, the merge that is to be made with more ancient data where lies the so-called “polar hole” (that the Sentinel 1 satellites cannot survey) is troublesome.

CMUG Phase 2 Deliverable

Reference: D3.1: Quality Assessment Report
Due date: June 2017
Submission date: 21 December 2017
Version: 4



The initialisation part being the key point in predicting future sea level contribution from Antarctica to sea level rise, we decided to investigate the Amundsen sea sector with the regional model. The main reason for this choice is, because of the rapidly changing glaciers there, the international glaciological community has had a wide opened eye over this region for the last three decades, and the amount of data available is much higher (even though not perfect) than in Dronning Maud Land, not only spatially but also temporally, meaning that older ice velocity data are available for initialisation and hindcast purposes. However, these changes did allow to reach our initial goals, i.e., to test the validity of IV data for model initialization.

Key results of CMUG research

The pattern of the initial state, composed of basal friction for grounded ice and stiffening factor, mostly for floating part, obtained from the IV processed from the Sentinel 1 satellites, is qualitatively consistent with analogous results obtained from previous ice velocity datasets.

The glaciers feeding the Amundsen sea sector have accelerated since the beginning of the 1990s, which is confirmed for the 2015-2017 period acquired by the Sentinel 1 satellites. The successive initial states obtained by the model show a clear decrease in basal friction between the bottom of the grounded ice sheet and the bed. However, partly because of poor initialisation and missing model physics (the bed beneath the Antarctic is barely known), this is so far not clear whether these changes arise from the decrease in ice-shelf buttressing, induced by an increased sub-shelf melting due to a warming ocean, or from physical changes that could occur beneath the grounded ice sheet (e.g., subglacial drainage changes). The inverse model shows also an inland propagation of shear margins of the Pine Island glacier ice shelf, which is the sign of ice shelf weakening and may indicate a disconnection of the central trunk (the main ice stream) from the ice sheet.

The 2 years period of acquisition from the Sentinel 1 satellites seems to be enough to produce an initial state, which is a major and crucial difference as opposed to the almost 20 years long mosaic that was used before (and currently) by ice-sheet modellers. For rapidly changing glaciers such as in this place of study, this is (and will be) improving the results of the ice-sheet models in the sense that they will be much closer to the actual state of the ice sheet.

Summary of work

Introduction.

A key aspect in projecting future Antarctic mass loss using ice-sheet models relies on the accuracy of the model initial state. Data assimilation methods enable to produce this initial state by keeping the initial ice-sheet geometry and surface velocity as close as possible to observations, which is done by optimising other unknown data, typically the basal friction coefficient (C) and ice stiffening factor (Φ) spatial fields.

CMUG Phase 2 Deliverable

Reference: D3.1: Quality Assessment Report
Due date: June 2017
Submission date: 21 December 2017
Version: 4



Until recently, the amount of data needed for initialisation (ice surface velocity and geometry fields) were too few and the ice-sheet modellers had to - and still - use data mosaics spanning the last 20 years. Although this might be sufficient for a steady state ice sheet, the Antarctic ice sheet, and especially its West Antarctic part, is losing mass and is thus not in steady state since at least the 1990s. Therefore, for the region of interest, data need to be collected over shorter time scales to reflect the correct state of the ice sheet for a short period of time. Acquiring the IV over the whole Antarctic ice sheet (apart from the polar hole) is now made possible by the Sentinel 1 satellites in about 2 years, which reflects more the time scales of changes that are currently occurring in West Antarctica.

Ice-sheet modelling.

We use the adaptive mesh finite-volume ice-sheet model BISICLES (<http://BISICLES.lbl.gov>). The model solves the shallow shelf approximation (SSA) and includes vertical shearing in the effective strain rate (Cornford et al., 2015), which makes the ice softer than the traditional Shallow Shelf Approximation approach at the grounding line, and induces similar ice sheet behaviour compared to non-approximated full-Stokes models (Pattyn and Durand, 2013), provided that sub-kilometric resolution is used at the grounding line when performing future predictions. The model can be used either to infer the initial state from data assimilation using a fixed geometry, or to perform transient simulations for future projections, for which the ice geometry can evolve. Here, we only used the former type of model, which is an “inverse model”.

Methodology.

The scientific purpose is to assess the temporal evolution of the Pine Island and Thwaites glaciers (Figure 1A) initial states (friction coefficient and stiffening factor) over the satellite era, covering 25 years of satellites observations. To do so, we use non-CCI and CCI data (Table 1). The most recent data of Ice Velocity are processed by ENVEO from the Sentinel 1 satellites and cover the 2015-2017 period. To produce an initial state, we also need the geometry of the ice sheet, which we reconstructed from various sources of data. Ice surface and bed elevation, firn air content and the geoid were combined to reconstruct the ice thickness for a close temporal period. We also used older datasets to produce older initial states. The purpose has an obvious scientific interest, because it can give a physical meaning to the recent acceleration of these giant glaciers, but it also enables to evaluate the consistency of the Ice Velocity data acquired and processed from the Sentinel 1 satellites.



Datasets

Datasets	2015-2017	2007-2009	1995-1996
Bed topography	Fretwell et al., 2013	Fretwell et al., 2013	Fretwell et al., 2013
Ice thickness	<u>Combination of</u> Chuter and Bamber, 2015 Helm et al., 2014 Ligtenberg et al., 2014 Forste et al. 2014	Fretwell et al., 2013	Fretwell et al., 2013
Ice temperature (for ice viscosity)	Pattyn, 2010	Pattyn, 2010	Pattyn, 2010
Ice surface velocity	Sentinel 1a-b (2015-2017)	Mouginot et al., 2017 (2007-2009)	ERS1&2 (1995-1996)

Table 1: Summary of datasets used for the different periods of time.

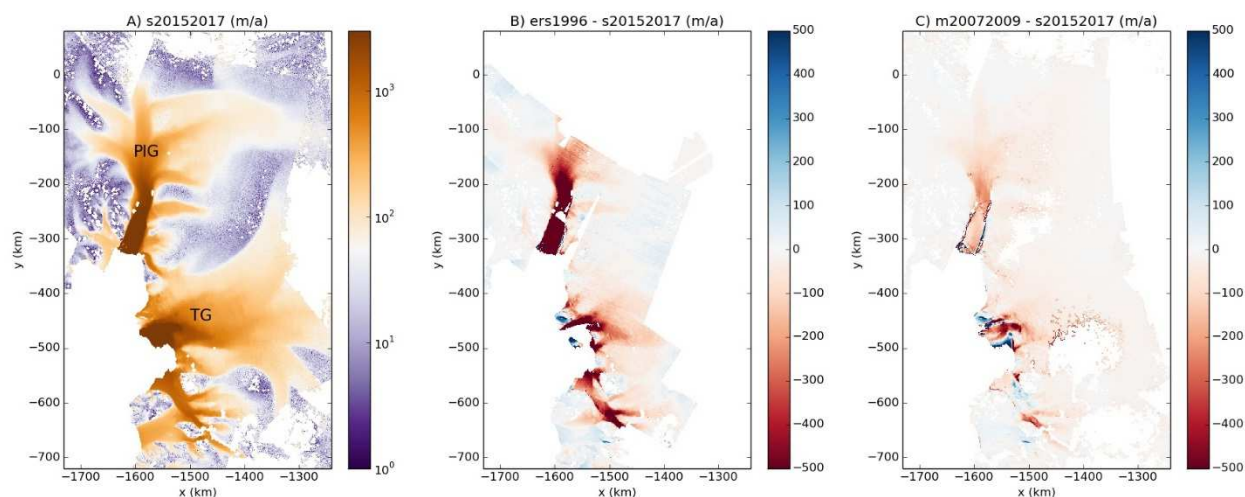


Figure 1: Ice velocity datasets from A) the Sentinel 1a-b satellites (ECV IV) for the 2015-2017 period of time, B) the ERS 1-2 satellites for the year 1995-1996 (Processed by Anders Kusk from DTU space), and C) a combination of different satellite sources (Mouginot et al, 2017). B) and C) are shown as absolute differences with A). In A) is shown the location of Pine Island glacier (PIG) and Thwaites glacier (TG). The white areas are for the ocean or for data not available.

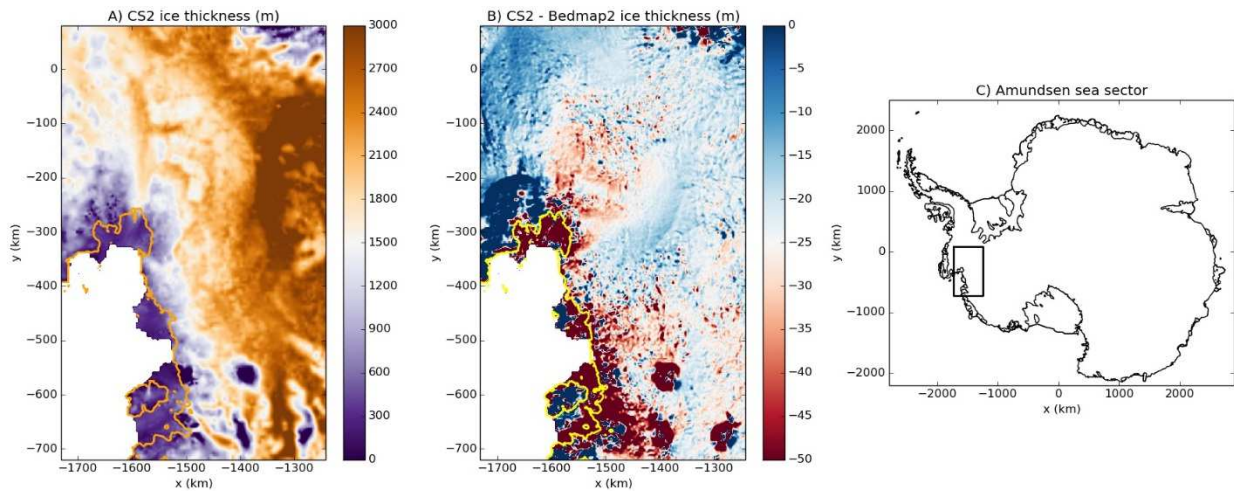


Figure 2: A) Ice thickness dataset reconstructed from the Cryosat 2 surface elevation for the 2011-2014 period (Chuter and Bamber, 2015 for the floating ice shelf and Helm et al., 2014 for the grounded ice sheet), the Firn air content (Ligtenberg et al., 2014) and the EIGEN-6C4 geoid (Forste et al., 2014) and the Bedmap2 bed elevation (Fretwell et al., 2013). B) Absolute difference between the older Bedmap2 ice thickness and the one shown in A). The orange and the yellow solid lines in A) and B) represent the limit between grounded and floating ice, the grounding line. C) Map representing the location of the Amundsen sea sector represented in the other panels.

The Sentinel 1 Ice Velocity dataset is clearly consistent and in line with the signal observed since the 1990s (Figure 1). In particular, the Pine Island (PIG) and Thwaites glaciers (TG) have constantly sped up and increased their cumulative contribution to sea level rise. The speed increase at the grounding line (that separates the grounded ice sheet from its floating ice shelf) is almost 1000 km/a since the 1990s and about 200 m/a for PIG and 500 m/a for TG. For TG, the speed-up at the grounding line is not uniform due to a nonlinear response to a partial unpinning from a submarine topographic high of the Eastern ice shelf (Rignot et al., 2014).

The ice thickness has decreased since the 1990s (Figure 2) because of both enhanced sub-shelf melting and its consequence: the loss of ice shelf buttressing that induced an upstream speed up of the ice and further thinning.

Results: initial states obtained from the inverse model

The initial state inferred by assimilating the recent data is shown in Figure 3A and Figure 4A for the friction coefficient and the stiffening factor, respectively. The results are in line with previous studies (Cornford et al., 2015) using a different set of data (ice surface velocity from Rignot et al., 2011 and ice geometry from Fretwell et al., 2013). The friction is relatively lower in the main trunks of the PIG and TG ice streams, and also in their tributaries, while it is very high for low velocity areas. Finally, the ice is made much softer in the areas where the ice is known to be

CMUG Phase 2 Deliverable

Reference: D3.1: Quality Assessment Report
Due date: June 2017
Submission date: 21 December 2017
Version: 4



fractured, which cannot be accounted for by the ice viscosity only, such as for instance the shear margins on both sides of the PIG central ice stream.

As shown by Figure 3 for the friction coefficient and Figure 4 for the stiffening factor, both resulting from the inverse model, the physical state of PIG and TG has evolved over the last two decades. The basal boundary has been more slippery during the 2015-2017 period than it was during the 2007-2009 period and even much more than it was during the 1995-1996 period. The central trunk of PIG and TG are known to slide over wet and loose sediments, which probably makes the relationship between ice velocity and the bed plastic. On the other hand, the ice shelves of PIG and TG have been thinning because of significant sub-shelf melting, which has decreased ice-shelf buttressing against the upstream ice. The consequence is to increase and transfer longitudinal stretching far upstream of the grounding line which, in the presence of a deformable plastic bed, increases the relative velocity between the ice sheet base and the bed, thus increasing basal slipperiness.

It seems that some shear margins areas, such as for instance the two located on both sides of the main ice stream of PIG, are currently extending inland, while some others, such as one separating the Eastern from the Western ice shelf of TG, are migrating sideways. In the former case, this may be the sign of drastic weakening of the ice shelf, of which the central trunk may be even more disconnected from the sideways inland ice. The latter case is more complicated insofar as the Eastern ice shelf of TG is pinned from beneath by a relatively higher topographic high (Rignot et al., 2014), and that the recent acceleration and sub-shelf melting of the TG may lead to a non-steady ice shelf unpinning, difficult to survey with accuracy.

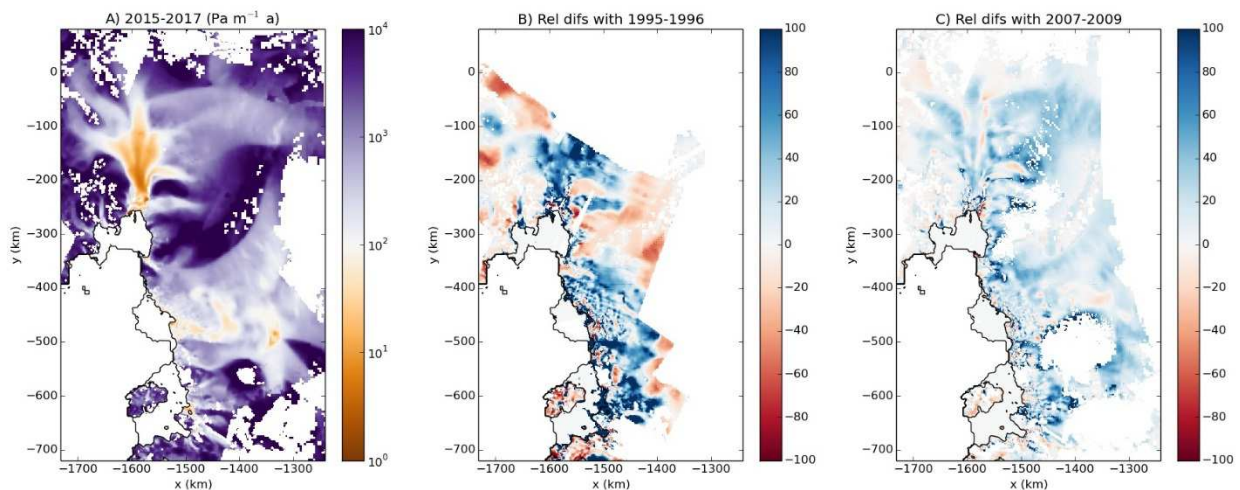


Figure 3: Friction coefficients inferred from the three datasets detailed in Table 1: A) shows the results obtained with the Sentinel 1 velocities, while B) and C) show the relative difference between these latter results and the one obtained from the other datasets detailed in Table 1. The blue colour in B) and C) thus shows that the base of the ice sheet is more slippery compared to older datasets. The white areas are for the ocean or for data not available.

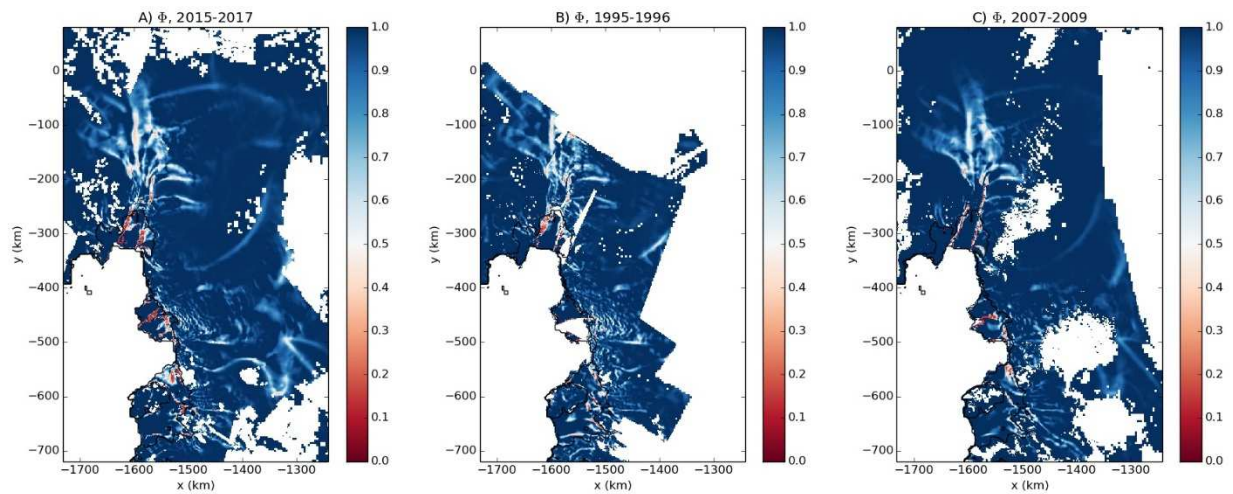


Figure 4: Stiffening factors (Φ) inferred from the three datasets shown in Table 1. A) shows the results obtained with the Sentinel 1 velocities, while B) and C) shows the results for older data. The ice is made softer by the inverse model when ice viscosity is not a sufficient parameter to describe the ice stiffness. We only authorize softening, the more red the softer the ice. For instance, the shear margins such as the two observed in Pine Island glacier ice shelf cannot be described by ice viscosity only and are thus made much softer by the inverse model. The white areas are for the ocean or for data not available.

Quality relevant outcomes

The IV product is not yet publicly available so the (minor) difficulties that we have been facing in its use may only reflect the fact that this is ongoing work.

Yet, the product appears to be quite robust in the sense that most of the IV products mapped are consistent. The spatial resolution is 200 m, which is at least 5 times better than the resolution of datasets currently used in ice sheet modelling. A major asset of this dataset is the temporal range of its acquisition to cover a substantial percentage of the Antarctic ice sheet. Two years of acquisition seem to allow consistent results obtained from our inverse model. The ice velocity dataset currently used by the ice sheet modelling community is a mosaic spanning an almost 20 years range. This may be fine for part of the ice sheet in steady state, but not at all for changing parts such as the glaciers feeding the Amundsen Sea embayment. Thus for studying the latter, this product is obviously a significant improvement.

This study was made in close collaboration with the scientific teams in charge of processing the data (ENVEO, DTU space and Leeds University), which enabled us to benefit from up-to-date data over the one year project. One of the main point when using data is how far we can trust those. This can be quantified by error maps but also by making available relevant information such as the DEM or the size of the track windows that were used, among others. All those information are crucial for ice-sheet modelling because they enable to be put in perspective with older data processed from other groups, and from which we can have a comprehensive view of ice sheet states over the satellite era. During our study, the IV product that we used was quite satisfying in

CMUG Phase 2 Deliverable

Reference: D3.1: Quality Assessment Report
Due date: June 2017
Submission date: 21 December 2017
Version: 4



the sense that the data look consistent with what was observed before. However, only the error maps and the different processing information can allow us to quantify the changes between different periods of time. For instance, looking at the evolution of the shear margins, it seems that those were moving sideways in some places, which may be interpreted as ice-sheet drastic changes, but could also be an artefact of different ways of processing the observations.

CMUG Phase 2 Deliverable

Reference: D3.1: Quality Assessment Report
Due date: June 2017
Submission date: 21 December 2017
Version: 4



3.15 Assessment of Greenland ice sheet ECVs for modelling [WP3.13]

Aims

We perform an integrated quality assessment of Greenland ice-sheet ECVs to assess their consistency within the VUB Greenland ice sheet model (GISM-VUB). An evaluation is made of their use to initialise the ice-sheet model to the current state as a prior step for future Greenland mass change and sea-level projections within ISMIP6 (CMIP6/ IPCC AR6).

The following scientific questions are addressed:

- Are the ice sheet ECVs good enough for assimilation purposes?
- What are the changes made to the analyses by assimilating the CCI data?
- Are the SEC and GMB products consistent with the modelled evolution of ice thickness and bed elevation?
- Are the uncertainties provided useful to assign observation errors to the measurements?
- Are the IV, SEC, and GMB ECVs mutually consistent from an ice-sheet assimilation point of view?

Key results of CMUG research

- Assimilation of Greenland ice sheet CCI IV surface velocity data significantly improves the representation of ice flow in the GISM-VUB ice sheet model. Missing values in the satellite products can be substituted with balance velocities, however unrealistic striping in the interior limits the use for slowly moving ice frozen to bedrock. We recommend a multi-annual averaged IV product be made available over the same time period as the SEC and GMB products for a more appropriate cross-ECV assessment.
- The SEC surface elevation change products appear as accurate and mature products for comparison with GISM-VUB output provided surface density and surface mass balance can be prescribed over the same time period. Temporal coverage is excellent, however radar altimetry data are not available along the steep margin of the Greenland ice sheet, where values are expected to be largest.
- The GMB gravimetric mass balance products have an excellent temporal and spatial coverage and appear as mature products. Incorporation of GMB products into an ice sheet modelling framework however requires to filter GISM-VUB output towards a GRACE-like spatial resolution.

Summary of work

CMUG Phase 2 Deliverable

Reference: D3.1: Quality Assessment Report
Due date: June 2017
Submission date: 21 December 2017
Version: 4



Work on the Greenland ice sheet ECVs started in October 2016 using the GISM-VUB model (Fürst et al., 2013). GISM-VUB is a higher-order 3-D thermomechanical ice flow model that freely simulates the size and shape of the Greenland ice sheet in response to changes in climate conditions. At the heart of the model is the solution of the time-dependent continuity equation for ice thickness H :

$$\frac{\partial H}{\partial t} = -\nabla \cdot (\vec{v}H) + M - S \quad (1)$$

where t is the time, \vec{v} is the vertically averaged horizontal velocity, M is the surface mass balance and S is the basal melting rate. The Greenland ice sheet CCI portal provides gridded datasets spanning various time periods on surface velocity (IV), surface elevation change from radar altimetry (SEC) and mass change trends from GRACE (GMB). These products all provide constraints on different terms in the continuity equation and can therefore be assessed within GISM-VUB. Prior to the analysis the CCI ECVs were first remapped from their original resolution (250 m and 500 m for IV, 5 km for SEC, and 40 km for GMB) to the native 5 km grid of GISM-VUB using the CDO (Climate Data Operators) bilinear interpolation tool. The experiments were performed on the ice sheet mask of GISM-VUB, thus excluding the peripheral glaciers and ice caps that surround the Greenland ice sheet.

Most of the work focused on the assimilation of observed ice velocity by a nudging procedure. The process involves adjusting the basal sliding coefficient in Weertman's basal sliding law in areas at the pressure melting point. This allows the modelled surface velocity to match the observed one. A similar procedure to adjust also the rate factor in Glen's flow law for interior regions frozen to bedrock is straightforward to implement, but was not attempted as the IV products at hand were deemed of insufficient quality in those regions, as discussed further below. Our assimilation procedure puts forward a steady state and assumes that a target field is available for every grid point. Missing pixels in the observations therefore needed to be filled in with balance velocities (e.g. Bamber et al., 2000; Huybrechts et al., 2000). The balance velocity corresponds to the depth averaged ice velocity that is required to discharge a fixed surface mass balance field given a steady state surface elevation and ice thickness. The calculated velocity values were converted into surface velocities using a multiplier corresponding to the ratio between surface velocity and vertically averaged velocity magnitude in a precursor initialisation experiment with GISM-VUB (Goelzer et al., 2013). In accordance with theory, the surface elevation field had been smoothed over a distance between 10 and 20 times the ice thickness H before being included in the balance velocity calculation. The result that provided the best fit with the observations at the overlapping pixels surrounding the missing pixels was adopted. In the assimilation procedure we used the IV product from Sentinel-1 from 2015-10-01 to 2016-10-31 added in March 2017 to the CCI data portal, as this was the dataset spanning the longest period with the least missing pixels on the 5 km grid of GISM-VUB (243 missing out of a total of 64716, or only 0.4%). In all experiments the geometric input (surface elevation, bedrock elevation and ice thickness) was taken from the Bamber et al. (2013) data set and the ice temperature was prescribed from a paleo-spin-up over several glacial-interglacial cycles, with some slight adjustments for our specific model requirements (Goelzer et al., 2013).

CMUG Phase 2 Deliverable

Reference: D3.1: Quality Assessment Report
Due date: June 2017
Submission date: 21 December 2017
Version: 4



Resulting surface velocity fields are shown in Fig. 70. The nudging was performed over 10000 years until a stationary solution was obtained with a relaxation timestep equal to 50 years for optimal results. To avoid unwanted behaviour observed velocities were only assimilated where they were larger than 5 m yr^{-1} and the adjustment of the basal sliding parameter was limited to a factor between 5 and 0.2. As expected, the modelled surface velocity is in better agreement with the observations in a simulation with data assimilation compared to a simulation without data assimilation. The improvement is particularly obvious for the NEGIS (Northeast Greenland Ice Stream). The root mean square of the normalized difference between the modelled and observed surface velocity decreases from 0.45 to 0.40 using IV. The correlation coefficient between the observed and the modelled surface velocity magnitude also displays an improvement from 0.61 for the simulation without data assimilation to 0.84 for the simulation with data assimilation.

CMUG Phase 2 Deliverable

Reference: D3.1: Quality Assessment Report

Due date: June 2017

Submission date: 21 December 2017

Version: 4

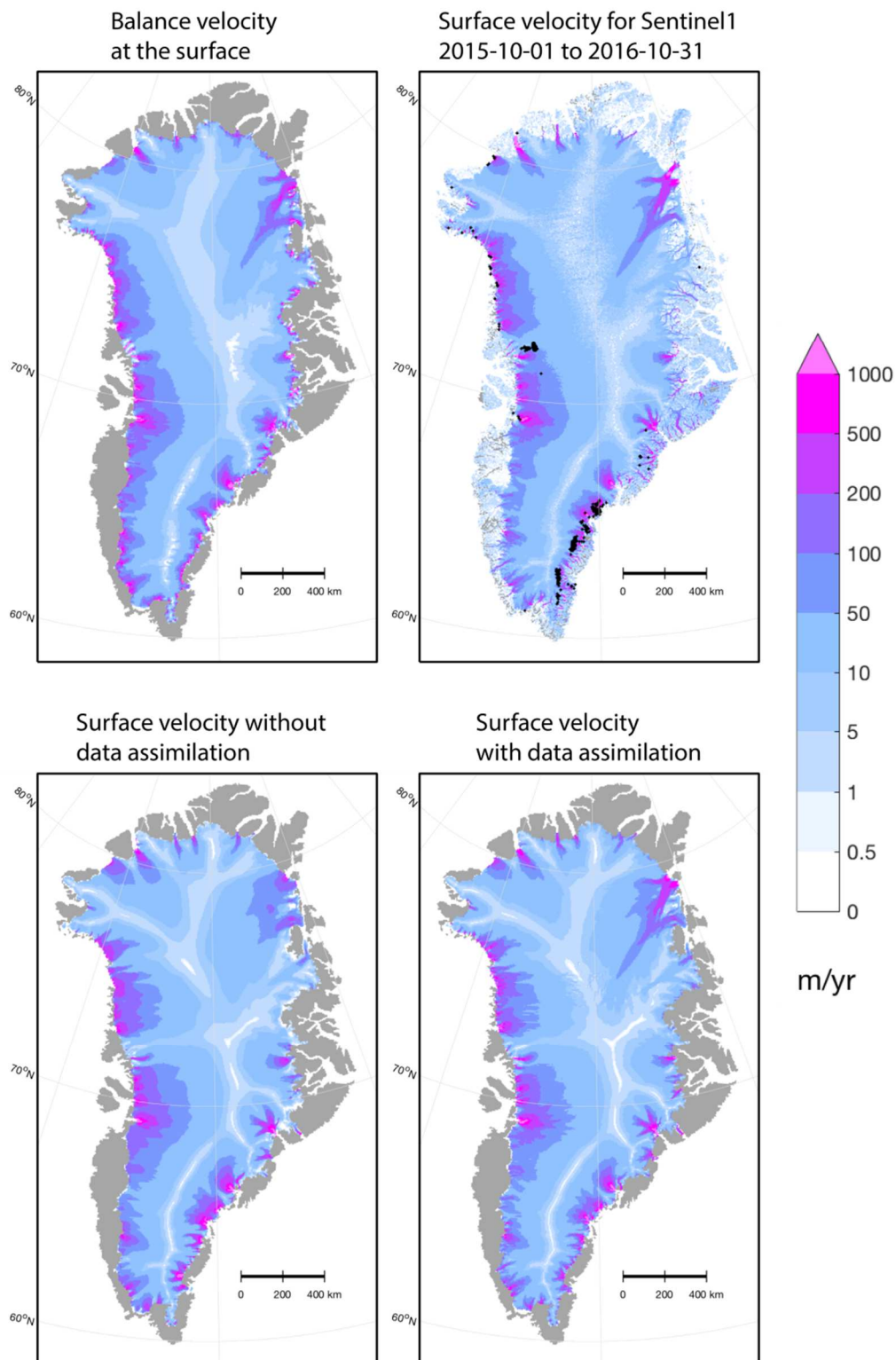


Figure 70: Surface velocity magnitude from models and observations as discussed in the text. Black spots in the Sentinel-1 data denote missing values in the best product available on the Greenland Ice Sheet CCI data portal.



The price to pay when nudging ice velocity is that ice thickness after the process will deviate from the observations, as shown in Fig. 71. Ice-sheet wide metrics such as the root mean square of normalized differences and correlation coefficients between modelled and observed ice thickness are similar in simulations with and without data assimilation, however the fit is improved in crucial areas after nudging. An optimal assimilation procedure should in fact include both ice velocity and ice thickness in a way to minimize the compounded error on both variables, which is a subject of future research.

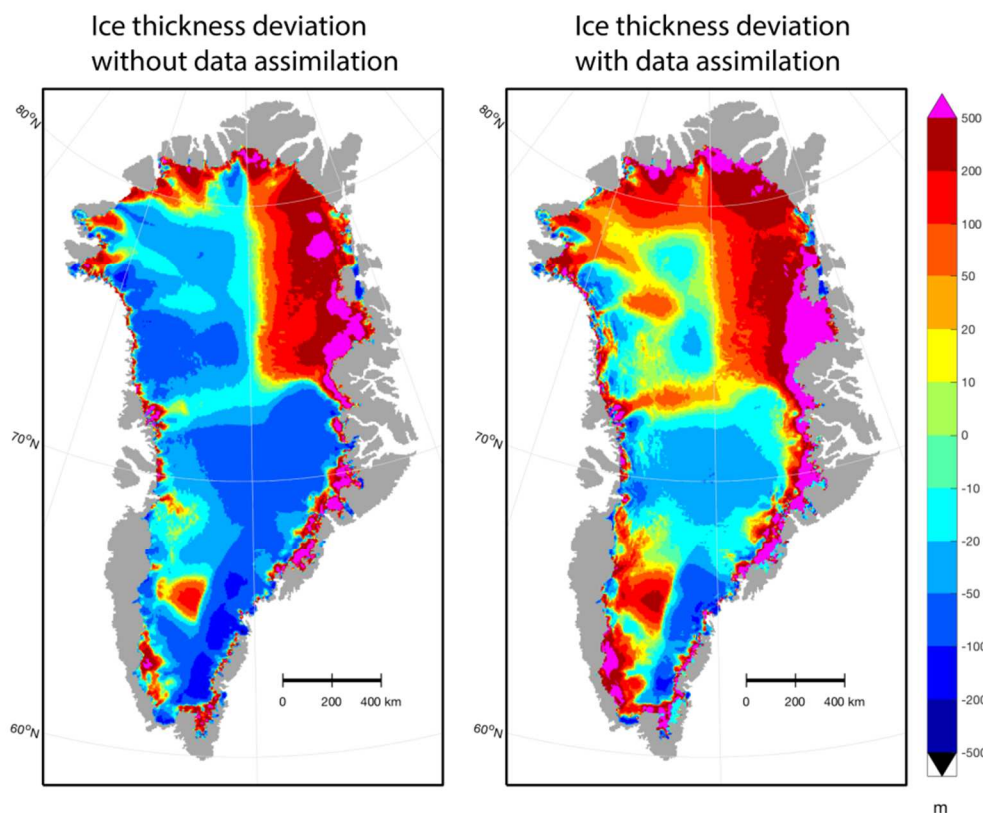


Figure 71: Difference between modelled and observed ice thickness for simulations with and without data assimilation over 10000 years. Observed ice thickness is derived from the Bamber et al. (2013) data set.

In principle it is also possible to include the observed imbalance in a data assimilation procedure to improve model initialisation. The Greenland ECVs of SEC and GMB are however not directly useable in GISM-VUB. SEC measures the real elevation change but this quantity also contains a component from bedrock elevation change and surface density change. GISM-VUB calculates mass changes in ice-equivalent meters. To be comparable with SEC these would need to be corrected for surface density. To first approximation a firm density equal to 50% of the ice density could be taken for the accumulation area. A firm assessment within an ice-sheet modelling framework would nevertheless require a well-validated surface density model. The GMB product, on the other hand, measures mass changes directly but suffers from a low spatial resolution to be directly comparable with GISM-VUB. As such GMB can only be usefully compared with an ice

CMUG Phase 2 Deliverable

Reference: D3.1: Quality Assessment Report
Due date: June 2017
Submission date: 21 December 2017
Version: 4



sheet model on an ice-sheet wide or basin-to-basin scale. An alternative approach would be to filter the GISM-VUB model output towards a GRACE-like spatial resolution to compare to the observations at the low resolution of GRACE. To assess the mutual consistence of IV, SEC, and GMB from an ice-sheet point of view it is important to realize that the flux divergence term in the continuity equation (Eq. 1) depends on slowly varying quantities, except adjacent to the ice sheet margin, but that the imbalance and surface mass balance terms have a large interannual variability. These latter terms are moreover expected to show a high mutual correlation. Hence a cross-ECV assessment requires the incorporation of the temporal evolution of the surface mass balance term M over the same time interval than the observations, as could be provided by e.g. a Regional Climate Model. Given the limitations on data availability and working time within CMUG CCI Phase 2, a more comprehensive cross-ECV assessment was not performed.

Quality relevant outcomes

Surface velocity

The IV data appear as a generally accurate and mature product that is useful for assimilation purposes in an ice sheet model. The spatial resolution of 250 to 500 m is excellent and superior to the 5 km resolution of GISM-VUB. There are however issues with the spatial and temporal coverage of at least 3 of the 4 Sentinel-1 SAR data sets available on the GIS CCI website. Either missing values comprise up to 6% of the Greenland ice sheet (3739 missing pixels out of 64716 for IV 20141101_20151201 and 3548 out of 64716 for IV 20151223_20160331), or the data cover less than 1 year, which is insufficient to average out any seasonal cycle. A common artefact to all CCI IV products are the stripes in the interior, which are not realistic. The stripes are due to ionospheric disturbances and are aligned approximately perpendicular to the satellite flight direction. These artefacts could be efficiently reduced by merging velocity data of multiple tracks (Nagler et al., 2015). Errors are not provided with the IV data, but these would be useful in more sophisticated assimilation procedures such as variational methods, Ensemble Kalman filtering, or particle filtering methods to estimate the standard deviation that weighs the importance of the observations at different locations. Errors may also be useful in the nudging approach to identify areas with stripes and to avoid assimilating these unrealistic data. For the purpose of data assimilation and cross-ECV assessment, we recommend a best covering multi-annually averaged product with reduced striping be made available over the same interval than the SEC or GMB products (3 to 5 year's average).

Surface elevation change

The SEC products are provided as 2, 4, or 5-year moving averages for the period between 1992 and 2016, which is very appropriate for comparison with GISM-VUB output. The data are given on a 5 km grid that is however slightly rotated from the 5 km grid of GISM-VUB. Errors are provided for all datasets on the website, and are usually an order of magnitude smaller than the signal itself. The products appear as an accurate and very mature product. There is however an issue with missing values towards the ice sheet margin all around the ice sheet. This is because the radar altimeter on board the ERS-1, ERS-2, Envisat, and Cryosat-2 satellites does not work on the steep terrain commonly found near the edge of an ice sheet. Unfortunately the largest surface elevation changes are expected to occur at the margin. The amount of missing values depends on the instrument, and ranges from 9.7%-11.7% of the total ice sheet area for ERS-1, ERS-2, and

CMUG Phase 2 Deliverable

Reference: D3.1: Quality Assessment Report

Due date: June 2017

Submission date: 21 December 2017

Version: 4



Envisat products to 3.6%-5.8% of the total ice sheet area for the more recent Cryosat-2 products. Fig. 72 illustrates the issue with the missing values around the margin of the Greenland ice sheet. The SEC product would only be useable in a formal assimilation procedure provided surface elevation changes can be transformed into ice-equivalent ice thickness changes and missing values can be filled in, for instance by extrapolation.

Gravimetric mass balance

The GMB products are provided as 5-year running averages since 2003 consistent with the SEC products, which is good. The GMB solutions are based on spherical harmonic functions and are presented as disks with a diameter of approximately 40 km on an icosahedron-based grid. There is no issue with spatial coverage as the entire Greenland ice sheet is represented. The GMB fields appear as mature products, however with the caveat that they represent a spatially smoothed field of mass change, and cannot be compared with GISM-VUB output directly on a pixel-by-pixel basis.

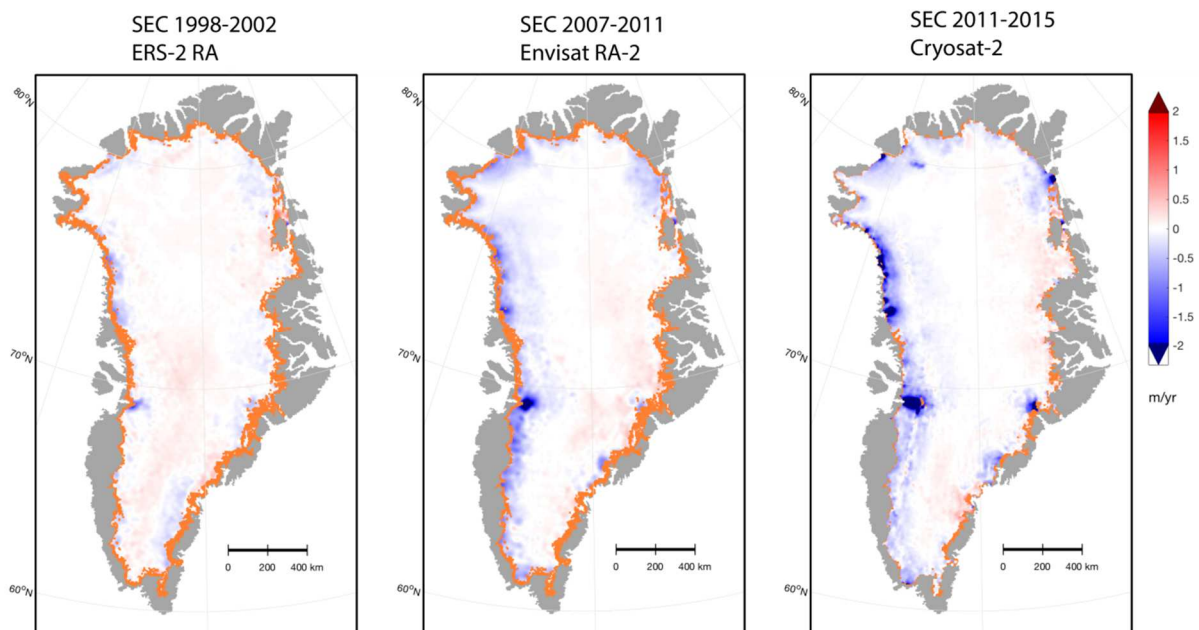


Figure 72: Examples of the SEC products available on the Greenland Ice Sheet CCI data portal. Orange values around the ice sheet margin denote missing values on the 5 km ice sheet mask of GISM-VUB.



4. References

- Adloff, F., G. Jordà, S. Somot, F. Sevault, T. Arsouze, B. Meyssignac, L. Li, and S. Planton, 2017: Improving sea level simulation in Mediterranean regional climate models. *Climate Dynamics*.
- Arheimer, B., Dahné, J., Donnelly, C., Lindström, G., Strömqvist, J. (2012). Water and nutrient simulations using the HYPE model for Sweden vs. the Baltic Sea basin – influence of input-data quality and scale. *Hydrology research* 43(4):315-329.
- Bahr, D. B., W. T. Pfeffer, and G. Kaser (2015): A review of volume-area scaling of glaciers. *Rev. Geophys.*, 53, 95–140. doi: 10.1002/2014RG000470.
- Bakker, D. C. E., Pfeil, B., Smith, K., Hankin, S., Olsen, A., Alin, S. R., Cosca, C., Harasawa, S., Kozyr, A., Nojiri, Y., O'Brien, K. M., Schuster, U., Telszewski, M., Tilbrook, B., Wada, C., Akl, J., Barbero, L., Bates, N. R., Boutin, J., Bozec, Y., Cai, W.-J., Castle, R. D., Chavez, F. P., Chen, L., Chierici, M., Currie, K., De Baar, H. J. W., Evans, W., Feely, R. A., Fransson, A., Gao, Z., Hales, B., Hardman-Mountford, N. J., Hoppema, M., Huang, W.-J., Hunt, C. W., Huss, B., Ichikawa, T., Johannessen, T., Jones, E. M., Jones, S., Jutterstrøm, S., Kitidis, V., Körtzinger, A., Landschützer, P., Lauvset, S. K., Lefèvre, N., Manke, A. B., Mathis, J. T., Merlivat, L., Metzl, N., Murata, A., Newberger, T., Omar, A. M., Ono, T., Park, G.-H., Paterson, K., Pierrot, D., Ríos, A. F., Sabine, C. L., Saito, S., Salisbury, J., Sarma, V. V. S. S., Schlitzer, R., Sieger, R., Skjelvan, I., Steinhoff, T., Sullivan, K. F., Sun, H., Sutton, A. J., Suzuki, T., Sweeney, C., Takahashi, T., Tjiputra, J., Tsurushima, N., Van Heuven, S. M. A. C., Vandemark, D., Vlahos, P., Wallace, D. W. R., Wanninkhof, R. and Watson, A. J. 2014. An update to the Surface Ocean CO₂ Atlas (SOCAT version 2), *Earth Syst. Sci. Data*, 6, 69-90.
- Balmaseda, M. A., K. Mogensen, and A. T. Weaver, 2013: Evaluation of the ECMWF ocean reanalysis system ORA-S4. *Quarterly Journal of the Royal Meteorological Society*, 139 (674), 1132–1161.
- Bamber, J. L., Griggs, J. A., Hurkmans, R. T. W. L., Dowdeswell, J. A., Gogineni, S. P., Howat, I., Mouginot, J., Paden, J., Palmer, S., Rignot, E. and Steinhage, D. (2013): A new bed elevation dataset for Greenland, *The Cryosphere*, 7(2), 499–510.
- Bamber, J. L., Hardy, R.J. and Joughin, I. (2000): An analysis of balance velocities over the Greenland ice sheet and comparison with synthetic aperture radar interferometry, *Journal of Glaciology*, 46(152), 67–74.
- Bellenger H, Guilyardi E, Leloup J, Lengaigne M, Vialard J (2014) ENSO representation in climate models: from CMIP3 to CMIP5. *Clim Dyn* 42:1999–2018.
- Bellprat, O., Massonnet F, Siegert S, Prodhomme C, Macias-Gomez D, Guemas V, Doblado-Reyes, F. Uncertainty propagation in observational references to climate model scales, RSE, submitted.

CMUG Phase 2 Deliverable

Reference: D3.1: Quality Assessment Report
Due date: June 2017
Submission date: 21 December 2017
Version: 4



- Boie, J., and L. Terray (2008), Uncertainties in summer evapotranspiration changes over Europe and implications for regional climate change, *Geophys. Res. Lett.*, *35*, L05,702, doi :10.1029/2007GL032417.
- Bryden, H.L., King, B.A., McCarthy, G.D. and McDonagh, E.L. 2014. Impact of a 30% reduction in Atlantic meridional overturning during 2009–2010. *Ocean Science*, *10*(4), pp.683-691.
- Calbó, J., Badosa, J., González, J.-A., Dmitrieva, L., Khan, V., Enríquez-Alonso, A. and Sanchez-Lorenzo, A. (2016), Climatology and changes in cloud cover in the area of the Black, Caspian, and Aral seas (1991–2010): a comparison of surface observations with satellite and reanalysis products. *Int. J. Climatol.*, *36*: 1428–1443
- Cavalieri, D. C et al. (1996) Sea ice concentrations from Nimbus-7 SMMR and DMSP SSM/I passive microwave data. National Snow and Ice Data Center. Digital media, Boulder.
- Cavalieri, D. J., P. Gloersen, and W. J. Campbell, 1984: Determination of sea ice parameters with the NIMBUS 7 SMMR. *Journal of Geophysical Research: Atmospheres* (1984–2012), *89* (D4), 5355–5369.
- Cheruy, F., A. Campoy, J.-C. Dupont, A. Ducharne, F. Hourdin, M. Haeffelin, M. Chiriaco, and A. Idelkadi (2013), Combined influence of atmospheric physics and soil hydrology on the simulated meteorology at the sirta atmospheric observatory, *Clim. Dyn.*, p. 2251–2269, doi :10.1007/s00382-012-1469-y.
- Cheruy, F., J. L. Dufresne, F. Hourdin, and A. Ducharne (2014), Role of clouds and land-atmosphere coupling in midlatitude continental summer warm biases and climate change amplification in cmip5 simulations, *Geophysical Research Letters*, *41* (18), 6493–6500, doi :10.1002/2014GL061145.
- Chevallier, M., and Salas Y Méliá, D., 2012. The role of sea ice thickness distribution in the Arctic sea ice potential predictability: a diagnostic approach with a coupled GCM. *Journal of Climate*, *25*, 3025–3038, doi:10.1175/JCLI-D-11-00209.1
- Chiodi, A. M., and D. E. Harrison, 2010: Characterizing warm-ENSO variability in the equatorial Pacific: An OLR perspective. *J. Climate*, *23*, 2428–2439, doi:10.1175/2009JCLI3030.1.
- Chiodi, A. M., and D. E. Harrison, 2013: El Niño impacts on seasonal U.S. atmospheric circulation, temperature, and precipitation anomalies: The OLR-event perspective. *J. Climate*, *26*, 822–837, doi:10.1175/JCLI-D-12-00097.1.
- Chuter, S. J. and Bamber, J. L. (2015). Antarctic ice shelf thickness from CryoSat-2 radar altimetry. *Geophys. Res. Lett.*, *42*(24):10721–10729.
- Clauss, K., Yan, H., and Kuenzer, C. (2016): Mapping Paddy Rice in China in 2002, 2005, 2010 and 2014 with MODIS Time Series. *Remote Sens.* *2016*, *8*, 434; doi:10.3390/rs8050434
- Coindreau, O., F. Hourdin, M. Haeffelin, A. Mathieu, and C. Rio (2007), Assessment of physical parameterizations using a global climate model with stretchable grid and nudging, *Monthly weather review*, *135* (4), 1474–1489.
- Collins, W. J., N. Bellouin, M. Doutriaux-Boucher, N. Gedney, P. Halloran, T. Hinton, J. Hughes, C. D. Jones, M. Joshi, S. Liddicoat, G. Martin, F. O'Connor, J. Rae, J., C. Senior, S. Sitch, I. Totterdell, A. Wiltshire, and S. Woodward (2011), Development and evaluation of an Earth-

CMUG Phase 2 Deliverable

Reference: D3.1: Quality Assessment Report
Due date: June 2017
Submission date: 21 December 2017
Version: 4



-
- System model - HadGEM2, *Geosci. Model Dev.*, 4, 1051-1075, doi: 10.5194/gmd-4-1051-2011.
- Comiso, J. C., 1995: SSM/I sea ice concentrations using the Bootstrap algorithm, Vol. 1380. National Aeronautics and Space Administration, Goddard Space Flight Center.
- Cornford, S. L., Martin, D. F., Payne, A. J., Ng, E. G., Le Brocq, A. M., Gladstone, R. M., Edwards, T. L., Shannon, S. R., Agosta, C., Van Den Broeke, M. R., Hellmer, H. H., Krinner, G., Ligtenberg, S. R. M., Timmermann, R., and Vaughan, D. G. (2015). Century-scale simulations of the response of the West Antarctic Ice Sheet to a warming climate. *Cryosphere*, 9(4):1579–1600.
- Cox, P. M., Pearson, D., Booth, B. B., Friedlingstein, P., Huntingford, C., Jones, C. D. and Luke, C. M. (2013). Sensitivity of tropical carbon to climate change constrained by carbon dioxide variability. *Nature*, 494(7437), 341-344.
- Dee, D., et al. 2011. The ERA-Interim reanalysis: Configuration and performance of the data assimilation system. *Quarterly Journal of the Royal Meteorological Society*, 137 (656), 553–597.
- De Rosnay, P., J. Polcher, M. Bruen, and K. Laval (2002), Impact of a physically based soil water flow and soil-plant interaction representation for modeling large- scale land surface processes, *Journal of Geophysical Research*, 107 (D11), 4118.
- Desroziers, G., Berre, L., Chapnik, B. and Poli, P. (2005), Diagnosis of observation, background and analysis-error statistics in observation space. *Q.J.R. Meteorol. Soc.*, **131**: 3385–3396. doi: 10.1256/qj.05.108.
- d’Orgeval, T., J. Polcher, and P. de Rosnay (2008), Sensitivity of the West African hydrological cycle in ORCHIDEE to infiltration processes, *Hydrol. Earth Syst. Sci*, 12, 1387–1401.
- Dorigo, W. A., Gruber, A., De Jeu, R. A. M., Wagner, W., Stacke, T., Loew, A., and Kidd, R. (2015). Evaluation of the ESA CCI soil moisture product using ground-based observations. *Remote Sensing of Environment*, 162, 380-395.
- Dorigo, W., W. Wagner, C. Albergel, F. Albrecht, G. Balsamo, L. Brocca, D. Chung, M. Ertl, M. Forkel, A. Gruber, E. Haas, P. D. Hamer, M. Hirschi, J. Ikonen, R. de Jeu, R. Kidd, W. Lahoz, Y. Liu, D. Miralles, and P. Lecomte (2017), Esa cci soil moisture for improved earth system understanding : State-of- the art and future directions, *Remote Sensing of Environment*.
- Dragani, R.: A comparative analysis of UV nadir-backscatter and infrared limb-emission ozone data assimilation, *Atmos. Chem. Phys. Discuss.*, doi:10.5194/acp-2016-96, 2016.
- Dufresne, J., and . co-authors (2011), Climate change projections using the ipsl-cm5 earth system model : from cmip3 to cmip5, *Climate Dynamics*, (00), 00–00.
- Dussin, R and Barnier, The making of the Drakkar Forcing Set 5, <http://www.drakkar-ocean.eu/forcing-the-ocean/the-making-of-the-drakkar-forcing-set-dfs5> (2015).
- Eastwood S. et al., 2014: Global sea ice concentration reprocessing: Product user manual, http://osisaf.met.no/docs/osisaf_cdop2_ss2_pum_sea-ice-conc-reproc_v2p2.pdf

CMUG Phase 2 Deliverable

Reference: D3.1: Quality Assessment Report
Due date: June 2017
Submission date: 21 December 2017
Version: 4



- Evensen, G., 2003: The ensemble Kalman filter: Theoretical formulation and practical implementation, *Ocean Dyn*, 53, 343–367 (2003).
- Evensen, G., 2007: *Data Assimilation—The Ensemble Kalman Filter*, Springer, N. Y. (2007).
- Ferry, N, L. Parent, G. Garric, B. Barnier, N. Jourdain, and the Mercator Ocean team, 2010: Mercator global eddy permitting ocean reanalysis glorys1v1: Description and results. Tech. rep., Mercator Ocean Q. Newsl., 36, 15–28.
- Ford, D. and Barciela, R. 2017. Global marine biogeochemical reanalyses assimilating two different sets of merged ocean colour products, *Remote Sensing of Environment*, <https://doi.org/10.1016/j.rse.2017.03.040>.
- Ford, D. A., Edwards, K. P., Lea, D., Barciela, R. M., Martin, M. J., and Demaria, J. 2012. Assimilating GlobColour ocean colour data into a pre-operational physical-biogeochemical model, *Ocean Sci.*, 8: 751-771.
- Förste, C., Bruinsma, S. L., Abrikosov, O., Lemoine, J.-M., Marty, J. C., Flechtner, F., Balmino, G., Barthelmes, F., and Biancale, R. (2014). EIGEN-6C4 The latest combined global gravity field model including GOCE data up to degree and order 2190 of GFZ Potsdam and GRGS Toulouse.
- Fretwell, P., Pritchard, H. D., Vaughan, D. G., Bamber, J. L., Barrand, N. E., Bell, R., Bianchi, C., Bingham, R. G., Blankenship, D. D., Casassa, G., Catania, G., Callens, D., Conway, H., Cook, A. J., Corr, H. F., Damaske, D., Damm, V., Ferraccioli, F., Forsberg, R., Fujita, S., Gim, Y., Gogineni, P., Griggs, J. A., Hindmarsh, R. C., Holmlund, P., Holt, J. W., Jacobel, R. W., Jenkins, A., Jokat, W., Jordan, T., King, E. C., Kohler, J., Krabill, W., Riger-Kusk, M., Langle, K. A., Leitchenkov, G., Leuschen, C., Luyendyk, B. P., Matsuoka, K., Mouginot, J., Nitsche, F. O., Nogi, Y., Nost, O. A., Popov, S. V., Rignot, E., Rippin, D. M., Rivera, A., Roberts, J., Ross, N., Siegert, M. J., Smith, A. M., Steinhage, D., Studinger, M., Sun, B., Tinto, B. K., Welch, B. C., Wilson, D., Young, D. A., Xiangbin, C., and Zirizzotti, A. (2013). Bedmap2: Improved ice bed, surface and thickness datasets for Antarctica. *Cryosphere*, 7(1):375–393.
- Fürst, J.J., H. Goelzer, and P. Huybrechts (2013): Effect of higher-order stress gradients on the centennial mass evolution of the Greenland ice sheet, *The Cryosphere*, 7, 183-199.
- Gehlen, M., Barciela, R., Bertino, L., Brasseur, P., Butenschön, M., Chai, F., Crise, A., Drillet, Y., Ford, D., Lavoie, D. and Lehodey, P., Perruche, C., Samuelsen, A., and Simon E. 2015. Building the capacity for forecasting marine biogeochemistry and ecosystems: recent advances and future developments. *Journal of Operational Oceanography*, 8(sup1), pp.s 168-s187.
- Giglio, L., van der Werf, G. R., Randerson, J. T., Collatz, G. J., and Kasibhatla, P.; Global estimation of burned area using MODIS active fire observations, *Atmos. Chem. Phys.*, 6, 957–974, (2006).
- Giglio, L.; Randerson, J. T.; Werf, G. R.; Kasibhatla, P. S.; Collatz, G. J.; Morton, D. C.; DeFries, R. S. Assessing variability and long-term trends in burned area by merging multiple satellite fire products. *Biogeosciences* 2010, 7, 1171–1186.

CMUG Phase 2 Deliverable

Reference: D3.1: Quality Assessment Report
Due date: June 2017
Submission date: 21 December 2017
Version: 4



- Goelzer, H., Huybrechts, P., Fürst, J. J., Nick, F. M., Andersen, M. L., Edwards, T. L., Fettweis, X., Payne, A. J. and Shannon, S. (2013): Sensitivity of Greenland ice sheet projections to model formulations, *Journal of Glaciology*, 59(216), 733–749.
- Good, S.A., Martin, M.J. and Rayner, N.A. 2013. EN4: Quality controlled ocean temperature and salinity profiles and monthly objective analyses with uncertainty estimates. *Journal of Geophysical Research: Oceans*, 118(12), pp.6704-6716.
- Groisman, P. Ya., et al., 2007: Potential forest fire danger over northern Eurasia: Changes during the 20th century. *Global Planet. Change*, 46, doi:10.1016/j.gloplacha.2006.07.029.
- Guemas V, Blanchard-Wrigglesworth E, Chevallier M, Day J J, Déqué M, Doblas-Reyes F J, Fučkar N, Germe A, Hawkins E, Keeley S, Koenigk T, Salas y Mélia D, Tietsche S, 2015, A review on Arctic sea ice predictability and prediction on seasonal-to-decadal timescales, *Quarterly Journal of the Royal Meteorology Society*, doi:10.1002/qj.2401.
- Guémas, V., Chevallier, M., Déqué, M., Bellprat, O., Doblas-Reyes, F., 2016. Impact of sea ice initialization on sea ice and atmosphere prediction skill on seasonal timescales. *Geophysical Research Letters*, 43, 3889-3896, doi:10.1002/2015GL066626.
- Hantson, S., et al 2016: The status and challenge of global fire modeling. *Biogeosciences*, 13, 3359–3375, 2016. www.biogeosciences.net/13/3359/2016/ doi:10.5194/bg-13-3359-2016
- Harris, I., Jones, P.D., Osborn, T.J. and Lister, D.H., 2014: Updated high-resolution grids of monthly climatic observations – the CRU TS3.10 Dataset. *Int. J. Climatol.*, 34, 623–642
- Haylock, M. R., N. Hofstra, A. M. G. Klein Tank, E. J. Klok, P. D. Jones, and M. New, 2008: A European daily high-resolution gridded data set of surface temperature and precipitation for, *J. Geophys. Res.*, 113, 1950–2006.
- Hazeleger, W., C. Severijns, T. Semmler, S. Ștefănescu, S. Yang, X. Wang, K. Wyser, E. Dutra, M. Baldasano, R. Bintanja, P. Bougeault, R. Caballero, A. M. L. Ekman, J. H. Christensen, B. van den Hurk, P. Jimenez, C. Jones, P. Kållberg, T. Koenigk, R. Mc Grath, P. Miranda, T. van Noije, T. Palmer, J. A. Parodi, T. Schmith, F. Selten, T. Storelvmo, A. Sterl, H. Tapamo, M. Vancoppenolle, P. Viterbo, and U. Willén (2010), EC-Earth, A Seamless Earth-System Prediction Approach in Action, *Bull. Am. Meteor. Soc.*, 91, 1357-1363, doi: 10.1175/2010BAMS2877.1.
- Heidinger AK, Foster MJ, Walther A, Zhao X. 2014. The pathfinder atmospheres extended AVHRR climate dataset. *Am. Meteorol. Soc.* 95: 909–922
- Helm, V., Humbert, A., and Miller, H. (2014). Elevation and elevation change of Greenland and Antarctica derived from CryoSat-2. *Cryosphere*, 8(4):1539–1559.
- Hemmings, J. C. P., Barciela, R. M., and Bell, M. J. 2008. Ocean color data assimilation with material conservation for improving model estimates of air-sea CO₂ flux. *J. Mar. Res.*, 66: 87-126.
- Horvat, C., Jones, D.R., Iams, S., Schroeder, D., Flocco, D. and Feltham, D. 2017. The frequency and extent of sub-ice phytoplankton blooms in the Arctic Ocean. *Science Advances*, 3(3), p.e1601191.

CMUG Phase 2 Deliverable

Reference: D3.1: Quality Assessment Report
Due date: June 2017
Submission date: 21 December 2017
Version: 4



- Hourdin, F., J. Grandpeix, C. Rio, C. Bony, A. Jam, F. Cheruy, N. Rochetin, L. Fairhead, A. Idelkadi, I. Musat, J.-L. Dufresne, M.-P. Lefebvre, A. Lahellec, and R. Roehrig (2011), From lmdz5a to lmdz5b revisiting the parameterizations of clouds and convection in the atmospheric component of the ipsl-cm5 climate model, *Climate Dynamics*, (00), 00–00.
- Hourdin, F., M.-A. Foujols, F. Codron, V. Guemas, J.-L. Dufresne, S. Bony, S. Denvil, L. Guez, F. Lott, J. Ghattas, P. Braconnot, O. Marti, Y. Meurdesoif, L. Bopp (2013), Impact of the LMDZ atmospheric grid configuration on the climate and sensitivity of the IPSL-CM5A coupled model, *Clim. Dyn.*, 40, 2167–2192, doi: 10.1007/s00382-012-1411-3.
- Huss, M., and D. Farinotti (2012), Distributed ice thickness and volume of all glaciers around the globe, *J. Geophys. Res.*, 117, F04010, doi:10.1029/2012JF002523.
- Huybrechts, P., D. Steinhage, F. Wilhelms, and J.L. Bamber (2000): Balance velocities and measured properties of the Antarctic ice sheet from a new compilation of gridded data for modelling. *Annals of Glaciology*, 30, 52-60.
- Ivanova, N., Pedersen, L. T., Tonboe, et al. (2015). Inter-comparison and evaluation of sea ice algorithms: towards further identification of challenges and optimal approach using passive microwave observations. *The Cryosphere*, 9(5), 1797–1817. <http://doi.org/10.5194/tc-9-1797-2015>
- Jackson, L.C., Peterson, K.A., Roberts, C.D. and Wood, R.A. 2016. Recent slowing of Atlantic overturning circulation as a recovery from earlier strengthening. *Nature Geoscience*, 9(7), pp.518-522.
- Jam, A., F. Hourdin, C. Rio, and F. Couvreux (2013), Resolved versus parametrized boundary-layer plumes. part iii : Derivation of a statistical scheme for cumulus clouds, *Boundary-Layer Meteorology*, 147 (3), 421–441, doi :10.1007/s10546-012- 9789-3.
- Jung, M., M. Reichstein, H. A. Margolis, A. Cescatti, A. D. Richardson, M. A. Arain, A. Arneth, C. Bernhofer, D. Bonal, J. Chen, D. Gianelle, N. Gobron, G. Kiely, W. Kutsch, G. Lasslop, B. E. Law, A. Lindroth, L. Merbold, L. Montagnani, E. J. Moors, D. Papale, M. Sottocornola, F. Vaccari, and C. Williams (2011), Global patterns of land-atmosphere fluxes of carbon dioxide, latent heat, and sensible heat derived from eddy covariance, satellite, and meteorological observations, *Journal of Geophysical Research: Biogeosciences*, 116 (G3), n/a–n/a, doi :10.1029/2010JG001566, g00J07.
- Karlsson, K.-G., A. Riihelä, R. Müller, J. F. Meirink, J. Sedlar, M. Stengel, M. Lockhoff, J. Trentmann, F. Kaspar, R. Hollmann, and E. Wolters (2013), CLARA-A1: a cloud, albedo, and radiation dataset from 28 yr of global AVHRR data, *Atmos. Chem. Phys.*, 13, 5351–5367, doi:10.5194/acp-13-5351-2013.
- Kaspar, F., Hollmann, R., Lockhoff, M., Karlsson, K.-G., Dybbroe, A., Fuchs, P., Selbach, N., Stein, D., and Schulz, J., 2009: Operational generation of AVHRR-based cloud products for Europe and the Arctic at EUMETSAT's Satellite Application Facility on Climate Monitoring (CM-SAF), *Adv. Sci. Res.*, 3, 45-51, doi: 10.5194/asr-3-45-2009
- Kato, S., N. G. Loeb, F. G. Rose, D. R. Doelling, D. A. Rutan, T. E. Caldwell, L. Yu, and R. A. Weller (2013), Surface irradiances consistent with ceres-derived top-of-atmosphere

CMUG Phase 2 Deliverable

Reference: D3.1: Quality Assessment Report
Due date: June 2017
Submission date: 21 December 2017
Version: 4



-
- shortwave and longwave irradiances, *Journal of Climate*, 26 (9), 2719–2740, doi :10.1175/JCLI-D-12-00436.1.
- Koster, R. D., Z. Guo, R. Yang, P. A. Dirmeyer, K. Mitchell, and M. J. Puma (2009), On the nature of soil moisture in land surface models, *Journal of Climate*, 22 (16), 4322–4335, doi :10.1175/2009JCLI2832.1.
- Krinner, G., N. Viovy, N. de Noblet-Ducoudre, J. Ogee, J. Polcher, P. Friedlingstein, P. Ciais, S. Sitch, and I. Prentice (2005), A dynamic global vegetation model for studies of the coupled atmosphere-biosphere system, *Global Biogeochem. Cycles*, 19 (1).
- Lau, K-M., H-T. Wu, and S. Bony, 1997: The role of large-scale atmospheric circulation in the relationship between tropical convection and sea surface temperature. *J. Climate*, **10**, 381–392
- Lasslop, G., K. Thonicke, and S. Kloster, SPITFIRE within the MPI Earth system model: Model development and evaluation, *J. Adv. Model. Earth Syst.*, **2014**, 6, 740–755, doi:10.1002/2013MS000284.
- Lebeaupin-Brossier, C, P., Drobinski, K. Béranger, S. Bastin, and F. Orain, 2013: Ocean memory effect on the dynamics of coastal heavy precipitation preceded by a mistral event in the northwestern Mediterranean. *Quarterly Journal of the Royal Meteorological Society* 139(3-4), 1583–1597, Doi: 10.1007/s00382-014-2252-z.
- L’Heureux, M., M. K. Tippett, and A. G. Barnston, 2015: Characterizing ENSO coupled variability and its impact on North American seasonal precipitation and temperature. *J. Climate*, **28**, 4231–4245, doi: <https://doi.org/10.1175/JCLI-D-14-00508.1>.
- L’Hévéder, B, L. Li, F. Sevault, and S. Somot, 2013: Interannual variability of deep convection in the Northwestern Mediterranean simulated with a coupled AORCM. *Climate Dynamics* 41(3-4), 937–960, Doi: 10.1007/s00382-012-1527-5.
- Liebmann, B., and C. A. Smith, 1996: Description of a complete (interpolated) outgoing longwave radiation dataset. *Bull. Amer. Meteor. Soc.*, **77**, 1275–1277.
- Ligtenberg, S. R. M., Kuipers Munneke, P., and Van Den Broeke, M. R. (2014). Present and future variations in Antarctic firn air content. *Cryosphere*, 8(5):1711–1723.
- Lindstedt, D., Lind, P., Jones, C., Kjellström, E., 2015. A new regional climate model operating at the meso-gamma scale; performance over Europe. *Tellus A* 67, 24138, doi: 10.3402/tellusa.v67.24138.
- Lindström, G., Pers, C., Rosberg, J., Strömqvist, J. and Arheimer, B. (2010) Development and testing of the HYPE (Hydrological Predictions for the Environment) water quality model for different spatial scales. *Hydrology Research* 41.3–4, 295-319.
- Loeb, N. G., Kato, S., Su, W., Wong, T., Rose, F. G., Doelling, D. R., Norris, J. R., and Huang, X.: Advances in Understanding Top-of-Atmosphere Radiation Variability from Satellite Observations, *Surv. Geophys.*, 33, 359–385, doi:10.1007/s10712-012-9175-1, 2012
- Loew, A., Stacke, T., Dorigo, W., Jeu, R. D., Hagemann, S. (2013). Potential and limitations of multidecadal satellite soil moisture observations for selected climate model evaluation studies. *Hydrology and Earth System Sciences*, 17(9), 3523-3542.

CMUG Phase 2 Deliverable

Reference: D3.1: Quality Assessment Report
Due date: June 2017
Submission date: 21 December 2017
Version: 4



- Madec, G., and the NEMO team: "NEMO ocean engine". Note du Pôle de modélisation, Institut Pierre-Simon Laplace (IPSL), France, No 27 ISSN No 1288-1619 (2016)
- Martens, B., D. G. Miralles, H. Lievens, R. van der Schalie, R. A. M. de Jeu, D. Fernandez-Prieto, H. E. Beck, W. A. Dorigo, and N. E. C. Verhoest (2017), Gleam v3 : satellite-based land evaporation and root-zone soil moisture, *Geoscientific Model Development*, 10 (5), 1903–1925, doi : 10.5194/gmd-10-1903-2017.
- Massonnet, F., et al., 2015: Prospects for improved seasonal Arctic sea ice predictions from multivariate data assimilation, *Oc. Modell.*, <http://dx.doi.org/10.1016/j.ocemod.2014.12.013>
- Megann, A., Storkey, D., Aksenov, Y., Alderson, S., Calvert, D., Graham, T., Hyder, P., Siddorn, J. and Sinha, B. 2014. GO5. 0: The joint NERC-Met Office NEMO global ocean model for use in coupled and forced applications. *Geoscientific Model Development*, 7(3), pp.1069-1092.
- Merchant, C. J., O. Embury, J. Roberts-Jones, E. K. Fiedler, C. E. Bulgin, G. K. Corlett, S. Good, A. McLaren, N. A. Rayner, and C. Donlon (2014b), ESA Sea Surface Temperature Climate Change Initiative (ESA SST CCI): Analysis long term product version 1.0, NERC Earth Observation Data Centre, 24th February 2014, doi: 10.5285/878bef44-d32a-40cd-a02d-49b6286f0ea4.
- Mitchell, T., and P. Jones (2005), An improved method of constructing a database of monthly climate observations and associated high-resolution grids., *International Journal of Climatology*, 25, 693–712, doi :10.1002/joc.1181.
- Mouginot, J., Rignot, E., Scheuchl, B., and Millan, R. (2017). Comprehensive annual ice sheet velocity mapping using Landsat-8, Sentinel-1, and RADARSAT-2 data. *Remote Sens.*, 9(4):1–20.
- Nagler, T., H. Rott, M. Hetzenecker, J. Wuite, and P. Potin (2015): The Sentinel-1 Mission: New Opportunities for Ice Sheet Observations, *Remote Sensing*, 7, 9371-9389.
- NASS (2012): United States, Summary and State Data. 2012 Census of Agriculture, Volume 1, Geographic Area Series, Part 51, National Agricultural Statistics Service (NASS), US Department of Agriculture, https://www.agcensus.usda.gov/Publications/2012/Full_Report/Volume_1,_Chapter_1_US/usv1.pdf.
- Orth, R., and S. Seneviratne (2017), Variability of soil moisture and sea surface temperatures similarly important for warm season land climate in the community earth system model, *Journal of Climate*, 30, 2141–2162, doi :doi :10.1175/JCLI-D- 15-0567.1.
- Palmer, J. R., and Totterdell, I. J. 2001. Production and export in a global ocean ecosystem model, *p-Sea Res. Pt. I*, 48: 1169-1198.
- Pattyn, F. (2010). Antarctic subglacial conditions inferred from a hybrid ice sheet/ice stream model. *Earth Planet. Sci. Lett.*, 295(3-4):451–461.
- Pattyn, F. and Durand, G. (2013). Why marine ice sheet model predictions may diverge in estimating future sea level rise. *Geophys. Res. Lett.*, 40(16):4316–4320.

CMUG Phase 2 Deliverable

Reference: D3.1: Quality Assessment Report
Due date: June 2017
Submission date: 21 December 2017
Version: 4



- Pekel, J.-F., Cottam, A., Gorelick, N., and Belward, A. S. (2016): High-resolution mapping of global surface water and its long-term changes. *Nature* 540, 418–422, doi:10.1038/nature20584.
- Portmann, F. T., S. Siebert, and P. Döll (2010), MIRCA2000—Global monthly irrigated and rainfed crop areas around the year 2000: A new high-resolution data set for agricultural and hydrological modeling, *Global Biogeochem. Cycles*, 24, GB1011, doi:10.1029/2008GB003435.
- Poulter B., N. MacBean, A. Hartley, I. Khlystova, O. Arino, R. Betts, S. Bontemps, M. Boettcher, C. Brockmann, P. Defourny, S. Hagemann, M. Herold, G. Kirches, C. Lamarche, D. Lederer, C. Otlé, M. Peters and P. Peylin: 2015: Plant functional type classification for earth system models: results from the European Space Agency’s Land Cover Climate Change Initiative. *Geosci. Model Dev.*, 8, 2315–2328, 2015, www.geosci-model-dev.net/8/2315/2015/ doi:10.5194/gmd-8-2315-2015
- Quartly, G. D., Legeais, J.-F., Ablain, M., Zawadzki, L., Fernandes, M. J., Rudenko, S., Carrère, L., García, P. N., Cipollini, P., Andersen, O. B., Poisson, J.-C., Mbajon Njiche, S., Cazenave, A., and Benveniste, J.: A new phase in the production of quality-controlled sea level data, *Earth Syst. Sci. Data Discuss.*, doi:10.5194/essd-2017-23, in review, 2017.
- Raddatz, T. J., C. J. Reick, W. Knorr, J. Kattge, E. Roeckner, R. Schnur, K.-G. Schnitzler, P. Wetzell, and J. Jungclaus (2007), Will the tropical land biosphere dominate the climate-carbon cycle feedback during the twenty-first century? *Clim. Dyn.*, 29, 565–574, doi:10.1007/s00382-007-0247-8
- Raghukumar, K., Edwards, C.A., Goebel, N.L., Broquet, G., Veneziani, M., Moore, A.M. and Zehr, J.P. 2015. Impact of assimilating physical oceanographic data on modeled ecosystem dynamics in the California Current System. *Progress in Oceanography*, 138, pp.546-558.
- Rayner, N. A., D. E. Parker, E. B. Horton, C. K. Folland, L. V. Alexander, D. P. Rowell, E. C. Kent, and A. Kaplan (2003), Global analyses of sea surface temperature, sea ice, and night marine air temperature since the late nineteenth century, *J. Geophys. Res.*, 108, 4407
- Reichle, R. H., Koster, R. D., Dong, J. and Berg, A. A. (2004). Global soil moisture from satellite observations, land surface models, and ground data: Implications for data assimilation. *Journal of Hydrometeorology*, 5(3), 430-442.
- Rignot, E. (2001). Evidence for rapid retreat and mass loss of Thwaites Glacier, West Antarctica. *J. Glaciol.*, 47(157):213–222.
- Rignot, E., Mouginot, J., Morlighem, M., Seroussi, H., and Scheuchl, B. (2014). Widespread, rapid grounding line retreat of Pine Island, Thwaites, Smith, and Kohler glaciers, West Antarctica, from 1992 to 2011. *Geophys. Res. Lett.*, 41(10):3502–3509.
- Roberts, C.D., Waters, J., Peterson, K.A., Palmer, M.D., McCarthy, G.D., Frajka□Williams, E., Haines, K., Lea, D.J., Martin, M.J., Storkey, D., Blockley, E.W. and Zuo, H. 2013. Atmosphere drives recent interannual variability of the Atlantic meridional overturning circulation at 26.5 N. *Geophysical Research Letters*, 40(19), pp.5164-5170.

CMUG Phase 2 Deliverable

Reference: D3.1: Quality Assessment Report
Due date: June 2017
Submission date: 21 December 2017
Version: 4



- Rio, C., F. Hourdin, F. Couvreux, and A. Jam (2010), Resolved Versus Parametrized Boundary-Layer Plumes. Part II : Continuous Formulations of Mixing Rates for Mass-Flux Schemes, *Boundary Layer Meteorology*, 135, 469–483, doi : 10.1007/s10546-010-9478-z.
- Rodell, M., P. R. Houser, U. Jambor, J. Gottschalck, K. Mitchell, C.-J. Meng, K. Arsenault, B. Cosgrove, J. Radakovich, M. Bosilovich, J. K. Entin, J. P. Walker, D. Lohmann, and D. Toll (2004), The global land data assimilation system, *Bulletin of the American Meteorological Society*, 85 (3), 381–394, doi : 10.1175/BAMS-85-3-381.
- Samuelsson, P., Gollvik, S., Jansson, C., Kupiainen, M., Kourzeneva, E., van de Berg, W., 2014. The surface processes of the Rossby Centre regional atmospheric climate model (RCA4). Report in Meteorology 157, SMHI, SE-601 76 Norrköping, Sweden.
- Schaap, M. G., F. J. Leij, and M. T. van Genuchten (2001), rosetta: a computer program for estimating soil hydraulic parameters with hierarchical pedotransfer functions, *Journal of Hydrology*, 251 (3), 163 – 176, doi : [https://doi.org/10.1016/S0022-1694\(01\)00466-8](https://doi.org/10.1016/S0022-1694(01)00466-8).
- Sevault F., S. Somot, A. Alias, C. Dubois, C. Lebeaupin-Brossier, P. Nabat, F. Adloff, M. Déqué, and B. Decharme, 2014: A fully coupled Mediterranean regional climate system model: design and evaluation of the ocean component for the 1980-2012 period. *Tellus A*, 66, 23967, <http://dx.doi.org/10.3402/tellusa.v66.23967>.
- Shepherd, A., Ivins, E. R., A. G., Barletta, V. R., Bentley, M. J., Bettadpur, S., Briggs, K. H., Bromwich, D. H., Forsberg, R., Galin, N., Horwath, M., Jacobs, S., Joughin, I., King, M. a., Lenaerts, J. T. M., Li, J., Ligtenberg, S. R. M., Luckman, A., Luthcke, S. B., McMillan, M., Meister, R., Milne, G., Mouginot, J., Muir, A., Nicolas, J. P., Paden, J., Payne, a. J., Pritchard, H., Rignot, E., Rott, H., Sorensen, L. S., Scambos, T. a., Scheuchl, B., Schrama, E. J. O., Smith, B., Sundal, a. V., van Angelen, J. H., van de Berg, W. J., van den Broeke, M. R., Vaughan, D. G., Velicogna, I., Wahr, J., Whitehouse, P. L., Wingham, D. J., Yi, D., Young, D., and Zwally, H. J. (2012). A Reconciled Estimate of Ice-Sheet Mass Balance. *Science* (80)., 338(6111):1183–1189.
- Siebert, S., Doll, P., Hoogeveen, J., Faures, J.-M., Frenken, K., and Feick, S. (2005): Development and validation of the global map of irrigation areas, *Hydrol. Earth Syst. Sci.*, 9, 535–547, doi:10.5194/hess-9-535-2005.
- Stengel, M., Mieruch, S., Jerg, M., Karlsson, K.-G., Scheirer, R., Maddux, B., Meirink, J.F., Poulsen, C., Siddans, R., Walther, A., Hollmann, R. 2013: The Clouds Climate Change Initiative: Assessment of state-of-the-art cloud property retrieval schemes applied to AVHRR heritage measurements, 2015: *Remote Sens. Environ.*, 162, 363–379
- Stengel M., C. Poulsen, G. Thomas, M. Christiansen, C. Carbajal Henken, R. Preusker, J. Fischer, O. Sus, S. Stapelberg, C. Schlundt, A. Devasthale, U. Willén, K.-G. Karlsson, A. Povey, D. Grainger, S. Proud, J. F. Meirink, A. Feofilov, and R. Hollmann (2016), Cloud property datasets retrieved from AVHRR, MODIS, AATSR and MERIS in the framework of the Cloud_cci project, manuscript submitted.
- Stevens, B., et al., 2013: Atmospheric component of the MPI-M Earth System Model: ECHAM6. *Journal of Advances in Modeling Earth Systems*, 5 (2), 146–172.

CMUG Phase 2 Deliverable

Reference: D3.1: Quality Assessment Report
Due date: June 2017
Submission date: 21 December 2017
Version: 4



- Storkey, D., Blockley, E. W., Furner, R., Guiavarc'h, C., Lea, D., Martin, M. J., Barciela, R. M., Hines, A., Hyder, P., and Siddorn, J. R. 2010. Forecasting the ocean state using NEMO: The new FOAM system. *Journal of Operational Oceanography*, 3: 3-15.
- Strandberg, G., Barring, L., Hansson, U., Jansson, C., Jones, C., Kjellstrom, E., Kolax, M., Kupiainen, M., Nikulin, G., Samuelsson, P., Ullerstig, A., Wang, S., 2014. CORDEX scenarios for Europe from the Rossby Centre regional climate model RCA4. Reports Meteorology and Climatology 116, SMHI, SE-601 76 Norrköping, Sweden.
- Taylor, K., R. J. Stouffer, and G. A. Meehl (2012), An overview of cmip5 and the experiment design, *Bull. Am. Meteorol. Soc.*, 93, 485498, doi :10.1175/BAMS-D-11-00094.1.
- Tietsche, S., Balmaseda, M. a., Zuo, H., & Mogensen, K. (2015). Arctic sea ice in the global eddy-permitting ocean reanalysis ORAP5. *Climate Dynamics*. <http://doi.org/10.1007/s00382-015-2673-3>
- Tietsche, S., Notz, D., Jungclaus, J. H., and Marotzke, J., 2013. Assimilation of sea-ice concentration in a global climate model – physical and statistical aspects. *Ocean science*, 9, 19-36.
- Valente, A., Sathyendranath, S., Brotas, V., Groom, S., Grant, M., Taberner, M., Antoine, D., Arnone, R., Balch, W. M., Barker, K., Barlow, R., Bélanger, S., Berthon, J.-F., Beşiktepe, Ş., Brando, V., Canuti, E., Chavez, F., Claustre, H., Crout, R., Frouin, R., García-Soto, C., Gibb, S. W., Gould, R., Hooker, S., Kahru, M., Klein, H., Kratzer, S., Loisel, H., McKee, D., Mitchell, B. G., Moisan, T., Muller-Karger, F., O'Dowd, L., Ondrusek, M., Poulton, A. J., Repecaud, M., Smyth, T., Sosik, H. M., Twardowski, M., Voss, K., Werdell, J., Wernand, M., and Zibordi, G.: A compilation of global bio-optical in situ data for ocean-colour satellite applications, *Earth Syst. Sci. Data*, 8, 235-252, doi:10.5194/essd-8-235-2016, 2016.
- Vancoppenolle, M. et al. Simulating the mass balance and salinity of Arctic and Antarctic sea ice. 1. Model description and validation. *Ocean Modelling*, 27(1), 33-53 (2009).
- van der Werf, G. R., Randerson, J. T., Giglio, L., Collatz, G. J., Mu, M., Kasibhatla, P. S., Morton, D. C., DeFries, R. S., Jin, Y., and van Leeuwen, T. T.: Global fire emissions and the contribution of deforestation, savanna, forest, agricultural, and peat fires (1997–2009), *Atmos. Chem. Phys.*, 10, 11707-11735, doi:10.5194/acp-10-11707-2010, 2010.
- Voldoire, A., E. Sanchez-Gomez, D. Salas y Méliá, B. Decharme, C. Cassou, S. Sénési, S. Valcke, I. Beau, A. Alias, M. Chevallier, M. Déqué, J. Deshayes, H. Douville, E. Fernandez, G. Madec, E. Maisonnave, M.-P. Moine, S. Planton, D. Saint-Martin, S. Szopa, S. Tyteca, R. Alkama, S. Belamari, A. Braun, L. Coquart, and F. Chauvin (2013), The CNRM-CM5.1 global climate model: description and basic evaluation, *Clim. Dyn.*, 40, 2091, doi: 10.1007/s00382-011-1259-y.
- Wagner, W., Dorigo, W., de Jeu, R., Fernandez, D., Benveniste, J., Haas, E., Ertl, M., 25 August–1 September 2012. Fusion of active and passive microwave observations to create an essential climate variable data record on soil moisture. In: XXII ISPRS Congress, Volume I-7. ISPRS Annals of the Photogrammetry, Remote Sensing and Spatial Information Sciences (ISPRS Annals), Melbourne, Australia, pp. 315–321.

CMUG Phase 2 Deliverable

Reference: D3.1: Quality Assessment Report
Due date: June 2017
Submission date: 21 December 2017
Version: 4



-
- Warren, S., Eastman, R., & Hahn, C. J. (2015). CLOUDS AND FOG | Climatology. In Encyclopedia of Atmospheric Sciences (pp. 161–169). <http://doi.org/10.1016/B978-0-12-382225-3.00113-4>
- Waters, J., Lea, D.J., Martin, M.J., Mirouze, I., Weaver, A. and While, J. 2015. Implementing a variational data assimilation system in an operational 1/4 degree global ocean model. Quarterly Journal of the Royal Meteorological Society, 141(687), pp.333-349.
- Wenzel, S., Cox, P. M., Eyring, V. and Friedlingstein, P. (2014) Emergent constraints on climate-carbon cycle feedbacks in the CMIP5 Earth system models. *Journal of Geophysical Research: Biogeosciences*, 119(5),794-807.
- While, J., Haines, K. and Smith, G. 2010. A nutrient increment method for reducing bias in global biogeochemical models. *Journal of Geophysical Research: Oceans*, 115(C10).
- Zuo, H., Balmaseda, M. A., and Mogensen, K. (2015). The new eddy-permitting ORAP5 ocean reanalysis: description, evaluation and uncertainties in climate signals. *Climate Dynamics*. <http://doi.org/10.1007/s00382-015-2675-1>

CMUG Phase 2 Deliverable

Reference: D3.1: Quality Assessment Report

Due date: June 2017

Submission date: 21 December 2017

Version: 4



Appendix 1: Status of WP research reported on in this deliverable

WP	Name	Lead partner	Status
3.1	Assessment of Marine ECVs in FOAM Ocean Model	Met Office	New results presented in this report.
O3.1	Integrated assessment of Marine ECVs in the ORA system	ECMWF	New results presented in this report.
3.2	Assimilation of several L2 ozone products in the ERA system	ECMWF	Work completed in 2016, no update.
3.3	Integrated assessment of the CCI Aerosols, GHG, and Ozone datasets	ECMWF	New results presented in this report.
3.4	Integrated assessment of CCI terrestrial ECVs impact in the MPI-ESM	MPI-M	New results presented in this report.
O3.4	Cross assessment of clouds, water vapour, aerosols, ozone, GHG, SST, radiation and soil moisture impact on global climate variability and trends	SMHI	New results presented in this report.
3.5	Coupled climate model assessment	IPSL	New results presented in this report.
3.6	Improved process understanding from Arctic and Antarctic cross ECV assessment	MPI-M	New results presented in this report.
3.7	Cross-Assessment of Aerosols, Cloud and Radiation CCI ECVs	DLR	Work completed in 2016, no update.
3.8	Cross assessments of clouds, water vapour, radiation, soil moisture for regional climate models	SMHI	Work completed in 2016, subsequent research in this area was redirected to WP3.14.
3.9	Cross assessments of ESA CCI glacier, land cover and sea level data for hydrological modelling of the Arctic Ocean drainage basin	SMHI	New results presented in this report.
3.10	Cross-assessment of CCI-ECVs over the Mediterranean domain	Meteo France	New results presented in this report.
O3.11	Assessment of sea ice concentration observational uncertainty from a data assimilation point of view	BSC	New results presented in this report.
3.12	Assessment of Antarctic ice sheet ECVs for modelling	ULB	New results presented in this report.
3.13	Assessment of Greenland ice sheet ECVs for modelling	VUB	New results presented in this report.